The ALICE Project at the IPN, OrsayR&D and software developments 1996-2003

Marion Maccormick

Habilitation à diriger les recherches

Marion MacCormick
January 2007

The ALICE Project at the IPN, Orsay

R&D and software developments 1996-2003

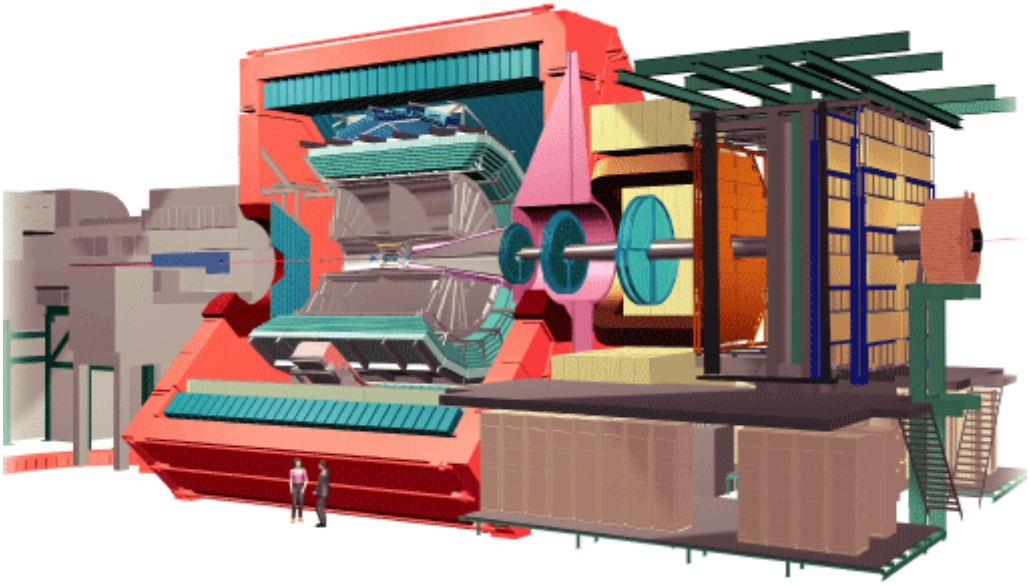

The ALICE detector

Université Paris Sud XI - UFR Scientifique d'Orsay
DIVISION de la RECHERCHE
Service des Etudes Doctorales

vvvvvvvvvv

N° d'ordre :

1010

HABILITATION À DIRIGER LES RECHERCHES

Vu l'arrêté du 25 Avril 2002

Vu l'avis favorable du Conseil Scientifique de l'Université du : 7 FEVRIER 2007

Vu l'autorisation d'inscription délivrée par le Président de l'Université le : 19 FEVRIER 2007

Vu l'autorisation de soutenance délivrée par le Président de l'Université le : 23 FEVRIER 2007

à Madame MAC CORMICK Marion

né(e) le 25 AVRIL à GLASGOW (ECOSSE)

Vu la délibération du jury réuni le : 21 MARS 2007

et composé de :

Monsieur POLYCHRONAKOS Venetios
Monsieur MITTIG Wolfgang
Monsieur SMITH Elton
Monsieur LE BORNEC Yves PRESIDENT
Monsieur BERTHIER Bernard
Monsieur BLUMENFELD Yorick

l'HABILITATION A DIRIGER LES RECHERCHES SCIENCES PHYSIQUES

est conférée à Madame MAC CORMICK Marion

pour en jouir avec les droits et prérogatives qui y sont attachés.

Signature du titulaire :

Fait à Orsay le, 21 MARS 2007

La Responsable Administrative
de la Division de la Recherche

UNIVERSITÉ PARIS-XI
CENTRE SCIENTIFIQUE D'ORSAY
DIVISION DE LA RECHERCHE

Madeleine PERRIN
Attachée Principale
Responsable Administrative

IQ 951101

The ALICE Project at the IPN, Orsay 1
R&D and software developments 1996-2003 1
About this document 5
The Quark-Gluon Plasma 7
Essential aspects of deconfinement 7
Energy and temperature dependence 7
Temperature calculation results 8
Thermal disassociation, interaction range and colour screening 9
The NA50 physics motivation 12
The NA50 experiment 13
Main NA50 Results 15
The dimuon invariant mass spectrum 15
The Drell-Yan (DY) reference process 16
Normal J/ψ and ψ′ absorption in p-A collisions 17
J/Ψ and Ψ′ production in Pb-Pb collisions 18
Measured-to-expected ratios 20
The Future at the LHC 22
An introduction to ALICE 24
The collaboration *(in 2001)* 24
Detector overview 24
Central barrel 24
Dimuon arm spectrometer in brief 25
Dimuon arm requirements 26
Fluxes 26
Interaction rate 27
Mass resolution and trajectory reconstruction 27
Detector spatial resolution 27
Chamber sizes 27
Efficiencies 28
Thickness 28
Layout 28
Tracking stations 30
Cathode pad chambers 31
General cathode pad chamber design 31
How does it work? 31
Impact point reconstruction using the induced charge 33
Understanding the key detector parameters – a personal note 36
The R&D Phase (1996-2000) – a personal overview 37
R&D foreword 37
Prototype Studies 37
The Electronics Project 40
Simulations – detector and the electronics response 41
Software codes for event readout and reconstruction 42
The postTDR period 42
Models and simulations (2001-2002) 43
The electronics mapping 44
Electronics implementation studies 45
R&D prototypes and tests 49
ALICE0 53
Aims 53
Detector geometry 53
Gas supply 55
Electronics 56

Readout/acquisiton 56
Online monitoring 57
ALICE0 Results 58
Gas gain estimation 58
Electronics and cathode plane response 59
ALICE1 63
Aims 63
Detector geometry 64
Gas supply and filling gas 65
Electronics 65
Readout/acquisition 66
Test beam setup 67
Online monitoring 69
Offline reconstruction 69
ALICE1 - Status Reports, Results and Simulations 71
June'97 tests at the PS Status report 72
Sept'97 tests at the PS Status report 75
April'98 tests at the SPS Status report 79
ALICE1 Simulations 88
Modelling the test-beam data 89
Introduction – ingredients for the model 89
Model conclusion 92
Electronics modelling 94
Using the detector model 94
Electronics noise 94
Dynamical range 95
Crosstalk 96
Other parameters 97
Calibration 98
Electronics conclusion *(text from 1999)* 100
ALICE 2 – full scale prototype of one quadrant 103
Aims 103
Mechanical issues 103
Electronics issues 103
Beam Tests 104
Detector geometry 104
Mechanics - Assembly and construction 105
Electronics 111
Local readout cards for 64 channels 111
Gas supply 116
Readout/acquisition 116
ALICE2 - electronics tests 118
GASSIPLEX and GAS64 tests 118
PLAC motherboard tests 118
GASSIPLEX and GAS64 test results *(from [16])* 119
Noise levels 119
Pedestal dispersion 120
Linearity measurements 120
Gain estimate 121
PLAC motherboard test results 122
Noise measurement – first test 122
Noise measurement – second test 122
Noise measurement – third test 122
ALICE2 - mechanical tests 124

The performance of different gas mixtures 124
Number of pads hit per event 125
Gain 126
Spatial resolution 127
ALICE 3 131
Aims 131
Detector geometry 131
Electronics 133
Readout/acquisiton 133
Test beam layout 134
Online monitoring 134
Offline reconstruction 136
Results 136
QUADRANT ZERO 141
Aims 141
Detector geometry 141
Gas supply 142
Electronics 142
The end of the R&D tests - a personal note 142
THE VIRTUAL DETECTOR IN AliROOT 145
ALICE 151
Closing comments 158
APPENDIX A 159
Ionization detectors – a brief history 161
Gas Gain 162
Describing gas gain through ionization – a potted history 162
Empirical Gas Gain Formulae 163
APPENDIX B - TestBeamToolBox.pdf 169
APPENDIX C - quadrant0.pdf 171
APPENDIX D - mappingPackage.pdf 173

About this document

This document is based on personal work carried out between 1996 and 2003.

In 1996, I became a member of two international collaborations, NA50 which was already up and running at CERN and ALICE, the future LHC project which was at the beginning of its R&D phase. The common theme in these projects is the study of ultra-relativistic heavy ion collisions, and in particular the study of heavy quarkonium states and the search for a possible quark-gluon plasma (QGP) phase transition.

I was actively involved in the NA50 data taking as of 1996 till the final run in 2000, and so in the opening chapter I recall the main ideas in the current theories describing of the behaviour of heavy quarkonia states in a very high energy density environment[♦]. The NA50 experiment measured quarkonia resonances, and found anomalous suppression of quarkonia resonances in the most violent head-on collisions. The question remains: were these resonances suppressed due to an accumulation of normal intra-nuclear effects? Or were they suppressed due to a change in the fundamental rules of physics, as would be expected with the formation of a QGP? Since the year 2000 the NA50 collaboration has made an extra-ordinary effort to carry out as many complementary analyses as possible, with the reworking of the different data sets using more efficient reconstruction algorithms, in order to deliver results of the highest precision. In this document the discussion on this subject will be limited to the citation of the most recent NA50 results of relevance to the QGP puzzle.

The bulk of this report is comprised mainly of "snapshots" of the R&D project that was pursued at the IPN in Orsay for the ALICE Dimuon Arm Collaboration. The idea here is to regroup the full set of prototype models, with the technical specifications and their associated test programs. The main results are given for each set of tests, but the details of how data sets were analysed are not included since those details are already available in other, more formal, write-ups. Full references to the associated documents are given. The result is a kind of "scrapbook" of the R&D phase associated with the ALICE dimuon arm station 1 tracker, one of the five tracker stations implemented in the Dimuon Arm Spectrometer.

After a general introduction detailing the main ALICE dimuon spectrometer specifications, there follows a very brief look at several key subjects useful for understanding the main detector characteristics. An attempt to place the subject in its historical situation is given in Appendix A. A general view of the different R&D topics is given, followed by the description of the successive prototypes. The amount of technical detail given in each case is a personal choice and reflects my own level of implication.

The R&D starts with the post-Technical Proposal period (1996), where we only had ideas, gleamed from the abundant literature, but no detector or electronics. Some postdocs had already worked on reconstruction techniques with a parameterization of the key detector parameters (see references [**1**] and [**2**]) and started to explore plausible detector layouts. I then participated in all the prototype developments that continued up to the publication of the Technical Design Report (1999) and the Addendum (2000). In this report I wanted to regroup the different detector models in such a way that the questions being asked at each stage are clear. This technical document is the only one that regroups them all, admittedly in a somewhat "dry" approach. Excerpts from real experimental logbooks are occasionally included as are the slides from several talks.

Beyond 2000, detector refinements were carried out, and I went on to work on the virtual detector construction. The detector details were now well established and they had to appear in the AliROOT

♦ The theoretical description is taken from a single reference by Helmut Satz, his description is far clearer than anyone else's, and I have adapted the relevant parts of his paper to fit the needs of this report. The aim is to provide the basic phenomenological arguments used in the interpretation the NA50 (and perhaps also for the future ALICE) experimental program.

software environment, and so I devoted the main part of my time to making this happen. There is less said in this report about those developments since they were fully documented at the time, and the main texts are included at the end of the report in Appendices C and D.

It is obvious that all aspects of this work are the result of collaborations between physicists, engineers and technicians from within and beyond the laboratory and so I aim to remain as neutral as possible in laying claim to any single part of the work. Nonetheless, I hope my responsibilities with respect to the students that I guided at different times will be apparent.

The Quark-Gluon Plasma

A phase transition, going from confined hadronic matter to deconfined partonic matter, was first proposed by Matsui and Satz in 1984 [**3**]**.** Their prediction was based on QCD calculations where, at high enough energy densities and temperatures the local parton densities are such that the individual hadron boundaries are indiscernible - the individual quarks are no longer bound in their parent hadron - resulting in a plasma of quarks and gluons where the quarks could be described to be in a deconfined state. This state, normally ruled out in our world of cold hadronic matter where all quarks are confined, would lead to a new state of strongly interacting matter, never observed before. The analogy is often made with the state of matter as it may have been at the beginning of the Universe in the Big Bang. In a simplistic view, the consequence of this phase transition is that the normal rules for hadronisation, and therefore the relative abundances of 'new' matter, would be modified since, in the very hot and dense medium it would be more favourable to produce a greater quantity of easy-to-make lightweight quarks whilst making life more difficult for the rarer heavy quarks to encounter each other, and so leading to a diminution in the resonant heavy quark production.

The mechanism that is of particular interest in the NA50 and ALICE studies is the production of heavy quarkonia resonances. However, in order to appreciate the NA50 results and understand the challenge facing ALICE, some of the relevant points from the theoretical front are presented in the following paragraphs. The aim here is to give a general view of the subject as opposed to a detailed review.

Essential aspects of deconfinement [*adapted from reference 4*]

Energy and temperature dependence

The transition from hadronic matter to a plasma of deconfined quarks and gluons has been extensively studied in finite temperature lattice QCD. A phase transition occurs when new degrees of freedom open up, and in this case the new degrees of freedom are the deconfinement of the quarks. These extra degrees of freedom should be associated with an increase in the energy density of the system. The argument can be understood by comparison with an ideal gas of massless pions, where the energy density is

$$\varepsilon_{\pi} = 3\frac{\pi^2}{30}T^4 \cong T^4$$

Corresponding to the three possible pion charges, while an ideal quark-gluon plasma, with two massless quark flavours gives

$$\varepsilon_{QGP} = \left\{2\times 8 + \frac{7}{8}\left[2\times 2\times 2\times 3\right]\right\}\frac{\pi^2}{30}T^4 = 37\frac{\pi^2}{30}T^4 \cong 12T^4$$

as determined by the 16 gluonic and 24 quark-antiquark degrees of freedom. So, around a critical transition temperature T_c the energy density increases by roughly a factor ten.

The results from finite temperature lattice QCD are shown in Figure 1 and Figure 2.

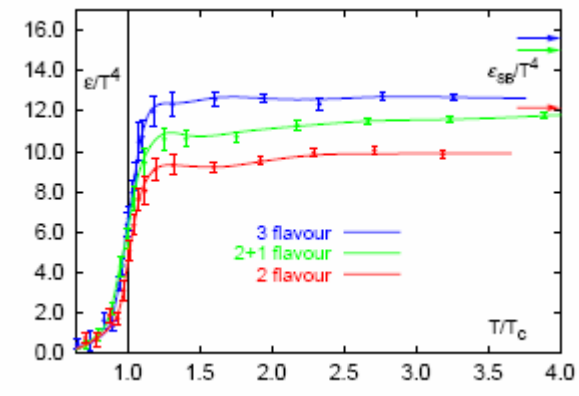

Figure 1 : Energy density versus T**.**

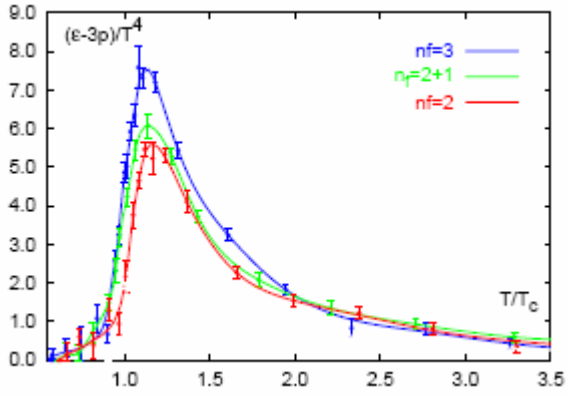

Figure 2 : The 'interaction measure', $\Delta = (\varepsilon - 3P)/T^4$ versus T.

Above the critical temperature the quarks and gluons are deconfined. This means that the requirement to form neutral colour states is removed, and that as shown in Figure 2, the measure of the strong interaction is non-negligible up to $T \approx 3T_c$ and does not vanish, as would be the case for an ideal gas of massless constituents.

Temperature calculation results

The critical temperature at which deconfinement could set in depends on the masses and the number of quark flavours and colours, but the transition is thought to coincide with the onset of the restoration of chiral symmetry for the lighter quark masses. In this latter case, supposing massless bare quarks in the chiral limit, then, under normal conditions, the quarks acquire an effective mass through gluon dressing. At the critical temperature, thermal motion removes the gluons and so the quark masses tend to their bare values (which is zero, in this chiral condensate model).

The critical temperature at which this gluon disassociation could occur has been the subject of much debate, but most studies indicate a value of $T_c = 175 \pm 10\text{MeV}$ as shown in Figure 3.

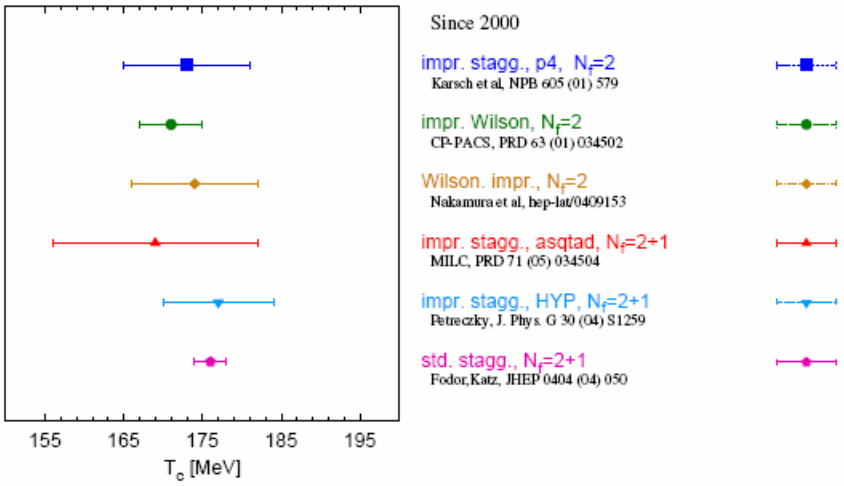

Figure 3 : Critical temperature results from different lattice studies.

Thermal disassociation, interaction range and colour screening

A scenario describing the hypothetical evolution of a heavy $Q\overline{Q}$ pair in a progressively hotter and denser medium has been developed and highlights the relationship between the temperature, the interaction range, and the means by which heavy quark coupling is disassociated through colour charge screening goes (roughly) as follows [**4**]**:**

Consider a finite box containing a medium of vanishing baryon density at temperature $T = 0$, ie. an empty box at $T = 0$. In the box we place a heavy (static) $Q\overline{Q}$ pair with a string tension defined as

$$F(r) \sim \sigma r$$

where $\sigma \approx 0.16\,\mathrm{GeV}^2$ is the string tension as determined in the spectroscopy of heavy quark resonances. So $F(r)$ increases as the separation increases, until it reaches the value of a pair of dressed light quarks (about the mass of a ρ meson), where it becomes favourable to produce a $q\overline{q}$ pair from the vacuum, break the string and form two light-heavy mesons ($Q\overline{q}$) and ($\overline{Q}q$). These can now be separated arbitrarily far without changing the energy of the system. The evolution is shown schematically in Figure 4.

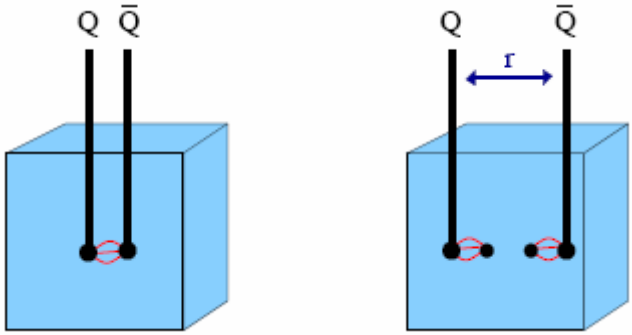

Figure 4 : String breaking for a $Q\overline{Q}$ system.

The string breaking energy for charm quarks is found to be

$$F_0 = 2(M_D - m_c) \approx 1.2\mathrm{GeV}$$

with the lowest lying open charm state $M_D = 1.87\mathrm{GeV}$ and $m_c = 1.25\mathrm{GeV}$.

For bottom quarks with $m_b = 4.65\mathrm{GeV}$ and the lowest lying open bottom state $M_B = 5.25\mathrm{GeV}$

one obtains the same value

$$F_0 = 2(M_B - m_b) \approx 1.2\mathrm{GeV}.$$

The string breaking occurs when the two heavy quarks are separated by a distance

$$r_0 \approx \frac{1.2\mathrm{GeV}}{\sigma} \approx 1.5\ \mathrm{fm},$$

and which is independent of the mass of the heavy quarks connected by the string.

If the system is then heated (ie. T>0) the medium begins to contain light mesons, and the large distance $Q\overline{Q}$ potential $F(\infty, T)$ decreases, since we can use these light hadrons to achieve an earlier string breaking, resulting in an effective screening of the interquark force. This idea is shown schematically in Figure 5.

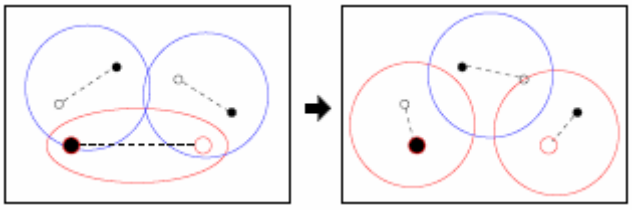

Figure 5 : In-medium string breaking through recoupling.

Further increasing the temperature up to the critical temperature T_c, at which deconfinement sets in, then the chiral symmetry restoration causes a sharp drop in the light quark constituent masses as the gluon dressings dissolve into the medium and consequently increase the density of constituents. Consequently, $F(\infty,T)$ continues to drop sharply. Above T_c, light quarks and gluons become deconfined colour charges, and this quark-gluon plasma leads to a colour screening, which limits the range of the strong interaction. The screening radius r_D, which determines this range, is inversely proportional to the density of charges, so that it decreases with increasing temperature. As a result, the $Q\overline{Q}$ interaction becomes more and more short-ranged.

Deconfinement is thus clearly reflected in the temperature behaviour of the heavy quark potential as the string breaks at shorter distances with the increasing temperature, and the interaction range shortens around the critical temperature.

This in-medium behaviour of heavy quark bound states implies that they can be used as a temperature probe of the state of matter in QCD thermodynamics. This can be illustrated with the bound charmonium states J/ψ, χ_c, and ψ′, each having different binding energies, the binding radii being 0.50, 0.72 and 0.9 fm respectively (as calculated using non-relativistic potential theory). The ψ′ being the least tightly bound implies that it will be the first charmonium state influenced by the shortening range of the strong interaction in the medium. When this range descends below the size of the ψ′, the c and $\overline{c}$ can no longer see each other, and the resonance 'melts' into the medium. Since the three charmonium states are of different sizes, the melting will happen sequentially, starting with the most loosely bound state. This is shown schematically in Figure 6.

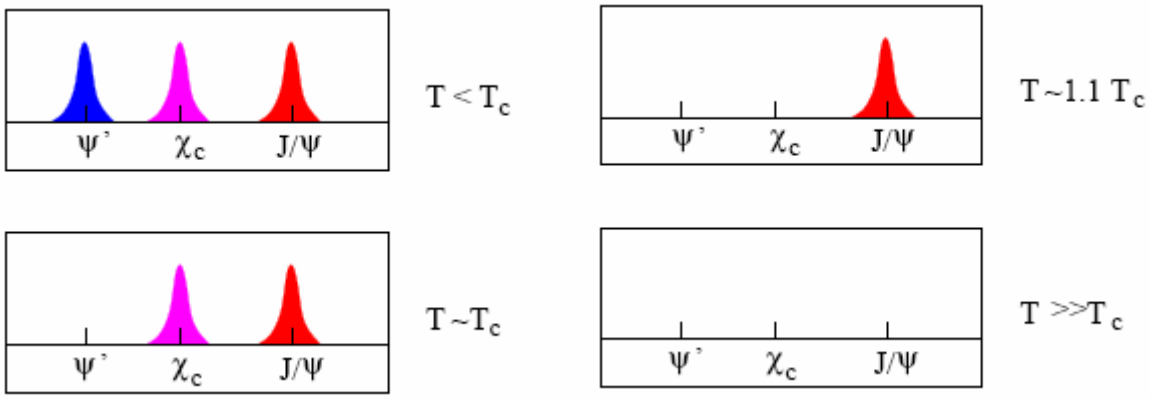

Figure 6 : Charmonium spectra at different temperatures.

Finite temperature lattice QCD also provides the temperature dependence of the energy density, the heavy quark states can therefore also be specified in terms of the energy density, ε. The overall behaviour in terms of disassociation radii, energy densities and temperature is summarized in Figure 7.

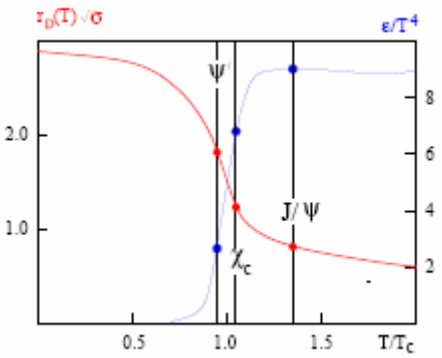

Figure 7 : Charmonium disassociation versus temperature and energy density.

The NA50 physics motivation

The NA50 experiment at CERN studied light- to heavy-ion collisions with the aim of putting Matsui and Satz' convincing proposal of a quark-gluon phase transition, to test. The hadroproduction of charmonia is viewed a three step process, starting with the creation of a $c\bar{c}$ due to gluon fusion. This pair is generally in a colour octet state and will neutralise its colour by interacting with the surrounding colour field. The precise nature of this interaction is not yet fully understood, but it is required for the physical J/ψ or ψ′ resonances to appear. All of this implies a certain formation time for the physical resonant state to appear, and so during this time, other strong interactions can intervene. The process is described schematically in Figure 8. So, the hadronic medium surrounding the newly formed $c\bar{c}$ pair will manifest itself differently depending on the J/ψ formation time, and the state of the surrounding matter.
In a quark gluon plasma, it is expected that the $c\bar{c}$ potential will be screened by the very high density of surrounding colour charges.

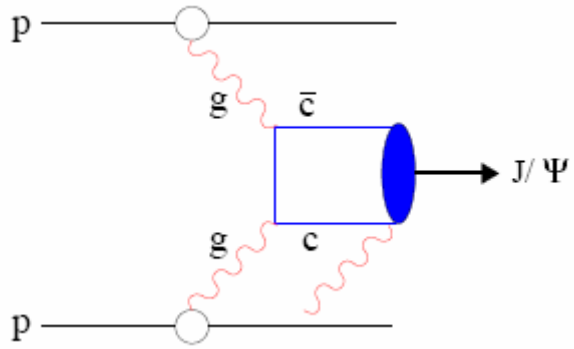

Figure 8 : Evolution of J/ψ production.

Dimuon production through the Drell Yan (DY) process is used to normalize the different NA50 data sets. This process, as shown in Figure 9, resulting in a dimuon pair through quark-antiquark annihilation between the target and projectile nuclei, is insensitive to the surrounding hadronic medium.

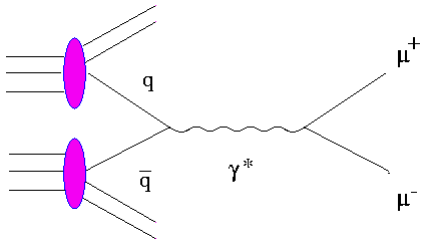

Figure 9 : Drell Yan process: dimuon production through quark-antiquark annihilation.

The interest in using DY as a reference lies in the fact that the cross section has been measured in several reactions [**5**, **6** and **7**] and is found to scale linearly with the number of NN collisions, going from p-p up to Pb-Pb. For the NA50 experiment it presents identical selection criteria as the charmonia and so in the normalization process most of the systematic errors cancel out. However, this channel has low statistics, particularly at higher invariant masses.

The p-A collisions cannot reach the energy densities required for a phase transition. The p-A systematic study therefore provides the reference for 'normal' J/ψ and ψ′ nuclear absorption. The A-A collisions however have access to much higher energy densities, depending on the centrality of the collision. If there is a phase transition, the J/ψ and ψ′ production rates are expected to be reduced when comparing central to peripheral collisions, with respect to the expected 'normal' intra-nuclear

absorption. Beyond this, as pointed out by Satz **[4],** the more loosely bound ψ′ state is expected to dissolve more easily as compared to J/ψ, and this effect is termed as sequential suppression.

To fix the numbers, only 60% of the J/ψ hadroproduction are from direct production, 30% come from the decay of the higher state $\chi_c \rightarrow$ J/ψ + *anything* and the final 10% are from the ψ′→ J/ψ + *anything* decay. The feed-down channels are each long-lived states (with decay widths < 1 MeV), and so any medium effects would first influence the initial particle state as opposed to the decay products. The ψ′ production in NA50 is all direct production.

The NA50 experiment

These experimental studies ran from the mid 1980's under the name NA38 and from the mid 90's till the year 2000 as NA50. The NA38 to NA50 name change is due to a detector upgrade. All the experiments used the NA10 dimuon spectrometer as the baseline equipment. The NA50 layout is shown in Figure 10.

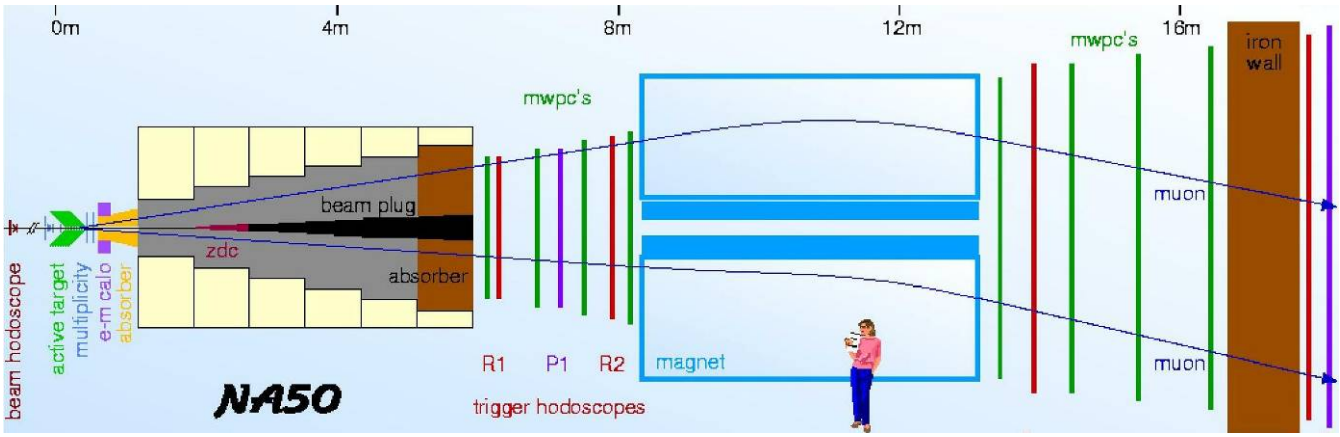

Figure 10 : The layout of the NA50 experimental apparatus.

The main characteristics of the apparatus are summarized below, and full details can be found in [**8**].

Kinematical domain

$2.92 \leq Y_{lab} \leq 3.92$ $|\cos\theta_{CS}| < 0.5$ $0 < y_{CM} < 1$

Acceptances (Pb-Pb at 158 GeV)

J/ψ	12.42 ± 0.02 (statistical) ± 0.17 % (systematic)
DY 2.9-4.5	13.79 ± 0.05 ± 0.16 %
ψ′	14.77 ± 0.03 ± 0.26 %

The experimental trigger was set for dimuon pairs, and the layout was optimized for J/ψ with a mass resolution of around 3 % (rms).

Between 1995 and 2000 NA50 carried out a series of measurements of charmonia production in p-A systems in fixed target experiments at 400 GeV and 450 GeV. Pb-Pb collisions at 158 GeV were also studied. All measurements were accomplished within the same equipment. A summary of the different data taking periods with the principle beam-target setup is given in

Table 1.

A segmented target was used to minimise multiple scattering in the target material, the interaction vertex of the outgoing muon pair being identified by a double coincidence in a system of quartz blades.

Year	Sub-targets	Target thickness	Beam intensity (ions/burst)	J/ψ	ψ′
1995	7 (in air)	17 % λ_{int}	3×10^7	50000	-
1996	7 (in air)	30 % λ_{int}	5×10^7	190000	-
1998	1 (in air)	7 % λ_{int}	5.5×10^7	49000	380
2000	1 (in vacuum)	10 % λ_{int}	7×10^7	129000	905

Table 1 : Summary of the different beam and target configurations and the approximate integrated particle production.

The different target materials studied in p-A collisions were Be, Al, Cu, Ag, W, and Pb. Special setups were used in different years in order to address particular experimental issues. In 1998, only one thin sub-target was used at a time. The aim was to look more closely at charmonium production in the more central collisions in a cleaner environment where rescattered peripheral collisions, that can simulate single head-on collisions, were greatly reduced. In 2000, Pb-air parasitic collisions were removed by placing the target in a vacuum, this allowed a cleaner sample of peripheral collisions to be collected and so give access to charmonia production at lower transverse energies.

The estimation of the centrality of the collisions is a key point in the experiment and so three independent centrality estimators were used, namely

- a Pb-scintillating fibres electromagnetic calorimeter used to measure the neutral transverse energy,
- a very forward hadronic calorimeter (Zero degree calorimeter) which essentially measures the energy of the beam spectator nucleons in the collision, and
- a silicon strip multiplicity detector used to sample the secondary charged particle production.

Full details of the many data analyses can be found in the papers referenced in the following paragraphs, and the references therein. Here, only the final results are summarized.

Main NA50 Results

The main, selected, results from NA50 shown in the following are:

- The Drell-Yan reference spectra used to normalize the quarkonia production [**9**]
- J/ψ and ψ′ normal nuclear absorption in p-A collisions
- J/ψ and ψ′ production and anomalous suppression in Pb-Pb collisions

The dimuon invariant mass spectrum

The invariant mass dimuon spectra are fitted for each of the seven centrality bins for five different contributions covering the J/ψ and ψ′ resonances, the Drell-Yan continuum, open charm ($D\overline{D}$) semi-leptonic decays and the unphysical combinatorial background due mostly to uncorrelated π and K decays. The exact recipe for disentangling these contributions is given, for example, in [**10**].

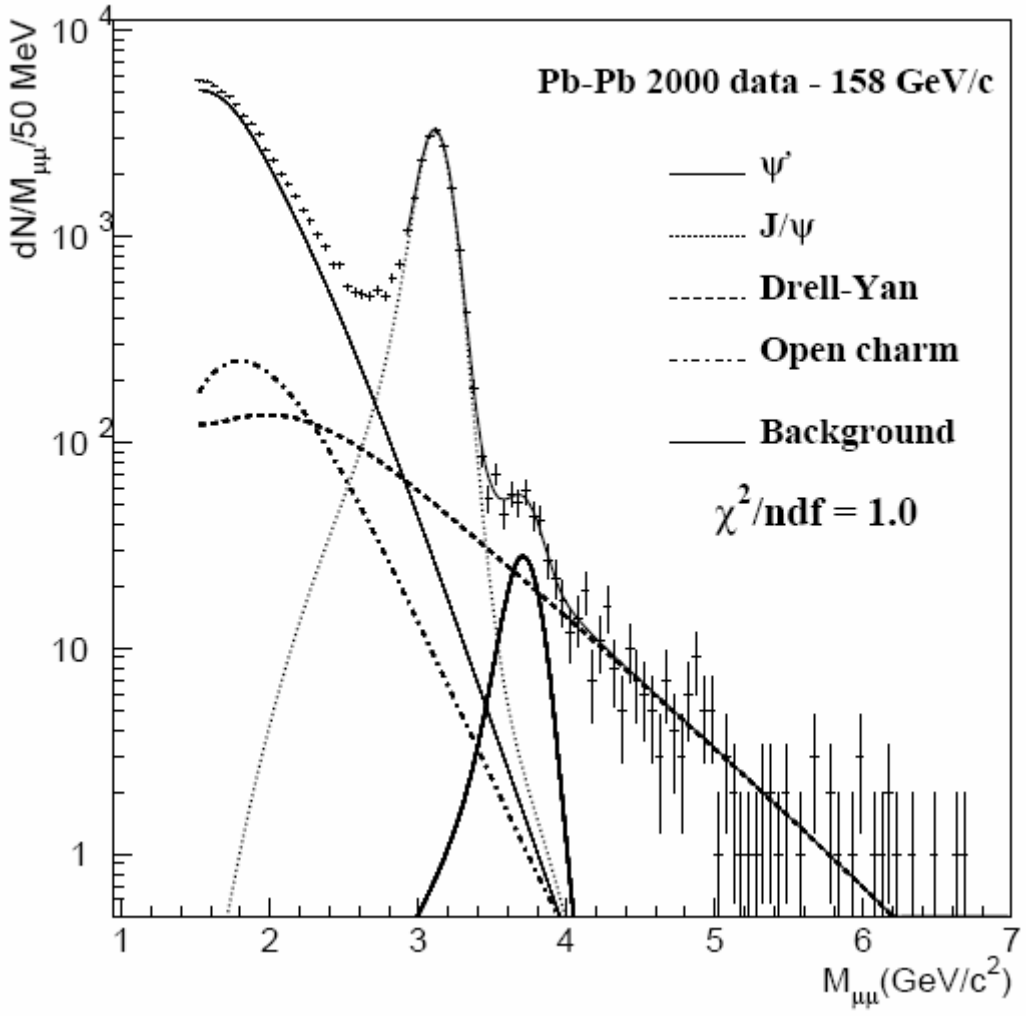

Figure 11 : An example of the fitted opposite sign dimuon invariant mass spectrum for mid-centrality Pd-Pb collisions.

The Drell-Yan (DY) reference process

The ratio between the measured and calculated DY cross section K_{exp} is shown in Figure 12. The constant behaviour in going from p-Be to Pb-Pb collisions shows that this process is proportional to the number of nucleon-nucleon collisions over the NA38/NA50 phase space. This confirms its validity as a reference for the hadronic production cross section

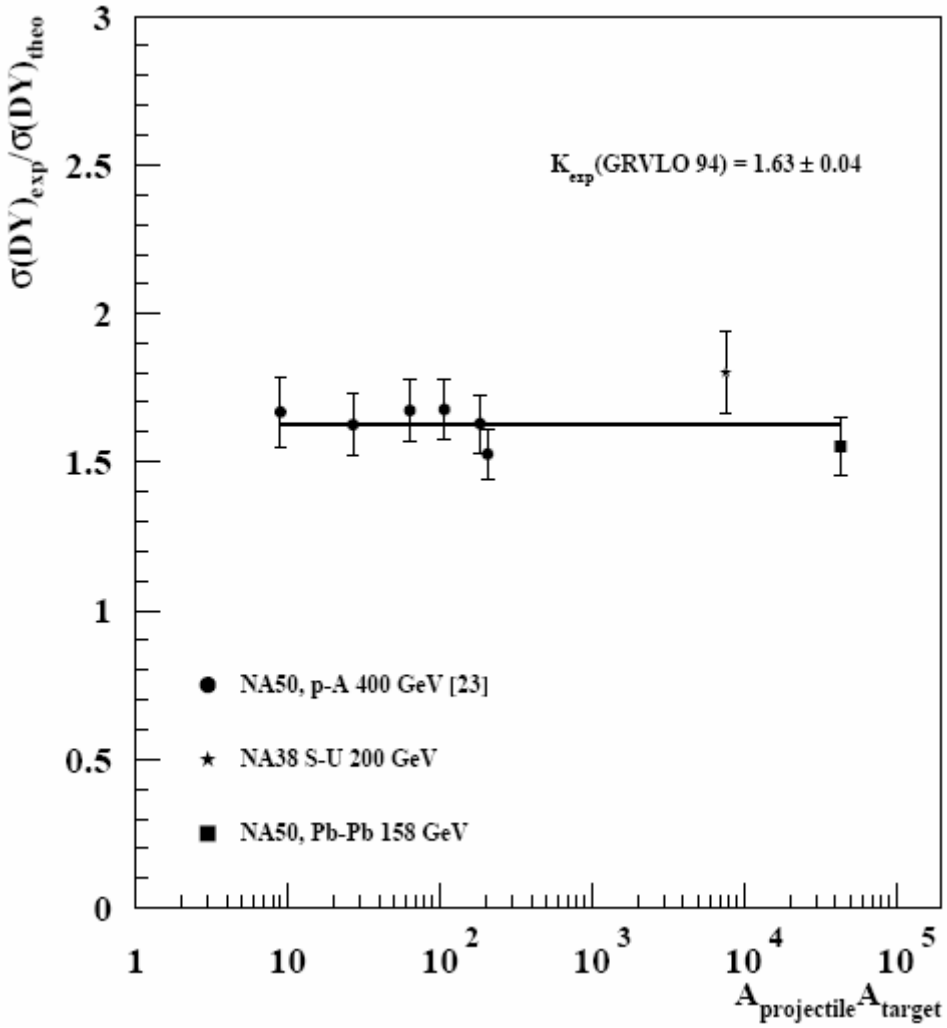

Figure 12 *:* Experimentally measured Drell-Yan dimuon pair production, for 158-400 GeV/c beam momenta in proton-A_{target} and $A_{projectile}A_{target}$ collisions, normalized to the lowest order theoretical Drell-Yan cross section. The K_{exp} factor is the ratio of the measured to calculated cross section **[9]**.

Normal J/ψ and ψ′ absorption in p-A collisions

The production cross sections were evaluated by three different methods [**11**]. Two results are shown in Figure 13 using the Glauber formalism. Within this framework, a proton-nucleus or nucleus-nucleus interaction is considered as a set of independent interactions between the target and projectile nucleons, assuming that the properties of the nucleons do not change after the first collision and that they can interact further with the same cross section. This is an approximation since a nucleon, after a collision, can be in an excited state and subsequently interact with another nucleon with a different cross section. This detailed model can be approximated, to first order, by a simpler 'ρL approximation' where ρ is the density of the nuclear matter and L is the average nuclear distance traversed by each outgoing charmonium state.

The different slopes, shown on a logarithmic scale in Figure 13, shows that the ψ′ clearly suffers a stronger nuclear absorption, as compared to the J/ψ state.

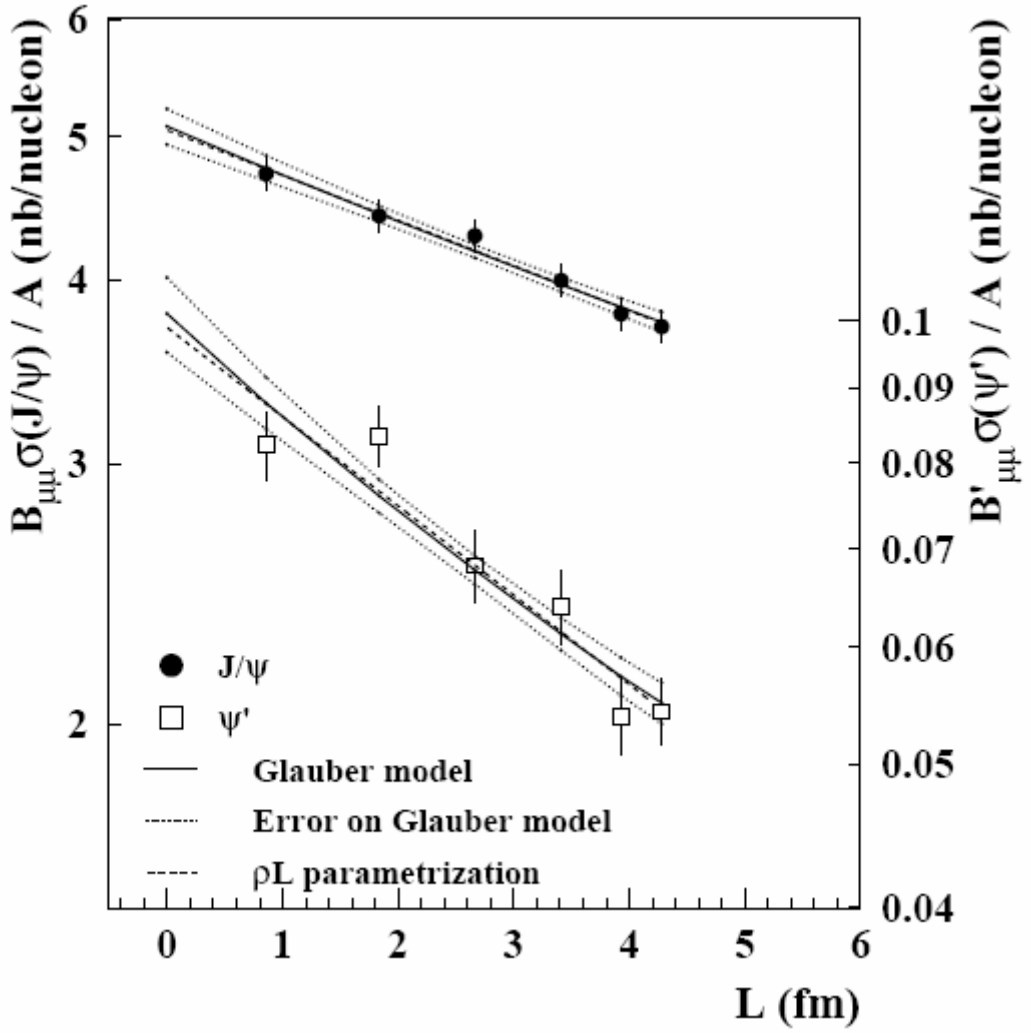

Figure 13 : Measured J/ψ and ψ′ production cross sections, per target nucleon, fitted with a Glauber model and shown with the ρL approximation **[11]**. Data come from 400 GeV/450 GeV fixed target proton collisions on Be, Al, Cu, Ag, W and Pb targets.

J/Ψ and Ψ′ production in Pb-Pb collisions

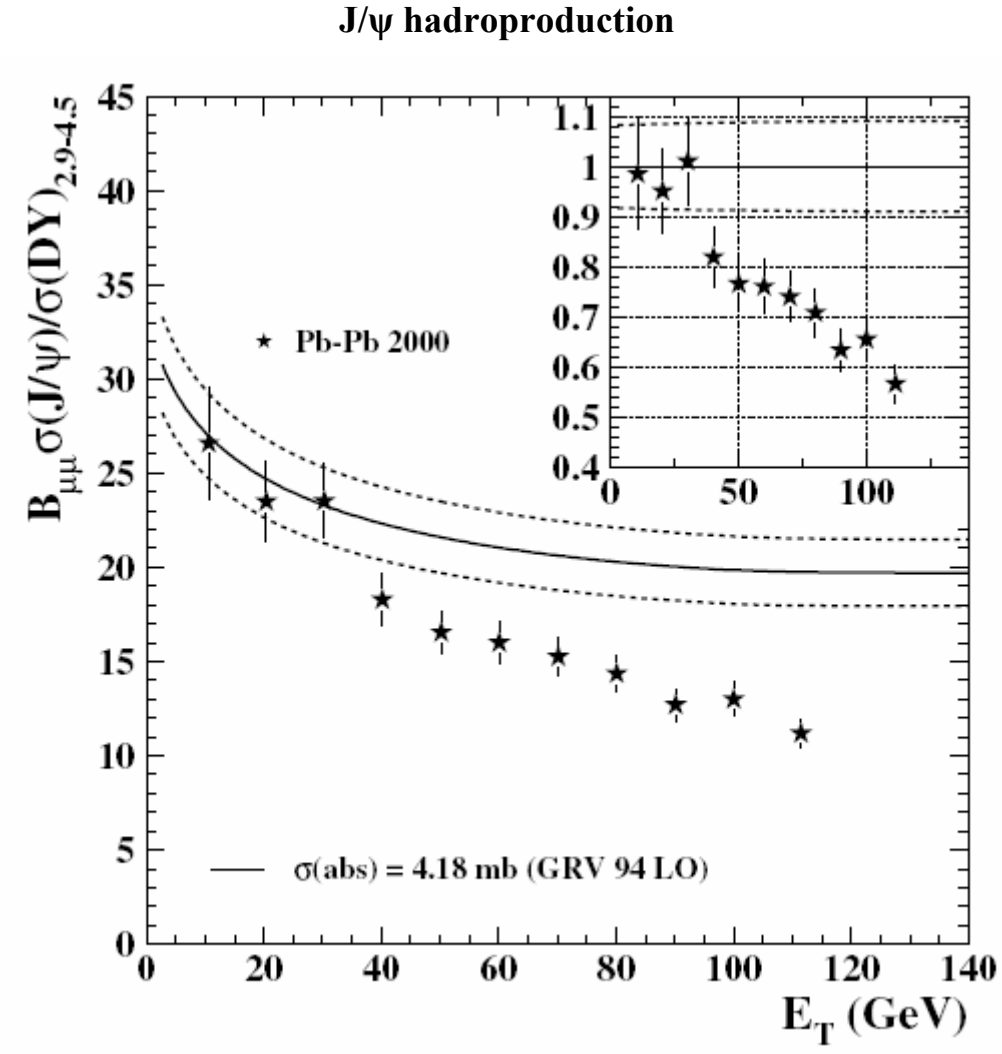

Figure 14 : The J/ψ /DY cross section ratio as a function of transverse energy for the Pb-Pb 2000 data. The normal absorption curve is shown with the combined error from the Glauber fit and the rescaling procedure (dashed curves) [**12**]. The inset shows the ratio Measured/Expected taking the normal nuclear absorption into account.

The peripheral J/ψ/DY ratio, as shown in Figure 14, is completely consistent with the pattern of normal nuclear absorption, as deduced from p-A collisions alone. The departure from the normal absorption pattern at E_T ~35 GeV, and the non-saturation at high E_T is clear.

This translates as normal nuclear absorption for impact parameters b > 0.85 fm, with σ_{abs} = 4.18 mb, derived from an extensive study of p-A collisions. For smaller impact parameters a departure from the normal nuclear absorption is observed, and persists up to the most central Pb-Pb collisions.

ψ´ hadroproduction

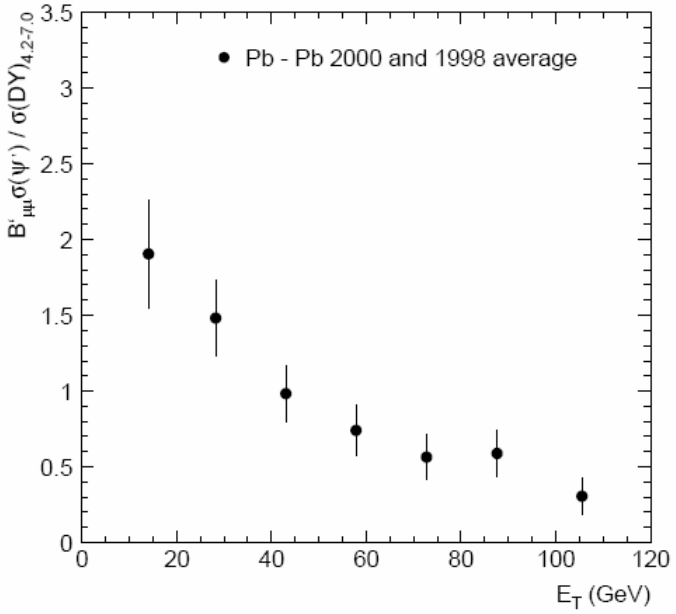

Figure 15 : The averaged ψ´/DY ratio, shown as a function of transverse energy, with the error bars as the quadratic sum of the statistical and systematic uncertainties **[9]**.

The corresponding result for the ψ´ hadroproduction is shown in Figure 15, full analysis details can be found in the associated reference.

Measured-to-expected ratios

Figure 16 shows the comparison between the expected and measured production rates for both particle states, and Figure 17 shows the two results, normalized to the expected production rate, allowing them to be presented in the same image. The results are shown as a function of L, the amount of nuclear matter traversed by the outgoing particle.

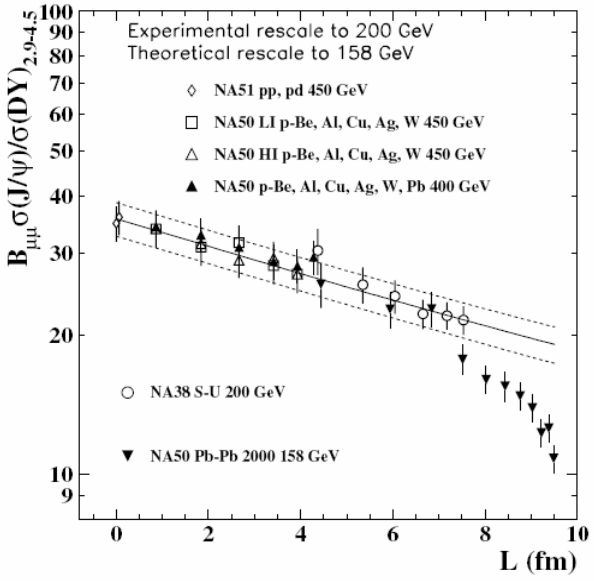

J/ψ

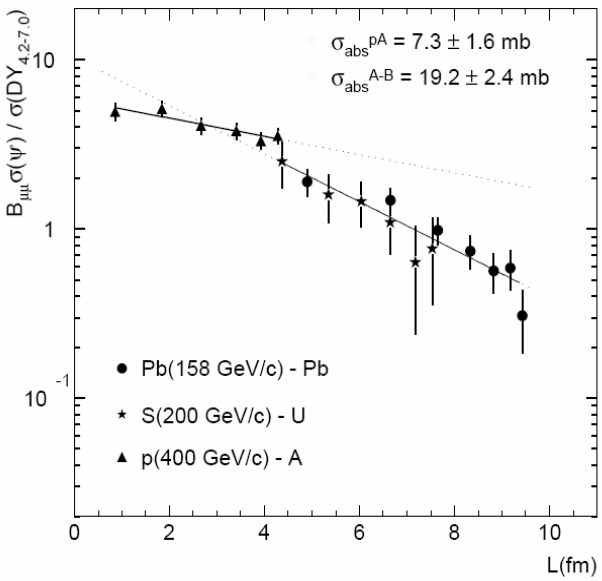

ψ´

Figure 16 : The measured-to-expected production rates for J/ψ and ψ´, and their behaviour as a function of the amount of nuclear matter traversed. The higher density collisions, from central Pb-Pb interactions create the larger systems and are correlated with high transverse energies. Statistical and systematic errors are added quadratically.

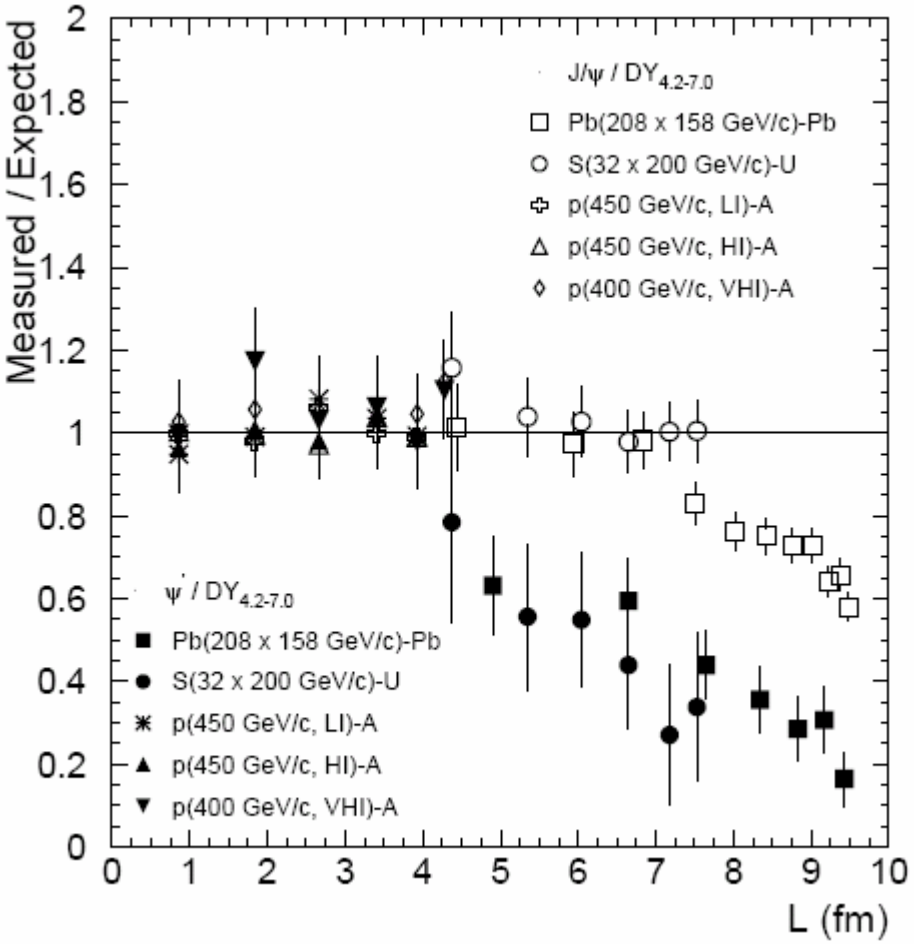

Figure 17 : Comparison of the J/ψ and ψ´ suppression patterns. The data are normalized to the expected production rates.

The anomalous suppression onset occurs at around 4.2 fm for the ψ´ as compared to 7.5 fm for the J/ψ. The general tendency is as expected for the case of colour charge screening due to a QGP phase transition. The more loosely bound ψ´ (337 keV wide) state is theoretically easier to dissolve as compared to the J/ψ (93 keV wide).

The J/ψ has two steps, at around 7.5 fm and 9.2 fm, with suppression factors of around 25% and an additional 15% respectively. This is interesting in the light of the sequential suppression scenario, where the J/ψ population measured in the NA50 experiment arises from feed-down of roughly 30% from the 2 MeV wide χ state and 10% from the ψ´ state. The χ would then be expected to dissolve first, followed by the ψ´ and finally the direct J/ψ state. The first two steps could be the source of the measured anomalous suppression.

These results alone, although convincing, are not enough to establish whether or not a phase transition did occur in the NA50 fixed target experiments since other correlated effects are expected, but were not measured in the same experiment. For example, the suppression of the J/ψ states could be correlated with a simultaneous increase in lighter, open charm states. It is only through the simultaneous measurement of several of the expected signals that a phase transition could be non-ambiguously identified and its basic characteristics extracted. This is the job of the current and next generation of experiments

The Future at the LHC

The ALICE experiment, currently being installed at the LHC in CERN also has a dimuon spectrometer dedicated to the same type of measurements as NA50. In addition to the J/ψ and ψ′ resonances, the bottomium $b\bar{b}$ pairs with the Y, Y′ and Y′′ at 9.46 GeV, 10.02 GeV, and 10.36 GeV respectively, will also be accessible. With the LHC, far higher energy densities can be obtained as compared to the SPS fixed target experiments as shown in Figure 18.

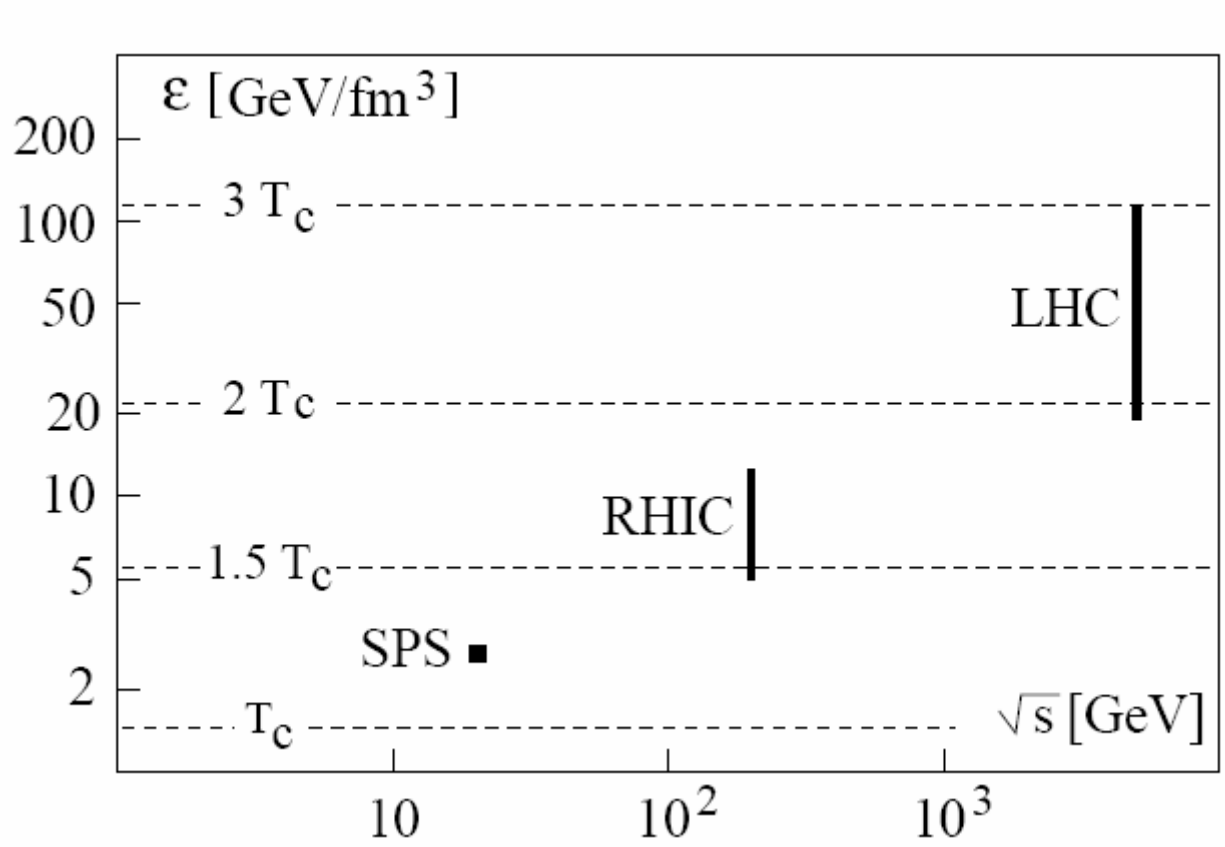

Figure 18 : Energy density estimates versus maximum collision energies, for the SPS, RHIC and LHC, with the corresponding temperatures.

The ongoing experiments, with the PHENIX experiment at RHIC in the United States, the NA50 and ALICE sister experiment, is currently up and running. No conclusive evidence of a QGP state has yet been observed. The experiments and analyses are still ongoing. The future LHC experiments will observe the most energy dense interactions ever produced, and should non-ambiguously determine whether - or not - there is indeed a QGP phase transition♥.

♥ *Two very clear and detailed reports by Satz on colour deconfinement and quarkonium binding are well worth consulting for full details on the current state of the art phenomenology, and are found in references* ***[3]*** *and* ***[4]****.*

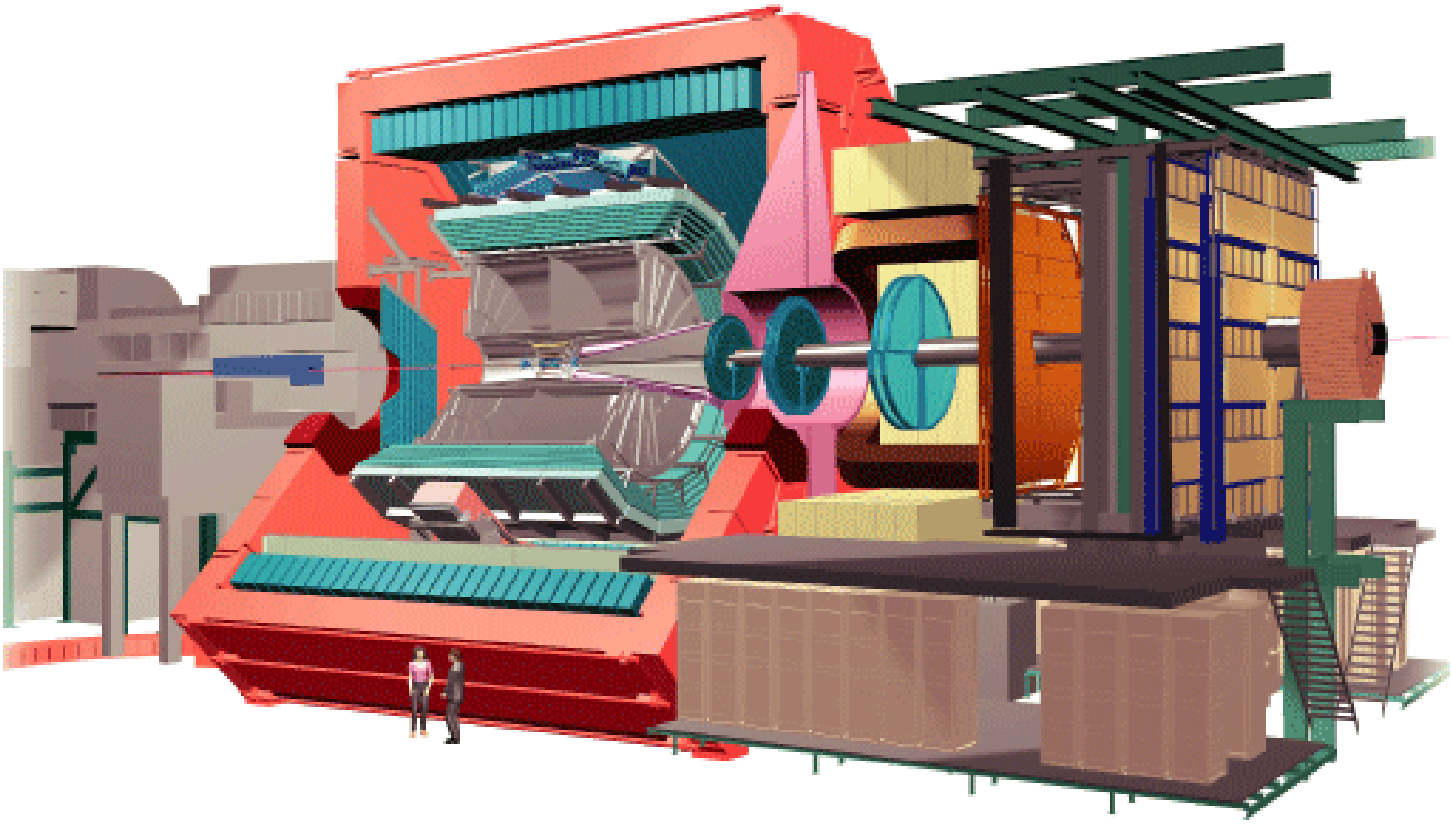

Figure 19 : The ALICE detector

An introduction to ALICE

The ALICE « A Large heavy Ion Collider experiment » project is a general-purpose heavy-ion experiment designed to study the physics of strongly interacting matter and the quark-gluon plasma in nucleus-nucleus collisions at the CERN LHC (Large Hadron Collider). The LHC will accelerate heavy – to light – ions providing a range of 5.5 TeV to 14 TeV per nucleon in the center of mass. One of the key ideas is to discover whether or not it is possible to induce a phase transition in the nuclear matter. This transition, discussed in the previous pages, should happen at very high temperatures (150 to 200 MeV) and/or high energy densities 5 GeV/fm^3 - that is 15 to 30 times the density of ordinary matter (~0.15 GeV/fm^3). This previously unobserved state is thought to correspond to the state of matter in the universe just after the Big-Bang, and should it exist, its study can tell us how the cold hadronic matter we see today was formed. In the laboratory it is possible to follow the thermal expansion and freezeout of the deconfined matter until it reaches thermal and chemical equilibrium.

Among the many proposed signatures of a phase transition is the suppression of the family of heavy vector mesons (or quarkonia), and in particular those composed of the $c\bar{c}$ and $b\bar{b}$ quark-antiquark pairs that make up the J/psi (J/Ψ, Ψ′, Ψ″) and Upsilon (Υ, Υ′ et Υ″) families. The presence of quarkonia can be measured via their distinctive dimuon ($\mu^+\mu^-$) channel disintegration. The interest in targeting the leptonic signature is that these particles should remain insensitive to the rapidly expanding hadronic matter of the cooling plasma, as so retain a maximum of information concerning their origin. By reconstructing the invariant mass of the dimuon pair, the production rates and masses can be measured as a function of the "violence" of the collision (i.e. head-on collisions to peripheral collisions).

The collaboration *(in 2001)*

The ALICE collaboration currently includes more than 900 physicists and senior engineers, from both nuclear and high-energy physics, from about 80 institutions in 28 countries.

The experiment was approved in February 1997. The detailed design of the different detector systems has been laid down in a number of Technical Design Reports issued between mid-1998 and the end of 2001 and construction has started for most detectors.

Since the first comprehensive information on detector and physics performance was published in the ALICE Technical Proposal (TP) [**13**, **14**] in 1996, the detector as well as simulation, reconstruction and analysis software have undergone significant development. The Physics Performance Report (PPR) [**15**] gives a comprehensive summary of the 2004 status and performance of the various ALICE subsystems, including updates to the Technical Design Reports (TDR) [**16**,**17**] published in previous years, as well as a description of systems which were not previously been published in a Technical Design Report.

Detector overview

The ALICE detector, as shown in Figure 19, is composed of a central barrel geared to the measurement of hadronic and dielectron signals and a forward dimuon arm spectrometer adapted to the quarkonia measurements.

Central barrel

One of the major challenges in the central barrel is the measurement of the extremely high charged particle multiplicities predicted in central lead-lead collisions. The central barrel characteristics were designed based on an upper limit of 8000 charged particles per unit of rapidity, at mid-rapidity. This directly dictated the granularity of the individual components as well as the detector surfaces as seen from the interaction vertex.

The central part, covering $\pm 45^0$ ($|\eta| < 0.9$) over the full azimuth, is embedded in a large magnet with a weak solenoid field. Outside of the inner tracking system (ITS), there is a cylindrical Time Projection Chamber (TPC), a transition radiation detector (TRD), and a large area Particle ID (PID) array of time-of-flight (TOF) counters. In addition there are two small-area single-arm detectors: an electromagnetic calorimeter (Photon Spectrometer, PHOS), an array of ring imaging Cerenkov counters (RICH) optimized for high-momentum inclusive particle identification (HMPID).

Dimuon arm spectrometer in brief

The dimuon spectrometer, designed for the measurement of $\mu^+\mu^-$ pairs resulting from the heavy quarkonia disintegrations, is comprised of five basic elements:

- the front absorber, which will attenuate the flux of hadrons and photons accompanying the quarkonia production,
- a 10-plane tracking system comprised of highly segmented double-cathode plane multi-wire proportional pad chambers (CPCs),
- a large area 0.7 Tesla dipole bending magnet,
- a passive muon filter wall followed by four planes of resistive plate counters (RPC) that serve as trigger chambers, and
- an inner beam shield (IBS) that provides added protection from high rapidity particles and their secondaries.

Dimuon arm requirements

Fluxes

As for the central barrel, the particle multiplicities present the main difficulty. The detectors were designed for simulated fluxes multiplied by a safety factor of two.

Predicted fluxes in 1996:

Station	Total hits	From charged	From gammas	From neutrons
TC 1/2	247	215	25.9	6.1
TC 3/4	265	200	50.6	14.5
TC 5/6	606	419	139	47.4
TC 7/8	358	229	97.3	31.6
TC 9/10	414	302	89.8	23.0

and in 1999:

Station	Total hits	From Charged	From gammas	From neutrons
TC 1/2	320	292	18	4
TC 3/4	340	304	24	4
TC 5/6	230	192	30	6
TC 7/8	380	286	70	14
TC 9/10	620	534	66	14

As can be seen, the predicted charged particle multiplicities substantially increased over the whole tracking system. These calculations provide the backbone of the overall tracking system performance requirements. The detector positions and granularities are based more or less entirely on these predictions. This highlights the importance of R&D as being an iterative process. What essentially changed between 1996 and 1999 was not the cross section used in the calculations, but a better definition of the detector environment. The beam pipe area and supports were less well defined in 1996, it became apparent that the beam pipe recesses, necessary for correct positioning of the tracking chambers (which allows the first two stations to be positioned perpendicular to the beam pipe which has a slight incline of 1.39%), coupled with the beam shield materials and geometry design modified the amount of leakage of charged particles.

The neutron background was reduced quite early on as it was seen that a certain part of the generated background, that increased the occupancy rate in the first station well beyond the acceptable 5% level, could be reduced by replacing the iso-C_4H_{10} component of the detector filling gas with a heavier molecular structure – CO_2 – thereby reducing the non-negligible n-p cross section arising from the H_{10} part of the isobuthane molecule.

Interaction rate

The interaction rates are strongly dependent on the beam type. For events triggering with minimum bias and a Pb beam at a luminosity of 10^{27} $cm^{-2}s^{-1}$ the rate is expected to be 8 kHz. For the Ca beam at 10^{29} cm^{-2} s^{-1}, 300 kHz is expected and finally, a 1 MHz interaction rate for protons at 10^{31} $cm^{-2}s^{-1}$. In this final case the nominal LHC luminosity is reduced by three orders of magnitude (from 10^{34} $cm^{-2}s^{-1}$ to 10^{31} $cm^{-2}s^{-1}$) in order to have a more manageable interaction rate.

Mass resolution and trajectory reconstruction

The basic requirement is to separate the heavy quark resonances, the most demanding being the separation of the Υ′ and Υ″ states which can only be done with a mass resolution better than 100 MeV. To this end five tracking stations comprised of two chambers each, with one station inside the spectrometer magnet, are used to over-determine the particle trajectories. Each station provides two independent bending-plane, and two independent non-bending plane, impact points. The minimum requirement for a trajectory reconstruction is one impact point per station.

Detector spatial resolution

The high resolution plane is defined as being the same plane as that due to the deviation from the bending magnet. From simulations it was deduced that a spatial resolution, per tracking plane, of $\sigma<100$ μm is required in order to meet the mass resolution criteria, and is shown in Figure 20 for the Y state. This is the overall effective resolution required after all degrading effects such as misalignments, deformations, vibrations and mechanical defaults are taken into account over and above the detector's intrinsic resolution.

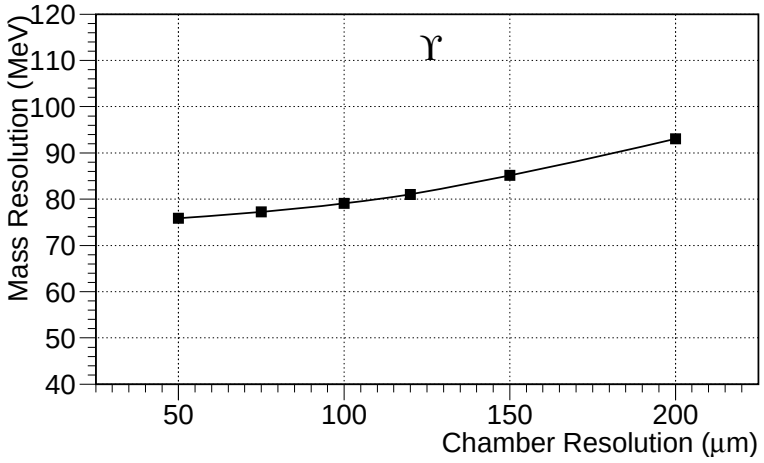

Figure 20 : Predicted mass resolution versus spatial resolution for the Y particle.

The resolution in the non-bending direction is less crucial and a resolution of roughly 2 mm is sufficient.

Chamber sizes

The muons are detected in a cone with an opening angle from 2˚ to 9˚. The active surfaces of the first three tracking stations cover the geometrical projection of this cone. Stations 4 and 5 have much larger active surfaces as their acceptance must also allow for the added kick from the dipole muon magnet. The active surfaces of each tracking station are recapped in the following table.

	Inner diameter (mm)	Outer diameter (mm)	Position (mm)
Station 1	364	1766	5400
Station 2	464	2238	6860
Station 3	660	3166	9750
Station 4	670	4405	12490
Station 5	670	5132	14490

Efficiencies

The invariant mass calculation requires two high resolution impact points per tracking station (one point per muon), this gives a total of 10 independent measures. Supposing an inefficiency of x% per tracking plane, the global inefficiency is of the order of 10x% in the worst case. The required efficiency per tracking plane is set at ≥99%.

Thickness

In 1996:

A maximum detector thickness of 3% of X_0 was imposed in order to avoid irreparable tracking degradation due to multiple scattering. The mass resolution as a function of the individual detector thickness is shown in Figure 21:

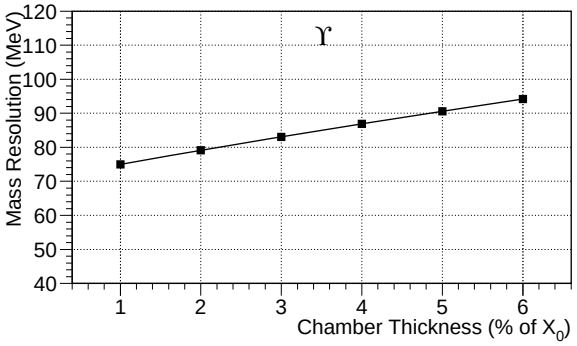

Figure 21: Expected mass resolution versus chamber thickness for the Y particle.

In 2000:

The acceptable thickness was revised in the light of the real density of the onboard electronics cards and the metals required for the pads themselves. Finally, up to 5% of a single radiation length in the most dense, central part of the tracking chambers was estimated to be reasonable for the very densely populated stations 1 and 2.

Layout

The overall layout of the dimuon arm spectrometer is shown in the following conceptual image. The positions of the five tracking stations are clearly situated with respect to the front absorber, the dipole magnet and muon absorber.

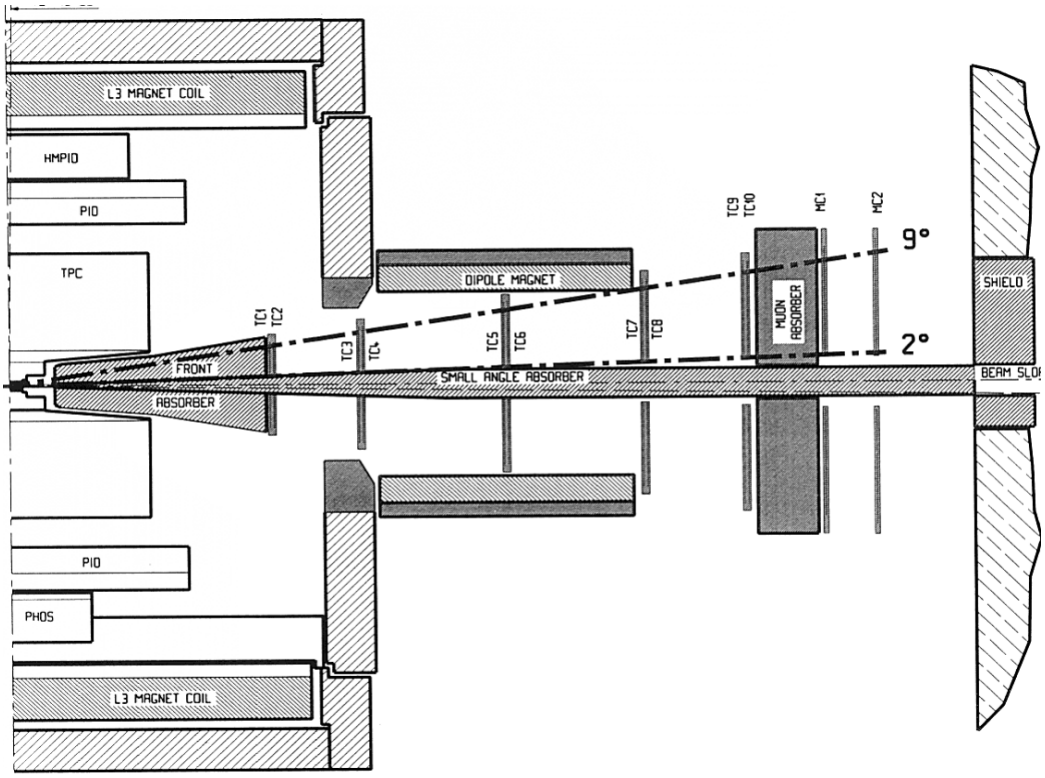

Figure 22 : General layout of the experiment as given in the technical proposal.

Tracking stations

The five tracking stations are based on a standard multiwire proportional chamber design. However, the individual detector designs have been adapted to meet the particular constraints imposed on each one. The three detector classes are:

***Stations 1 and 2**:* these 2 stations cover the smallest surface area in the forward cone and are destined to observe the highest local particle densities with up to $8 \cdot 10^{-2}$ hits/cm^2 for station1 in the area nearest the beam pipe. This imposes a high granularity readout structure with associated high density on-board readout electronics. These stations have two fully implemented cathode planes and are subject to stringent temperature controls. Since they are located inside the forward absorber support, the air circulation has to be forced. The aim is to keep the ambient temperature stable, below 40˚C, and to evacuate any generated heat away from the ALICE cavern. The final detectors are circular in shape, and composed of four individual quadrants that fit tightly around the beam pipe.

Station 3: this station sees lower particle fluxes (generally below $6 \cdot 10^{-3}$ hits/cm^2) but has the particularity of being situated in the dipole magnet. Due to its location, multiple scattering effects should be minimised in order to preserve the mass resolution. A single readout cathode plane with on-board electronics was chosen as a more suitable choice in this case. This decision was taken at the end of the R&D phase, after exploring other possibilities. The active surface is composed of slats, similar to those used for stations 4 and 5, as opposed to quarters as used for stations 1 and 2.

Stations 4 and 5: are in an intermediary situation in terms of particle fluxes, but the very large surface areas pose particular mechanical problems for the wire lengths and the ability to maintain a large surface planarity and rigidity in the face of added hydrostatic overpressure. A multi-module design with two active cathode planes was preferred.

All these differences imply the use of different strategies for the mechanical construction of each station class but based on a common elementary geometry.

Cathode Pad Chambers

General Cathode Pad Chamber design

The station 1 Cathode Pad Chamber (CPC) is the simplest MWPC (multi-wire proportional counter) chamber design. It consists of two parallel earthed cathode planes with a central plane of anode wires placed between. The detector is filled with a multi-component noble gas mixture which is easily ionized by traversing charged particles. The cathode planes are engraved with small rectangles, or pads, over the whole surface. Each pad is equipped with its own charge readout electronics. The anode-cathode gap and the anode wire pitch are of the order of a couple of millimetres. The cathode planes are grounded, and the anode wires are submitted to a high voltage of a couple of thousand volts. This results in a very intense, non-linear electric field in the neighbourhood of the anode wires.

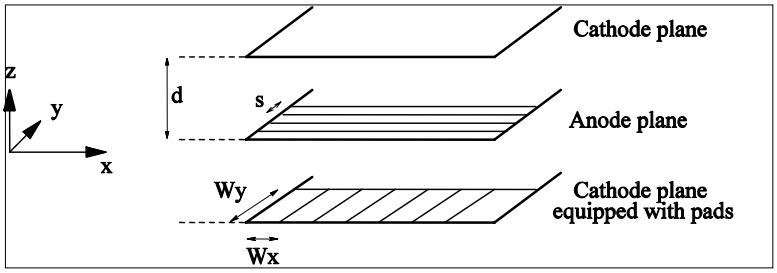

How does it work?

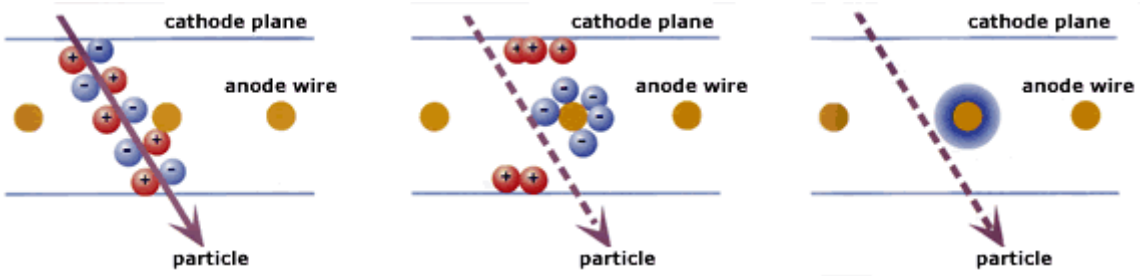

Figure 23 : The three main phases to make a signal: particle ionizes the gas; electrons are pulled to the anode, ions (more slowly) to the cathode; electrons are exponentially multiplied in the strong electric field near the anode wires [**18**].

The passage of a charged particle in the detector leaves a track of primary ionization centers in the detector gap. The liberated electrons are drawn to the anode wires, gaining energy as they go under the influence of the very intense electric field at the anode. At a given distance from the anode wire, each primary electron will have gained sufficient energy for it to ionize the gas, so giving rise to a next generation of electrons. The multiple ionizations create several generations of secondary electrons that are further accelerated as they swarm towards the anode wires before being absorbed them. This is known as the avalanche process and typical ratios between the number of initial primary ionizations and final secondary electrons in the avalanche is of the order of 10^4 – 10^5; this characterizes the detector gain. This electron signal develops over a distance of 10-100 μm on the nanosecond scale.

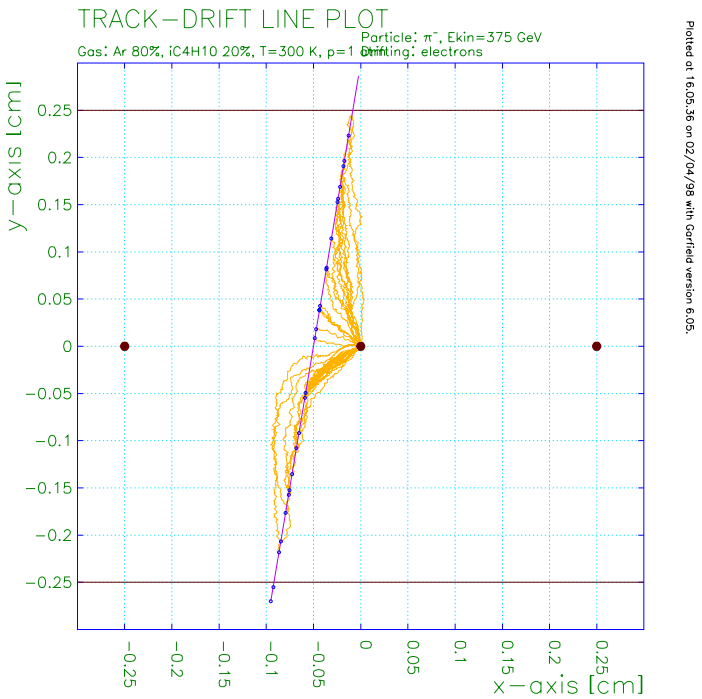

Figure 24 : Simulated primary ionization track in a detector. The blue points symbolize the primary ionization electrons and the yellow lines, their journey to the nearest anode wire. The simulation comes from Rob Veenhof's GARFIELD [**19**] program.

In the case of a cathode pad chamber it is the induced ionic signal that is of interest. The migrating ions move at much lower speeds and the major part of the ions arrive at the cathode planes in the microsecond range, the whole recombination process can take up to several hundred microseconds. The recombination speed dictates the maximum repetition rate. The detector geometry is designed so that a small number of cathode pads are influenced by the induced ionic signal. Charged particle impact points are reconstructed from the analysis of the correlated charge amplitudes measured on each of the cathode planes.

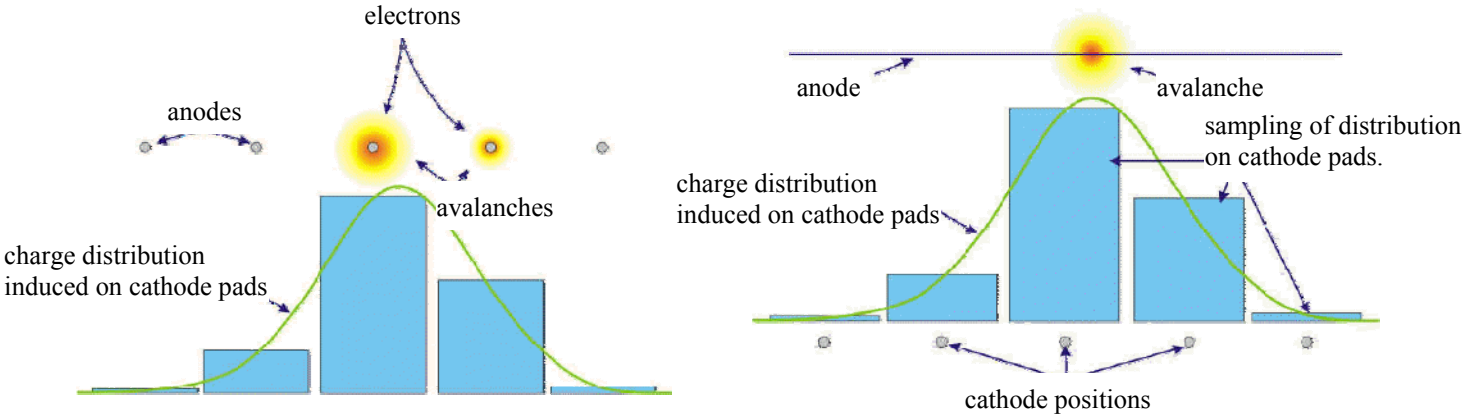

Figure 25 : Head-on and side views of the signal amplitudes on the cathode plane.

Impact point reconstruction using the induced charge

There are several techniques for impact point reconstruction depending on the geometry of the charge measurements. For a single plane impact point reconstruction the most appropriate method consists of analysing the relative charge amplitude spread over neighbouring pads. These signals, being the image of the anode signal, are distributed over a restricted number of pads along the length of the anode wire in the direction that is defined to be the high resolution plane. The lower resolution plane runs perpendicular to the anode wires and the resolution depends essentially on the anode wire pitch.

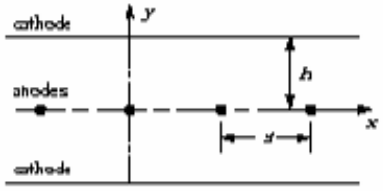

There are numerous reconstruction methods based on charge distribution measurements (see **[2]** and references therein) but the distribution used for station 1 is based on Mathieson's work [**20**]**.** He deduced the much used empirical formulae that give the most precise fit to the internal charge distributions, using only the basic detector geometry. These distributions are also used to model the relative charge amplitudes for different detector configurations. Mathieson established two free parameters, k1 and k2 that are used to fit the Gatti charge distribution function. More details can be found in his very easy to read original work (included here), and for me to rewrite his words would not bring any extra insight to the subject and would be somewhat pretentious.

Nuclear Instruments and Methods in Physics Research A270 (1988) 602–603
North-Holland, Amsterdam

Letter to the Editor

CATHODE CHARGE DISTRIBUTIONS IN MULTIWIRE CHAMBERS: 4. Empirical formula for small anode–cathode separation

E. MATHIESON

Physics Department Leicester University, Leicester, LE1 7RH, England

Received 2 March 1988

Single parameter values for the Gatti empirical formula describing cathode charge distribution in a symmetrical MWPC are presented, graphically, for small values of anode–cathode separation.

In applications of multiwire chambers where knowledge of the distribution of induced charge is required, the empirical formula proposed by Gatti et al. [1] is generally of quite sufficient accuracy. It has further been shown that this distribution may be conveniently described in terms of a single parameter only [2]. Let $\rho(\lambda)$ represent the cathode induced charge distribution in a symmetrical chamber, where $\lambda = x/h$, the x-axis being either parallel to or normal to the anode wire direction. The anode–cathode separation is h. Then the single-parameter formula may be written

$$\frac{\rho(\lambda)}{q_a} = K_1 \frac{1 - \tanh^2(K_2\lambda)}{1 + K_3 \tanh^2(K_2\lambda)}, \tag{1a}$$

where

$$K_1 = \frac{K_2\sqrt{K_3}}{4 \tan^{-1}\sqrt{K_3}}$$

and

$$K_2 = \frac{\pi}{2}\left(1 - \frac{\sqrt{K_3}}{2}\right). \tag{1b}$$

Here q_a is the net anode charge.

Values of the single parameter K_3 have been presented (fig. 2, ref. [2]) as a function of chamber parameters, r_a/s and h/s, where r_a is the anode wire radius and s is the anode wire pitch. The values of h/s covered the range 1.4 to 6.0. However, in certain applications, in order to increase the relative cathode charge at a particular time, considerably smaller values of h/s are advantageous [3]. The purpose of this present note therefore, is to extend the information on K_3 down to these smaller values of h/s.

It was pointed out in ref. [2] that the calculated (approximate) empirical distributions ρ_1 (parallel to the anode wire direction) and ρ_2 (normal to the anode wire direction were slightly different. This difference is somewhat emphasised at very low values of h/s so that K_3 values for both distributions are shown separately, in figs. 1 and 2. Both distributions tend, as h/s and r_a/s tend to zero, to the Endo distribution [4,2], $\rho/q_a = 0.25 \operatorname{sech}(\pi\lambda/2)$, that is $K_3 = 1.0$. However the rate of convergence is quite different for the two cases, as illustrated by figs. 1 and 2. At normally accessible values of r_a/s the two distributions are not greatly different, as seen in fig. 3.

It must be stressed of course that the simple empirical formula above can only represent an average behaviour since it does not recognise any angular localisation of the avalanche. These aspects have already been discussed in refs. [2,5,6]. For illustration, at a very small value of h/s, fig. 3 compares, for a particular geometry, the empirical distribution, eq. (1),

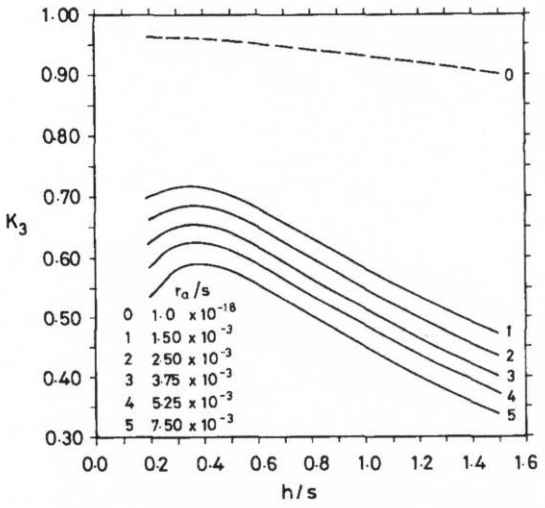

Fig. 1. Values of K_3 as a function of chamber geometrical parameters h/s and r_a/s, for empirical distribution ρ_1 (parallel to anode wire direction).

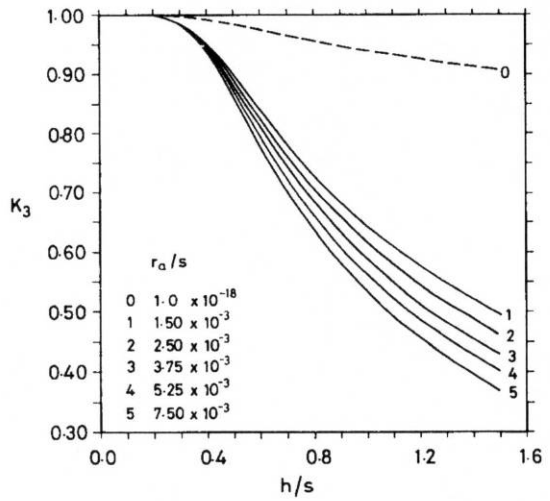

Fig. 2. Values of K_3 as a function of chamber geometrical parameters h/s and r_a/s, for empirical distribution ρ_2 (normal to anode wire direction).

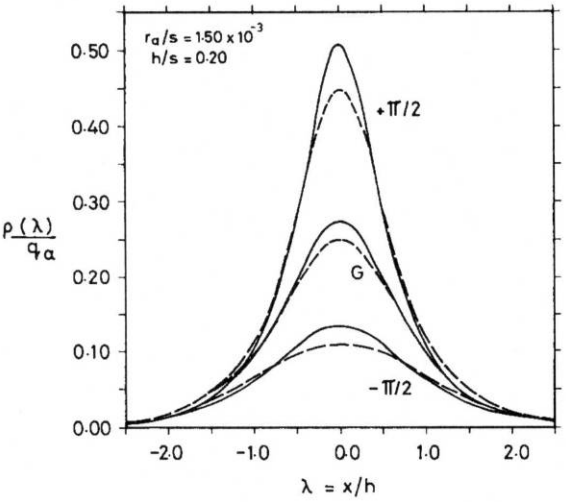

Fig. 3. Comparison of empirical distributions, G, with exact distributions; ρ_1 (full curves) and ρ_2 (broken curves). The exact distributions were calculated at a time 1.0 μs, for avalanche angular positions $\alpha = +\pi/2$ and $-\pi/2$, with rms angular spread $\sigma = 40°$, and for $s = 3.0$ mm, $V_a = 0.8$ kV and $\mu = 1.9$ cm^2/V$_s$. The total cathode charges, relative to the net anode charge, are -0.71 (ρ_1 and ρ_2) for $+\pi/2$, 0.29 for $-\pi/2$ and necessarily 0.5 for G. The empirical distributions represent $K_3 = 0.70$ for ρ_1 and 1.0 for ρ_2.

with the more exact distributions as calculated by the methods of refs. [2,6]. The conditions and geometry for these calculations are given in the figure and caption. It is seen from eq. (1) that the FWHM, relative to the anode–cathode separation h, is given by

$$\mathrm{FWHM} = \frac{4\tanh^{-1}(2+K_3)^{-1/2}}{\pi\left(1-0.5\sqrt{K_3}\right)}. \qquad (2)$$

For the two approximate distributions shown in fig. 3 $K_3 = 0.70$, FWHM $= 1.55$ for ρ_1, and $K_3 = 1.0$, FWHM $= 1.68$ for ρ_2. For the more exact distributions the values of FWHM are, for $\alpha = +\pi/2$, 1.13 for ρ_1 and 1.29 for ρ_2 and for $\alpha = -\pi/2$ 1.88 for ρ_1 and 2.38 for ρ_2.

References

[1] E. Gatti, A. Longoni, H. Okuno and P. Semenza, Nucl. Instr. and Meth. 163 (1979) 83.
[2] E. Mathieson and J.S. Gordon, Nucl. Instr. and Meth. 227 (1984) 277.
[3] G.C. Smith, J. Fischer and V. Radeka, IEEE Trans. Nucl. Sci. NS-32 (1985) 521.
[4] I. Endo, T. Kawamoto, T. Mizuno, T. Ohsugi, T. Taniquchi and T. Takashita, Nucl. Instr. and Meth. 188 (1981) 51.
[5] J.S. Gordon and E. Mathieson, Nucl. Instr. and Meth. 227 (1984) 267.
[6] J.R. Thompson, J.S. Gordon and E. Mathieson, Nucl. Instr. and Meth. A234 (1985) 505.

Understanding the key detector parameters – a personal note

Before building a detector prototype it is obvious that some basic detector model should be used to simulate the critical features beforehand. In the case of the CPC technology, given the abundant amount of literature available, this was a fairly straightforward task. The aim is to show that the detector behaviour is understood (at least on paper), and that was done by modelling known detectors and predicting their (already known) performances. That being successful, it was assumed that the key detector parameters and physics input were sufficiently well described. The next step was to vary the detector parameters to obtain the desired performances. The full detector specifications list is fairly lengthy, but the most fundamental one is certainly the spatial resolution of less than 100 μm. This parameter is essentially governed by the cathode plane geometry and the gas gain, and, as will become apparent, the gas gain is intimately related to the detector geometry.

Before continuing with the detectors' technical details, it's worth taking the time to briefly pause and place the detector technology and accompanying detector physics in their historical context. The multi-wire proportional counter (MWPC) is one of a long series of gaseous detectors, or "electron imagers", as they are sometimes called.

In Appendix A, a brief history of the major detector developments is given.

Given that the MWPC operating principle relies on the use of controlled electron avalanches, a closer look at the historical development of understanding electron avalanches through the description of the gas gain is of interest and presented in the Appendix. An extra-ordinary amount of literature is available on the subject, but one remarkable feat is that although the understanding of electronic behaviour in gases has evolved over a century, it turns out the first prescription proposed by Townsend in the early 1900's is the most robust gas gain formula and continues to be used today.

Townsend's work provided the fundamental basis of today's understanding of the proportional - and non-proportional (all the way up to the Geiger-Muller discharge region) - gas gains. After the "potted history", there follows by a "photograph" of the understanding of the avalanche/streamer processes at the beginning of the 1940's. This date was chosen since it's at this time that the contribution of low energy photons, as well as electron ionization, to the secondary ionization was well understood and described by Loeb and Meek, and independently by Raether. They established the limits of breakdown through the description of the streamer mode. It is worth noting the 40 year gap till Allison and Cobb published the PhotoAbsorption and Ionization (PAI) model in 1980 [**21**], underlining the time required for the understanding and knowledge basis to evolve to the point where a successful computing model could be built.

Between 1941 and the mid-1980's several authors attempted to refine the gas gain formula, generally through empirical approaches. One of the most successful descriptions was given by Diethorn in his 1956 thesis [**22**], and so a more detailed look at his work is given. The next major point is marked by Charles, a close collaborator of Mathieson, who in 1971, pointed out that the ballistic default in the electronics measurements had probably not been correctly taken into account in most work prior to that date - and went on to propose another gas gain formula [**23**]. Finally, Zastawny, who first published on this subject in 1966 [**24**, **25**] (and whose current measurements were not submitted to the ballistic default of the other authors' charge measurements) came round to the conclusion, in a 1997 paper [**26**], that the original Townsend prescription is probably the most appropriate.

Today, the main effort is concentrated on describing the more recent class of "micro"- detectors (pin detectors, microstrip detectors and the little gem detectors to name but a few), which all operate in near-saturation mode, involving higher electric field strengths and greatly reduced anode-cathode gaps.

The R&D Phase (1996-2000) – a personal overview

R&D foreword

The experimental R&D program had several facets that ran in parallel. The detector designs were tested in the lab and at the test beam facilities in CERN. Simultaneously, the data readout system, monitoring programs, and reconstruction programs were developed, and wherever possible, interfaced to the detector models and simulation programs. In the following each of these different themes will be addressed, the intention being to give an overview of the major themes, detailed discussions can be found in the associated documents in the reference list.

Prototype Studies

In order to get and idea of the chronological development of the iterative R&D process the key steps are given in the following table. There was not much breathing space between the different prototype development, the test beams and data analysis. The group's activities also involved data taking periods for the NA50 experiment, these periods are also included to give a fuller picture:

November/December 1996 **NA50** SPS (Pb-Pb @ 158 GeV.A)	
ALICE0 (prototype 0)	
March 97 – end of May 97	Tests in the lab with a Fe55 source
ALICE1 (first prototype, with integrated FEE and tested at CERN)	
June 97	PS (pions @ 6 GeV/c)
September 97	PS (pions @ 3.5 GeV/c)
March 98	SPS (pions @ 350 GeV/c)
November/December 1998 **NA50** SPS (Pb-Pb @ 158 GeV/c)	
ALICE2 (full size mechanical prototype)	
November 98	PS (pions @ 6 GeV/c)
May 99	SPS (pions @ 375 GeV/c)
April 99 to July 99 – **TDR** writing (Technical Design Report)	
October/November 1999 **NA50** SPS (Pb-Pb @ 40 GeV.A)	
ALICE3 (prototype with two active cathode planes, first correlated charge measurements)	
May/June 2000	SPS, measurements in « single-hit » mode
June 2000	SPS, mesurements in « multi-hit » mode
October/November 2000 **NA50** SPS (Pb-Pb @ 158 GeV.A)	
Software Developments	
TestBeam ToolBox – A first Object Oriented TestBeam Monitoring/Offline Analysis Suite	
Detector Modelling for AliROOT	
Detector Mapping – autogenerated sensitive surfaces using the mapped electronics coordinates	
Full scale detector simulation	
Data reconstruction/ electronics breakdowns at different levels	
Physics performance with full detector simulation	

Another way of visualising the overall project development is through the different themes that naturally appear. This gives a different kind of overview of the different types of experimental studies compared to the chronological approach:

GENERAL THEME	SUBJECTS STUDIED
In the Laboratory – Test Bench	
Detector Mechanics (envelope)	Materials, ageing, thickness, electrical compatibility
Internal detector conditions	Filling gas, electrostatics, wire voltages, cathode segmentation, anode-cathode gap
Electronics	Pre-amplifier, amplifier, filter and shaping times, coding precision, noise levels, charge sensitivity, gains
Primary and secondary signal formation	Ionisation process, recombination time, gas gain
Signal readout	Acquisition chain, evt/evt data recording
Bench tests with a source	Online monitoring program with a graphics interface (histos, etc…)
Test Beams (CERN PS and SPS)	
Test Beam data taking at the PS	Silicon strip tracking detectors – straight line reconstruction program
Test Beam data taking at the SPS	Cathode Pad Chamber – Multi-hit straight line reconstruction program
Test Beam preparation	Online monitoring program, mappings, online impact point reconstruction
Test Beam analysis	Analysis programs
Simulation of the different Test Beam setups	Modelling the experimental conditions
Simulation of the different prototypes	Modelling the detector layout, internal gain, electronics filters and coding precision, overall response function
Detector Construction	**Detector Model Construction**
Mechanical structure, electronics integration, acquisition architecture, data management Detector mapping, impact point reconstruction, trajectory reconstruction, invariant mass particle reconstruction	Mechanical structure, electronics integration, acquisition architecture, data management Detector mapping, impact point reconstruction, trajectory reconstruction, invariant mass particle reconstruction
Simulations	
Detector performances, algorithm performances	Using measured Test Beam data
Performance predictions	Using physics models and realistic detector response functions

Three small-scale models (ALICE0, ALICE1 et ALICE3), one large scale prototype (ALICE2) and the first full scale chamber (QUADRANT ZERO), originally intended to be the spare detector, were constructed in the RDD (Recherche et Développements en Détecteurs) laboratory at the l'IPN.

ALICE0 (1996) was designed as a first test of the construction process, choice of construction materials, and to generally allow both the physicists and engineers to familiarise themselves with the detector. The first attempts at reading the detector signal, estimating the internal detector gain and defining the basic electronics readout characteristics all happened at this stage. This detector never left the laboratory and was an excellent "trainer" detector.

ALICE1 (1997) was built specifically to address the question of the most appropriate internal geometry (anode wire spacing, height and width of the readout pads, anode-cathode distance). This detector saw both PS and SPS beams at CERN, and many lessons were learned. One of the more interesting situations, was the abandon of the very first beam-tests due to a severe gas problem.

This was a fairly cleverly designed detector as a large numbers of geometrical configurations could be studied by a simple adjustment of the relative anode and cathode positions and the electronics cards. A spatial resolution of 23 μm was obtained for a particular configuration, corresponding to a world record for this type of detector. The characteristics of the front end electronics (FEE) were deduced from the experimental analysis of this test beam data.

ALICE2 (1998) was the first « full scale » detector, and although it didn't have the exact external shape as the final quadrants, it was 1 m^2 and had 10,000 individual readout channels (not all equipped with FEEs). One of the main aims was to identify potential problems associated with the mechanical construction of such a large detector. Beyond the mechanical precision, the operational detector is required to have a homogenous response, imposing particular constraints on the gas circulation and allowable pressure variations, the stability of 1 m long wires under electrostatic forces, and material displacements due to temperature variations. This detector was tested at the SPS and a spatial resolution of 43 μm was measured, well within the upper limit of 100 μm established in the detector requirements.

Beyond the mechanical studies, different gas mixtures were also tried and tested.

ALICE3 (2000) was a reduced model that had two fully equipped cathode planes, and so allowing correlated charge measurements for the first time. The opposing cathode planes were composed of pads with a half pad offset between the two planes. This geometrical trick resulted in greater detection efficiency, consequently allowing the operation HV to be lowered, and this in turn led to lower detector occupancy. The half-pad offset between detector cathodes also simplified the reconstruction procedure for certain types of events.

QUADRANT ZERO (2001-2002) was the first full quadrant to be constructed. After studying the dimuon arm TDR some important detector modifications were requested by the LHCC, leaving little time for testing in the lab and at the test beam. The original detector aluminium support frames were estimated to be too thick; they cast an important shadow on the acceptance of the other stations. "Frameless" detectors were therefore proposed – and so some substantial mechanical changes were implemented. More recent simulations predicted a rise in the background fluxes, this was the direct consequence of - the now more stable - beam pipe design with its flanges and recesses. The station 1 occupancy rose above the acceptable limit of 5%, to combat this; the internal detector geometry was modified to have a smaller pad size on the cathode planes. In order to maintain reasonable charge distributions (at least three pads hit per particle impact point) the anode-cathode gap had to be reduced.

The LHCC had stringent requirements for the delivery of a final Addendum to the original TDR. The fast pace imposed meant very little time was available for detailed testing, but tests did show insufficient cathode plane rigidity for this frameless detector. A central fixation point had been designed, but had not been implemented. The construction phase was started in July 2001, without full testing this new central support, and so without knowledge of the consequences it could have on the internal electric field.

The first "real" detector saw the day in June 2002. It was tested in the laboratory with a source and, very briefly, in the test beam at the CERN PS in July 2002.

The Electronics Project

One of the first priorities was the development of the front end electronics (FEE) since our group in Orsay had been attributed the lead role on this subject. The main challenge was to construct a system suitable for 1.2 million individual channels. From the outset the choice was based on an integrated charge measurement, each channel having a high enough signal to noise ratio to allow the required reconstructed 100 μm impact point resolution. As a starting point the technology already developed at CERN for the readout of a RICH (Ring Imaging Cherenkov) [**27**] was used. These circuits were based on the GASSIPLEX preamplifiers developed in 1.5 μm technology by J.C. Santiard [**28**]. These pre-amplifier/amplifier chips were daisy chained before being sent to a sequenced ADC coder. The coder worked off a 2 MHz clock that sequentially took a snapshot of the integrated charge in each channel.

In 1996-1997, in the company of a specialist electronics engineer, I participated in the first bench tests. At the time our aim was simple – to discover the gain, linearity and dynamical range of the GASSIPLEX chips and to compare them with the specifications on paper. The aim was simple, but the reality was more complex. We did not have a sufficiently well defined circuitry, and most of our "measurements" disturbed the chip's performance. Nonetheless, we did get a glimpse of the extended linearity of the dynamical range, but absolute measurements were not possible.

A more serious detailed electronics definition resulted from the 1998 beam tests. The measured and simulated electronics response was compared. Based on the excellent quality of the simulations, the new GASSIPLEX characteristics were defined. The modifications were included in the new CERN chip based on 0.7 μm technology to give an extended dynamical range and a lower intrinsic noise contribution.

Given the high density of FEE the most logical solution was to integrate the pre-amplifier, amplifier and ADC on a single electronics card. It was with this aim that the first Multi-Chip Module (MCM) was developed. This small electronics card (7.5x2.5 cm^2) contained 4 GASSIPLEX (and so regrouping 64 individual channels), a 12 bit ADC coder and an LCA (Logical Cell Array) that coordinated the local logic signals (readout sequencing, pedestal subtraction, zero suppression, and output data formatting). With this solution, the electronics cards could be put on a common control bus, and any broken cards could easily be taken out of the readout sequence. This was a first step in obtaining a more robust readout system. Prior to this very long daisy chains has been used – with the major flaw that a break in the chain meant the loss of all the data beyond the fault. The second main advantage of the new MCM approach was a considerable reduction in the overall power consumption since the analog signals did not have to be driven along very long lines to the detector edge. The MCM coordination was ensured via a series of DSPs (Digital Signal Processors) placed on the outer edges of the detector, before being sent on the central ALICE acquisition system (DATE).

Simulations – detector and the electronics response

The detector development relies, for a major part, on simulations which intervene at several different levels. One of the most basic, and important, simulations concerns the predicted particle fluxes with background physics and secondary processes included, these simulations were carried out by Andreas Morsch, member of the ALICE collaboration. Correlating the fluxes with the expected interaction rate immediately imposes the desired detector count rates and granularities. In my work I concentrated more on the detector modelling and the interplay between the internal physical processes, electronics filtering and shaping that lead to the final coded electronics signal.

I started with a fast simulation code that was used in the RHIC PHENIX experiment tracking chamber simulations [**29**]. I went on to explore the basic ionization process, on an event-by-event (and charge-by-charge) basis with the help of Rob Veenhof and his detailed simulation program *GARFIELD* **[19]**. He introduced me to Steve Biagi and his work on modelling gas ionization characteristics (ionization and attachment coefficients) and, electron and ion transport properties, with his programs *IMONTE* and *MAGBOLTZ* [**30**]. A more detailed view of primary cluster formation was developed by Igor Smirnov, where he implemented the full PAI model **[21]** in his program *HEED* [**31**], and interfaced it to the *GARFIELD* program. These simulations allowed me to become more familiar with the question of signal formation in the detector, and led me quickly to the conclusion that, in my case, measurements would probably be more valuable. This work was carried out simultaneously with the ALICE0 laboratory tests, and a summer student helped to collate the overall internal properties of our very first prototype.

I simulated the ALICE1 and ALICE2 PS and SPS experiments. The main part of these calculations were presented in Liliane Kharmandarian's thesis (as a complement to her experimental analysis) and then again, in the dimuon arm TDR. The program developed was based on the simulation of the detector signal, using a Mathieson charge distribution around one (and in a later version two) anode wires. The analytical signal form was then digitized on the cathode planes - by integrating the induced charge over the appropriate cathode pad sizes - and the consequently "observed" impact point calculated by minimizing the "measured" (simulated) charge distribution to another/or the same Mathieson function [**32**]. I developed this program, over a number of years, to include as many experimental details as possible (beam profiles, different ADC coders, two readout planes, noise levels, cross talk possibilities, Landau/Vavilov energy loss distributions, etc…). I also wrote the usual set of documentation and secondary analysis programs for event display, statistical compilations and support programs that allowed particular experimental/simulation studies to be done.

After numerous tests and iterations the final model, where each elementary step in the signal formation was parameterised, successfully reproduced the experimental response. To test the quality of these simulations the 1998 PS experimental results were predicted. These predictions, insofar as the experimental charge distributions and spatial resolutions were concerned, were in excellent agreement with the measured response and values. It became possible to confidently evaluate the effects of individual channel thresholds, noise contributions, and the effects of varying the electronics dynamical range, on the final results. It transpired that the limited electronics dynamical range was the biggest contributor to the overall poor efficiency. Using these calculations I then helped to establish the more ideal electronics specifications (basically a wish list). Detailed characteristics were parameterized and studied, and included: thresholds; cross-talk; dynamical range; relative gain dispersion; coding precision; calibration precision, and electronics noise. The dynamical range was consequently extended by a factor of three, the coding precision was changed from 10-bits to 12-bits and a noise level less than 1000 electrons ENC (equivalent noise charge) was imposed.

Software codes for event readout and reconstruction

All the detector tests required appropriate acquisition programs, online monitoring and reconstruction codes. One of my most persistent contributions to the ALICE project was to write these codes, either in their entirety, or build them up from already existing bits and pieces. To give an idea, a typical online monitoring program for the PS data taking period was composed of several parts. The group was provided with a basic generic code that consisted of the straight line reconstruction code for the reference tracker detectors [**33**]. I would then implant our detector decoding, interpretation, reconstruction and graphics outputs into this generic code. Given the numerous different detectors tested over the years, with the different geometries and electronics layouts, it was always surprising how little of the code was truly re-useable. With hindsight, the code had to change and evolve, becoming more sophisticated with time, in keeping with the evolution of the experimental questioning.

An agreeable aspect of this work was the possibility of sharing the resultant code with colleagues in other laboratories. In the same way our group "inherited" the straight-line reconstruction code, we also passed our code on to our colleagues in France and abroad. This also meant taking the time to comment and organise the code as well as possible, to make it as transparent as possible for new users.

A successful code is one that works, and where the newcomer can become a competent user in the space of a day, without being aware of the months of development and fine tuning that went on behind the scenes.

One of the most obvious challenges in our test experiments was to be continuously efficient. Certain experiments, such as ALICE0, required extensive sets of online spectra, and others, such as the ALICE1 and ALICE3 tests, required more effort on the electronics-to-spatial coordinate mapping. In the latter tests the detector, and the electronics, and the internal geometry were all variables - and the reconstruction code had to be as flexible as possible in order to efficiently re-implement the different experimental configurations in the reconstruction code.

It was through these (sometimes seemingly endless) code adjustments that my understanding of the "mapping problem" matured. I had two main pre-occupations: How to simultaneously calibrate 10,000 electronics channels without saturating the entire ALICE acquisition system for more than a day; and how to handle the 10,000 different readout pad locations, on both cathode planes, correctly relate the channel ID to a physical and logical volume and correlate opposing cathode planes.

In reply to the first question - I still don't have an answer; however, the second one was resolved by the creation of a "mapping program". I used the experience acquired from the numerous test beams and analyses to conceive a suitable architecture for the final detector. This code, which is now an integral part of the ALICE software, was developed in several stages over three years. The write-up of this work is included in Appendix D.

On another front, that of the laboratory and test-beam experiments, it was obvious that a correctly conceived set of programmed library tools would allow us to be far more flexible in our data monitoring and analysis. After discussions with our "computing guru" Fons Rademakers, I designed a "TestBeam ToolBox" which was implemented in our experiments as of 2001. This project was completed quickly and efficiently thanks to the collaborative efforts of our thesis student, David Guez. This project was our very first step in object oriented programming and our write-up on this subject is included in Appendix B.

The postTDR period

As of 2001, after the publication of the Addendum to the TDR **[16]** the project completed the R&D phase and moved into the station 1 chamber construction phase. The electronics project became a separate issue, and the full scale production had to be addressed separately. At this time I decided to change direction and to move closer to the full scale detector modelling, since its characteristics were now known.

Models and simulations (2001-2002)

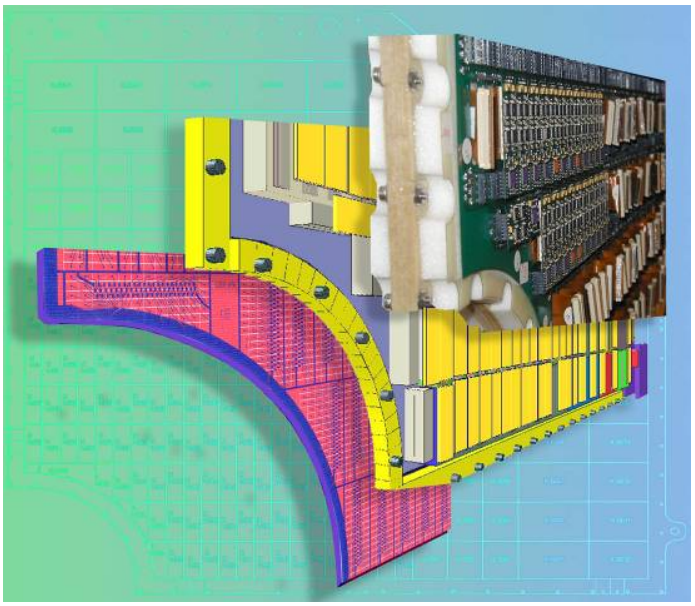

Figure 26 : Several images of the internal arc of a station 1 quadrant. The red and blue design is taken from the real pad circuit blueprint; the middle, mainly yellow image is the simulated detector model - complete with electronics cards and nuts and bolts in the detector frame; the rightmost image is a photograph of the ALICE2 full-scale detector quadrant. The ensemble is superimposed on a background describing the first mapping layout.

A full inventory if the detector construction materials was carried out in order to make a more precise evaluation of the amount radiation lengths and also to allow a more exact model to be built. The detector specifications imposed an upper limit of 3% (which eventually became 5%) of a radiation length on the average detector thickness. Given the very high density of electronics components near the beam pipe are for station 1, it was clear that this constraint could be difficult to meet. The outer support frames were designed to be made of Aluminium - and came complete with steel nuts and bolts (see Figure 26), this was obviously not going help the detector transparency. Once one of our J/Ψ or Y decayed lepton pair (μ^+ or μ^-) are scattered, they deviate from their original trajectory through the spectrometer and the subsequently reconstructed invariant mass (if at all possible) is smeared. Keeping to within the limits of <100 MeV for the reconstructed invariant mass is essential to the success of the experiment (allowing to separate the Y′ from the Y′′ state).
A *very* detailed report, giving the complete detector material inventory was published as an internal note in April 2002. This project also provided the opportunity for me to explain the detector - in all its gory details - to a new colleague, who had just joined our group in Orsay. This report is included in Appendix C.

The next step was to transform the inventory into the more useful GEANT3 model in AliROOT. I guided, and collaborated with, our thesis student through all this work. The aim was to develop three models, each having fewer levels of detail, but all reproducing the overall material thicknesses, volumes, and surfaces. The simplified model was then used as the basis for the GEANT3 station 1 detector model.

The electronics mapping

The total number of coding channels over the five tracking stations amounted to roughly 1.2 million. A mapping system allowing to "easily" relate the electronics ID to its location on the detector cathode plane was necessary. This was not so simple given the variable, non-repetitive nature of many of the electronics circuits. Just to add another level of difficulty, the inverse mapping also had exist, ie. given a two-variable coordinate on any detector face, "easily" and "efficiently" find the associated electronics ID amongst the million possibilities.

Beyond this, the reconstruction algorithm was based on locating the "nearest neighbour". Establishing this neighbour (if it even physically exists) for repetitive pad layouts is not overly difficult, however, the station 1 pad layout is variable over the surface, and not exactly in the same way for opposing cathode planes.

The mapping is therefore an essential piece of software for the detector to be useable.

I developed this project, and used the talents of D. Guez (thesis student) and I. Hrivnacova (computing expert), to implement and test an appropriate architecture. The mapping package is now an integral part of the ALICE software, and in despite of the very strong resistance at the time, this model has been adopted by the collaboration.

In the next step, the combined description of the model - with the simplified, but precise material budget - and the mapping package, were implemented in AliROOT. This part of the software, completed in 2003, allowed for the first time, a full scale and realistic simulation of station 1. This work opened the way to studies that concentrated more on improving the reconstruction methods.

Electronics implementation studies

An important aspect of our project was the robustness of our electronics implementation. Given that very few human interventions in the detector cavern were foreseen during the LHC running periods (two to three at most per year), it became obvious that ways of minimising the risk of losing data ought to be looked into. The likelihood of no electronics breakdowns occurring during closed periods being fairly weak (especially at the outset), different scenarios were envisaged and simulated.
At the time, the precise scenario for regrouping the electronics chains at different nodes was not yet established. A single chain generally carried the information from a few hundred electronics channels, and groups of five chains were sent to the same "concentrator card" or node. The breakdown of such a node or a chain would directly influence the particle reconstruction efficiency - and this differently depending on the way in which the chains and nodes are connected. These studies are described in detail in D. Guez's thesis, where different scenarios are investigated. A large number of channels can potentially be lost depending on the physical location of a breakdown. Our aim was to take the global architecture into account and to discover the layouts where even partial data loss could still allow the reconstruction of particle impact points. The aim was also to differentiate between partial loss and total loss scenarios.

.

R&D prototypes and tests

R&D prototypes and tests

The following section is a sort of scrap book of the chronological development of the main R&D aims. The detector images and comments are generally excerpts from the logbooks, some results were not presented elsewhere, and various “photographs” of status reports are given as they were presented at the time. The different prototypes with the associated experimental aims and some results – warts and all - are presented. No attempt is made to brush over the “happy accidents” that did occur, mainly because through such errors, more was gained than lost in understanding the detector. As a contrast, the later sections regroup the more polished and compact formal write-ups of the R&D work that were destined for the LHCC.

The following sequence of sections will be used to summarize the prototypes one by one (where appropriate).

- Aims
- Detector geometry
- Gas Supply
- Electronics
- Readout/Acquisition
- Results

ALICE0

ALICE0

This was the first "test" detector built and tested at the IPN in Orsay in early 1997. It was a "trainer" detector used essentially to test the basic manufacturing process and the electric and electronic environments. The first discussions for the design were started in October 1996; the prototype was ready by March 1997 and was tested in the laboratory with a source.

Aims

The main objectives for this first test detector were to test the chosen construction materials, and construction procedure and to experimentally understand the basic detector behaviour. The newly acquired GASSIPLEX electronics **[28]** were used with this detector, and the learning process took several months of continuous effort. A first simple gas supply system was renovated, the first electronics circuits for charge injection on the anode wires, and reading the output pad/strip responses were implemented. An already existing acquisition system was adapted to the set-up [**34**]. The relative times for the signal formation and transit times in the detector were to be discovered. Finally the first on-line monitoring programs were written.

Several strategies were used to study the detector and its electronics:

- Anode wire charge injection to study the cathode plane response (with no gas, no HV in detector)
- ^{55}Fe source to study the gas gain (with gas and HV)
- Charge injection via a test capacitor on the GASSIPLEX to study the electronics gain (with the GASSIPLEX mounted on detector)

This detector never left the laboratory, but represented an important step in the R&D process.

Detector geometry

The general views of the detector as well as the electronics readout strategy are shown in Figure 27 and 5. As for all prototypes, full details can be found in the experimental logbooks and the Orsay RDD engineering archives.

The list of main technical details is given so that an easy comparison with subsequent prototypes can be made.

Dimensions:

- Active surface 152 mm x 122 mm
- Full cathode plane surface 210 mm x 122 mm
- 48 soldered anode wires, diameter φ 20 μm
- 4 guard wires
- 16 cathode strips with w/d = 2; w= strip width and d = anode-cathode gap
- 8 cathode strips with w/d = 1.5
- 14 cathode strips with w/d = 1
- 16 cathode pads with w/d = 1 and divided in two unequal lengths
- Pad separation = 0.254 mm
- Anode-cathode distance = 2.54 mm
- Wire pitch = 2.54 mm

Materials:

- Outer frame, Al
- Cathode support, four-layer PCB, 0.8 mm total thickness
- Readout strips/pads, gold plated
- Anode wires 20 μm
- Window, Aluminized Mylar 25 μm
- Frame nuts and bolts – metal
- Anode wire guides – plastic pins
- Air-tight joints, Nytril diameter 4 mm
- Readout – two connectors - soldered 96 point male, 96 point female ribbon cable
- DN10 gas supply joints
- HV via SHV connector
- Anode charge injection via a BNC connector
- Al plated Mylar window

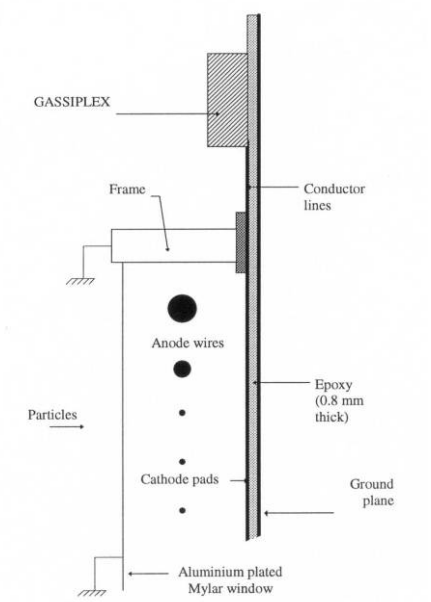

Figure 27 : Side view showing the general scheme for the detector layout.

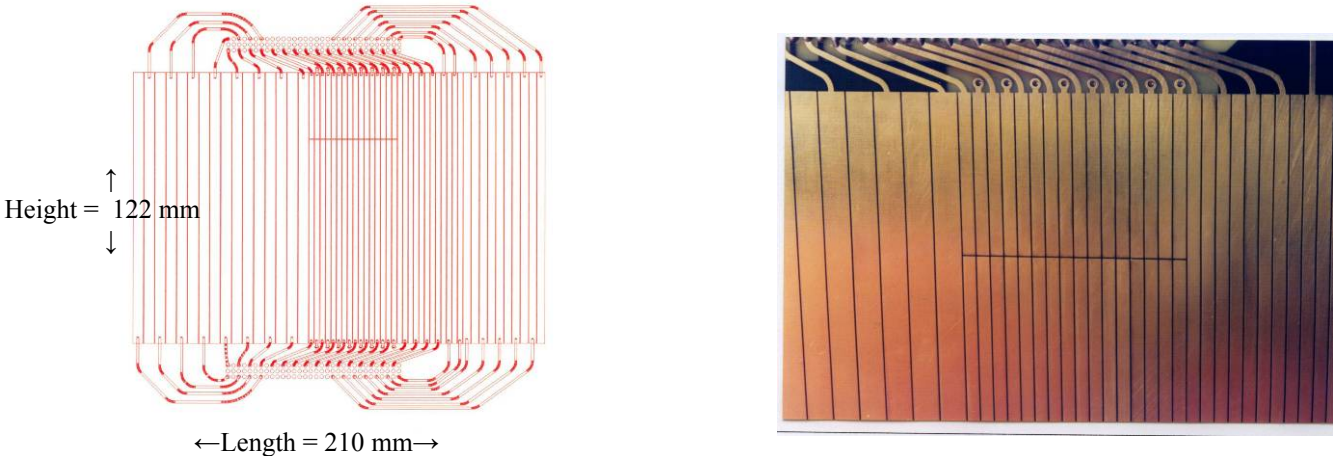

Figure 28 : The LHS shows the design of the cathode plane layout with the different pad sizes and the readout strategy. The RHS shows the upper central area of the finished object.

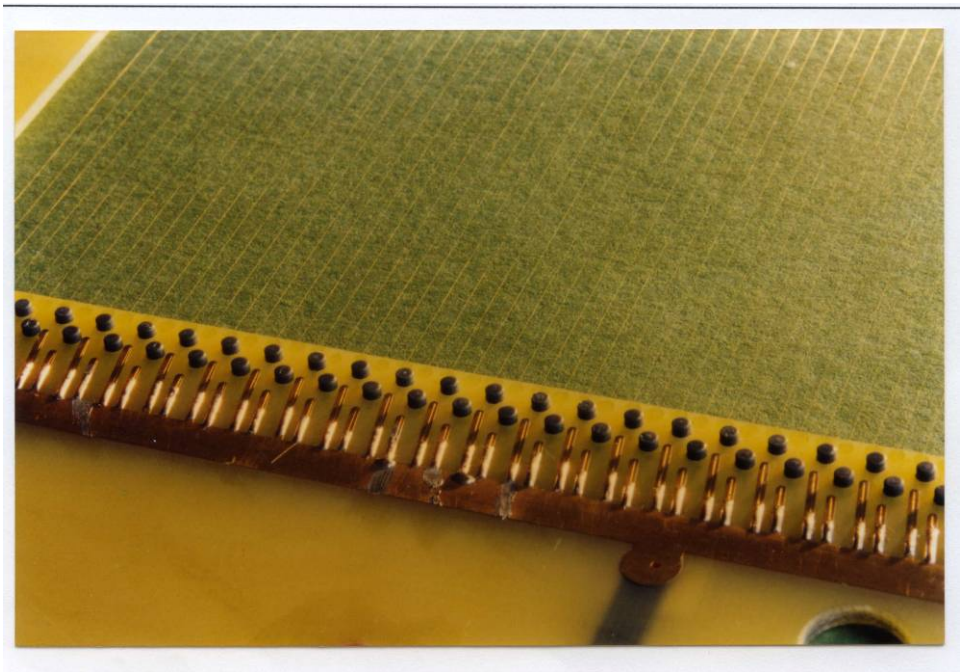

Figure 29 : A photograph of the anode wire plane placed against a dark background to improve the visibility of the 20 μm wires. The black pins are used to align the individual wires, each wire being glued and soldered to the surrounding copper conductor.

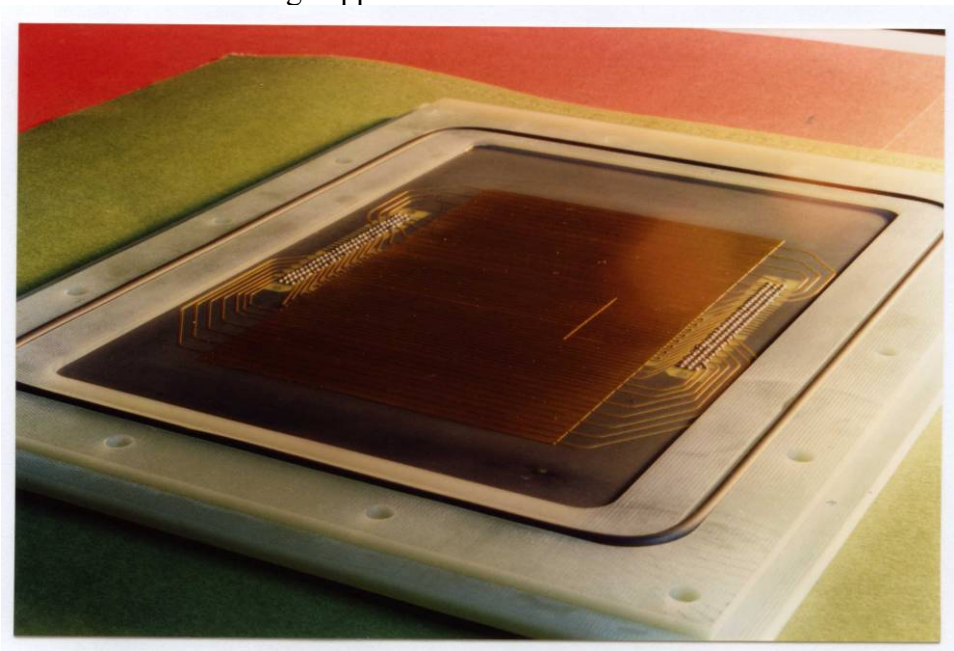

Figure 30 : The cathode plane inserted in the epoxy frame, before the placing of the anode-wire plane. The air tightness is ensured by the rubber joint.

Gas supply

A first, very simple, two channel gas supply system was constructed to deliver the gas mixture. The system has two channels, working in a master/slave mode with mass dependent flow control meters. A mixture of Ar/iso-C_4H_{10} was chosen since previous reports showed that this mixture generally provides a satisfactory gas gain. High purity gases were chosen, perhaps not a real need since the supply tubes were of standard plastic tubes (Rilsan™), and are known for their particular contamination features. For long-life detectors care is taken when choosing not only the detector construction materials, but also the gas supply system. For example, inert materials, such as steel-plated tubing would be preferred to porous plastics.

Electronics

In reality, several electronics circuits were used on ALICE0. The first tests were carried out with the older standard modular electronics, with a preamplifier/amplifier placed as close to the detector as possible. The amplified and shaped analog signal was then sent over several meters to the VME crate where the ADC coder was installed. Very quickly the more interesting CERN designed 1.5 µm GASSIPLEX chip was used. This chip provides the charge pre-amplification, filtering (suppression of the long ionic tail from the detector) and CR–$(RC)^2$ shaping for each of the 16-channels. The integrated charge output is given as a constant level for each channel.

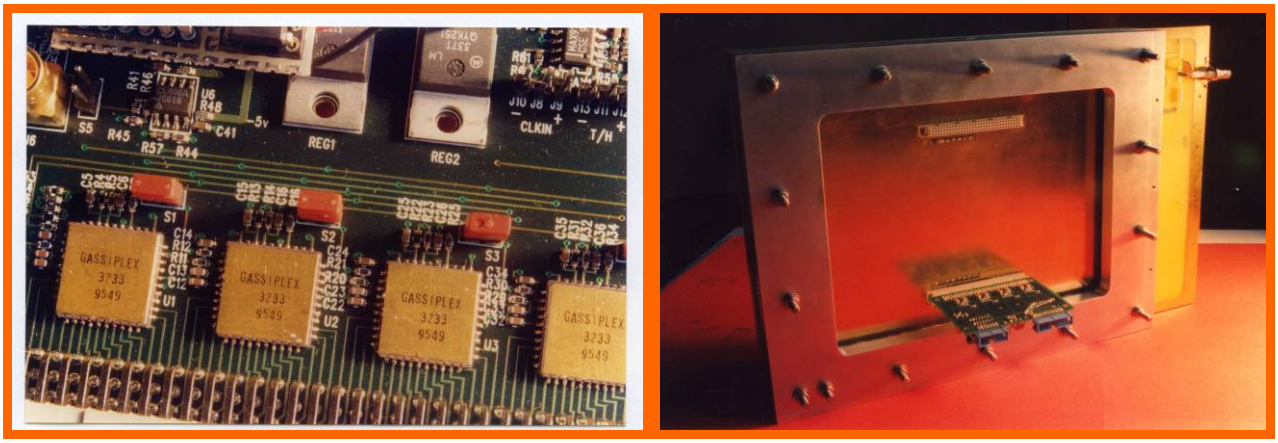

Figure 31 : On the left hand side (LHS), a close-up of the GASSIPLEX chips, each chip capable of measuring the charge amplitude on 16 individual pads. The chips are read in sequence through a common bus. On the right hand side (RHS), the first GASSPLEX card at the IPN, Orsay, mounted on the detector.

Readout/acquisiton

To give an idea of the acquisition state at the start of the project the following paragraph describes the basic equipment. The idea of sequential ADC readout was retained in the final solution, but was implemented in a far more elegant manner.

The first acquisition system used in the laboratory was the already existing Oasis **[34]** system. The acquisition cycle was based on the sequential readout of the ADC ♠. The four 16-channel GASSIPLEX chips per readout card gives 64 daisy-chained channels. In the acquisition cycle, a clock pulse is sent to the ADC, and the constant pulse level is recorded for each of the 64 channels in turn. During this time no further charge is measured and the GASSIPLEX are effectively "frozen" by the "HOLD" signal until all the ADC coding has been done and transferred.

The overall time to convert the 64 channels was estimated to be 42 µs and the acquisition was run at a very reasonable rate of 2 MHz. The relative timing for the signals was not well established at the time, and the first attempts used the timing sequence shown below in Figure 32.

♠ CAEN V550 10-bit ADC and the V551B programmable controller.

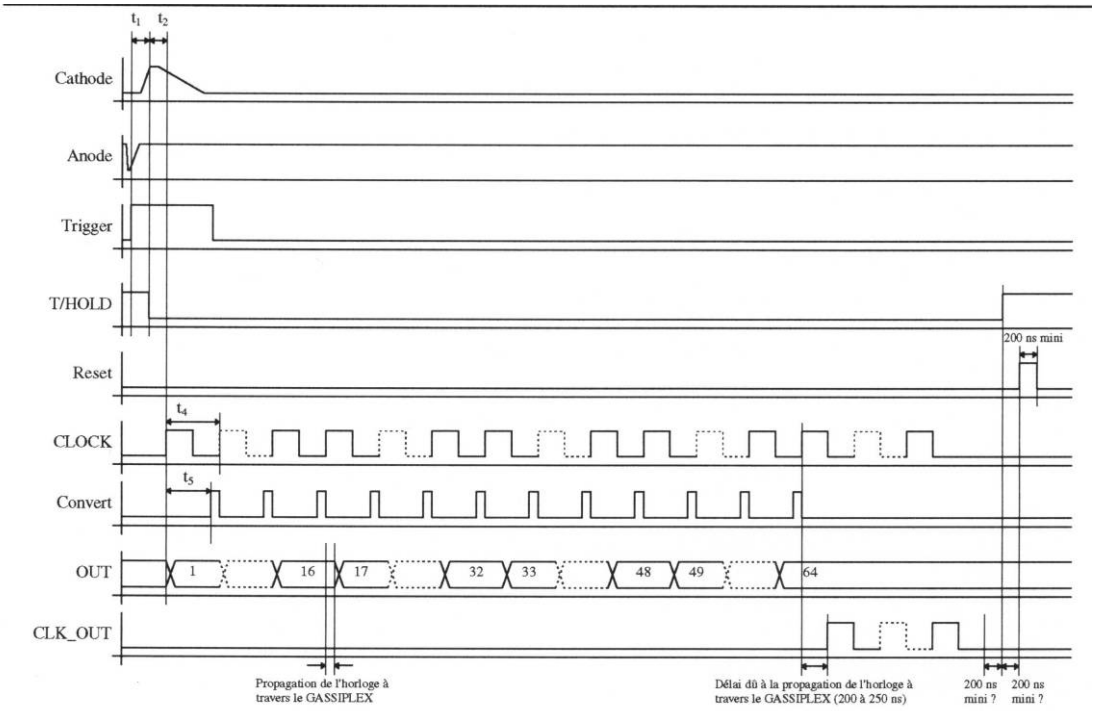

Figure 32 : Timing sequence for the sequential ADC readout with t1 = 700 ns, t2 = 170 ns, t3 = 260 ns (not shown on image), t4 = 520 ns, and t5 = 260 ns

Online monitoring

The Oasis system was used to decode and see the online histograms. The cathode plane layout with the output connector pin numbering and attributed ADC channel number are shown schematically below in Figure 33. This was the first encounter with the question of mapping and was the simplest configuration used in all of the prototype tests. Nonetheless, we managed to mix up numbers and directions as we discovered the importance of keeping fixed references. This image is only included to show where we started from, and to provide a point of comparison with the final, much more complex, mapping layout.

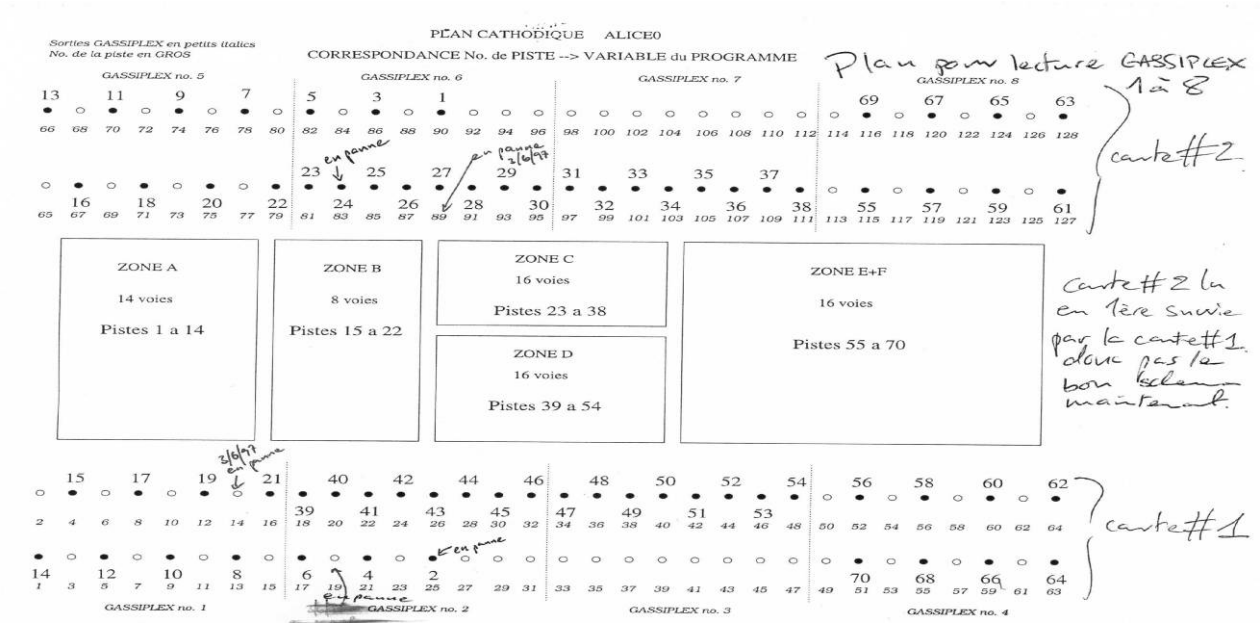

Figure 33 : View of the detector zones, A-F, and the associate readout mappings. Large numbers are the strip ID numbers and small numbers are the GASSIPLEX pin attributions.

ALICE0 Results

Gas gain estimation

A first estimate of the detector gain was made using a ^{55}Fe source (5.89 keV X-ray line). In this setup the anode wire signal was recorded via a pre-amplifier/amplifier of already known characteristics, and recorded single channel ADC. The anode voltage was set at 1600 V and the detector was filled with an Ar/iso-C_4H_{10} (20%) mixture. The following is a translated excerpt from the logbook, and details the logic used to estimate the detector gain:

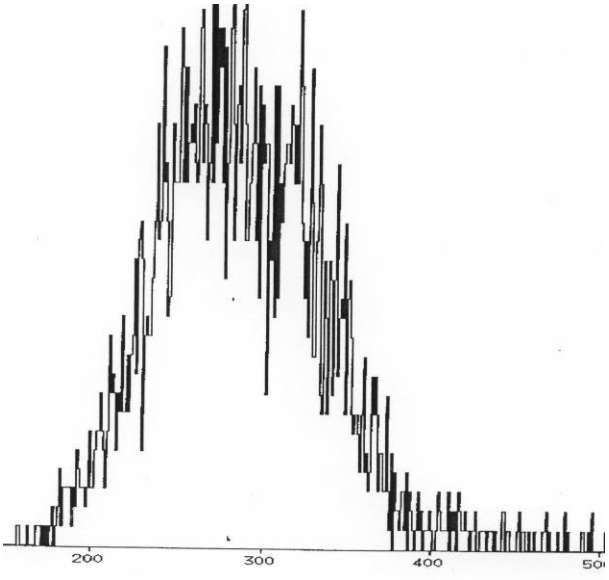

Figure 34 : Counts versus ADC channel in response to a ^{55}Fe source and 1600V HV, amplifier x65.

The pedestal subtracted ADC peak is estimated to be in channel 253. Converting to a charge measurement directly at the chamber output (and so before the amplifier) that is approximately

$$Q = 0.250 \text{ x } 253/65.5 = 965.7 \text{ fC} = 6.035\ 10^6 \text{ electrons}$$

Taking the average ionization potential to produce one electron-ion pair in Ar as 26.4 eV and 23 eV for isoC_4H_{10} then the number of primary electron-ion pairs created by the 5.89 keV X-ray can be estimated to be

$$N = 5890 \text{ x } (0.8/26.4 + 0.2/23) = 230 \text{ pairs}$$

This implies a gas gain of

$$G = 6.035\ 10^6 / 230 = 2.610^4$$

Supposing that the cathode plane (unmeasured here) is receptive to 50% of the charge collected at the anode, then each cathode should receive a charge of

$$Q_{cathode} = 966/2 = 483 \text{ fC}$$

This charge is distributed over several pads in the chamber, however, for certain geometries a pad will receive up to 80% of this charge, that is 386 fC, a value that is too high for the GASSPILEX dynamical range (as they were limited to a range of -120 fC to 250 fC at that time).

This rough estimate of the required dynamical range was subsequently confirmed through the detailed simulation and measurement of the prototypes that were to come.

Electronics and cathode plane response

The first tests were purely electronic in nature and were aimed at ensuring the good working order of the basic components. The first test was carried out in the lab, with no gas in the chamber or HV on the anode wires. A simple pulse, of known characteristics was injected on the anode wires. A fast pickoff was used as a trigger and the image of the charge on the cathode plane, on one channel, was measured with the GASSIPLEX. The following image is one of the first histograms obtained with the full acquisition logic and electronics boards in place. It has no great meaning in itself (the GASSIPLEX electronics were saturated) but it marked the first step in successfully decoding the detector response.

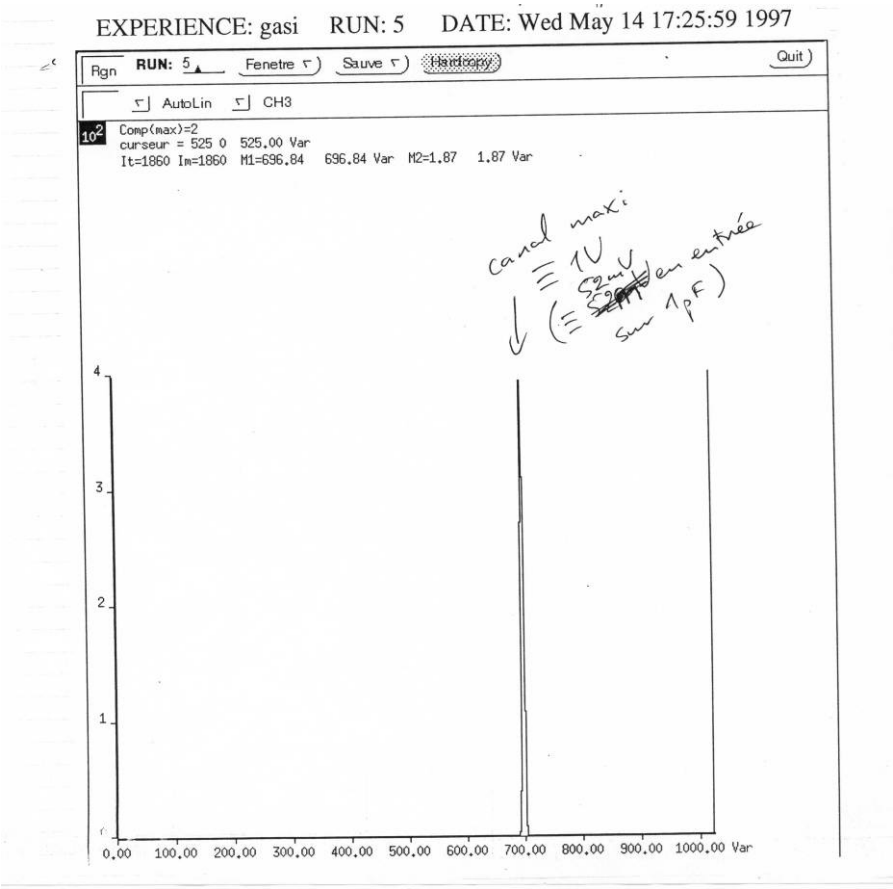

Figure 35 : Laboratory test, total charge response to an injected anode charge of 52 mV on a 1 pF capacitor

Over a short period (March-early June 1997), laboratory tests were carried out as physicists, engineers and technicians all learned how to "play" with the detector. The next symbolic step was the successful recording of the full set of strips plugged on the electronics. Of the 128 GASSIPLEX channels, 70 were plugged to the readout and the results are shown in Figure 36.

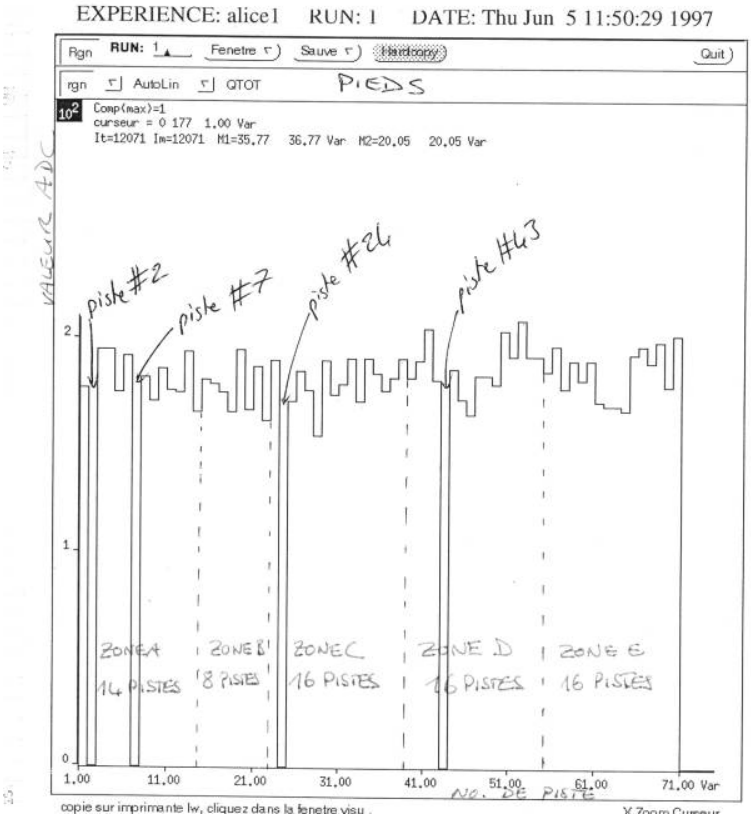

Figure 36: One of the first online histograms and represents the ADC pulse height versus channel number.

The image in Figure 36 has four gaps; each gap corresponds to a "dead" detector strip (on channels 2, 7, 24 and 43). The other 66 channels are clearly live, the different cathode plane regions are difficult to discern.

No results from this first test prototype were published.

ALICE1

ALICE1

ALICE1 was built during the period when ALICE0 was being tested. The list of specifications was established at the beginning of February'97, and the first HV and gas leak tests took place in mid-June. The detector was a multi-geometry prototype. It had one active cathode plane, with a more detailed pad layout structure. The anode wire plane was replaced with a new plane comprising two different wire pitches. The anode-cathode gap was variable in the sense that the detector was designed to be "easily" opened and the anode-cathode mechanical support could be interchanged with a support of a different thickness. With the exception of the wire radius, all the other detector parameters were variable. The prototype underwent three test beam periods; at the CERN PS (on line T10) with 6 GeV pions in June 1997 and 3.5 GeV pions in September 1997 and again, at the SPS (in H4) in April'98 with 350 GeV pions. It also ran with the new ALICE acquisition system DATEv2 [2], and used the new gas supply system that was being developed for use with the whole ALICE experiment. The general ALICE architecture was constantly being refined, and the estimation for the delivery of the general (global) zero level trigger meant that the FEE RC integration constant had to be increased, and so we moved from 0.7 μs to 1.2 μs. This also imposed a greater acquisition dead time.

Aims

The overall experimental objective was to establish the different detector responses to different geometrical configurations. The beam impact points were to be reconstructed for the different detector geometries, and the HV operational plateau versus spatial resolution was to be explored; the optimal detector geometries were to be deduced.

There were four main phases associated with this detector

- A first formative test period in June'97
- A second set of tests at the PS in Sept'97
- A third "high resolution" experiment at the SPS in April'98
- The simulation of the second and third phases and predictions for future electronics behaviour and expected resolutions. The main development of the offline reconstruction programs, mapping strategies and reconstruction algorithms were associated with this phase and the strategy for future programs established.

[2] ALICE DATE V2, first release April 98

Detector geometry

A schematic view is shown in Figure 37.

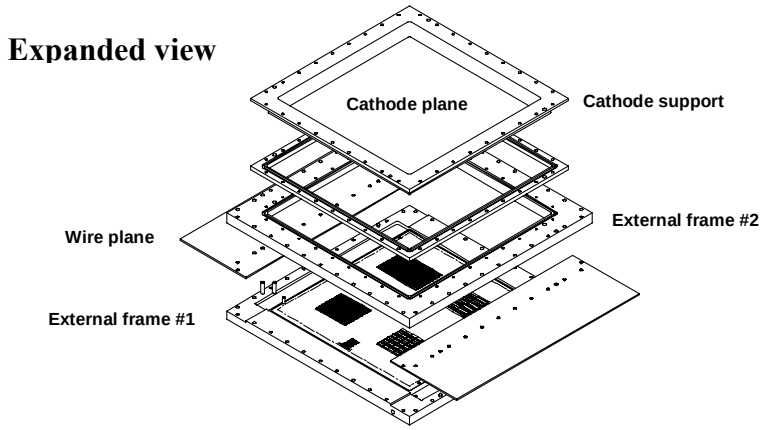

Figure 37 : ALICE 1 expanded view.

The external frames were square, measuring roughly 560 x 560 mm^2. The different elements were constructed so that an 180° rotation of the anode plane with respect to the cathode plane gave another detector layout.

The cathode plane pad structure is shown with the various pad lengths and widths in Figure 38,

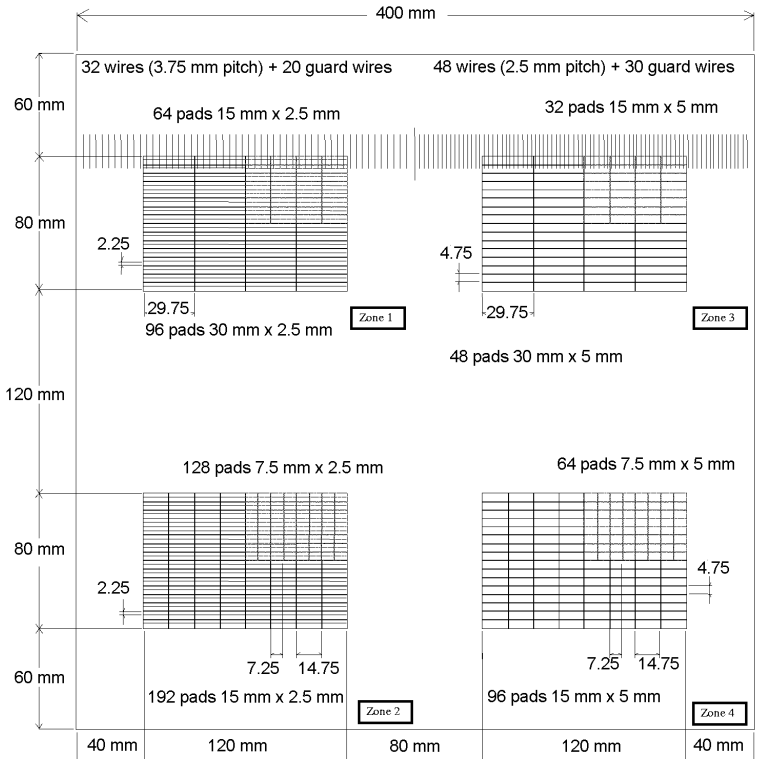

Figure 38 : pad layout scheme

and anode the wire plane with the different wire pitches follows on in Figure 39.

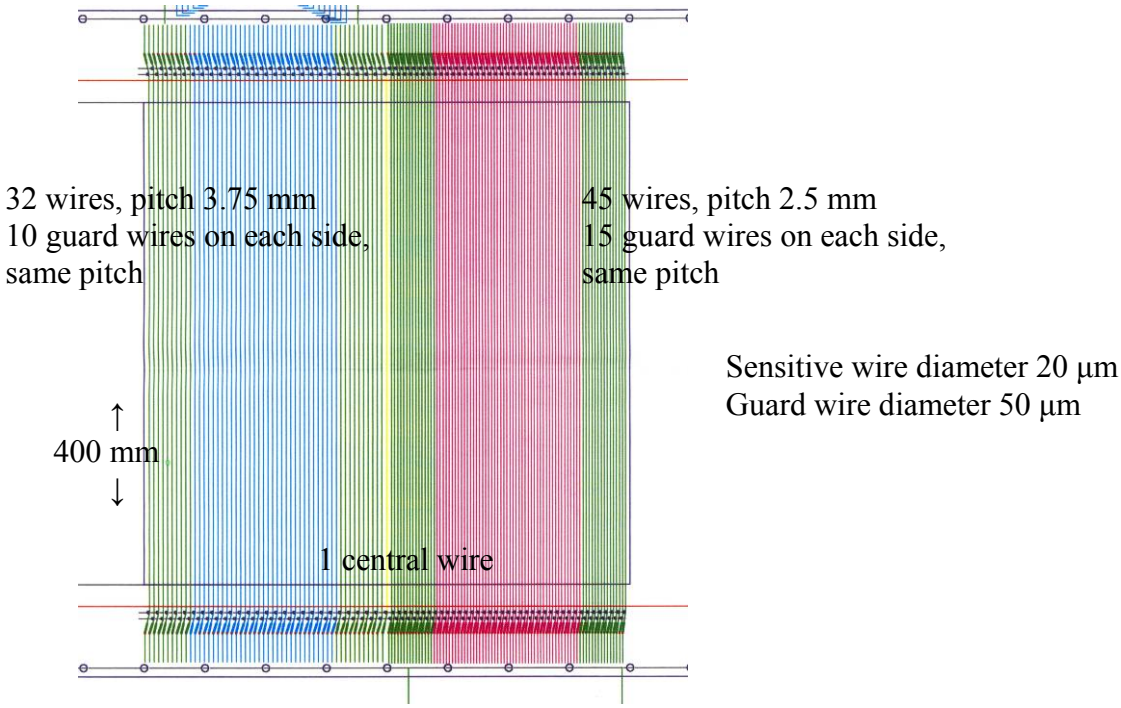

Figure 39 : anode wire plane layout.

The two sets of anode wires had independent HV supplies, providing independent gain control for each of the different wire pitches.

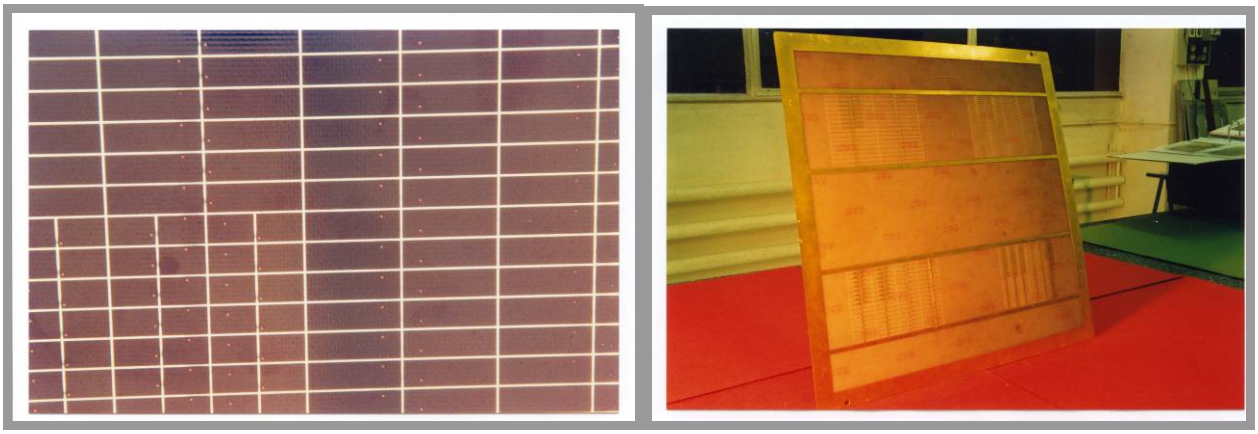

Figure 40 : Photographs of the copper pad plane (LHS), the feed through holes on each pad are visible. This image shows the junction between two pad sizes. The other image (RHS) shows the back side of the pad plane engraved on the PCB. The four distinct pad areas are visible.

Gas supply and filling gas

June'97: Ar/Ethane(20%) at 600-700 sccm during 48 hours, CERN manually controlled supplies.

Thereafter: Ar/iso-C_4H_{10}(20%) at a high flow rate.

Electronics

One of the new electronics evolutions was the use of flexible Kapton connectors for the signal readout. The very high electronics density expected for the inner zone station 1 implied the use of lightweight, flexible, short and robust readout cables. The well known Kapton solution fitted the bill. Various Kapton qualities, thicknesses and multi-layering methods were tried and tested by our detector R&D group. The mechanical tests involved repeated folding and bending and thermal resistance.

Our first batch of Kaptons suffered from an interesting design flaw. The initial solder points were circles, and under the thermal effect of the soldering iron, the wire-to-solder point broke on most attempts to solder. This was problem was resolved by designing a softer transition form for the solder point at the wire end. As well as this, the protective outer coating was not uniform and sections of bare wires were visible. These problems had immediate consequences on our quality control, and a full set of connector tests were conceived. Every soldered point and connection has since been individually and systematically tested with the help of a specially designed control box.

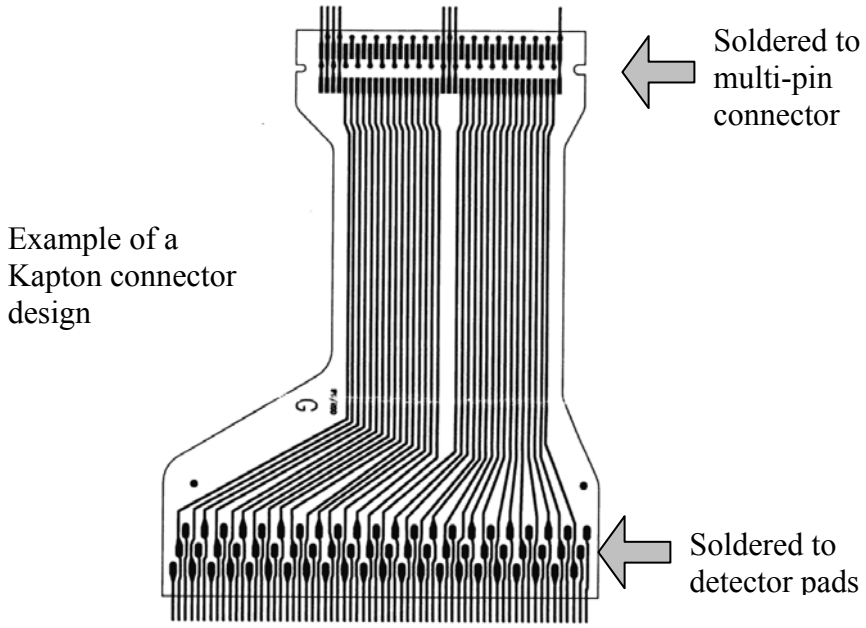

More of the 1.5 μm technology 64-channel GASSIPLEX cards were used to readout the different pad areas.

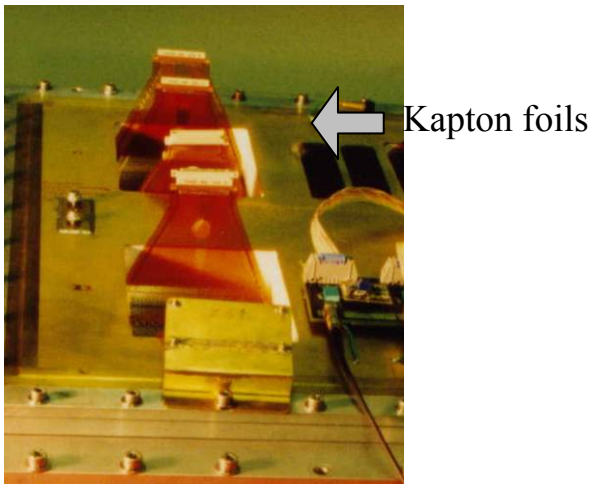

Figure 41 : Kapton foils mounted on the ALICE1 prototype.

Readout/acquisition

The main new point was the daisy chaining for up to 192 GASSIPLEX channels. This was the longest chain implemented at this point, and we ran with this configuration for the first time as beta testers of the new ALICE acquisition system, DATE.

Test beam setup

The CERN test beam facilities at the PS and SPS also included the provision of a set of silicon trackers, readout with the DIGIPLEX **[27]** cards and a trigger setup based on multiple scintillator coincidences. The associated online and reconstruction codes were provided by the Bari (Italy) group **[33]**, who specialized in, among other things, the development of these detectors.

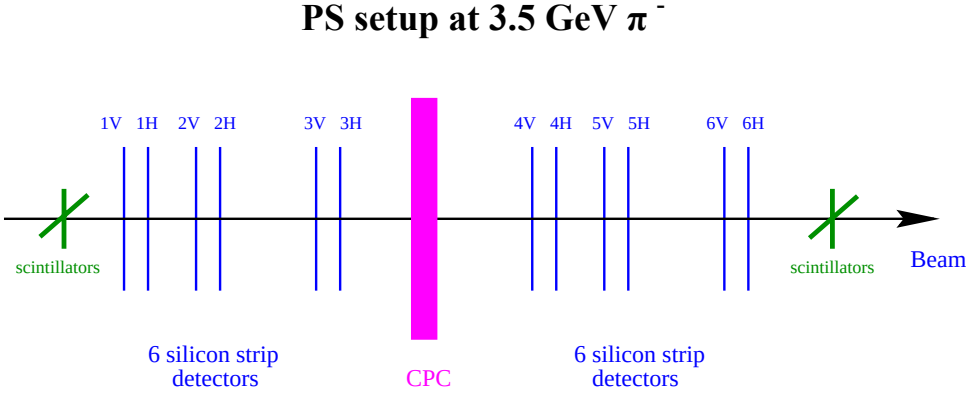

Figure 42 : Principle of the PS test beam layout: the trigger for the 3.5 GeV pions is given by a four fold coincidence between the two crossed scintillators and collimates the selected trajectories over 1 cm^2. The CPC, along with 6 horizontal silicon strip and 6 vertical silicon strip detectors were readout with the DATEv2 acquisition system.

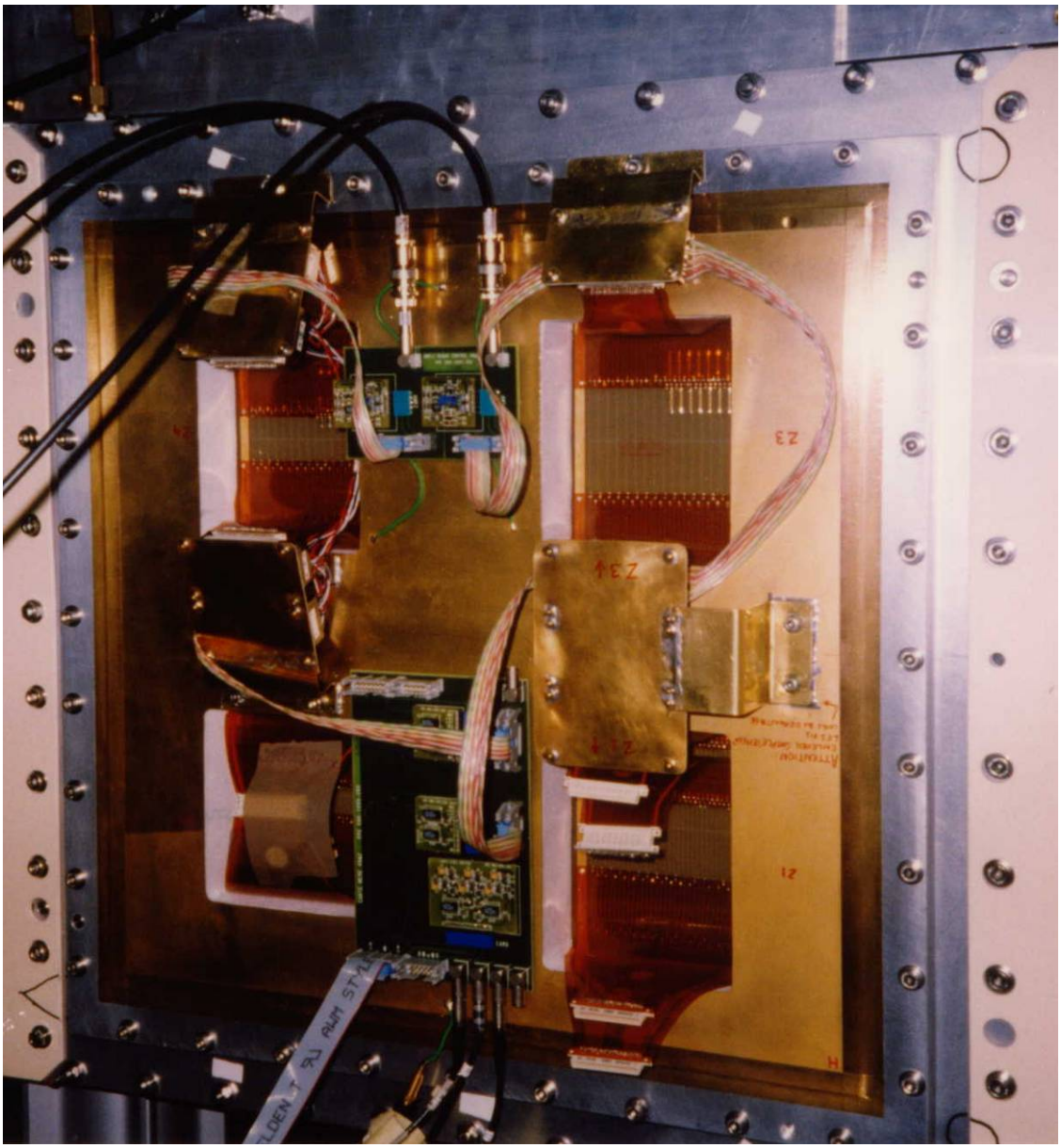

Figure 43 : ALICE1 in situ at the PS in CERN. The multiple scattering contribution was minimized by placing the electronics on the side of the active surfaces. The effective thickness was estimated to be 1.2% of a radiation length.

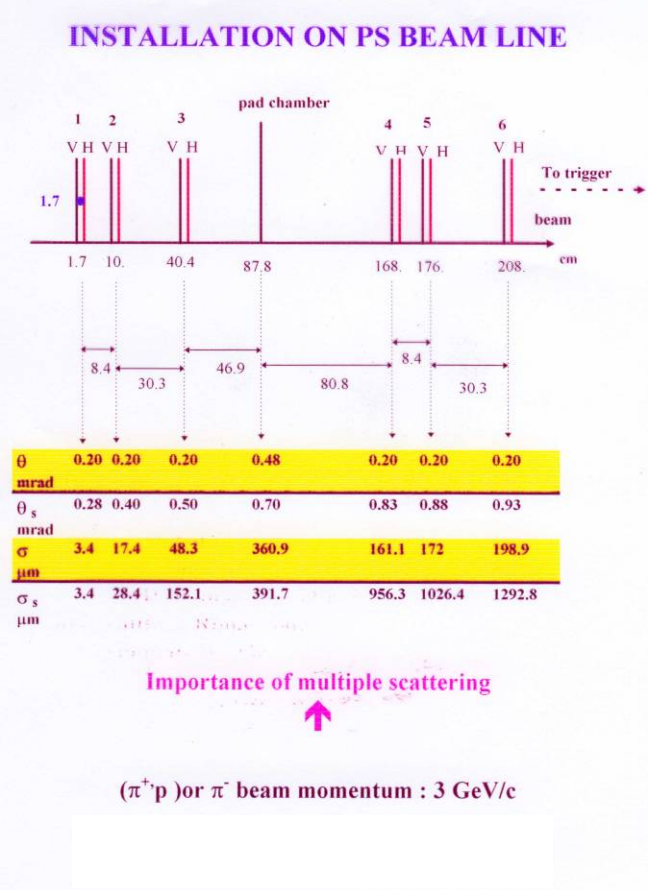

6 tracker planes, Vertical and Horizontal and their relative positions along the beam-line.

Inter- plane distances.

Multiple scattering per plane (in mrad)
Cumulative multiple scattering (in mrad)

Contribution to the spatial resolution per plane (in µm)
Contribution to the overall spatial resolution (in µm)

Figure 44 : Above is a quantified view of the overall layout, taken from a presentation given at the time. The evaluation of the detector thicknesses appear for the first time, and was a handicap for the spatial resolution measurements at the PS. The main scattering contribution came from the accumulated thickness of the silicon trackers. The ALICE1 electronics was not in the beam path and the overall detector thickness was estimated at 1.2 % of a radiation length.

SPS setup 350 GeV π^-

The SPS experimental layout for this series of tests was the same as for the PS test period.

At both the PS and SPS test beam sites, the detector was mounted on an adjustable, remote controlled displacement system that easily allowed different detector zones to be placed in the 1 cm^2 beam spot.

Online monitoring

The code provided by the Bari group came complete with the tools for straight line reconstruction through the Silicon tracker. Correct adjustment of this code meant an easy comparison with the CPC reconstructed impact point could be made. In reality, only the hit pad patterns were observed online as the detector-to-detector alignment procedure was rather delicate, and the monitoring setup was not optimized for this. As well as this, each online "calculation" slowed down the acquisition cycle as new data buffers waited for the preceding ones to be analysed before continuing.

Offline reconstruction

The reconstruction codes were developed to compare the Mathieson-Gatti charge distribution reconstruction method and the barycenter method. The mappings used for this detector were multiple

and difficult to control. Numerous errors in the notation and in defining the detector's orientation considerably slowed down the data analysis. This was compounded by a problem in the FEE readout where channels occasionally “disappeared” from the data stream. This meant the subsequent channel numbering was offset by the number of missing (badly coded) electronics channels. The main lesson learned here was to adopt a more rigorous method for mapping controls and more checks on data coding in future experiments.

ALICE1 - Status Reports, Results and Simulations

As previously indicated, the more polished results presentations can be found elsewhere, in this case in Liliane Kharmandarian's thesis [**35**] and the dimuon arm TDR (**[16]** from 1999). Nonetheless, a set of results are given for each test period.

The chronology of the report is as follows:

- June'97 tests at the PS Status report
- Sept'97 tests at the PS Status report
- April'98 tests at the SPS Status report

After the selected slides from these talks, models and simulations derived from this data set are given.

The main subjects studied were the HV dependency of the spatial resolution, incident particle angle, reconstruction efficiency and gain. An estimate of the overall homogeneity of the detector response was made.

All in all, six different geometries, with three to six HV settings per configuration and five different angular settings were studied; giving 39 different settings to be analysed.

June'97 tests at the PS Status report

(from a talk given at CERN in October/November'97)

STATUS REPORT

ORSAY CATHODE PAD CHAMBER TESTS

DETECTOR DESCRIPTION

JUNE TESTS - UNSTABLE GAIN

SEPTEMBER TESTS

GASSIPLEX OBSERVATIONS

RAW DATA SPECTRA

PRELIMINARY RESULTS

THE FUTURE.....

JUNE TESTS

MAJOR PROBLEMS: -

GAIN STABILITY

GASSIPLEX BREAKDOWN

good points:-

- No major acquisition problems
- On-line spectra easily obtained
- Trigger system already set-up

not-so-good points:-

- Gas proportions difficult to control
- Some noisy "pads"
- Loss of data through gassiplex breakdown
- Bad resistor in HV line

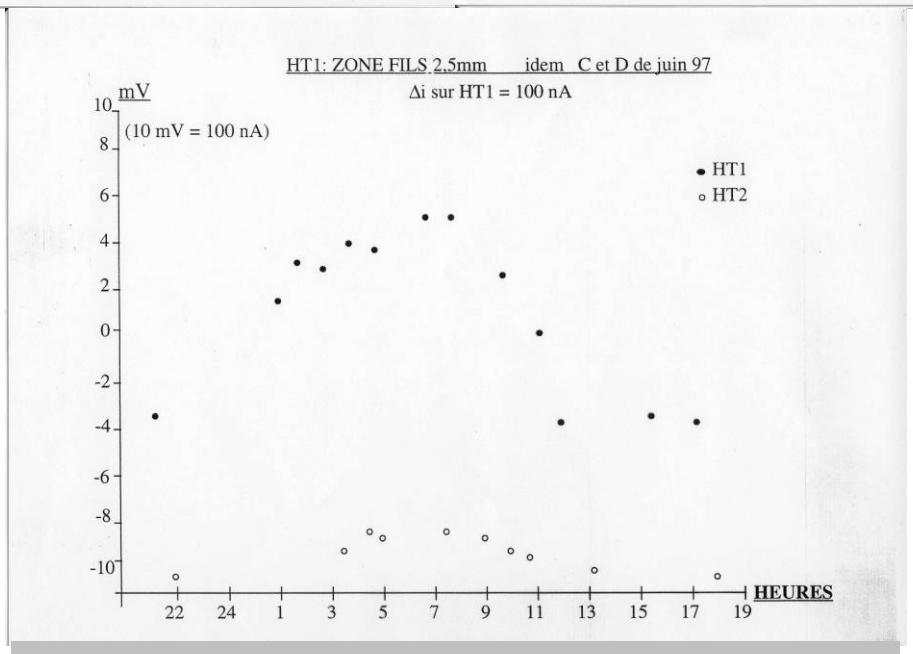

Current variations on the two proportional wire grids as measured in the lab on a test bench. Thought to be due to temperature/pressure variations.

UNSTABLE DETECTOR GAIN (part 1)

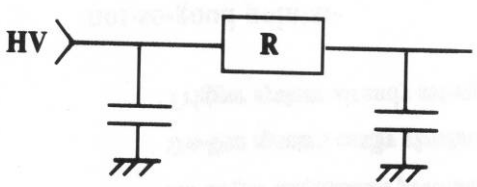

R = 5 x 10^8 Ω (construction error)

If the current changes by Δ I = 100 nA

then Δ U = 100 nA x 5.10^8 = 50 V

→ **drop of 50 V across the resistor**

→ **drop in detector gain**

Effect of the bad resistor on the proportional wire gain to explain observed gain variations.

Experimental rapid current variations on the 3.25 mm pitch proportional wire grid.

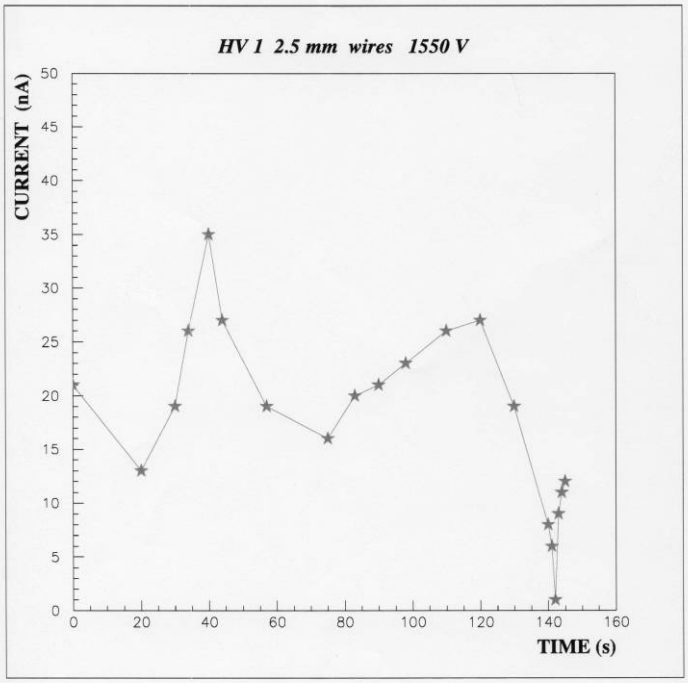

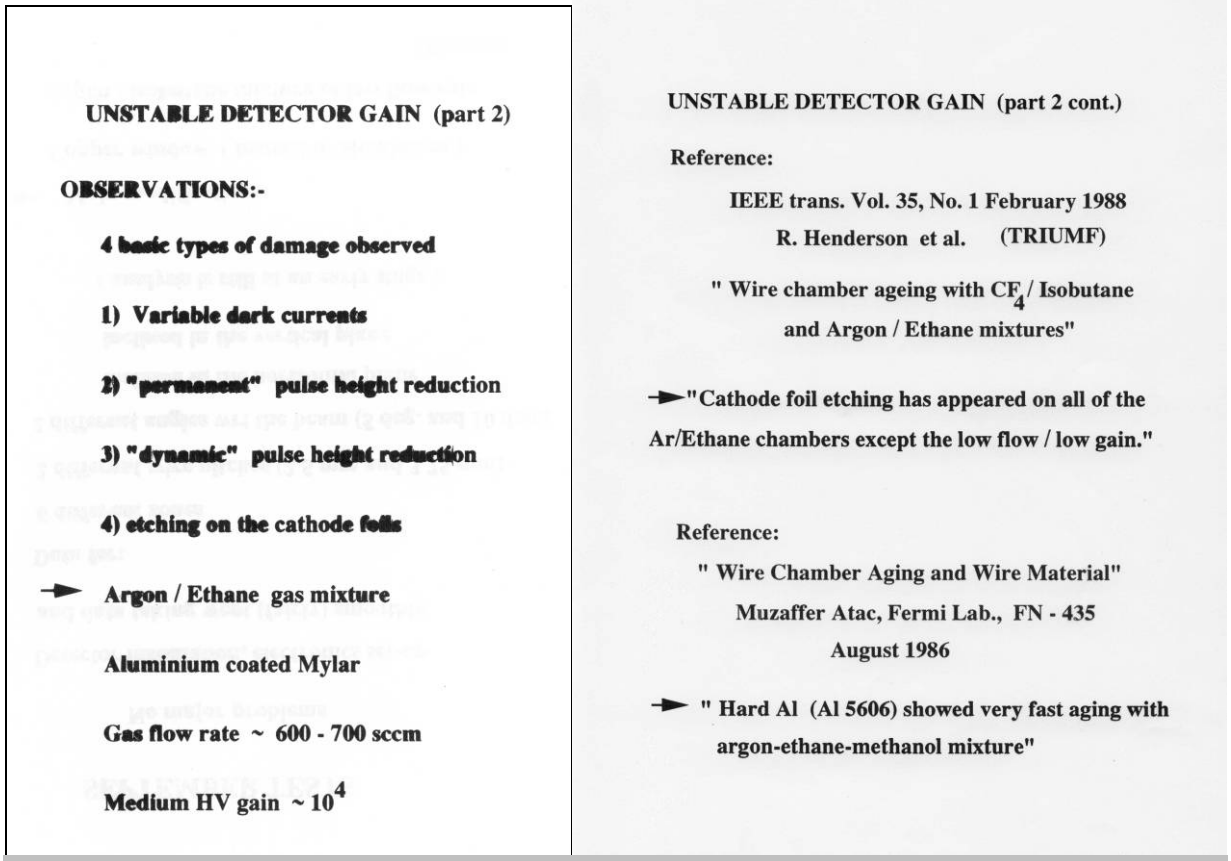

UNSTABLE DETECTOR GAIN (part 2)

OBSERVATIONS:-

4 basic types of damage observed

1) Variable dark currents

2) "permanent" pulse height reduction

3) "dynamic" pulse height reduction

4) etching on the cathode foils

→ **Argon / Ethane gas mixture**

Aluminium coated Mylar

Gas flow rate ~ 600 - 700 sccm

Medium HV gain ~ 10^4

UNSTABLE DETECTOR GAIN (part 2 cont.)

Reference:

IEEE trans. Vol. 35, No. 1 February 1988
R. Henderson et al. (TRIUMF)

" Wire chamber ageing with CF_4 / Isobutane and Argon / Ethane mixtures"

→ **"Cathode foil etching has appeared on all of the Ar/Ethane chambers except the low flow / low gain."**

Reference:

" Wire Chamber Aging and Wire Material"
Muzaffer Atac, Fermi Lab., FN - 435
August 1986

→ **" Hard Al (Al 5606) showed very fast aging with argon-ethane-methanol mixture"**

Analysis of the effect of the Ar/Ethane gas in contact with Aluminium. Apparently not a good combination.

Sept'97 tests at the PS Status report

(from a talk given at CERN in October/November'97)

SEPTEMBER TESTS

No major problems

Detector installation, electronics set-up and data taking went (fairly) smoothly

Data for:

6 different zones

2 different wire pitches (2.5 mm and 3.75 mm)

2 different angles wrt the beam (5 deg. and 10 deg.)

inclined in the horizontal plane

inclined in the vertical plane

(analysis is still at an early stage)

→ **Main modifications:**

Copper window (instead of aluminium)

Argon / isobutane mixture at low flow rate 100 sccm

Summary of the tests

EXPERIMENTAL OBSERVATIONS

GASSIPLEX BEHAVIOUR

RAW DATA SPECTRA

Main subjects of the talk.

GASSIPLEX OBSERVATIONS

Threshold setting:

Disparity between the offsets

→ **Higher threshold for all channels**

→ **thresholds all aligned to the worst case**

→ **Lower dynamical range**

CRAMS coder codes strictly negative signals over a fixed range (0 to -1.5 V)

→ **No flexibility**

One dead GASSIPLEX channel leads to the loss of information for all following channels (problem encountered in the June data taking)

Observation of the electronics behaviour

GASSIPLEX CALIBRATION

Individual charge injection via a calibrated capacitor on the test line CAL_IN

Acquisition triggered randomly

Gating signals via the SUBATECH module

Measure V_injected (V_in) and ADC response

Linear fit: V_in = slope * ADC + B

slope = GASSIPLEX gain

B = pedestal value

Electronics gain calibration

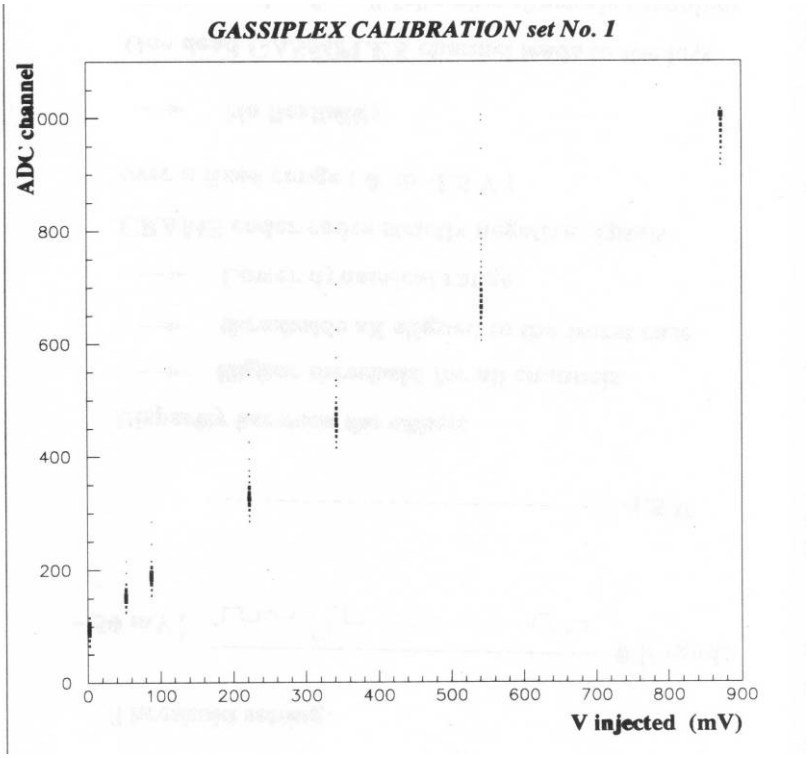

ADC response to 7 different injected charge values for 192 daisy chained channels. These points were then fitted with straight lines to determine the gain (slope) and calculate pedestal levels (the constant B *below).*

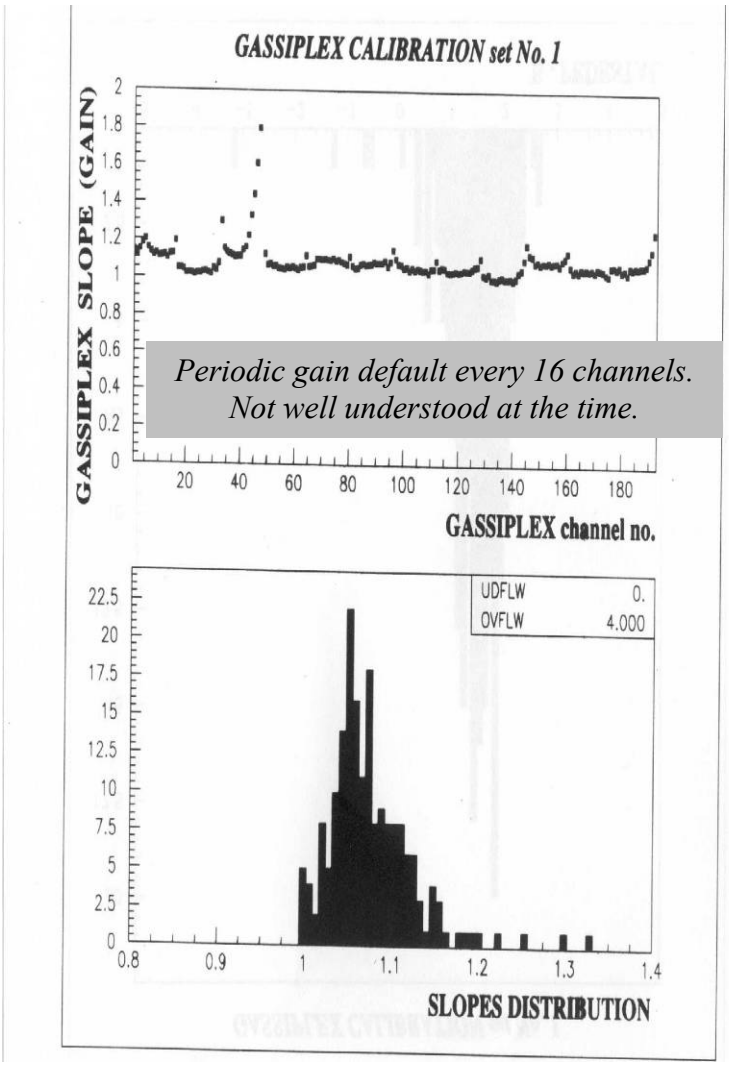

Periodic gain default every 16 channels. Not well understood at the time.

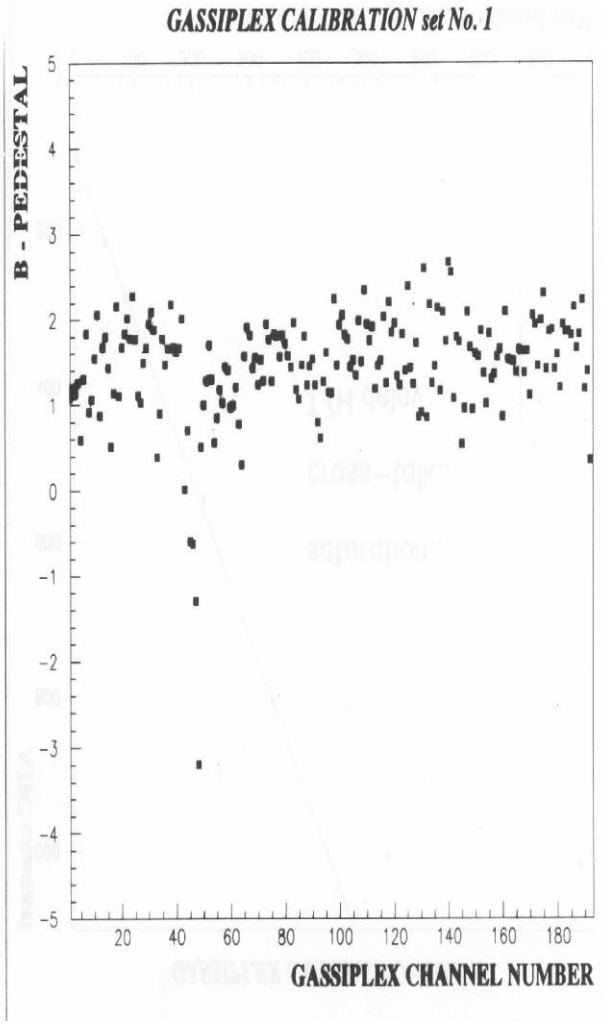

Calibration curves for 192 channels comprised of the straight line fit results.

Cathode plane response to single charged particle impacts.

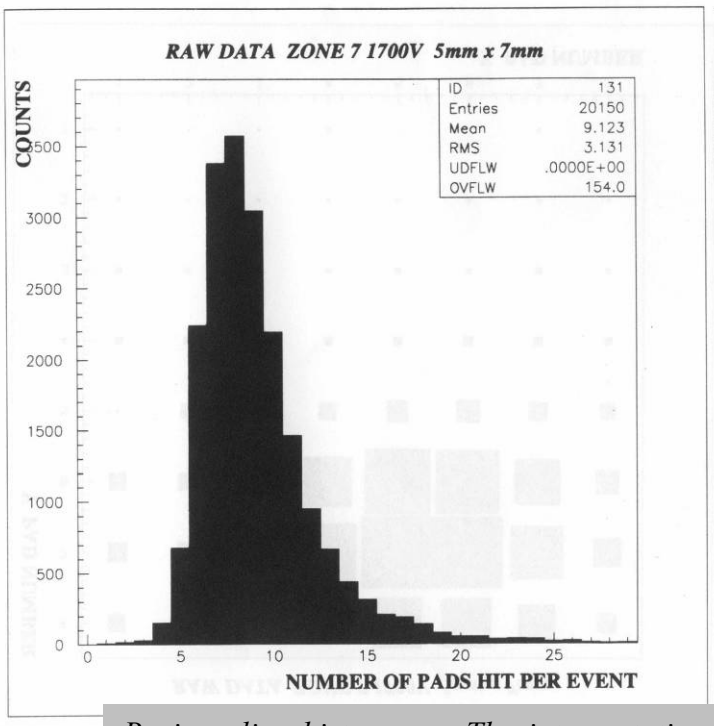

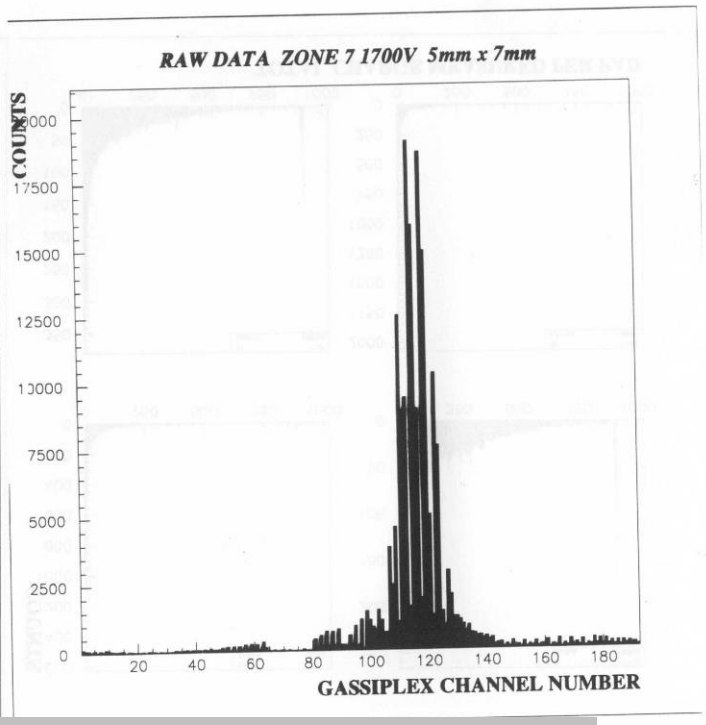

Basic online histograms. The interpretation of the channel number in terms of spatial coordinates is not yet done at this level.

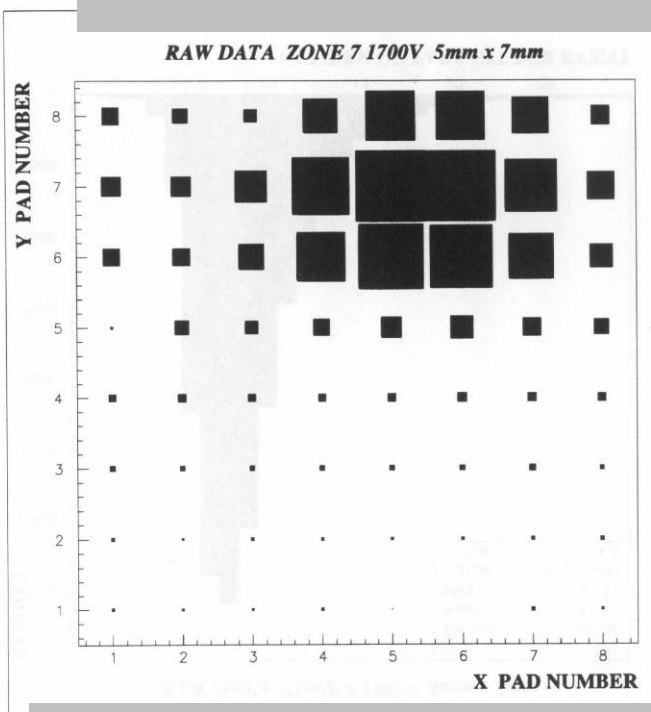

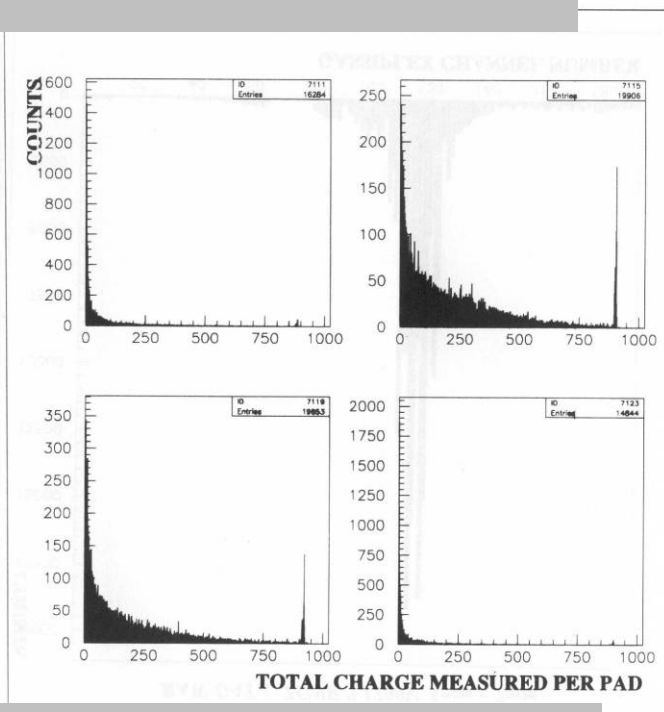

A first level reconstruction algorithm maps the gassiplex channel numbers to digital (X,Y) impact points. The beam impact area is obvious on the left hand figure. The four most frequently hit pads are analyzed. Their amplitudes are shown on the right hand side image. Apart from the general form of the distributions, the number of saturated pads indicates whether the electronics dynamical range is sufficient for the particular detector gain setting.

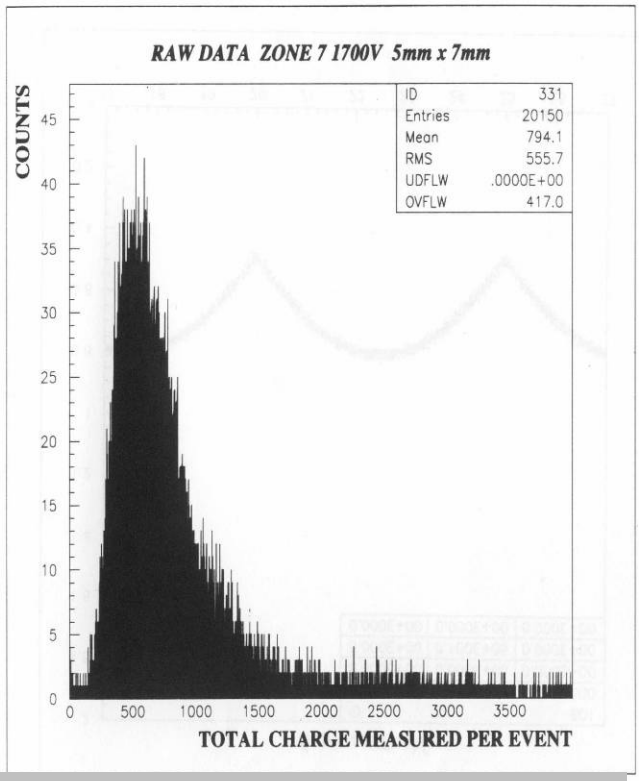

The results of a more detailed analysis of the charge distribution per event after threshold cuts and pedestal subtraction. The shape is a rough Vavilov distribution, the peak is indicative of the chamber gain

CURRENT ANALYSIS

Detector thickness = 2.7 radiation lengths ! 2.7 % of X_0

→ 0.65 mrad due to multiple scattering

Tracking detector alignment

Variable charge acceptance due to variations in the electronics response

Modular program to allow for different geometries, graphical display, different fit routines and statistical analysis (efficiencies etc.)

NEXT STEPS

Optimise detector readout system to minimize the risk of losing data

Better GASSIPLEX uniformity

Find a calibration method

1 m^2 chamber already under construction

April'98 tests at the SPS Status report

(Talk given at CERN in June'98)

This data set was very productive, an extensive set of different geometries and HV settings were explored and gave better overall understanding of the detector response. The bulk of the results were presented in the TDR.

Orsay CPC beam tests results (SPS April 1998)

L. Bimbot, P. Courtat, R. Douet, P. Fauche, D. Jouan,
L. Kharmandarian, Y. Le Bornec, M. Mac Cormick,
J.M. Martin, N. Willis

Presented by M. Mac Cormick

Prototype constructed by the Orsay R&D Department

CERN Alice week - June 1998

Orsay CPC beam tests results (SPS April 1998)

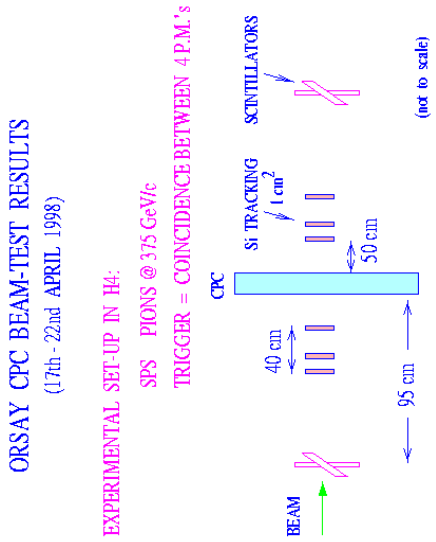

Experimental layout

Orsay CPC beam tests results (SPS April 1998)

EXPERIMENTAL PROGRAMME

MEASURE THE DETECTOR RESPONSE (2 PARAMETERS)

HIGH VOLTAGE → PROPORTIONNALITY PLATEAU
GAIN FACTOR

GEOMETRY → RECONSTRUCTION EFFICIENCY
SPACIAL RESOLUTION
GEOMETRICAL EFFECTS

DETECTOR HOMOGENEITY

RESPONSE AS A FUNCTION OF THE INCIDENT ANGLE

TEST PERIOD OF 5 DAYS

6 DIFFERENT GEOMETRIES STUDIED

3 TO 6 HV STEPS PER GEOMETRICAL CONFIG.

5 DIFFERENT INCIDENT ANGLES

→ 32 POINTS MEASURED SUCCESSFULLY

~ 200,000 EVENTS PER POINT

A LOT OF GOOD LUCK - 1 ELECTRONIC BREAKDOWN
SUCCESSFUL DATE2 ACQUISITION TEST — RAYMOND DOUET

Orsay CPC beam tests results (SPS April 1998)

SELECTION OF RESULTS FROM A FIRST ANALYSIS

COMPLETE EXAMPLE FOR ONE ZONE:

ZONE 7 - PADS = 5.0 x 7.5 mm WIRE SPACING = 2.5 mm

REMINDER : 20 micron DIAMETER TUNGSTEN WIRES
COPPER PADS 17.5 microns THICK
FILLING GAS 20% ISOBUTANE + 80% ARGON

SOME RESULTS FROM THE MATHIESON FIT ANALYSIS
(Geometrical effects, resolutions, reconstruction efficiency, gains)

SOME RESULTS THE CENTER OF GRAVITY ANALYSIS
(Uncorrected residuals, correction function, position dependant residuals)

RESULTS FOR ALL THE GEOMETRICAL CONFIGURATIONS

ANGULAR RESIDUALS

SOME PARTICULAR COMPARISONS

NEXT ANALYSIS STEPS

CONCLUSIONS

Talk overview

Orsay CPC beam tests results (SPS April 1998)

ZONE 7 WIRES = 2.5mm PADS = 5.0 x 7.5 mm^2

HV = 1700V

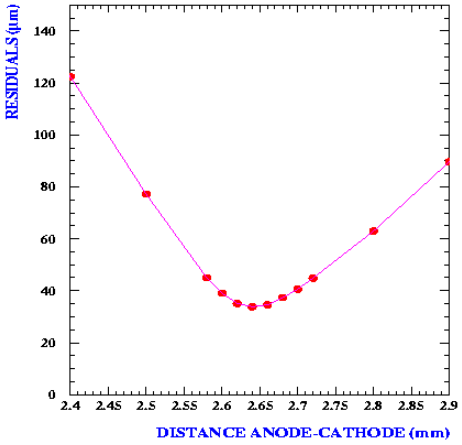

Residuals supposing different anode-cathode distances in minimizing the charge distribution fit.

Orsay CPC beam tests results (SPS April 1998)

MATHIESON FIT: CHARGE DISTRIBUTION
GEOMETRY AND 1 EMPIRICAL PARAMETER (k3)

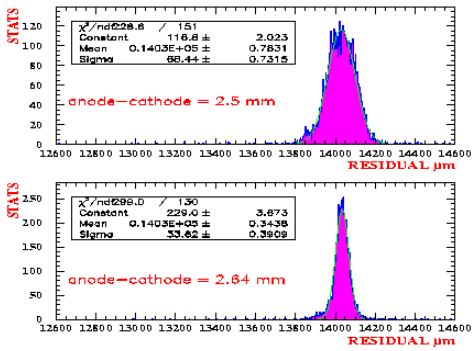

ZONE 7 WIRES = 2.5 mm PADS = 5.0 x 7.5 mm^2

Mathieson fit results: Residuals for one configuration, but supposing two different anode-cathode distances. 2.5 mm gives 68 μm and 2.64 mm gives 33 μm. The nominal setting was 2.5 mm.

Orsay CPC beam tests results (SPS April 1998)

UNCORRECTED CENTRE OF GRAVITY (μm)
SUM OF ALL IMPACT POINTS
OVER 1 PAD WIDTH

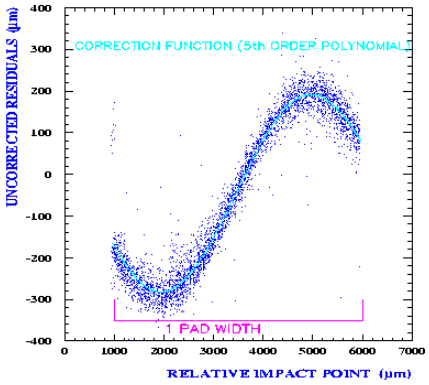

COG algorithm: Basic form of the uncorrected reconstructed impact point with respect to the reference impact point for one pad length.

Orsay CPC beam tests results (SPS April 1998)

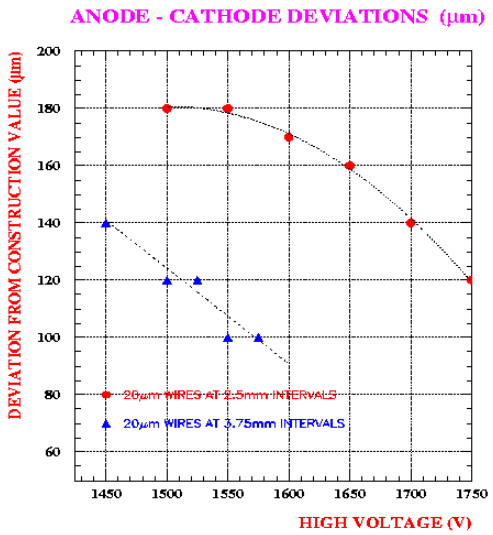

Estimated variations of the "true" anode-cathode distance with respect to the mechanical specifications, and this for different HV values

Orsay CPC beam tests results (SPS April 1998)

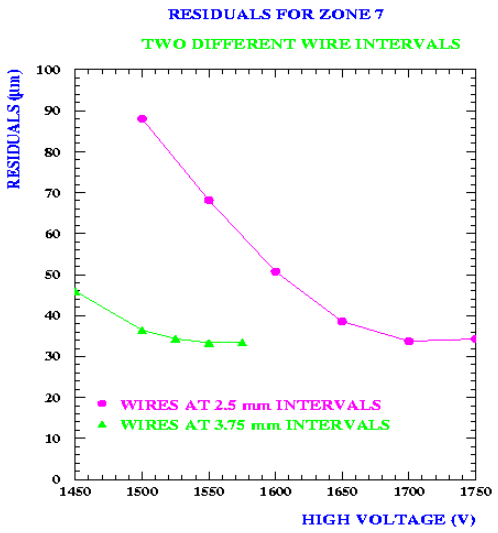

Residuals for two different wire pitches and varying HV.

Orsay CPC beam tests results (SPS April 1998)

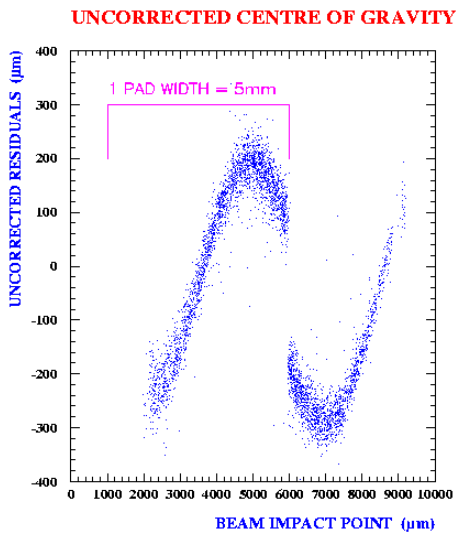

COG algorithm: Basic form of the uncorrected reconstructed impact point with respect to the reference impact point for one pad length.

Orsay CPC beam tests results (SPS April 1998)

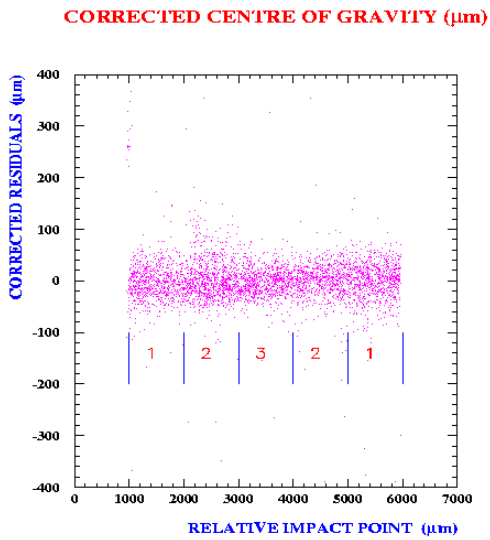

COG algorithm: corrected residuals with slices used to define the center, off center and edge areas of a single 5 mm pad width.

Orsay CPC beam tests results (SPS April 1998)

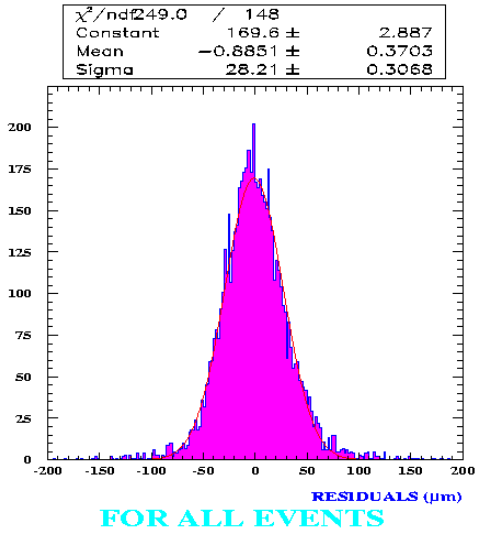

COG algorithm: projection of the corrected residuals. Overall resolution is 28 µm.

Orsay CPC beam tests results (SPS April 1998)

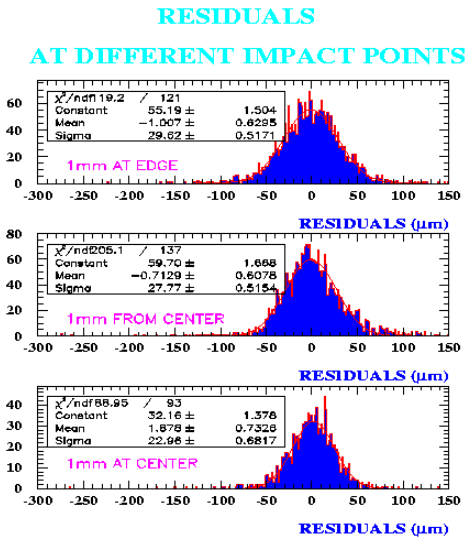

COG algorithm: projection of the corrected residuals for different positions along one pad length. Results are 30 µm, 28 µm and 23 µm going from top to bottom.

Orsay CPC beam tests results (SPS April 1998)

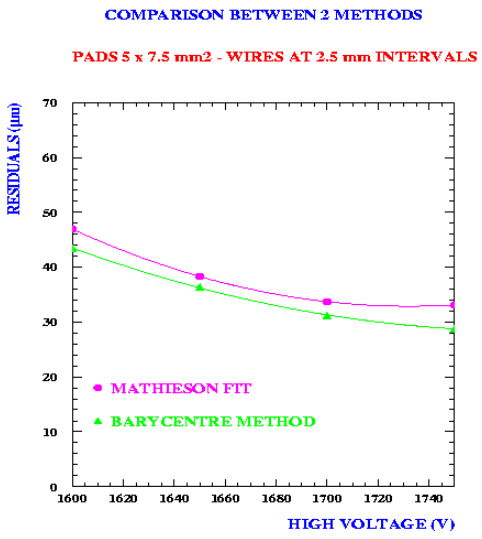

Residuals versus HV for the two reconstruction algorithms and the same geometrical layout.

Orsay CPC beam tests results (SPS April 1998)

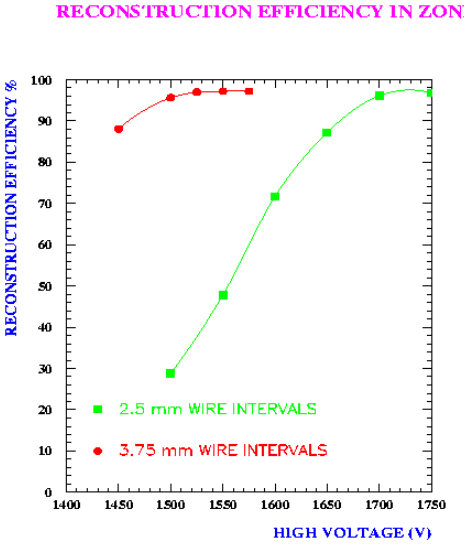

Reconstruction efficiency for the two anode wire pitches and the same pad layout.

Orsay CPC beam tests results (SPS April 1998)

RECONSTRUCTION EFFICIENCIES

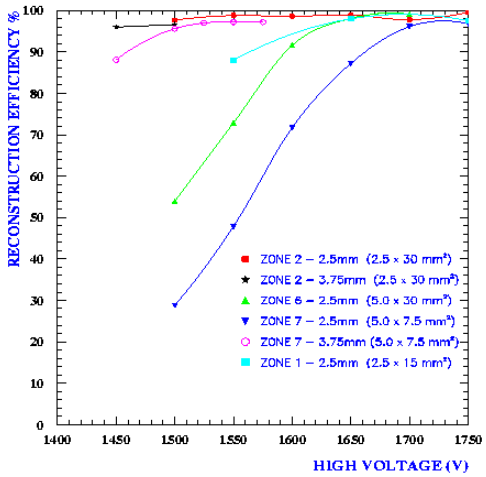

Reconstruction efficiencies for the different pad geometries and anode wire pitches and their HV dependencies.

Orsay CPC beam tests results (SPS April 1998)

"GAIN" ZONE 7

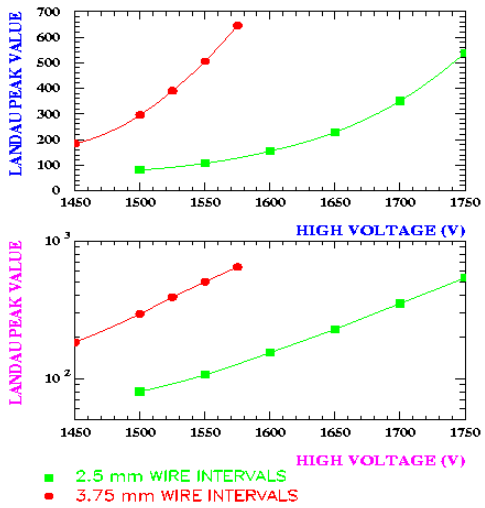

Gain evolution for different wire pitches on a linear (top) and log (bottom) scale.

Orsay CPC beam tests results (SPS April 1998)

GAIN CHANGES (ADC CHANNELS)

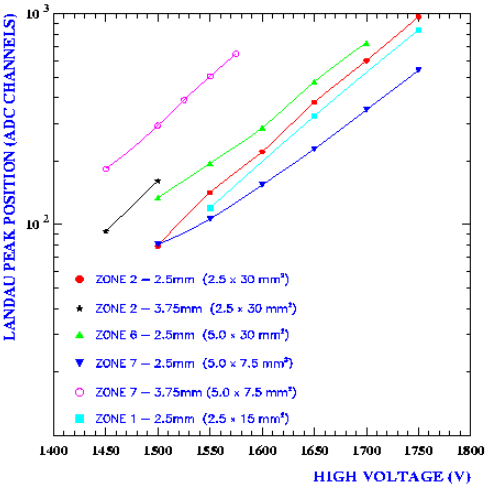

Gain evolution for all the different pad/strip sizes.

Orsay CPC beam tests results (SPS April 1998)

ANODE - CATHODE DEVIATIONS (μm)

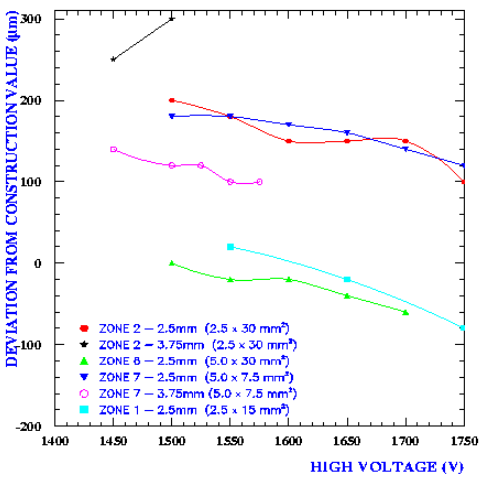

Apparent anode-cathode shifts for all the different pad/strip sizes. Based on the optimal charge minimization and leaving the anode-cathode parameter free to change.

Orsay CPC beam tests results (SPS April 1998)

ZONE 7 (5.0 x 7.5 mm^2) RESIDUALS (µm)

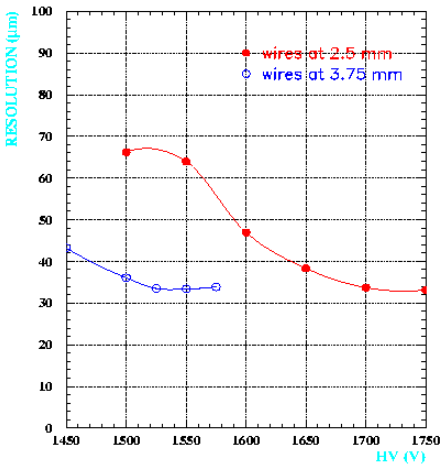

Resolutions for the two different wire pitches as a function of HV.

Orsay CPC beam tests results (SPS April 1998)

TWO DIFFERENT ZONES
SAME WIRES, SAME LENGTHS
DIFFERENT WIDTHS

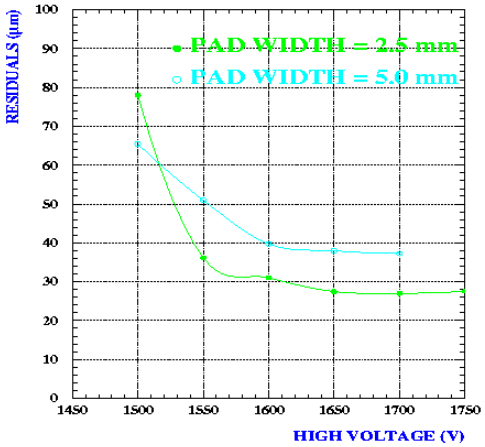

Resolutions for two different pad widths as a function of HV.

Orsay CPC beam tests results (SPS April 1998)

TWO DIFFERENT ZONES
SAME WIRES, SAME WIDTHS
DIFFERENT LENGTHS

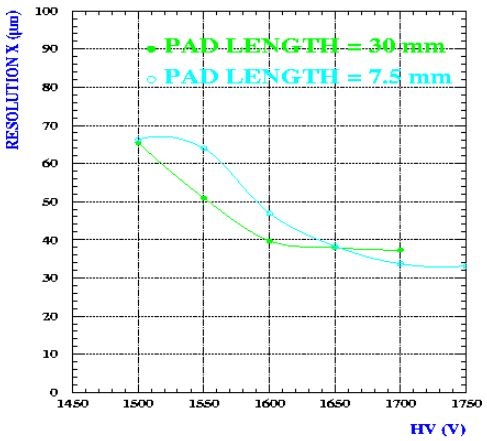

Resolutions for two different pad lengths as a function of HV.

Orsay CPC beam tests results (SPS April 1998)

ANGULAR STUDY

RESIDUALS (µm)

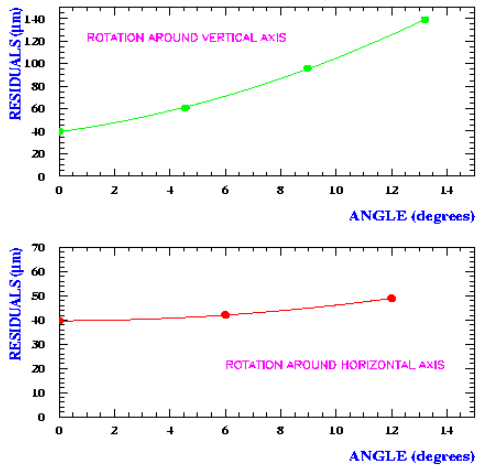

*Resolutions for varying angles on 30 mm long strips and with a 2.5 mm wire pitch at 1600 V. More details can be found in reference **[35]**, pp.93-95.*

Center of Gravity (COG) algorithm

residual = tracker determined impact - detector COG coordinate

Orsay CPC beam tests results (SPS April 1998)

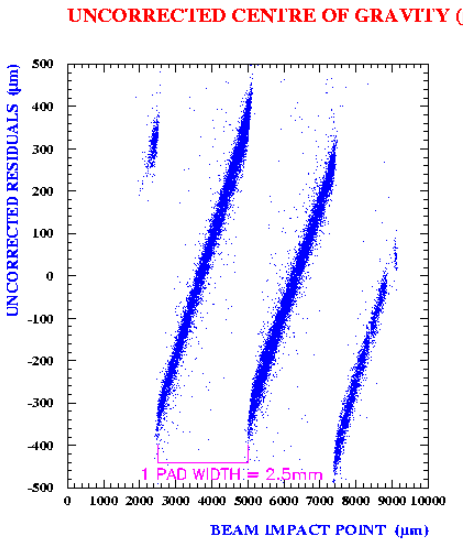

Step 1: Uncorrected residuals versus tracker calculated impact point. For a given geometry the default should be the same for all pads.

Orsay CPC beam tests results (SPS April 1998)

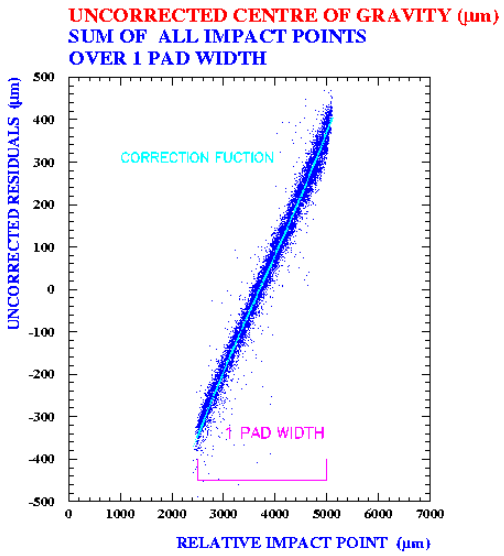

Step 2: Superimposed residuals. Same correction function is to be applied for all pads.

Orsay CPC beam tests results (SPS April 1998)

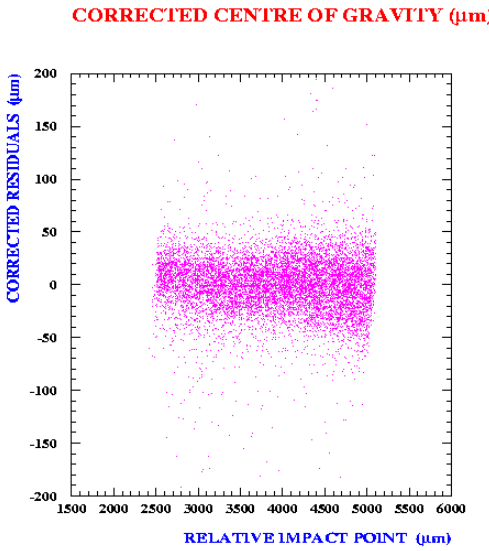

Step 3: After application of the empirical polynomial correction function.

Orsay CPC beam tests results (SPS April 1998)

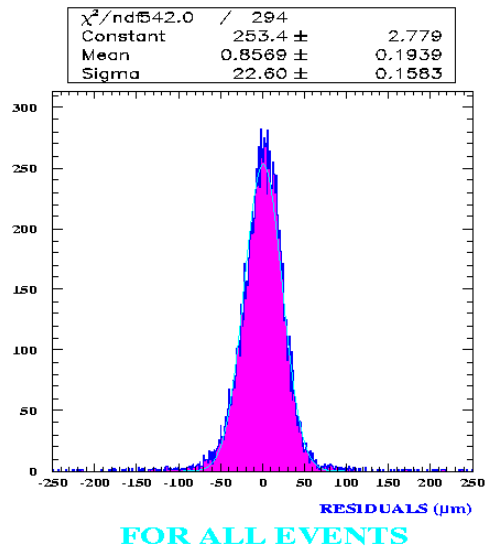

Step 4: Projection of the corrected residuals. The resolution is 23 µm.

Orsay CPC beam tests results (SPS April 1998)

$\sigma = 20\ \mu m$

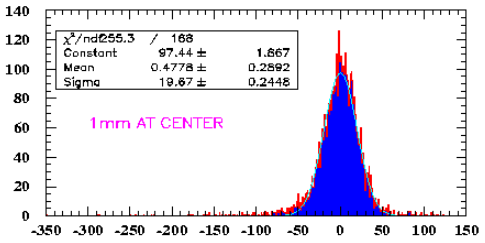

$\sigma = 24\ \mu m$

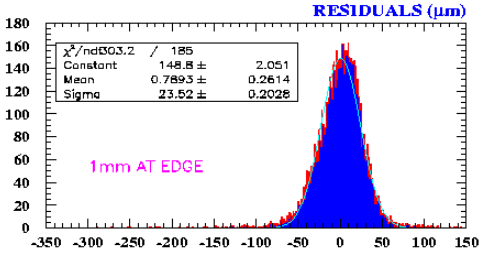

Position dependent results

Orsay CPC beam tests results (SPS April 1998)

WORK IN PROGRESS

CORRECTLY DESCRIBE THE "GOODNESS" OF THE FITS

MORE DETAILED ANALYSIS WITH CHI-SQUARE CUTS

TRY THE "5 - PAD" ALGORITHM

A MORE DETAILED SAGGING CALCULATION
- GARFIELD (AND R. VEENHOF)

TESTS WITH A Fe-55 SOURCE UNDER WAY
- GAIN STUDIES

Note : These resolutions, being well within the required specifications, were voluntarily degraded in subsequent developments. This adjustment allowed the optimization of the anode-cathode gap and the total number of electronics channels.

ALICE1 Simulations

After the data analysis, both the PS and SPS experiments were simulated - the general idea being to get a better grasp of the detector behaviour. Once the main experimental observations were successfully reproduced, the detector model was used to predict the detector behaviour with different electronics characteristics. The expected spatial resolution was evaluated for several different potential electronics defaults (noise, cross-talk, threshold level, and relative gain). The actual electronics and "ideal" electronics were both simulated.

This work was presented several times, and the following section is an adaptation of the TDR:

Modelling the test-beam data

Introduction – ingredients for the model

The experimental model used the following ingredients:

- Landau distribution
- beam profile
- Gaussian noise function
- Mathieson charge distribution
- impact position-reconstruction algorithm
- detector segmentation

The individual contributions were evaluated from the experimental data taken with the first prototype at the PS in September 1997. Using the basic model several studies were carried out to evaluate the behaviour of the resolution and/or detector efficiency as a function of the key detector parameters. The studies covered:

- the dependence of the spatial resolution on the electronics noise
- calibration/gain precision vs. resolution
- threshold cuts (in ADC units) vs. efficiency
- crosstalk vs. resolution
- all of the above for two different dynamical ranges.

Landau distribution: Before the CPC prototypes were built, the original CPC simulations were attempted with the gas detector simulation program GARFIELD **[19]** and the code provided by the PHENIX team at BNL **[29]**. The major difficulty was to accurately simulate the energy loss of charged particles in the detector gas volume. During the PS data taking period the total energy loss was measured and so better models could be constructed. The work presented in the following pages was carried out over a period of 1-2 years, and was based on simulated Mathieson charge distributions, and the best reconstruction techniques of the time **[32]**. In Figure 45 the total charge, as measured in ADC units, is shown. The experimental distribution describes the energy loss perceived after accounting for threshold cuts, noise effects, calibration and ADC saturations. The aim was to discover the unmeasured Landau distribution that accurately describes all energy losses before the experimental mask is applied. Figure 52 on page 96 shows the Landau distribution used at the input of the model, all subsequent total charge measurements and individual pad measurements were derived from this distribution alone.

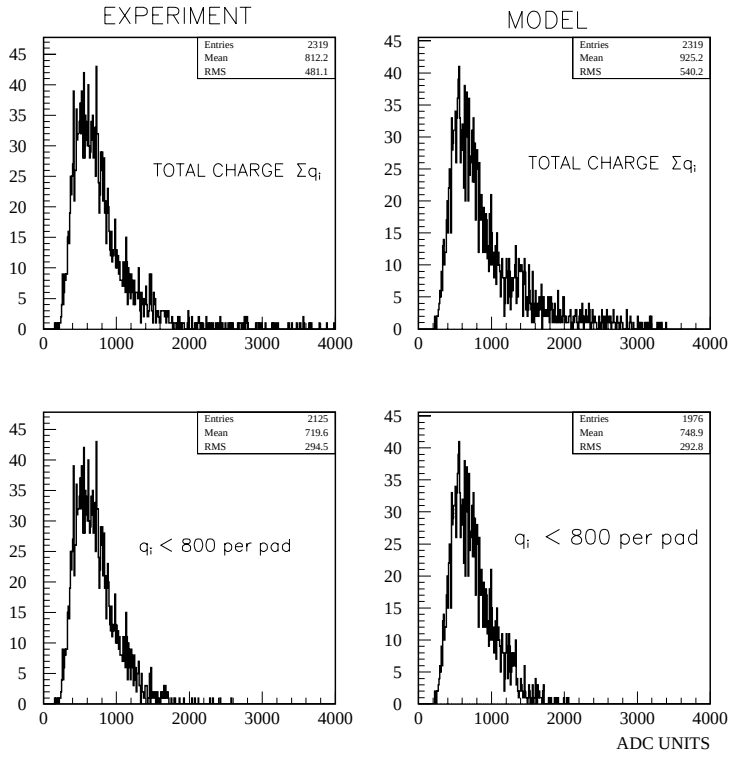

Figure 45 : Experimental and modelled total charge distributions in the detector. The left-hand images correspond to the PS experimental data and the right-hand ones to the modelled version. The upper images describe the total charge measured per event for a given run. Individual pad measurements saturate at around 800 ADC units. The lower images correspond to the total charge measurements after application of saturation cuts per pad at 800 ADC units.

Beam profile: The CPC resolution is position dependent. The best resolutions are achieved for impact points near the edge of a pad in the high-resolution plane; this is simply a consequence of the relative charge distribution on the pads. In order to accurately model the experimental data the X and Y beam-profiles, as reconstructed with the external reference tracking system, were used.

Noise distribution: The experimental noise distribution was measured during pedestal runs and was found to be stable throughout the seven days of data-taking, at an average of 1.2 ADC channels; as expected the distribution is Gaussian in shape.

Mathieson–Gatti charge distribution: The basic formulae describing the Mathieson–Gatti charge distribution function is described in detail in reference **[20]**. The experimental pad response function to the distribution is shown in Figure 46 and is compared to the calculated one.

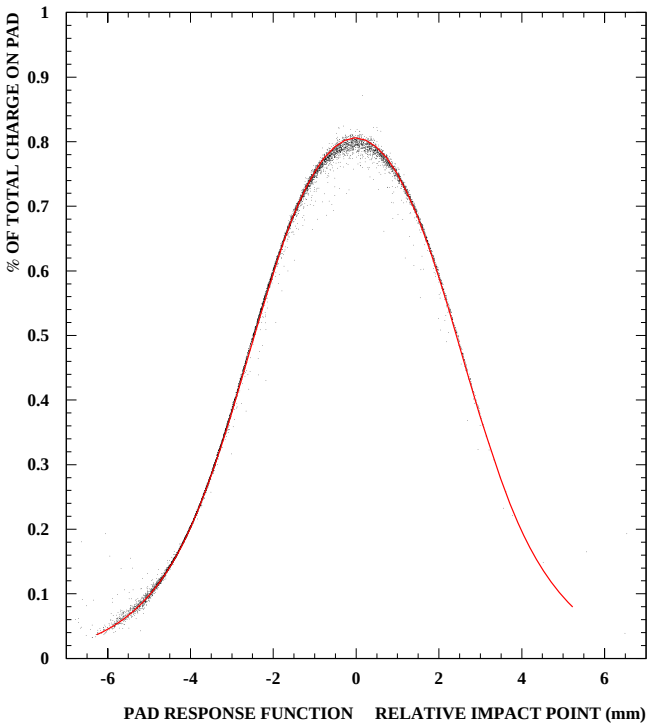

Figure 46 : The experimental pad response function compared to the calculated Mathieson–Gatti charge distribution. The uneven left–right distribution of the experimental points reflects the experimental beam profile.

The reasonable agreement between the experiment and modelled response for individual pads is visible in Figure 47.

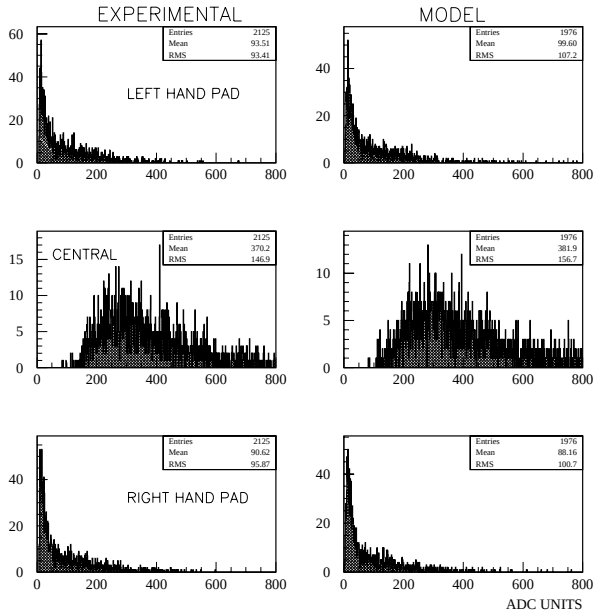

Figure 47 : Experimentally measured and modelled charge distributions on individual pads. The modelled values were obtained by distributing the total charge measurements over the individual pads using the Mathieson–Gatti distribution function.

Detector geometry: Numerous geometrical configurations were simulated, but only one particular configuration is discussed here. The detector model was developed with a pad size of 5 mm×7.5 mm and an anode wire spacing of 3.75 mm. However, the configuration deemed to be the most difficult to handle - and of more interest here - concerns the same pad size, but with a 2.5 mm anode wire pitch

(see reference **[14]**). The systematic study, which is described later on page 94, was done for this particular case.

Model conclusion

The basic energy-loss characteristics in this detector were successfully simulated. General trends such as threshold cuts and calibration factors were implemented in the more detailed study and most experimental responses were successfully reproduced with the basic model. It was not possible to reproduce accurate residual values as there was a large amount of multiple scattering in the detector and tracking telescope, and the model being purely analytical contains no physics. In addition to this, there were a large number of dead strips in the tracking telescope which produced a complicated 'dead strip' mask on the data. The multiple-scattering contribution was estimated as being of the order of 50 μm. The resolution was more successfully modelled when compared with the April 1998 data taken at the SPS, where the multiple scattering was an order of magnitude smaller. The simulated result is shown in Figure 48, and this is to be compared with the experimental result shown (with all the results) in Figure 49.

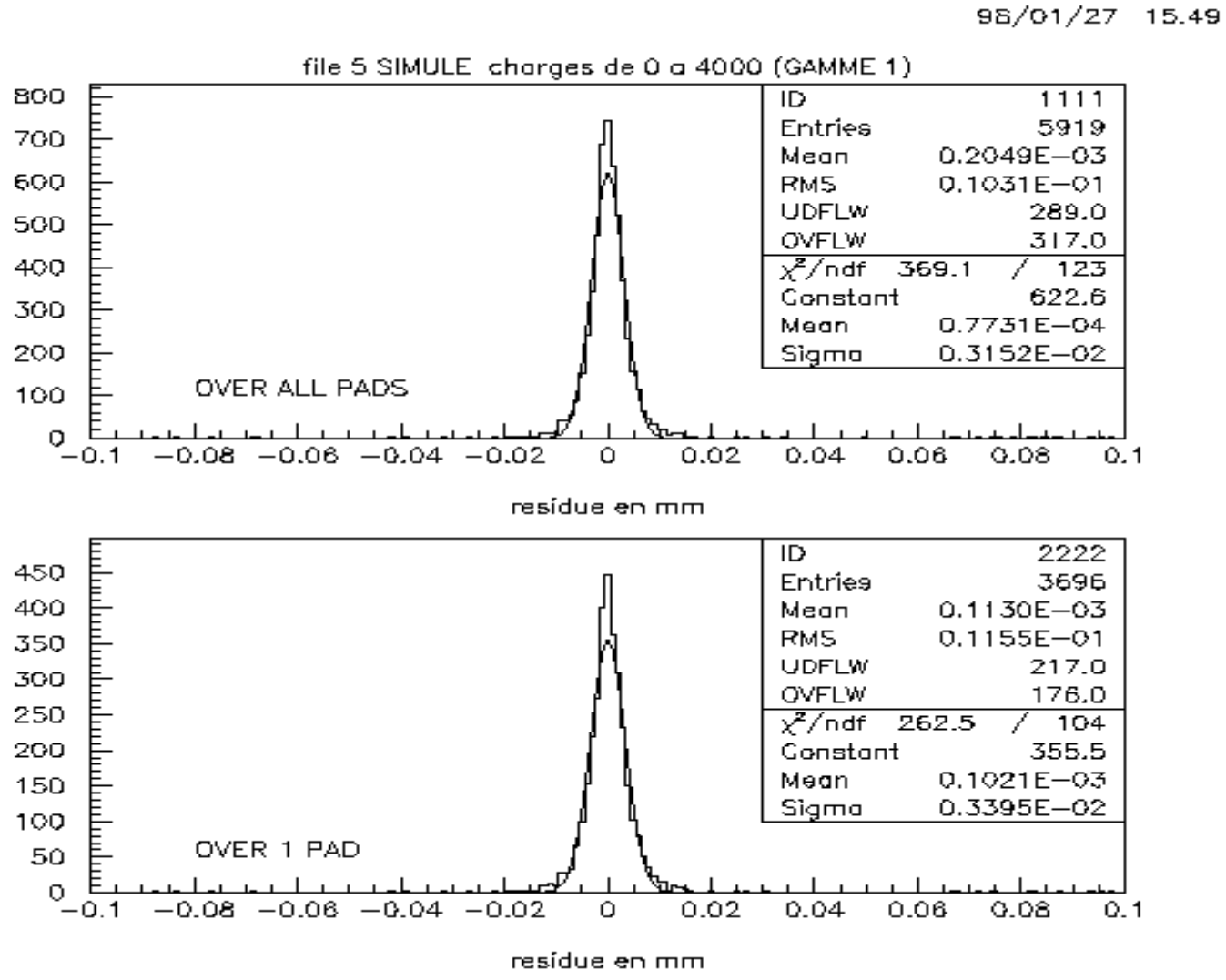

Figure 48 : Simulated residuals based on the September 1997 PS data. The residuals for the PS beam profile are 32 μm, and 34 μm over one pad width. This result is to be compared with the April 1998 SPS experimentally measured 33 μm.

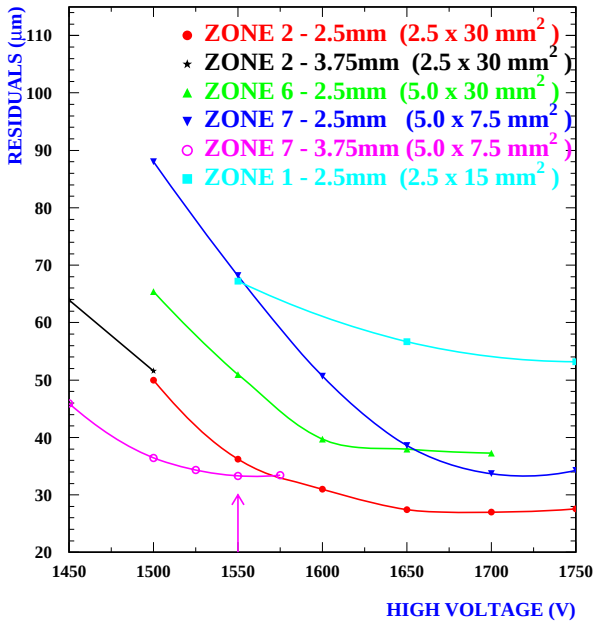

Figure 49 : All the experimental residuals, for all the April'98 measurements, and their HV dependencies. The pink arrow indicates the point that can be compared with the simulated one.

The date of the simulation appears on the top right hand corner of Figure 48 and precedes the April 1998 SPS data-taking period. Although the simulation shows a remarkable agreement with the experimental data, prudence is required in the interpretation. Secondary effects, due to delta electrons in particular, are not simulated. Similarly, large energy deposits are simulated with the Landau distribution, but the ionic cloud behaviour associated with these events is not.

Electronics modelling

Using the detector model

Using the modelled detector response the next step was to take out the experimental beam profile, and test the hypothetical detector response under a uniform beam profile. The perceived charges were studied over two dynamical ranges, both being subsequently coded on 10 bits. The aim was to see if any major degradation could be expected from using electronics with one-third of the gain at the preamplifier level as compared to the original system.

In the following the September'97 PS experimental data is discussed and compared to the modelled behaviour. All resolutions and efficiencies were systematically evaluated for three pad impact points:

- over 1 mm at the centre of a pad,
- over 1 mm at the edge of a pad,
- over a whole pad width (5 mm).

Electronics noise

The experimental noise was measured with the standard 1.5 μm GASSIPLEX modules. A sample of typical electronics raw spectra is shown in Figure 50 (for 1152 daisy chained inputs). The units are in elementary ADC bins and correspond to 1.5 V on 1024 ADC channels, i.e. 1.46 mV per ADC channel. The overall average noise level is 1.77 mV with a dispersion of $\sigma = 0.13$ mV between channels.

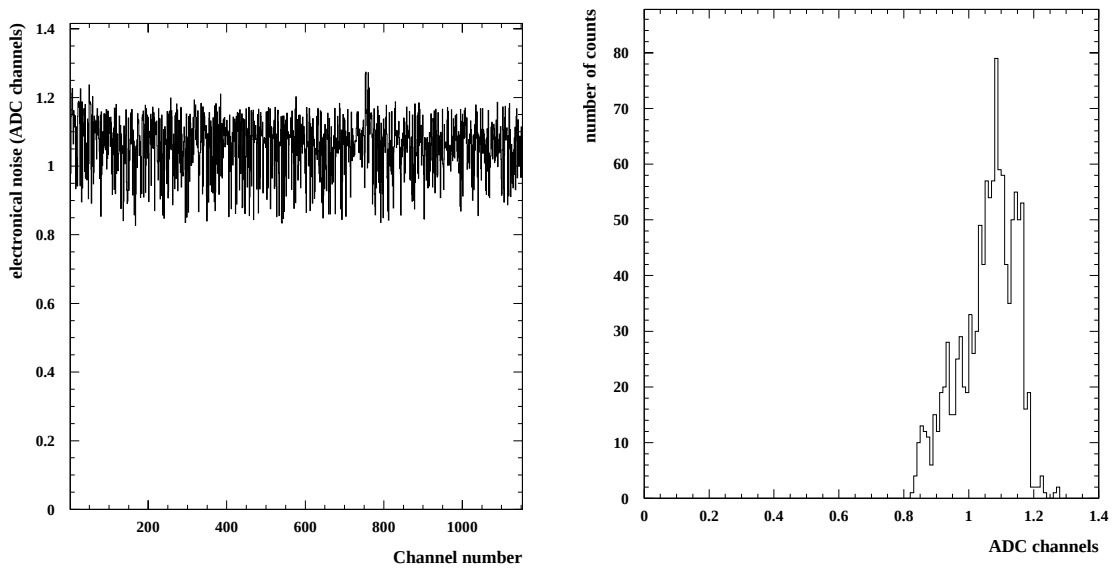

Figure 50 : Typical noise level per channel (LHS) and the projected distribution for 1152 channels (RHS).

The gain, as given by the GASSIPLEX specifications is 10 mV/fC to 12.3 mV/fC, and so an average gain of 11.2 mV/fC is assumed. This results in an experimental noise level of 0.158 fC, i.e. 990 electrons. There are essentially three contributions to the noise:

- the noise at 0 pF, equal to 650 electrons r.m.s. for a 0.6 μs peaking time;
- a noise slope of 15 electrons r.m.s. for a 0.6 μs peaking time;
- the LSB of the 10-bit ADC coder.

The final calculation gives an electronic-noise contribution of 1.61 mV (i.e. 900 electrons) or a capacitive equivalent of 16 pF.

For the next generation of 0.7 μm GASSIPLEX chips, the specifications are:

- the noise at 0 pF, equal to 585 electrons r.m.s. for a 1 μs peaking time;
- noise slope of 11.2 electrons r.m.s. for a 1 μs peaking time.

Basic estimations lead to a capacitive noise of 17 pF, or 770 electrons (r.m.s.).

In Figure 53(a) the modelled behaviour of the resolution as a function of the noise contribution is shown for both the 1.5 μm and 0.7 μm GASSIPLEX chips. The spatial resolution has a linear noise dependence. Based on these results, a maximum limit of 900 electrons (r.m.s.) of noise was requested for future developments and so staying well within the limits imposed by the experimental requirements.

Dynamical range

In Figure 51 an example of an experimentally measured charge distribution is given. The measurement was carried out on pads of 5 mm × 7.5 mm (anode–cathode gap = 2.5 mm and wire pitch = 3.75 mm) at a high-voltage setting of 1550 V.

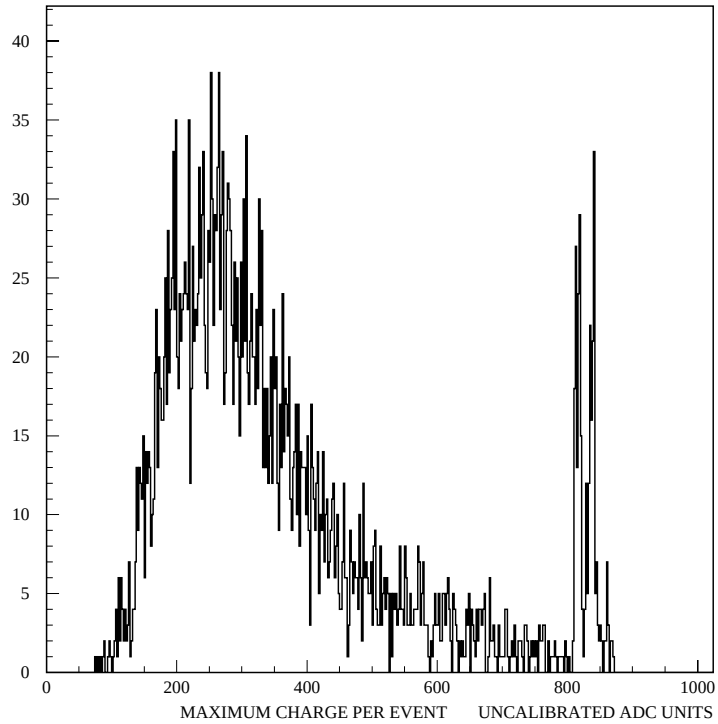

Figure 51 : An example of an experimental spectrum for the maximum charge measured per event on an individual pad. The spectrum is re-dimensioned to two channels per bin for clarity. As can be clearly seen, the coders saturate just above ADC channel 800. The pedestal setting was around channel 100. It can be seen from the two saturation peaks that there are two main pad contributions, each of which saturates at a slightly different level. The lowest saturating channel dictates the overall dynamical range for all the neighbouring pads.

Several points are worth noting. The saturation peak at the end of the ADC scale is seen to be at channel 800 and not 1024 (the true full-scale maximum). This low saturation value arises from the dispersion of the pedestal levels. In order to code the data, all signal levels require a negative offset value. Since this electronic chain has only one offset potentiometer per GASSIPLEX chain, then the

channel with the highest (most positive) offset level dictates the overall pedestal setting. The consequence of this is severe, and reduces the overall dynamical range of the chain. The saturation level corresponds to roughly 105 fC.

Modelled data were used to evaluate the equivalent charge that corresponds to a 99% charge acceptance. As was shown in Figure 45 and Figure 47, the modelled and experimental data are in good agreement. It is reasonable to suppose that the unmeasured part of the spectrum from the model can reproduce an extended dynamical range. The modelled Landau distribution (in elementary ADC channels) is shown in Figure 52. The two cuts at 89% and 99% correspond to the actual total charge acceptance (89%) and the desired acceptance (99%). To achieve the 99% level the dynamical range needs to be extended by a factor of 3.15, that is an equivalent range of 0 to 330 fC. This evaluation does not take into account the effect of differing pad lengths, but simple calculations indicate that a factor of 3 should be sufficient for all pad geometries.

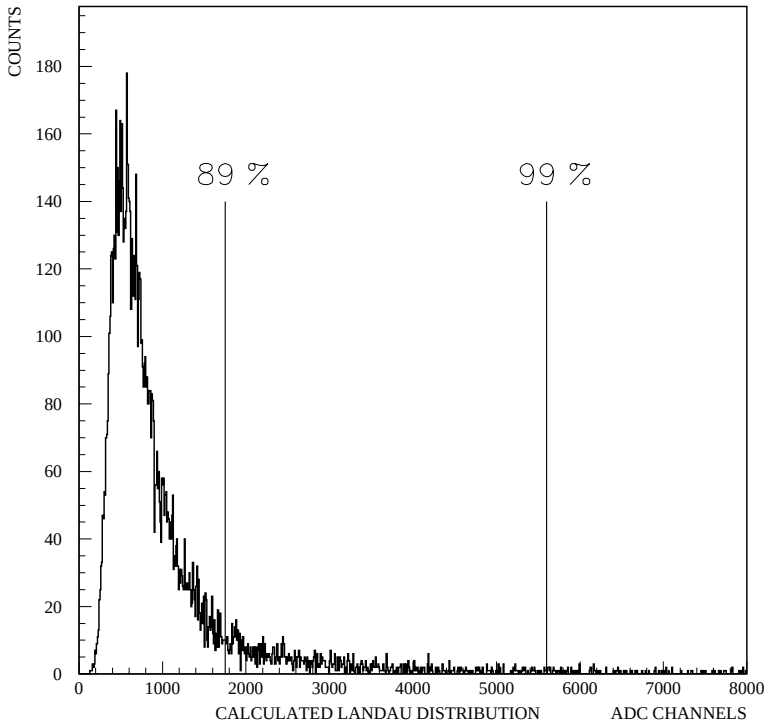

Figure 52 : The Landau distribution evaluated with the model. With the original 1.5 µm version GASSIPLEX only 89% of the charges are unsaturated. This gives an unacceptable global efficiency of 31%. The 99% limit should be attained with future GASSIPLEX versions and corresponds to increasing the dynamical range by a factor of 3.

Crosstalk

Experimentally there was no evidence of any noticeable crosstalk contribution. Nonetheless, it is important to try and estimate such an effect. A given crosstalk situation could be quite complex to describe, so only a simple (but realistic) situation was modelled. Crosstalk at the pad level could occur through imperfections in the mechanical construction of the pad segmentation. This effect was modelled over three neighbouring pads, by supposing that a certain percentage of the charge on each pad is picked up by the nearest neighbour. The overall charge measured on each pad is then

$$Q_{M\text{-}centre} = Q_{T\text{-}centre} - 2\varepsilon Q_{T\text{-}centre} + \varepsilon Q_{T\text{-}left} + \varepsilon Q_{T\text{-}right}$$

$$Q_{M\text{-}left} = Q_{T\text{-}left} - \varepsilon Q_{T\text{-}left} + \varepsilon Q_{T\text{-}centre}$$

$$Q_{M\text{-}right} = Q_{T\text{-}right} - \varepsilon Q_{T\text{-}right} + \varepsilon Q_{T\text{-}centre}$$

where $Q_{T\text{-}position}$ describes the true charge that would have been measured, $Q_{M\text{-}position}$ describes the measure corrupted by crosstalk and ε is the fraction of the original signal induced on the nearest neighbour. In Figure 53(b), the modelled results are shown for the two dynamical ranges corresponding to the two GASSIPLEX versions.

Other parameters

Beyond the direct GASSIPLEX modelling, the influence of threshold cuts and relative gain precision were modelled. It is clear that the threshold level directly influences the detection efficiency and the modelled result for the current and future dynamical range are shown in Figure 53(c). In the model, the noise contribution was kept constant at the experimentally measured value of 1.2 ADC channels.

Calibration

The current calibration procedure does not require the measurement of absolute gains, but of relative gains. These values are determined by charge injection on the GASSIPLEX test line. The procedure relies on knowing the injected charge value for each measured ADC output per channel. If all the injector capacitors are of the same value then the relative gain for each channel is easily determined. However, if the dispersion in these capacitance values is non-negligible, then the relative gain values will be false and consequently the fitting routine for the impact-point determination will use distorted data, and so degrade the resolution. The problem is that the test capacitors are difficult to measure and therefore future production methods should try to ensure as much homogeneity as possible. Figure 53(d) shows the results obtained when it is supposed that one particular pad (the one to the left of the maximum pad in this case) is allocated a wrong gain factor. The percentage error is directly proportional to the percentage error in the test injection capacitor. For example, a 5% difference on the capacitor corresponds to an additional 18 μm in the spatial-resolution value. The effects between the resolution at the centre and edges of the pad are very different as the relative charge varies rapidly with respect to the impact point (see the pad response function in Figure 46).

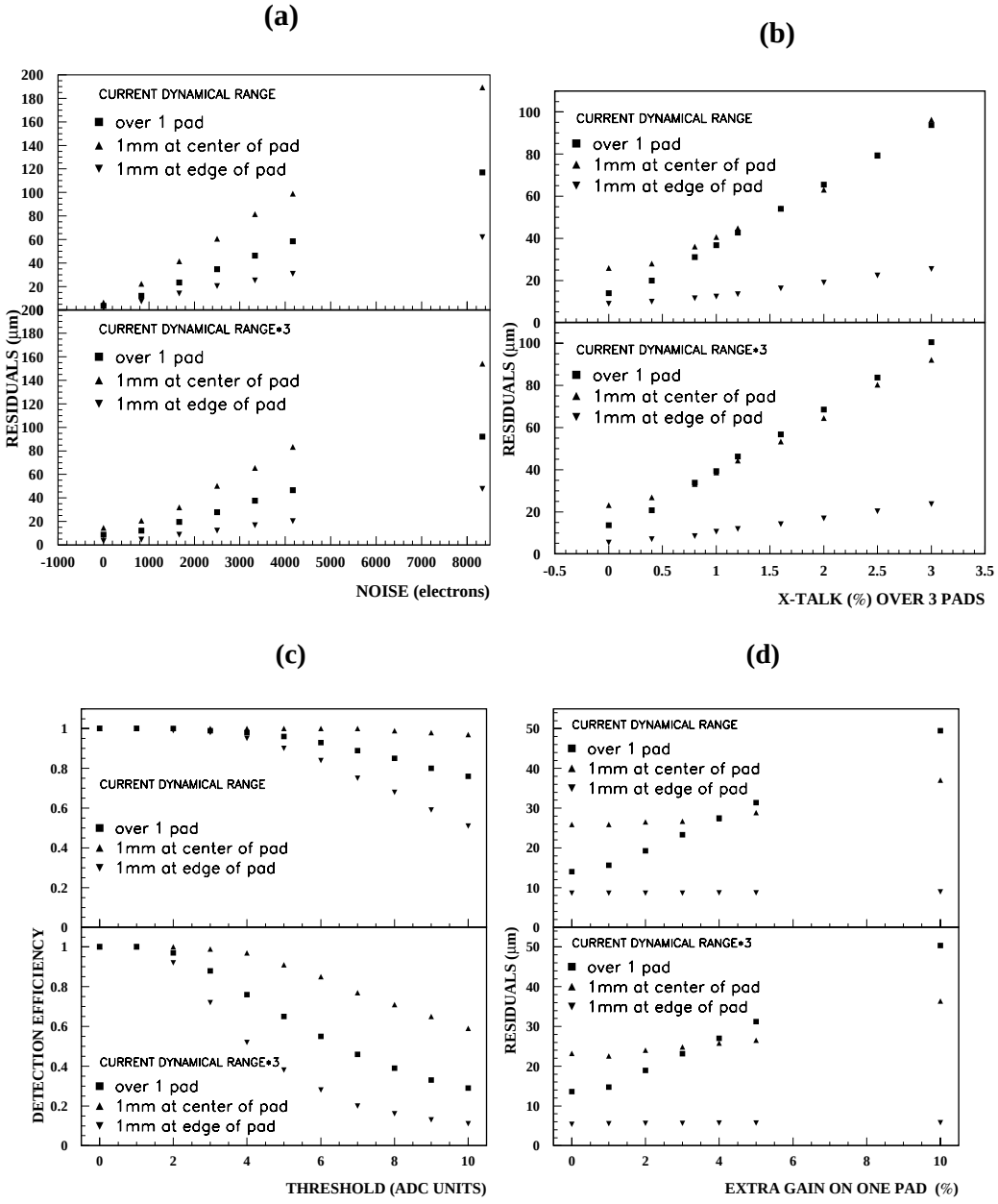

Figure 53 : (a) The spatial resolution versus noise in electrons. The upper image describes the current 1.5 μm GASSIPLEX modules, and the lower image the modelled 0.7 μm version; (b) the spatial

resolution versus crosstalk; (c) the detection efficiency versus the threshold value (in elementary ADC channels); and (d) the resolution versus the percentage error in the relative gain for one particular pad.

Electronics conclusion *(text from 1999)*

The total number of readout channels for the ten chambers in the dimuon spectrometer will be of the order of 1.2 million. This high channel count, associated with the large size of the chamber planes requires a highly modular design for the readout electronics. The main design issues are high noise immunity, high reliability, low unit cost and ease of manufacture, installation and repair. The large size of the cathode planes prohibits the dispatching of low-level analog signals to the edge of the chambers. This imposes the use of locally embedded charge amplifiers and multiplexers. The VLSI chip GASSIPLEX, developed at CERN, has been selected for this function. Each chip can handle 16 cathode pads and several chips can be daisy chained in order to reduce the number of ADCs. A new version (MANAS-16) is currently under development (*in 1999*), using1.2 μm technology. The local multiplexing of analog channels into common paths still does not solve the long-distance issues. In addition, the readout of all analog signals per trigger leads to large event sizes, most of which bear no useful information (no hit registered). Data should therefore be zero-suppressed as early as possible in the readout process. These two criteria have led to the solution of local digitizing and local signal processing.

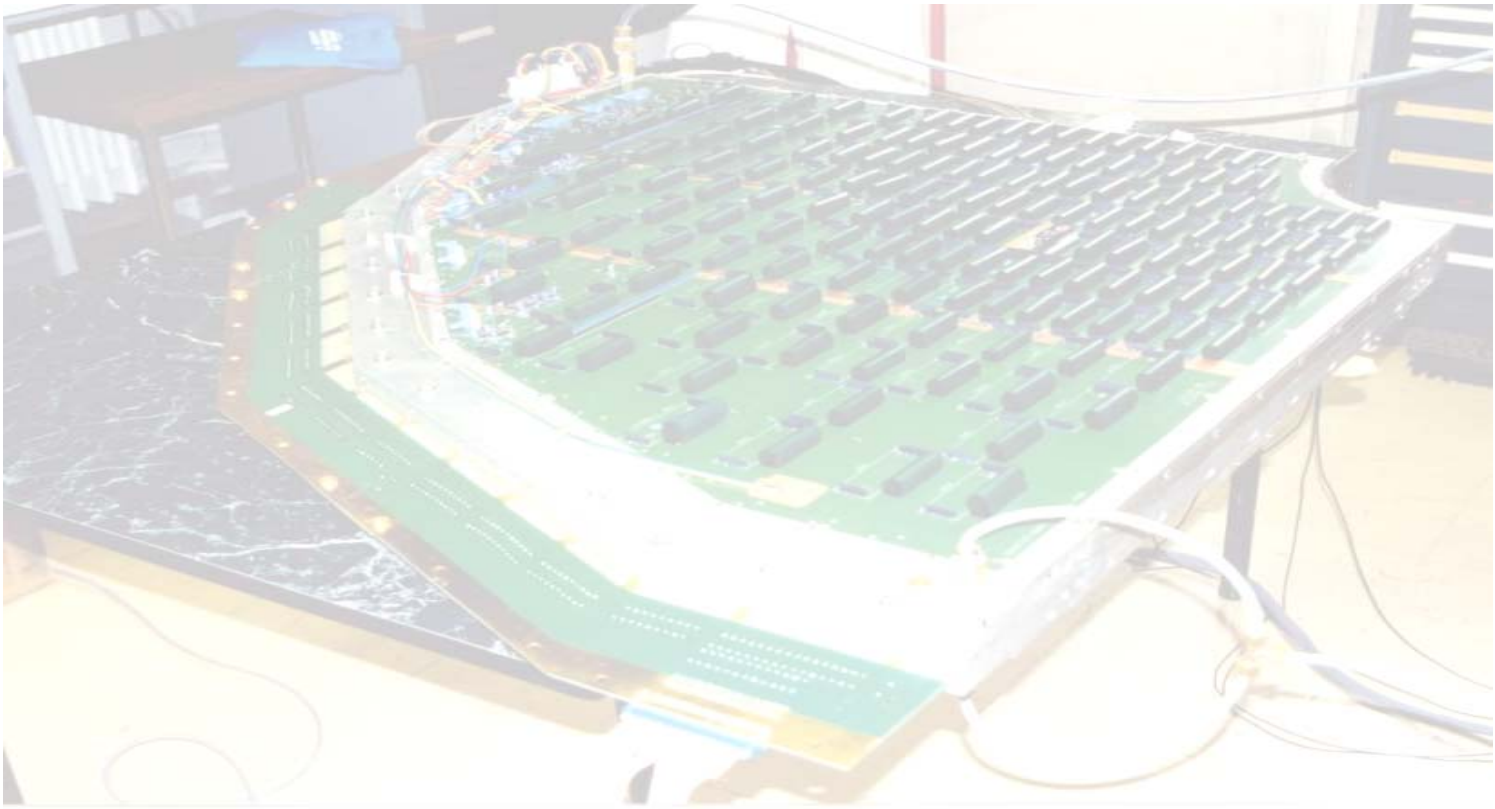

ALICE2

ALICE 2 – full scale prototype of one quadrant

Aims

A full-scale prototype of one quadrant of Station 1 was constructed and whereas the previous prototype was used for detailed geometrical studies, this one was destined for the study of full-scale mechanical and electronics implementation issues. Nonetheless, the resolution and reconstruction efficiency, as well as the homogeneity of the detector response were evaluated. Different ratios of a well-known gas mixture were also tried with this prototype, the idea being to move away from the use of the flammable iso-C_4H_{10} component.

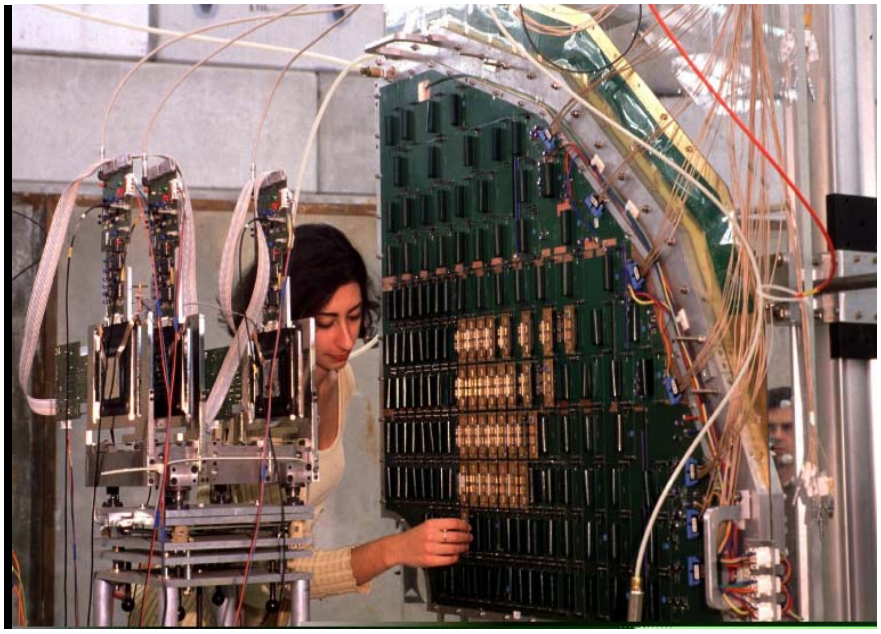

Figure 54 : A photograph of the full-scale prototype installed at the PS in November 1998.

Mechanical issues

The feasibility of extrapolating the construction method and tools to a larger scale had to be shown and several mechanical factors, that could potentially alter the detector response, were to be tested. The detector walls had to be shown to be rigid enough to resist the deforming hydrostatic pressure of the gas in the detector; the minor mechanical defaults from the gluing of several PCB pieces that compose the active pad surface should not affect the detector response; and the 1 m long (maximum length) anode wire plane should be stable - and this over the whole surface. The detector's spatial resolution, reconstruction efficiency and gain evolution were measured with the test beams at the PS in November 1998 (6 GeV/c pions) and the SPS in May 1999 (375 GeV/c pions).

A photograph of the detector in the beam-line at the PS in November 1998 is shown in Figure 54 and gives an idea of the overall scale. Three planes of silicon trackers are clearly visible to the left of the ALICE2 prototype.

Electronics issues

The larger detector scale implied longer transmission lines for power supplies and signal communications to and from the remote acquisition crate; tests for voltage drops, correctly adapted signals and signs of pickup were carried out.

The Nov'98 tests focussed more on assessing the performance of the high density of transmission lines in the FEE (front-end electronics) daughter-boards. The general layout and density corresponding more or less to the projected design for the next generation of electronics circuitry, it was appropriate to check for undesired defaults such as crosstalk, elevated noise levels, and timing defaults. These tests were carried out with PLAC (see Figure 67 on page 112), the new electronics supply board (or motherboard) and a specially adapted reduced size PCB daughter board (GAS64, see Figure 67 and Figure 71(a)) containing four GASSIPLEX preamplifier chips. ADC coding was carried out with the 10-bit C-RAMS - as used in the previous tests - and were located in the acquisition crate at a distance of several meters from the detector.

Between the November'98 and May'99 tests, a new electronics card, with a 12-bit coding ADC implemented locally on the FEE (NULOC, see Figure 69), was designed and tested. This "multi-chip module" (MCM, see Figure 71(b)) was tested during the May'99 SPS tests.

Beam Tests

This detector was used in two sets of beam tests:

- November'98 at the PS with negatively charged pions at 6 GeV/c, and
- May'99 at the SPS with negatively charged pions at 375 GeV/c.

Detector geometry

The main characteristics of the detector prototype are as follows:

- active surface: 0.63 m^2
- radius: 915 mm
- PCB thickness: 0.4 mm
- Copper thickness: 17.5 µm
- pad sizes: 5×7.5; 5×15 and 5×30 mm^2
- total active pad count: 9866
- number of anode wires: 371
- anode wire material: gold-plated Tungsten
- wire diameter: 20 µm

Mechanics - Assembly and construction

A detailed view of the chamber is shown in Figure 55 with a general view in Figure 56 (LHS). The chamber is based on ‘composite sandwich’ technology. The main materials used are stabilized aluminium, epoxy resins (FR4), Kapton (polyimide), copper, nickel/gold and Rohacell foam.

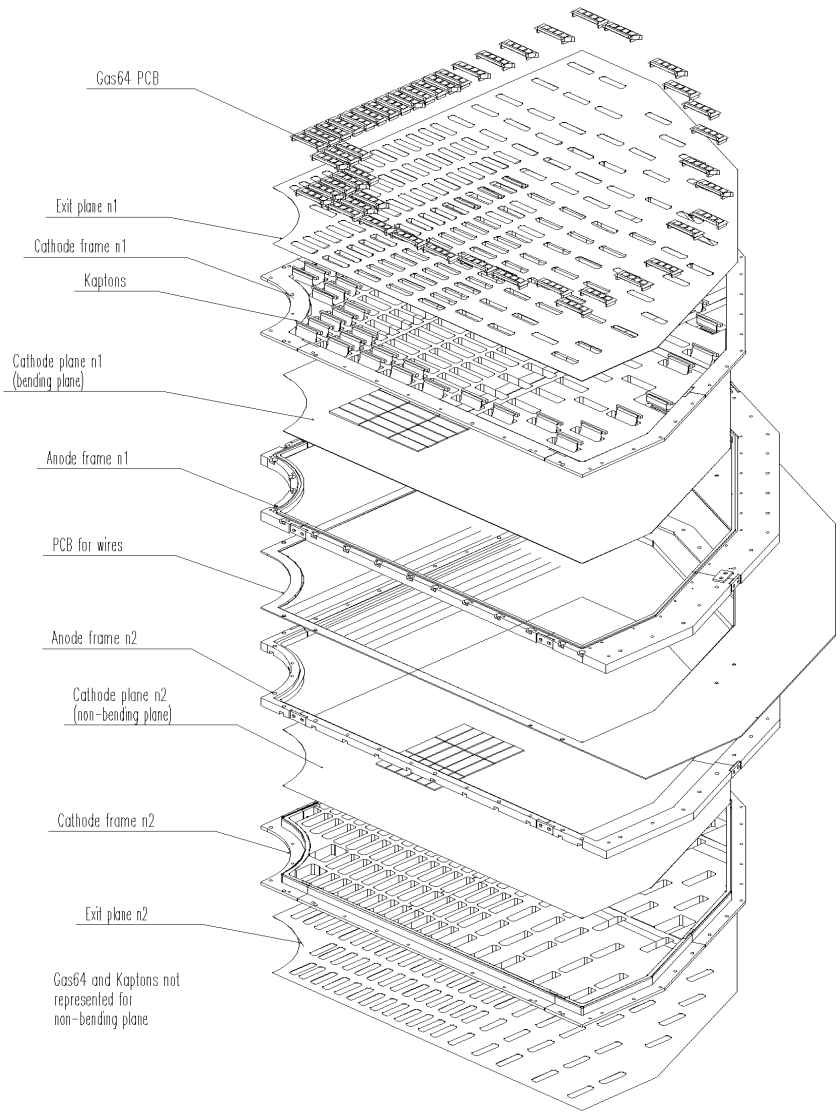

Figure 55 : Expanded view of the ALICE2 prototype. There are two exit planes (n1 and n2) to allow easy dismantling: the first is the mechanical one and the second is the electrical one. For the final design, these two planes are merged. The 'Gas64 PCB' represents the front-end electronics modules.

As shown on the RHS of Figure 56, the cathode plane PCBs (1) are assembled on aluminium frames (2) so that the distance between the two cathode planes is constant. The rigidity of the assembly is provided by Rohacell foam (3) (and Figure 57) glued to the cathode and exit planes (4). The front-end electronics (5) can be mounted at this level. The anode plane (6) is positioned exactly in the middle of the two cathode planes by the aluminium frames.

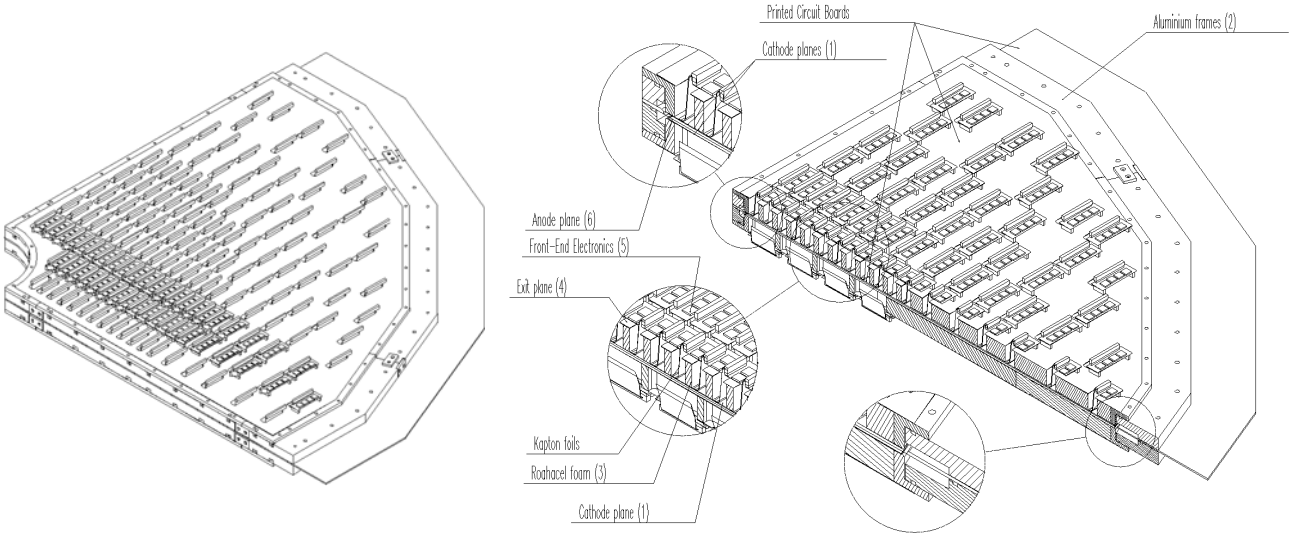

Figure 56: General view of the ALICE2 prototype (LHS) and cross section cut (RHS).

As shown in Figure 57, the connection between the cathode plane pads and the front-end electronics is achieved by Kapton foils. Four different foil designs were required to match the different accesses to the high density front-end electronics on the chamber. Each foil contains between 52 and 64 connections, two ground lines on each edge, and is attached to a 70-pin connector.

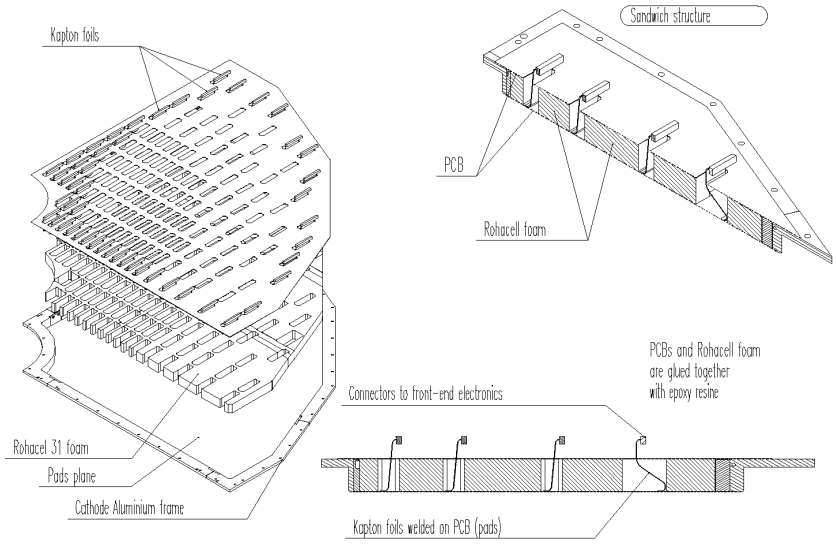

Figure 57: Cathode mechanical structure. The rigidity of the design is ensured mainly by the Rohacell foam which constitutes the heart of the structure.

The holes that allow the electrical connection between the pads and the back face of the PCB are filled directly by the PCB manufacturer with a photosensitive varnish. This varnish is used to render the surfaces airtight (see Figure 58).

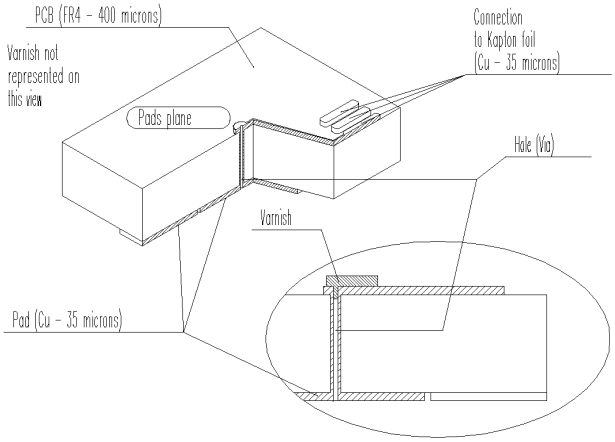

Figure 58: The holes of the cathode PCB are filled with varnish to render them airtight.

The cathode pads are connected to the ground reference through the input impedance of a GASSIPLEX module. The connections are kept as short as possible to reduce the impedance between the front-end electronics and the local ground for the high-frequency component of the signal. The ground potential of the cathodes is ensured by the exit plane, as defined in Figure 55, and by ground lines on the cathode circuit. To make the current return path as short as possible, the back face of the cathode plane (PCB) is partially covered with ground lines. These lines are connected to the aluminium frames every 8 to 10 cm. The frames provide the reference ground potential for the whole detector. The design of these ground lines is shown in Figure 59. The vertical lines are parallel to the length of the pads and strips. This explains their smaller width compared to the horizontal lines. In this way capacitive coupling between pads is minimized whilst ensuring good ground continuity.

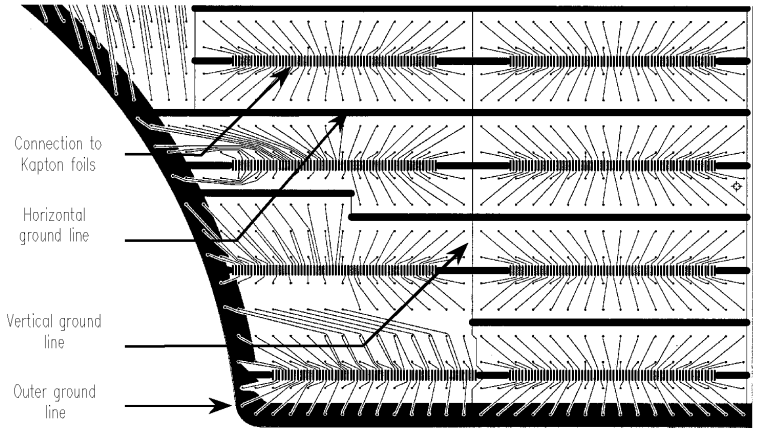

Figure 59: Ground lines and connections to the Kapton foils (pad plane).

Figure 60 : Detail of the backside of the cathode plane PCB showing the very high density of connections between the pads in the innermost arc and the readout connector.

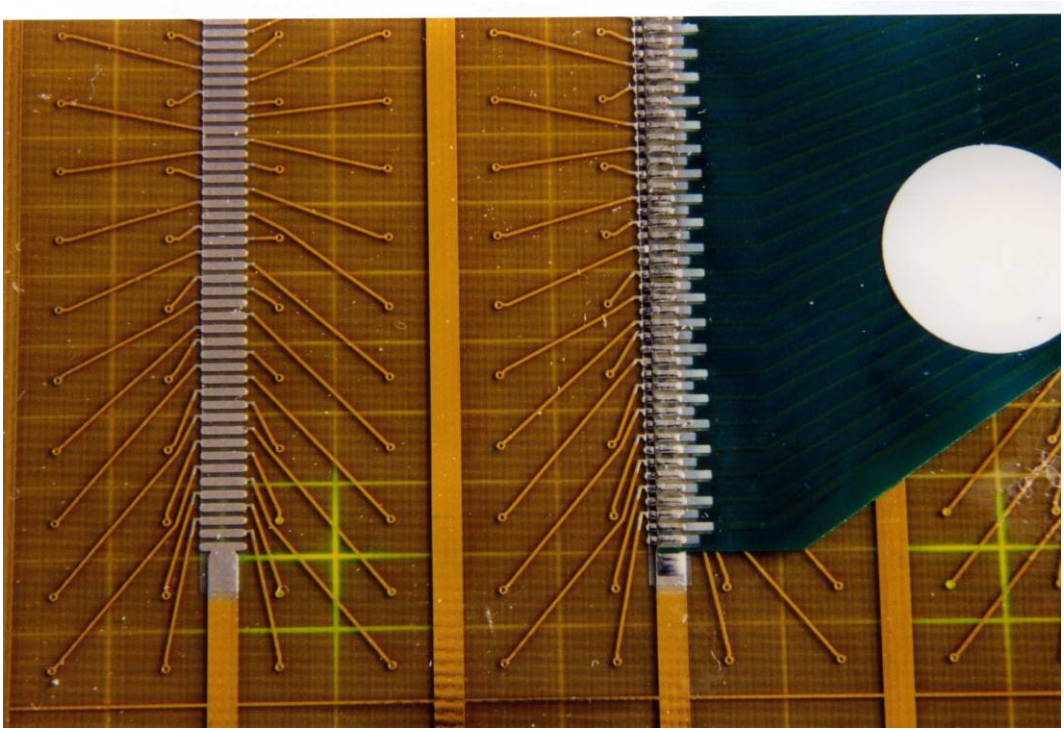

Figure 61 : Fine detail of a (hand) soldered Kapton connector (in green).

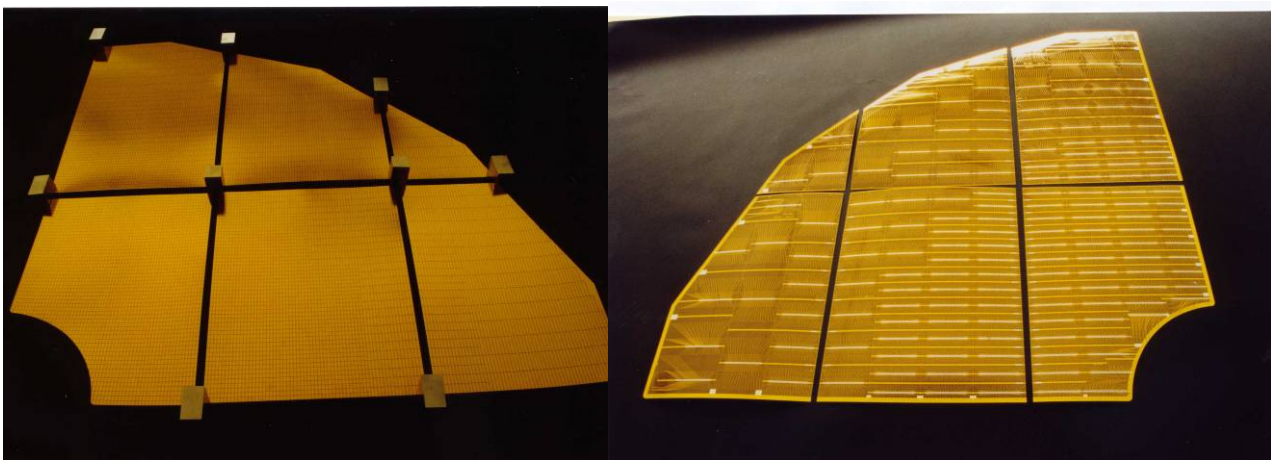

Figure 62 : Photograph of the 6 individual PCB's used to build up the full cathode plane. The left hand side shows the view of the pads and the right hand side shows the backside with the readout circuits. The variable pad and connector densities are visible.

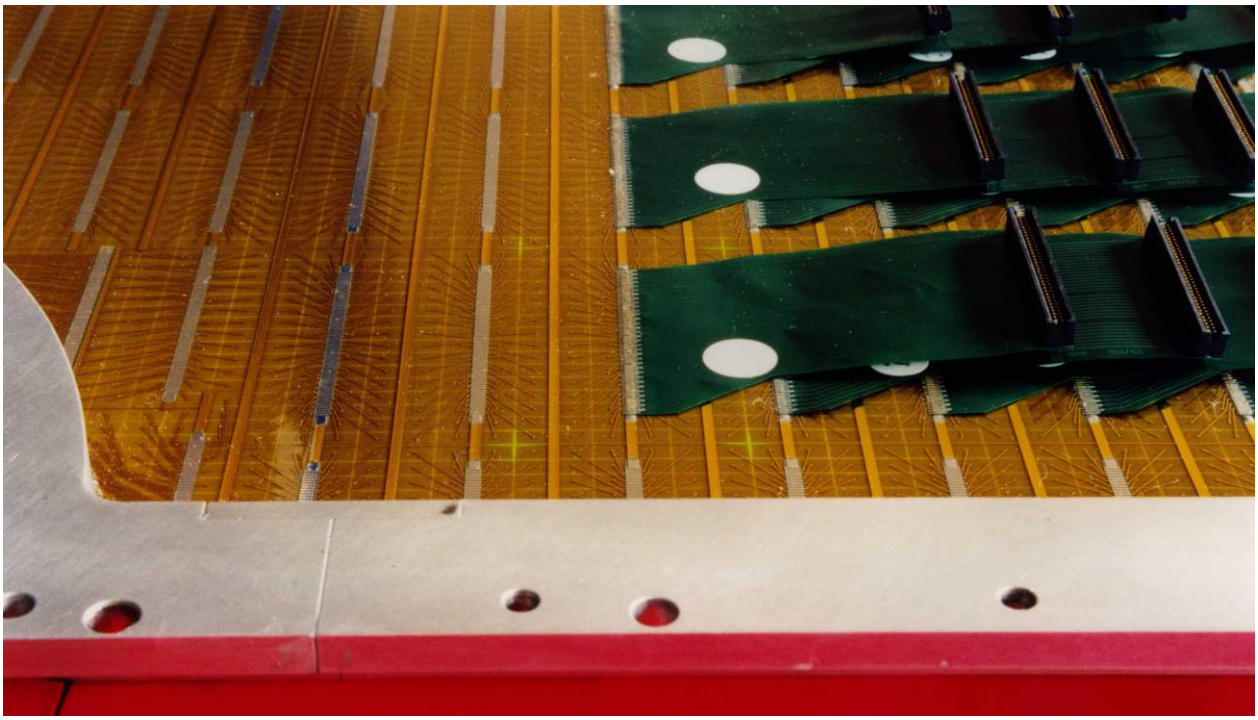

Figure 63 : View of the hand soldered Kapton connectors before the addition of the Rohacell support layer. The black readout connector on each Kapton regroups the pads in sets of 64 and is plugged directly to the GASSIPLEX inputs.

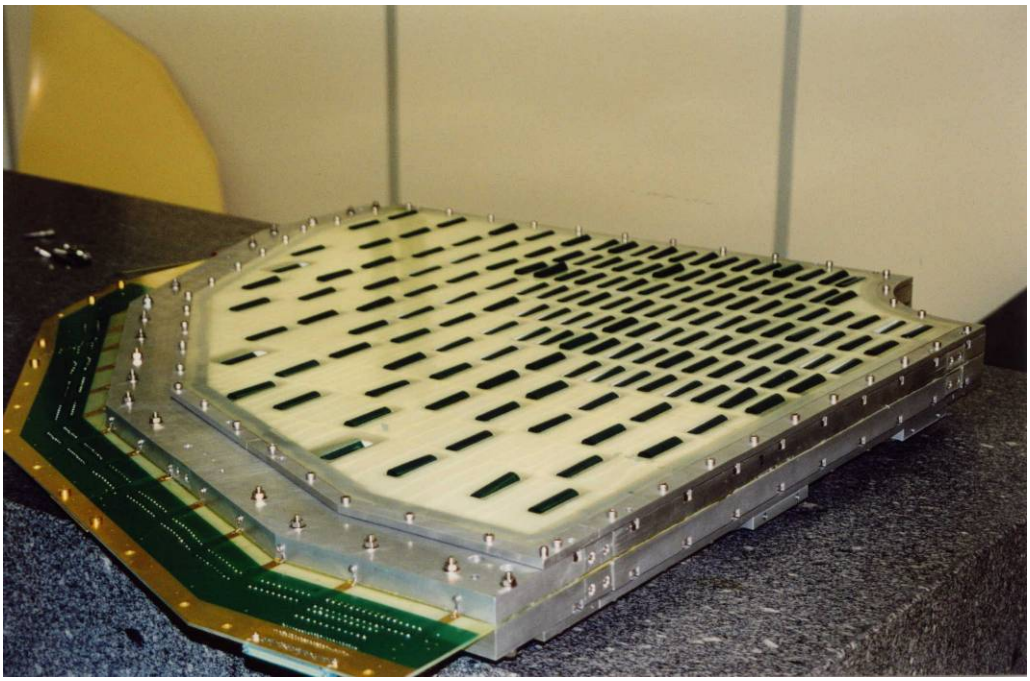

Figure 64 : The white Rohacell plane, providing the lightweight mechanical support for the pad plane is seen with the green coloured Kapton foils in folded over in their pigeon holes (to protect them during the mounting process). The anode plane skirt is visible round the outer edge of the detector, extending beyond the aluminium support frames.

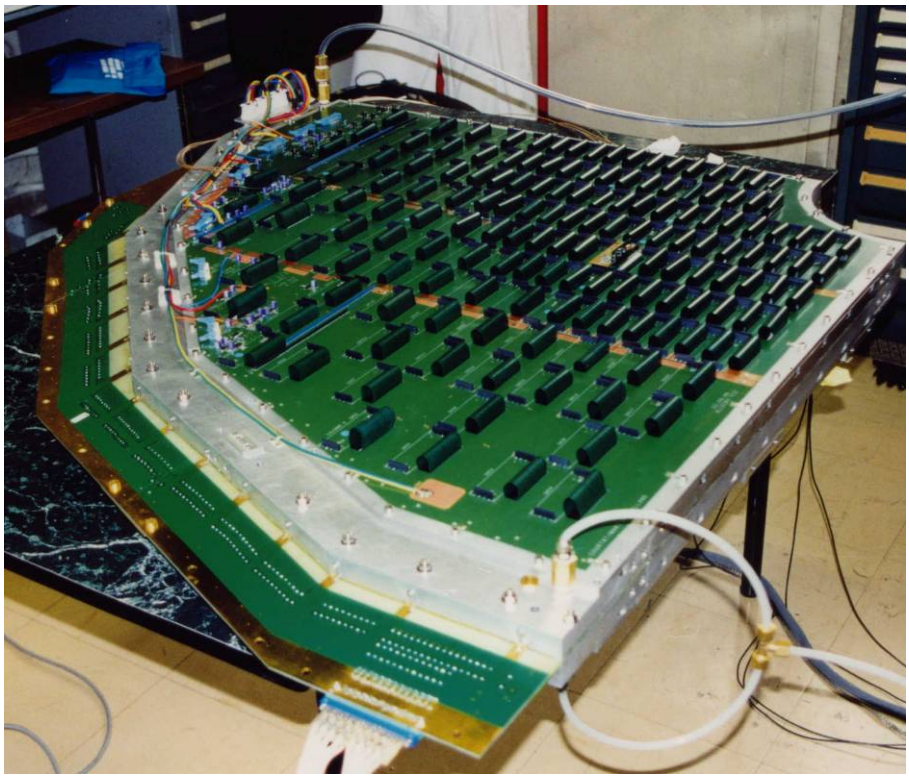

Figure 65 : A view of the final detector, before the addition of the electronics. The three PLAC circuits cover the active surface area. In this photograph the gas supply is attached, the detector was undergoing tests for air tightness at the time. The denser area of connectors on the outer (upper left-hand side of the image) edges of the PLAC circuits are the connectors used to transmit the outputs to the general (remote) acquisition.

Electronics

Local readout cards for 64 channels

The FEE was developed in several stages and these are summarized in the following slides (from ALICE meetings).

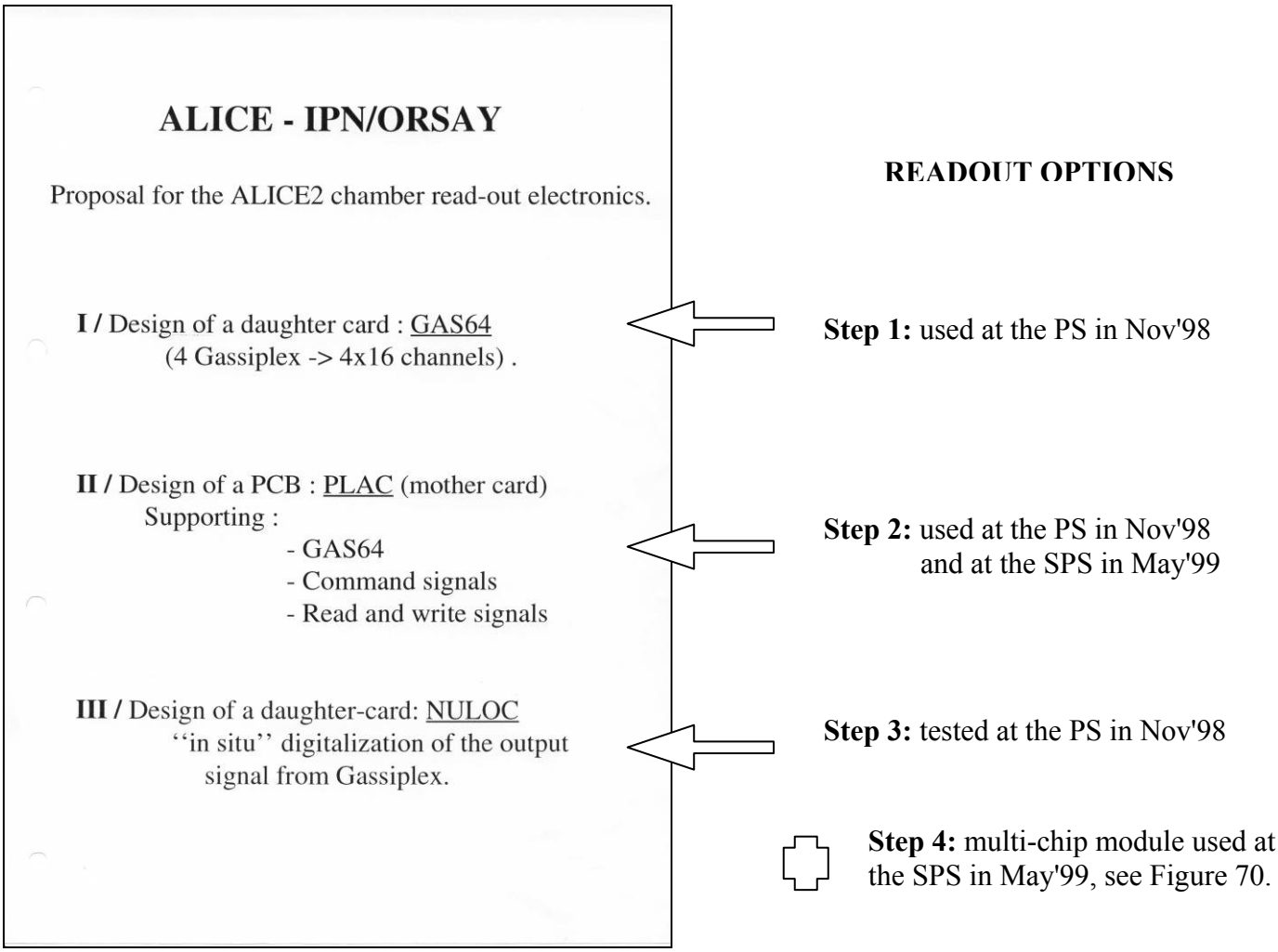

Figure 66 : Summary of the electronics development phases.

The slide shown in Figure 66 gives a summary of the first two readout methods tested on this detector. The first method (**I**) describes the classical method used up to this point namely, four 1.5 µm ceramic encapsulated GASSIPLEX chips (**GAS64**) mounted on a reduced sized PCB daughter board. The analog output was transmitted over several meters to the standard C-RAMS ADC coder placed in the remote acquisition crate. This technique was used during data taking at the PS in November 1998.

The **second** method (combining **II** and **III** in Figure 66) involves local ADC coding and the transmission of a digital signal to the general DAQ crate (step 3 above). This layout was tried for the first time at the PS in Nov'98 in a series of tests dedicated uniquely to electronics and acquisition issues. No useable detector charge measurements were taken with this intermediate test layout which involved the use of two new pieces of electronics, namely PLAC and NULOC.

The motherboard PCB (PLAC) used for the distribution of the low voltage supplies and transmission of control signals was developed during this period (step 2 above) and evolved throughout the tests to accommodate the different layouts. A photograph of the first PLAC motherboard is shown in Figure

67 along with a summary of the different electronics issues to be tested/developed with this board. Three PLAC boards were used to cover the whole detector surface and the overall layout of three boards joined together to cover the whole surface is summarized in Figure 68.

Figure 67: View of the first PLAC motherboard (prototype Dec'97) and the GAS64 (prototype Dec'97) daughter boards.

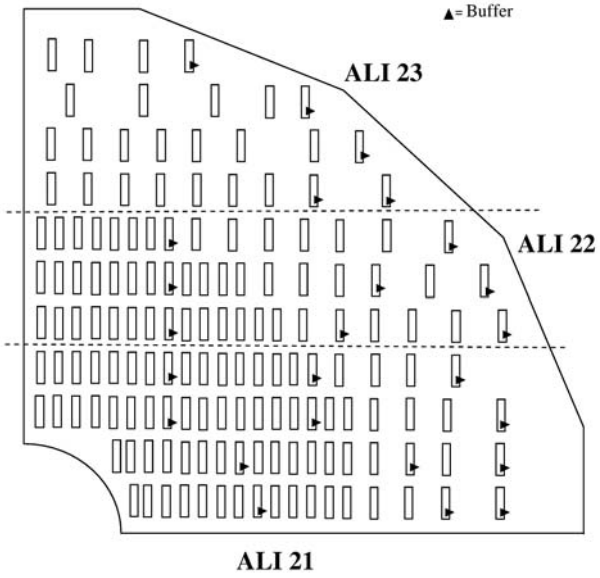

Figure 68 : Three PLAC circuits, ALI21, ALI 22 and ALI 23 are joined to cover the whole detector surface. The arrowheads indicate positions of readout connections that regroup eight daughter boards at a time. The long term aim was to readout the whole row. The final object can be seen, mounted on the detector, in the photograph of Figure 54 on page 103.

The layout logic and high density of electronics lines of the final multi-chip module (MCM) were first tested with the NULOC card (Figure 69). This card was designed to be mounted piggyback on the GAS64 daughterboard, and was the first attempt at coding the GAS64 analog signal on the detector backend. The transmission of the coded signals, over six parallel digital lines to the remote acquisition crate, was also tested with the NULOC cards.

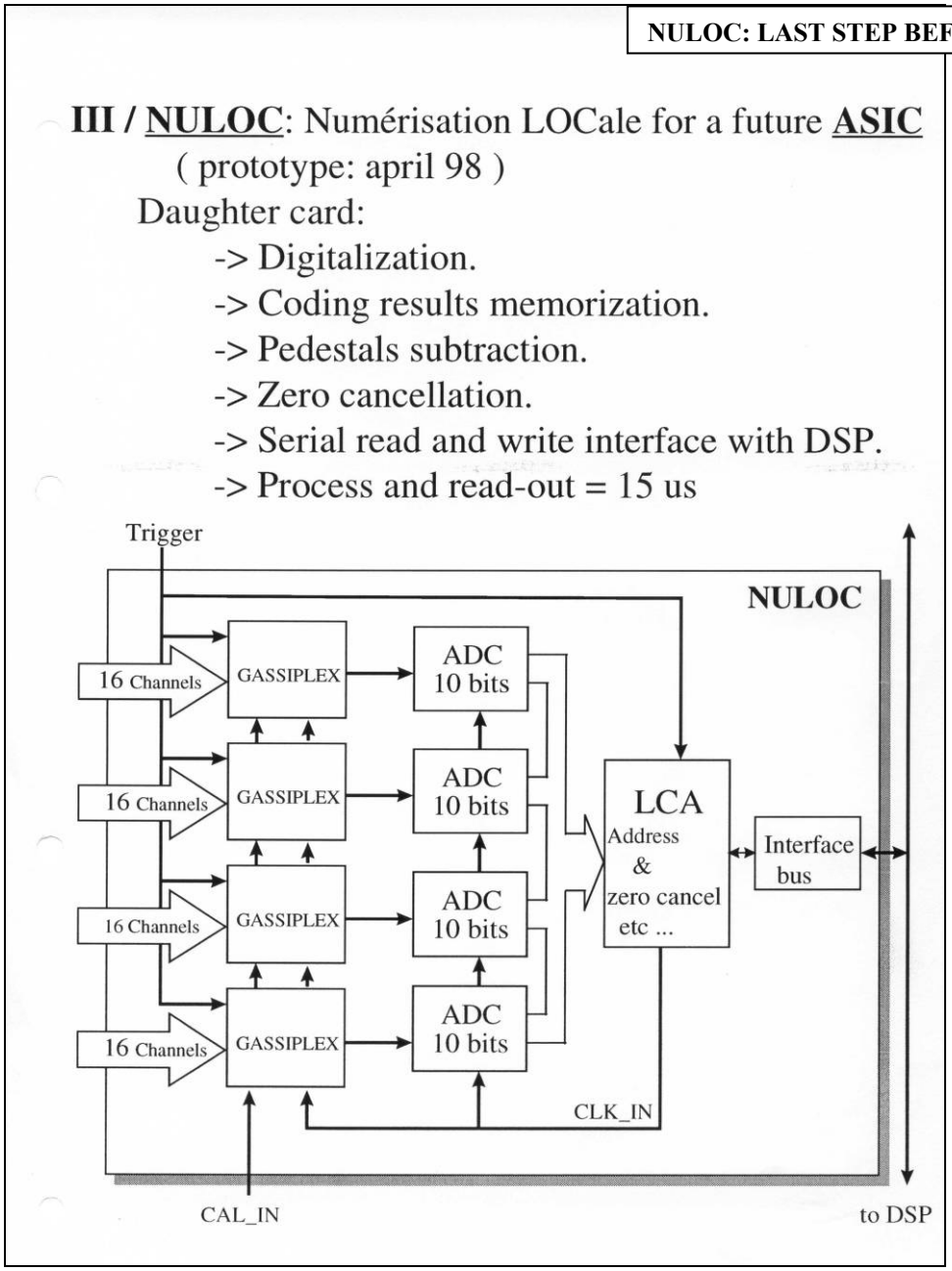

Figure 69 : Summary of the GAS64/NULOC logic (prototype April'98); LCA = logical cell array.

The main MCM ideas are given in Figure 70 and the GAS64 to MCM physical transformation can be seen in Figure 71.

MCM

- Based on the architecture of GAS 64 and NULOC
- Phase of contacts with industries to estimate the technical feasibility
  - . - 10 contacted, 8 met
  - . large range of prices
  - . wafer test → final product tested
  - . replacing a wire-bonded die before depositing the resin.

PROPERTIES:

- . PCB support 0,4 mm thickness, 27 mm x 75 mm, classe 6, 4 layers.
- . Mixed technology : SMT and WIRE BONDING.
- . Astute layout of burried layers.
- . 10 years life duration.
- . Testability.

- 10 prototypes at the beginning of 99 with Gassiplex 1,5 μm → test of the industry.
- Next prototype with Gassiplex 0,7 μm.

IPN - ORSAY - SEP
ALICE-2 23/06/98

Figure 70 : MCM summary.

MCM (after)

GAS64 (before)

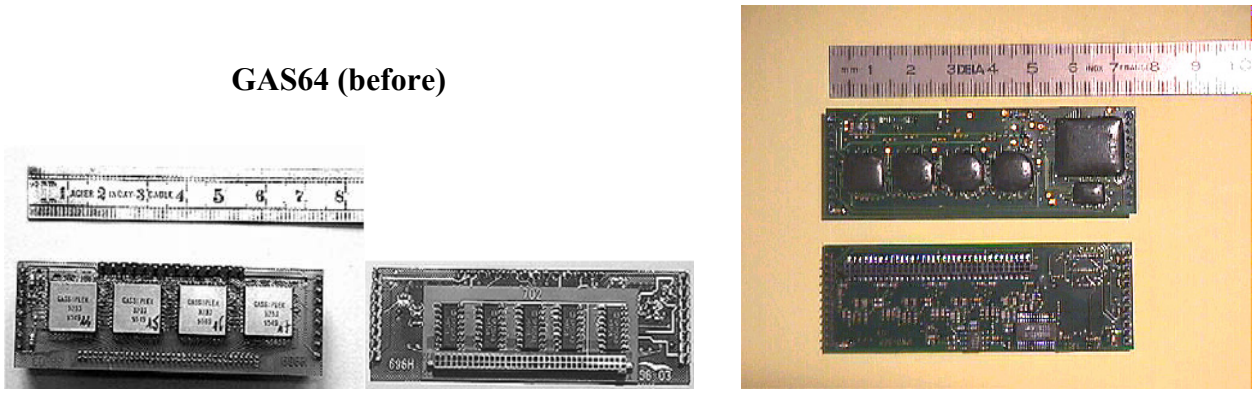

(a) (b)

Figure 71: (a) GAS64: on front view the four 1.5 µm ceramic encapsulated GASSIPLEX chips are visible, on the back side the HV discharge protection circuits are visible and (b) a view of the two sides of the fully packaged MCM with the plastic encapsulated 1.5 µm GASSIPLEX chips, DSP controller and ADC on the upper image.

Gas supply

Ar/iso-C_4H_{10}(20%) with the new gas distribution system providing an automated mass flow control operated through a Bridgeview interface on a standard PC. This was a first "slow control" test, with access to the temperature and pressure as measured by the detector on the roof of the DELPHI experiment.

Readout/acquisition

The new FEE electronics layouts implied new strategies for the acquisition cycle that take into account the two-way communication between the final numerical coded charge and the local event builder. This was done using DSP (Digital Signal Processor) technology controlled by a LCA (Logical Cell Array), The DSP being physically placed on the readout buffer on the backside of the detector, and the LCA near the VME interface card. The general communication was controlled though the SPAC card, a processor using a protocol specially developed for this application.

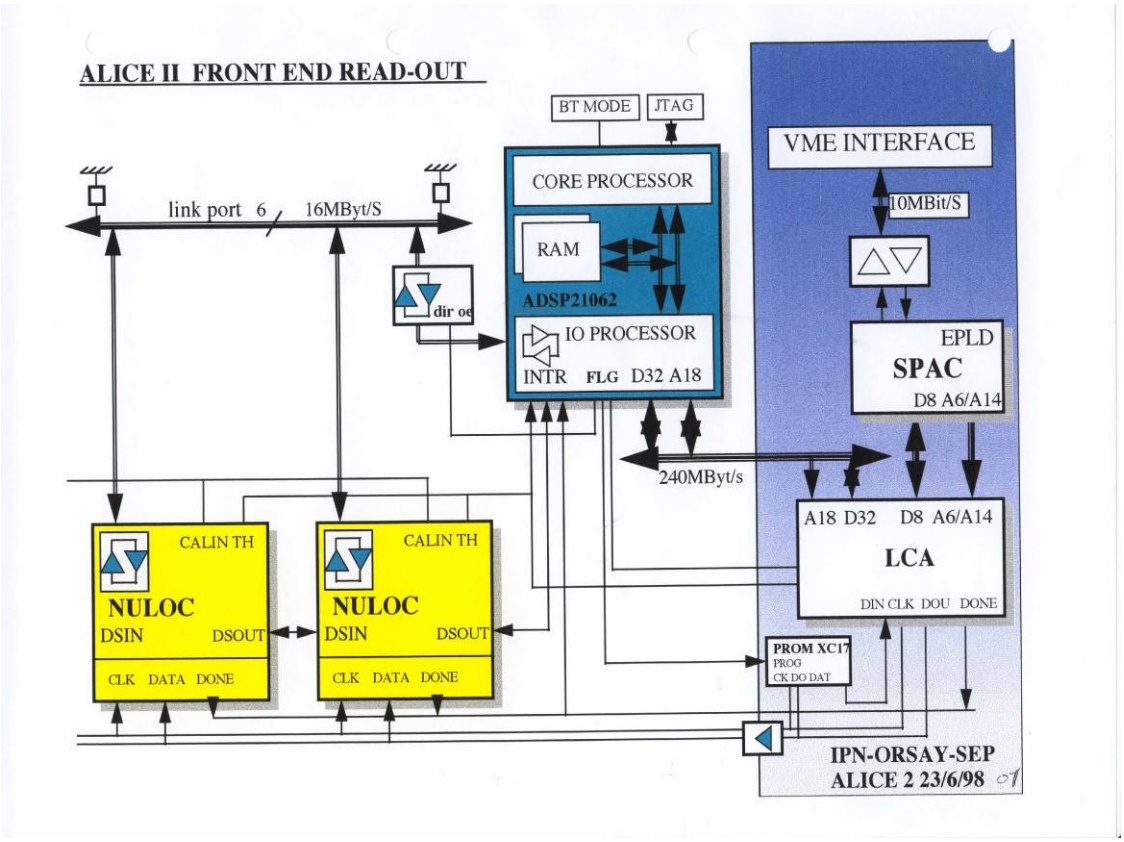

Figure 72: DAQ scheme using the local digitization NULOC cards. The Logical Chip Array (LCA) communicates the logical actions to the six parallel GAS64+NULOC buses. The SPAC element is a DSP (Digital Signal Processor) and ensures the two-way communication with the VME crate.

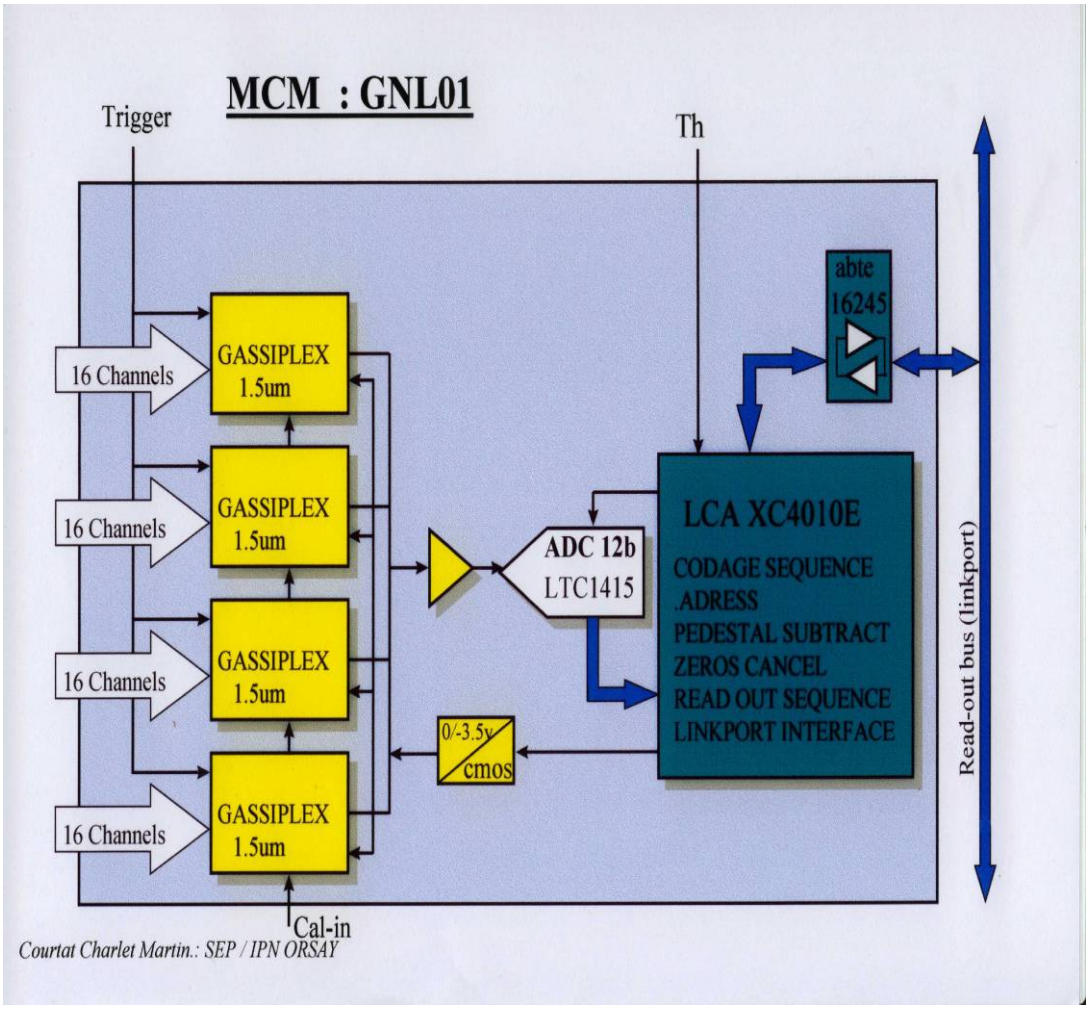

Figure 73: Modified part of the DAQ logic with the new MCM card. The logical functions programmed in the LCA are listed and are: the address coding sequence; pedestal subtraction; zero cancellation; readout sequence, and the link-port interface.

ALICE2 - electronics tests

GASSIPLEX and GAS64 tests

The analog performance of these modules was first evaluated in a stand-alone test-bench experiment. Noise levels, pedestal dispersion and linearity response were measured on 18 modules (totalling 72 GASSIPLEX and 1152 inputs) using the usual C-RAMS ADC coder. The chips were sorted into four typical offset classes. Chips belonging to the same class were mounted on each GAS64 to optimize the overall dynamic response resulting from the different pedestal levels. A common resistor was then adjusted to obtain a minimum offset on groups of modules.

Measuring conditions:

- Preamplifiers: 1.5 μm ceramic encapsulated GASSIPLEX chips.
- Input sensitivity: 12.5 mV/fC.
- Resolution: 10 bits.
- ADC range: 0–1.5 V i.e. 1.465 mV/channel.
- Readout frequency: 500 kHz.

PLAC motherboard tests

The aim of the first tests was to study the layout methods for grouping several modules and to investigate the analog issues such as noise, crosstalk and power-supply voltage drops. The PLAC motherboard was a double-sided FR4 PCB with a size of 100×40 cm^2 and a copper thickness of 17.8 μm. It was tailored to accommodate 56 GAS64 modules, wired together through the analog bus in subsets of eight. Prior to the Nov'98 tests at the PS, it became obvious that the PCB area available for signal routing was very tight and long analog paths were to be avoided. This led to the MCM development discussed above.

GASSIPLEX and GAS64 test results *(from [16])*

Noise levels

In Figure 74 the average noise value measured for 1152 channels is shown. The values show the noise on the GASSIPLEX+ADC chain; the electronics was not mounted on the detector for this set of measurements. The scale is in elementary ADC units. It can be seen that the average noise level is within a range of 0.85 to 1.2 ADC channels and that there is an excellent homogeneity between the different channels. In the same Figure the projection of the noise levels is shown, giving the frequency of each noise value. The average noise level corresponds to 1.056 elementary ADC channels i.e. 1.55 mV. Given a GASSIPLEX sensitivity of 12.5 mV/fC and an output buffer gain of 0.96, the average electronic noise is estimated to be

$$1.056 \times (1.45/0.96) \times (6250/12.5) = 800 \text{ electrons}$$

Again, looking at the RHS of Figure 74, the width of the noise distribution is roughly $\sigma = 0.09$ channels, i.e. around 0.125 mV.

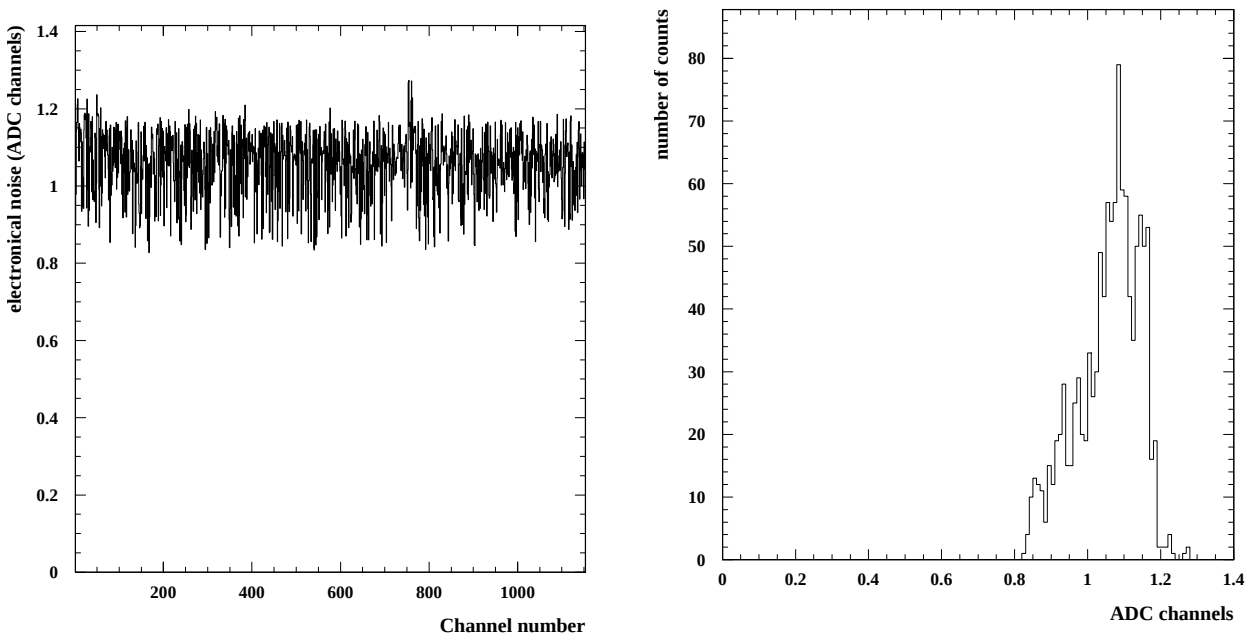

Figure 74 : The experimental electronic noise per channel is shown on the left, and the overall distribution on the right.

Pedestal dispersion

Figure 75 shows the average pedestal value after selection, measured for 18 GAS64 boards as a function of the channel number. The projection of this figure, as shown on the RHS of the same Figure allows the pedestal distribution to be quantified over all the channels to consequently determine the overall effective ADC dynamical range.

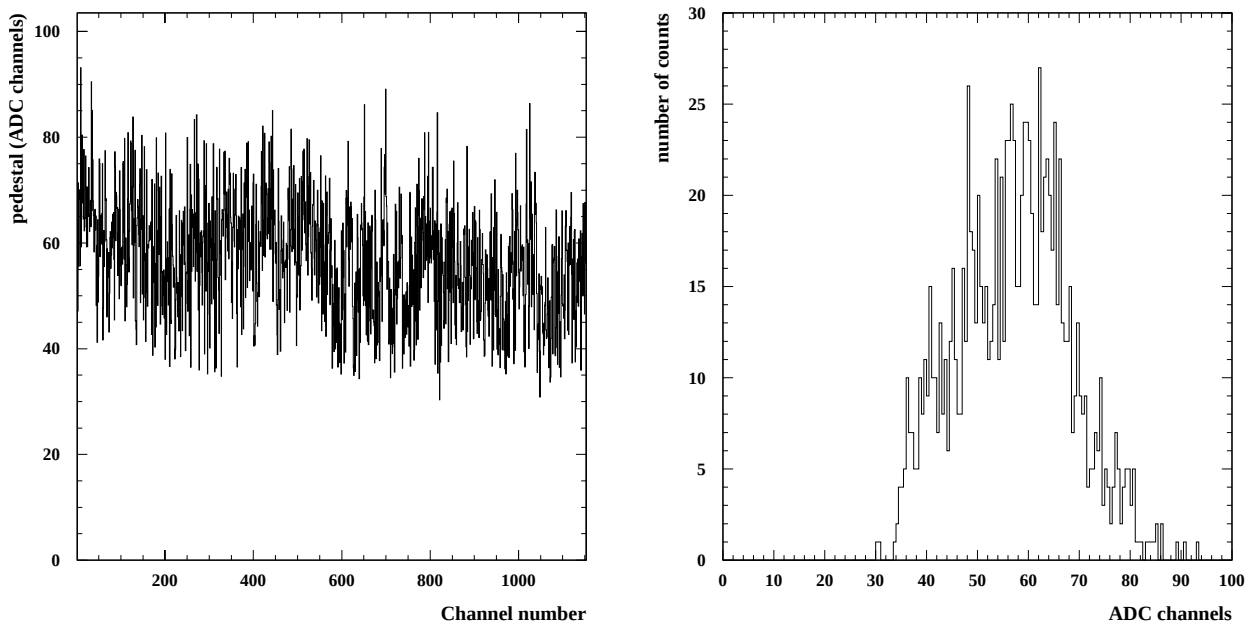

Figure 75 : Pedestal values versus per channel number (on the left) and the projected distribution (on the right).

Linearity measurements

The linearity of each channel was measured during the test-beam runs by injecting a signal on the test line of each GASSIPLEX module. Roughly seven different amplitudes were injected using a passive attenuator and the measured output ADC values were recorded. Due to the internal GASSIPLEX chip wiring, there is a noticeable difference in the perceived effective gain for certain GASSIPLEX channels. The injected charge transits through the module going from the sixteenth channel to the first. The sixteenth channel systematically shows a higher effective gain as there is some parasitic pickup between this channel and the injected charge. This is due to the way in which the GASSIPLEX chips were embedded in the GAS64 PCB. The injected charges vary from 0 mV to 1300 mV. It is important to note that in the 0 mV measurement the input to the passive attenuator is open, as opposed to the GASSIPLEX input, in order to maintain the same impedance on the test line. A typical set of calibration curves for 512 channels is shown in Figure 76(a).

Each individual channel is fitted by a straight line:

$$\text{ADC channel} = \text{effective gain} \times V_{\text{injected}} + \text{pedestal}$$

In a given chain of GASSIPLEX chips, the channel that saturates the quickest is noted and is used for software cuts in the offline analysis. The 0 mV measurement is not included in the fit as it corresponds to the pedestal measurement. Instead, using the straight-line fit, the pedestal measurement is calculated and compared to the equivalent measurement taken online during the data acquisition. In all the tests carried out so far the predicted pedestal values and experimental values correspond to within the

measured noise levels. This confirms that the calibration configuration is comparable to the data-taking set-up.

In Figure 76(b), the effective gains per electronic channel are shown for 512 channels. The gain values correspond to the slope of the straight line from the individual fits. Figure 76(c) shows the gain distribution values and Figure 76(d) shows the difference between the calculated and experimental pedestal values per channel. Finally, Figure 76(e) displays the distribution of the values, shown in Figure 76(d). It is worth noting that the distribution peaks at 1.2 ADC channels, which is the experimental noise level measured. One in every 16 channels shows an apparent higher gain than the average values. This is due to pickup on the test injection line for the sixteenth channel of every GASSIPLEX.

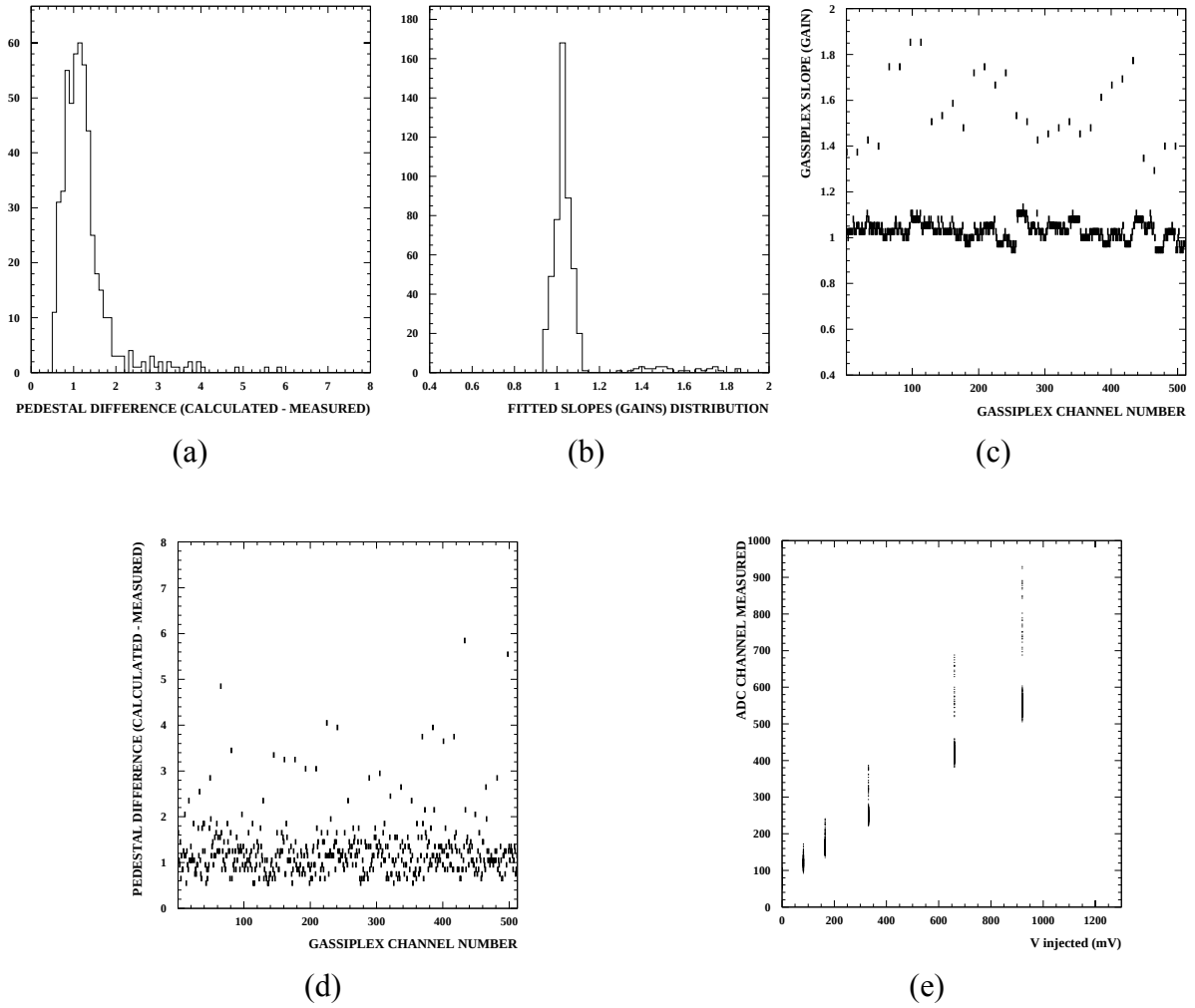

Figure 76 : (a) A histogram of 512 channels from a calibration run; (b) the effective gains evaluated from a straight-line fit and (c) the calibrated gain distribution. (d) The difference per channel between the calculated and measured pedestal levels with (e) its distribution.

Gain estimate

As the value of the test-line capacitor per GASSIPLEX module is difficult to determine, it is hard to obtain a precise gain value since the precise amount of injected charge is not known. Nonetheless, using reasonable assumptions, a gain of roughly 12 mV/fC is estimated and compares well with the manufacturer's specifications.

PLAC motherboard test results

Noise measurement – first test

Figure 77 shows the results for the electronic noise measurements carried out on 1152 inter-connected channels. The configuration was the GAS64 and remote C-RAMS ADC coding. The average noise level is roughly 1.06 channels, i.e. 1.55 mV. Given the GASSIPLEX sensitivity is estimated to be 12.5 mV/fC, and the output buffer gain was estimated to be 0.96, the average electron equivalent noise is 800 electrons. The noise dispersion is approximately $\sigma = 0.125$ mV.

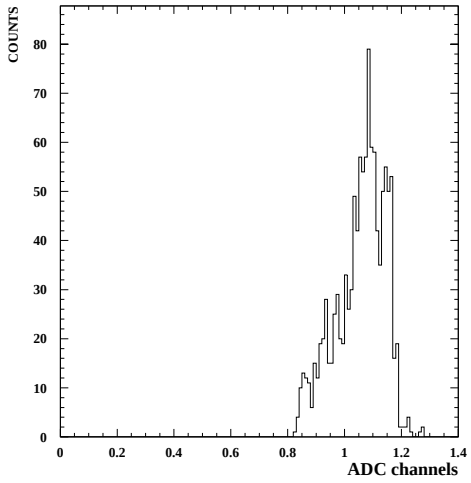

Figure 77: Raw data spectrum of the 1152 inter-connected GASSIPLEX channels on the PLAC motherboard.

Noise measurement – second test

A digital board (NULOC) was then added to each GAS64 board in order to test the local analog-to digital conversion. The buses became digital and were routed all the way through the chamber plane up to a peripheral card acting as the master processor (INV). The total load on the bus was 10 units per set (three NULOC and seven passive place-holders). The data were read out with a VME crate using a fast serial link (SPC). The INV processor card was linked to the upper level through a fast serial link (SPAC) leading to a VME interface board (Spac-master). The VME master processor was a Power-PC running the CERN acquisition software DATE3.

Noise measurement – third test

The full-scale prototype was then tested in-beam on the SPS line with the first production set of MCM boards. The test configuration was the following: A special interface board was used to connect a strip of six MCM to the PLAC prototype base board. The purpose of this interface board was to provide a mechanical fixing for the modules, the power distribution and the Patch-bus interconnections. It had been designed to fit into any place on the chamber plane to allow several electronic densities to be tested. The bus was linked to the INV processor board through a ribbon cable and the processor itself was remotely read by the VME crate as before. The pedestals and noise levels were measured at several locations on the chamber. The same measurements were performed using the C-RAMS modules in order to compare the performances. The noise levels obtained with the MCM appear to be slightly improved (1.6 mV compared to 1.8 mV for the C-RAMS set-up). Figure 78(a) and (b) show some experimental results from the May 1999 SPS test-beam data.

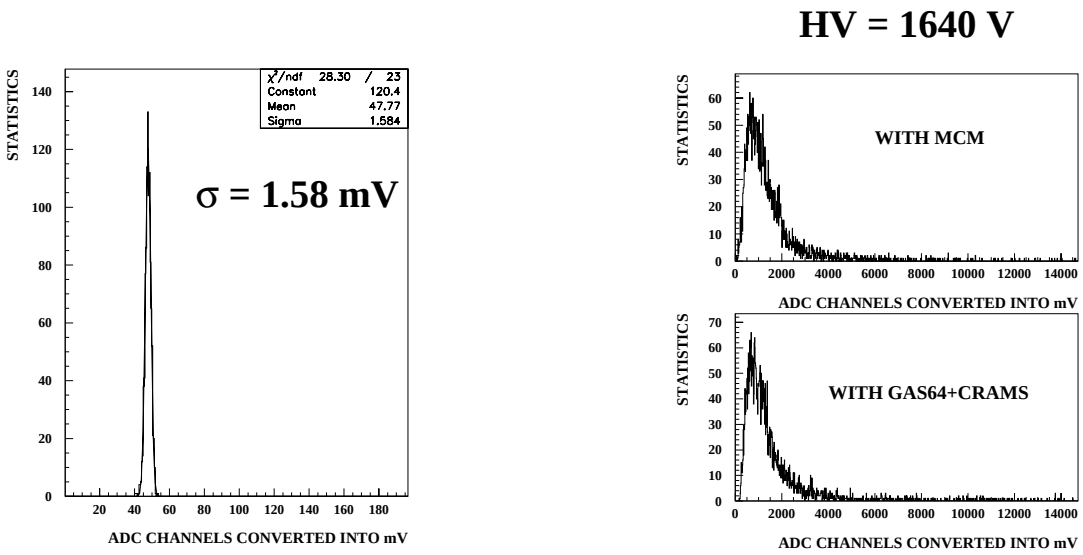

(a) (b)

Figure 78 : (a) MCM noise distribution giving an equivalent σ value of 1.58 mV. This can be compared to the 1.2 ADC channels, or 1.8 mV equivalent, found with the GAS64+C-RAMS setup. (b) Two charge measurements (shown in equivalent mV units) taken from the May'99 SPS test-beam data. Experimental conditions were the same for both measurements; the MCM coded result is shown above the GAS64+C-RAMS one. The two results are in agreement, showing that the new MCM performs satisfactorily.

ALICE2 - mechanical tests

The mechanical defaults on this full-scale prototype were tested through charge response to single particle impacts. For a constant HV setting, this integrated charge per impact point is expected to give a constant Landau peak position - to within the precision of the individual pad threshold. A significant change in the Landau peak position reflects a different internal gain factor, the main culprit being the mechanical geometry (with the reasonable supposition of a homogeneous gas environment and no local poisoning that could influence the internal gas gain).

The cathode pad plane is composed of six smaller planes, glued together. The detector gain was measured at several points along the glued junctions to see if there was any noticeable effect. A left- to right-hand scan was also carried out. The aim here was to compare, for constant settings, the gain as measured on the outer edge and inner region. A variation is expected if the inter-cathode and anode-cathode distances are not constant (once again supposing a homogeneous gas environment).

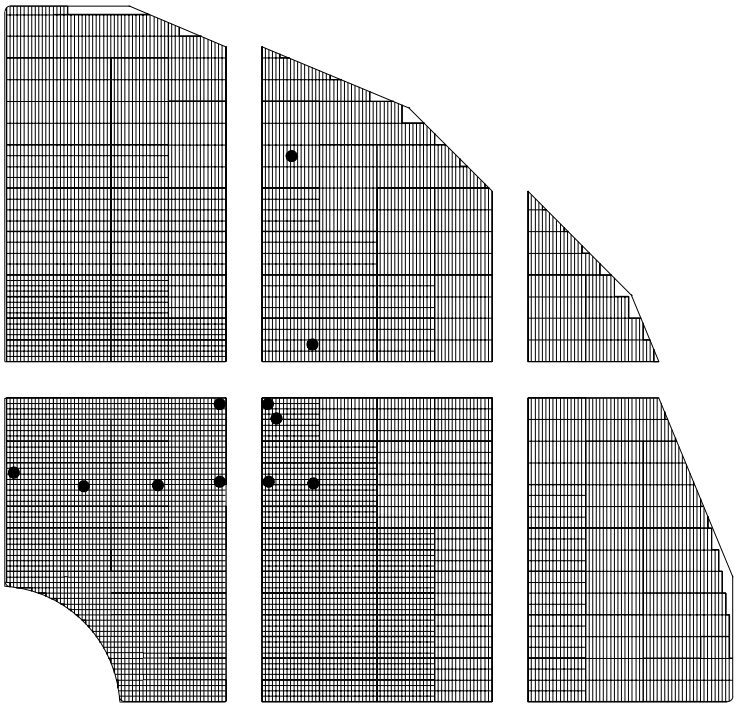

Figure 79: The individual PCB cathode pieces showing the test points near glued junctions and a scan from the edge to the inner detector.

The final results showed that the overall gain was stable for all nine points tested, to within 12% of the average response. A gas mixture of 20% CO_2/Ar was used and a HV of 1650 V was applied to the anode wires.

The performance of different gas mixtures

The well known gas mixture of Ar/CO_2 was tested with this full scale prototype. The aim was to see if this stable mixture, for which no ageing affects have ever been observed, could provide a sufficiently high gas gain. This would allow the migration to a cleaner, non-toxic and non-inflammable gas mixture, in keeping with the new CERN legislation. The number of pads hit in response to the passage of a single particle, as well as the gain estimation and spatial resolution were measured. The causes of inefficiency were looked at more closely with this data set.

Number of pads hit per event

The number of pads hit per event, regardless of the spatial resolution or gain, is an important quantity as it gives the basic occupancy per single particle. The Mathieson-Gatti pad response function, which gives the relative charge on each pad, can be used to predict the number of hit pads. In this case they were simply measured.

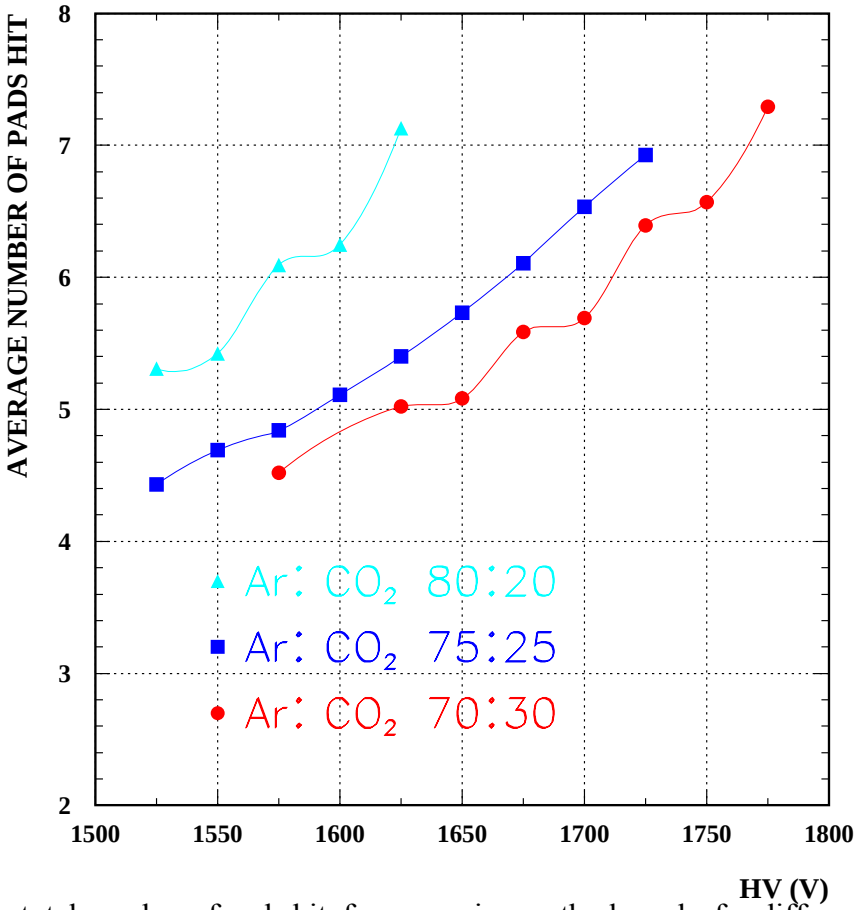

Figure 80 : The total number of pads hit, for same sizes cathode pads, for different gas mixtures and HV settings. *The initial image (shown in reference **[17]**) contained an error.*

Gain

The peak position of the total charge measured in the detector, the spatial resolution, and the total reconstruction efficiency were evaluated for three basic gas mixtures: Ar/CO_2 with proportions70:30, 75:25, and 80:20.

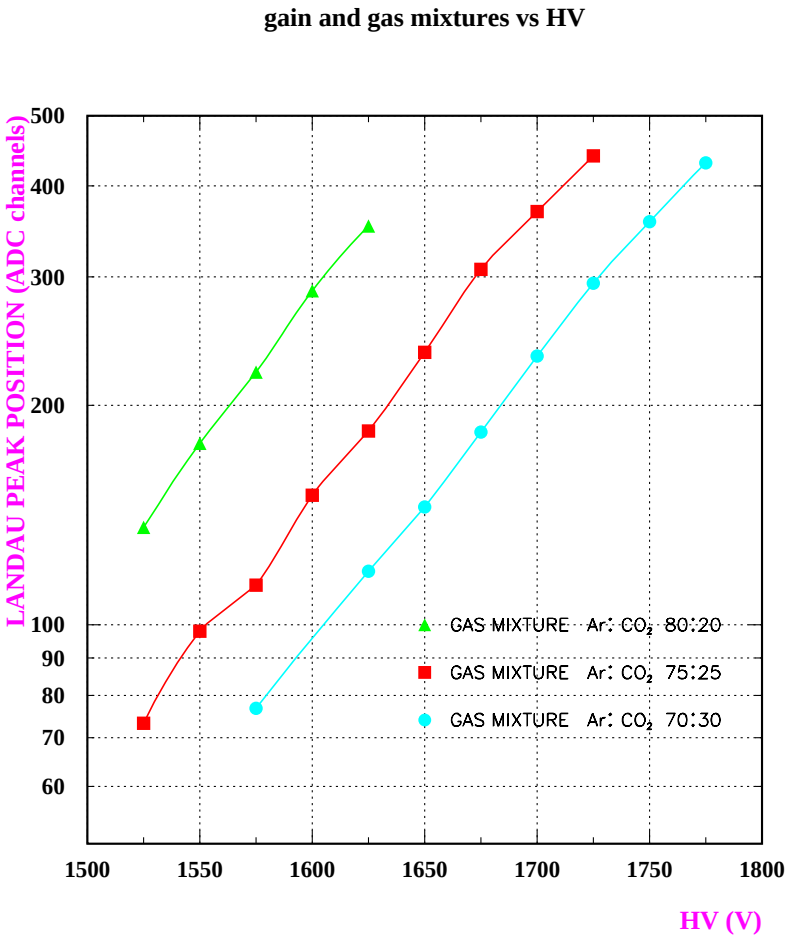

Figure 81 : Evolution of the peak charge value measured for similar setups with 350 GeV/c pions at the SPS in May'99. The highest gain is obtained with the largest Argon gas portion. The gain evolution is similar for all three mixtures and doubles roughly every 80 V.

Spatial resolution

The spatial resolutions for single particles, using the basic centre-of-gravity reconstruction algorithm, were evaluated for the three gas mixtures. The different HV ranges reflect the electronics saturation limits - which depends on the gas gain, and therefore the gas mixture. The detector's linear plateau extends beyond these limits, but was not measurable with the 1.5 µm GASSIPLEX chips employed at the time.

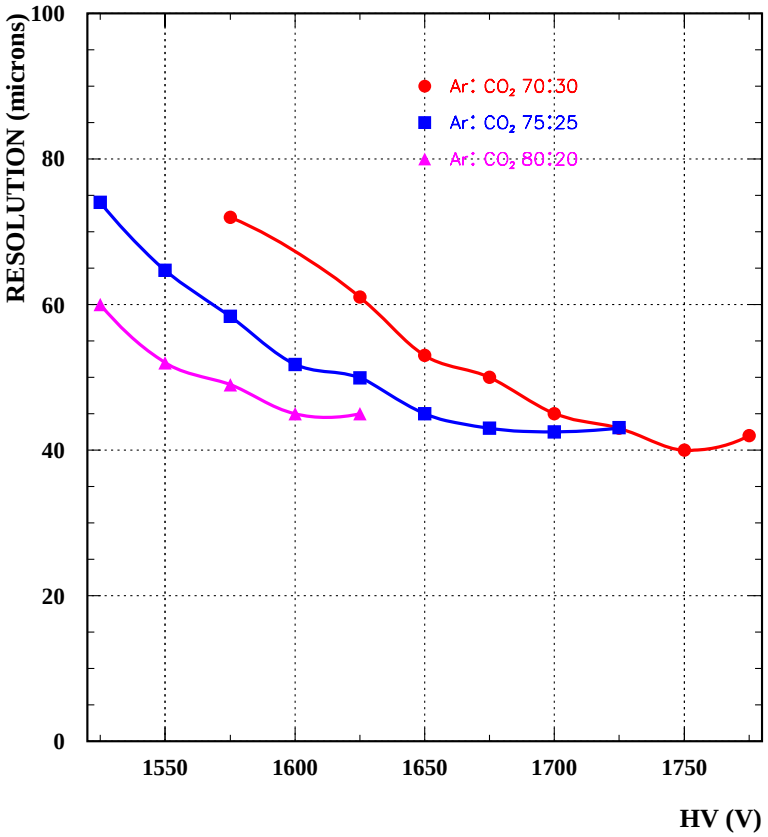

Figure 82: Experimental spatial resolutions as measured at the SPS with 375 GeV/c incident pions. For each mixture, increasing the gain betters the position resolution.

More detailed and extended results and discussions can be found in Chapter4 of reference **[35]**.

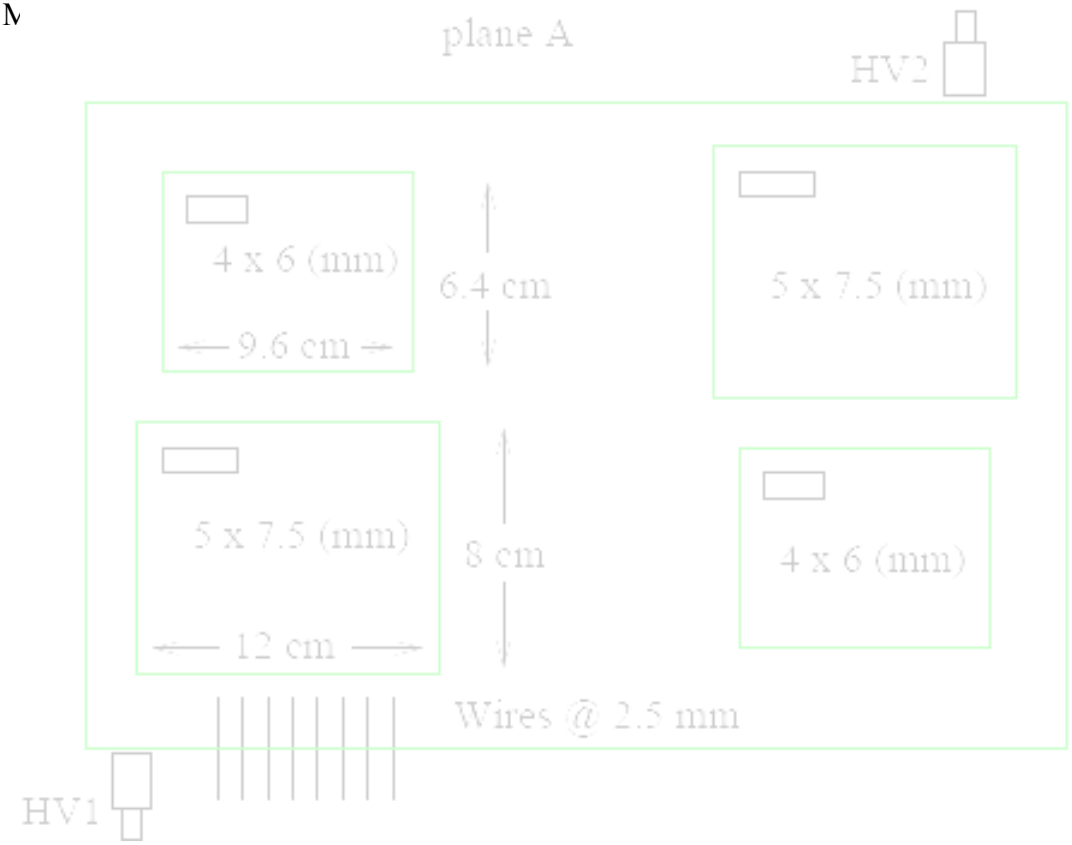
plane A
HV2
4 x 6 (mm)
9.6 cm
6.4 cm
5 x 7.5 (mm)
5 x 7.5 (mm)
12 cm
8 cm
4 x 6 (mm)
Wires @ 2.5 mm
HV1

ALICE3

ALICE3
plane B
HV2
ZONE 4
4 x 6 (mm)
9.6 cm
6.4 cm
ZONE 1
ZONE 3
5 x 7.5 (mm)
12 cm
8 cm
ZONE 2
Wires @ 2.5 mm
HV1

ALICE 3

Aims

There were two separate test periods at the SPS with different aims:

- Single hit setup – for the study of spatial resolution, single hit efficiencies, new geometries, correlated cathode plane measurements.
- Multi-particle setup at SPS/H4 – a first measurement of the double hit resolution with correlated cathode planes.

The main idea behind this detector was to evaluate the detector response with two active cathode planes. This was the first detector constructed specifically for correlated charge measurements using fully implemented opposing cathode planes. In the light of the LHC Committee report on the prototype tests preceding the ALICE3 prototype, new pad geometries and anode-cathode separations were to be tested. The proposed geometries were to test 5 mm x 7.5 mm pads with a 2.5 mm anode-cathode gap, and 6 mm x 4 mm pads with a 2 mm gap. The LHCC report clearly leaned toward a 2 mm anode-cathode gap to reduce the overall occupancy per event, a problem that took on a greater importance in the light of background physics simulations showing unfavourable (>>5 %) occupancies over the detector surface. Single- and multi-hit experiments were carried out at the SPS in June 2000 with a 350 GeV/c π^- beam and, ideally, the chamber efficiency, linearity plateau, spatial resolution and number of pads hit per particle impact were to be evaluated. Unfortunately, the very short time window for constructing and testing this prototype meant that the data set was not fully exploited. The multi-hit analyses (looking for the double hit separation limit) were left unfinished, leaving a sense of frustration. However, decisions had to be made within stringent time limits and this particular analysis was not thought to be critical at the time.

The 1.5 μm GASSIPLEX chips were the only electronics available at the time, and so the tests were carried out with them, even though they meant using a limited dynamical range.

Detector geometry

The outer shell of the ALICE1 prototype was used to house the new ALICE3 cathode planes. The anode wire plane was composed of two separate wire grids, one with 2.5 mm spacing and the other with 3.75 mm spacing. The two wire grids had separate HV supplies.

The "multi-geometries" accessible with this prototype are shown in the images that follow.

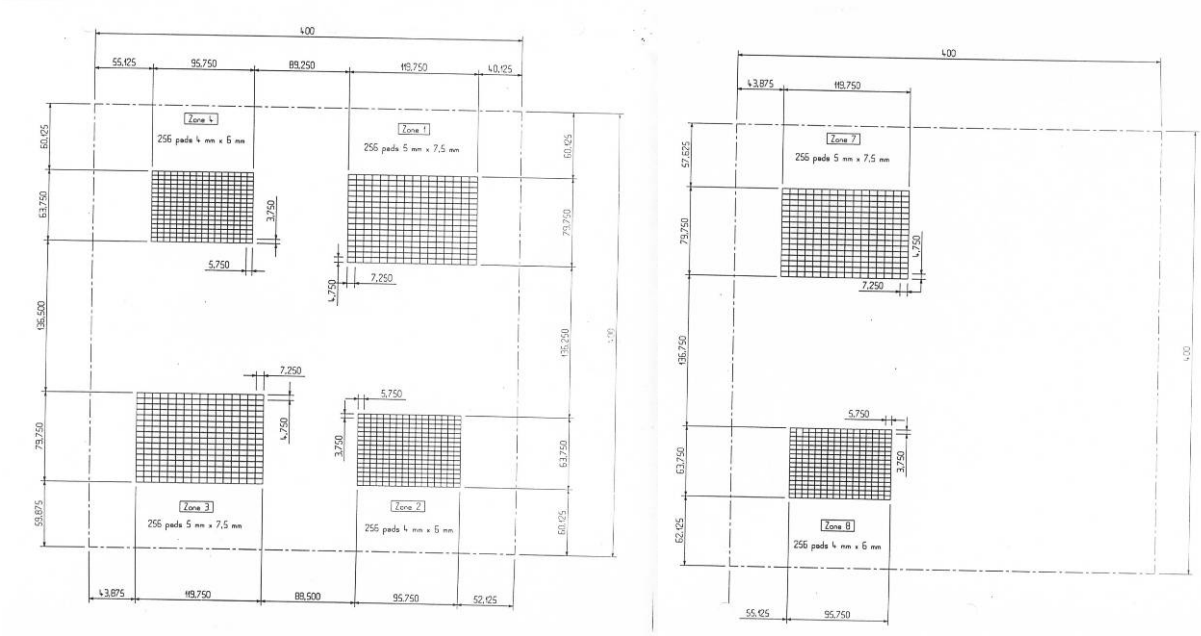

Figure 83: Cathode Pad layout for "Plane A" (on the LHS) containing four separate pads regions, labelled zones 1 to 4, and "Plane B" (on the RHS) with two separate pads regions, labelled zones 7 and 8. Plane A has two zones of pads at 4 mm x 6 mm and two at 5 mm x 7.5 mm. Plane B has one zone of with each pad size.

The geometry is such that the two cathode planes have opposing pads aligned either with a half-pad offset in one - or both - directions. This means that the same charge distribution (in the vicinity of the anode wires) will be distributed differently on opposing cathode planes. This simple - but astute - detector layout provides access to several cathode plane and anode wire combinations, but only a couple were really of interest since a good idea of the final geometry was already in view, but had yet to be tested.

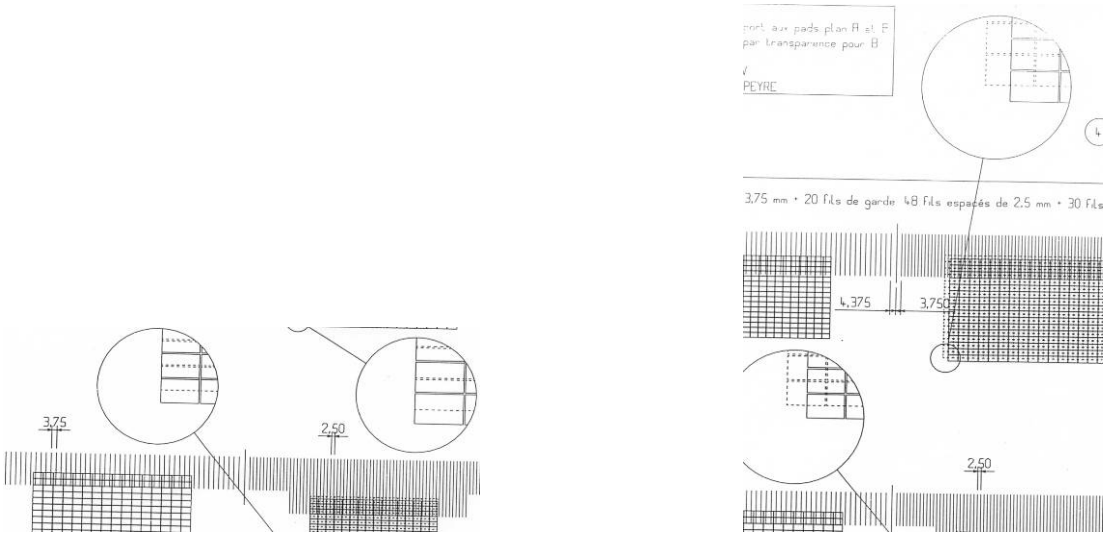

Figure 84: The two images show the relative pad positions through a transparent view of the cathode planes. The magnified part of the images shows the plane A pads drawn as full lines, with respect to the Plane B pads which are drawn with dashed lines. On the LHS the pads are offset by a half-pad in one direction and on the RHS, with Plane A rotated through 180°, the pads are offset by one half-pad in two directions. The wire grid can be seen in these images with the two different wire spacings at 3.25 mm and 2.5 mm.

Electronics

The GAS64 integrated circuits were used with the same implementation as for the ALICE2 prototype.

Readout/acquisiton

The general ALICE acquisition program DATE was used for the beam tests. Version 3 of the DATE developments was used and results from the test beam performances were used to define some of the version 4 characteristics. The output buffer was sent to a separate PC for offline monitoring.

Test beam layout

The multi-particle layout required that the support tracking detectors cover a larger area, and this was done with a 1 m^2 CPC detector.

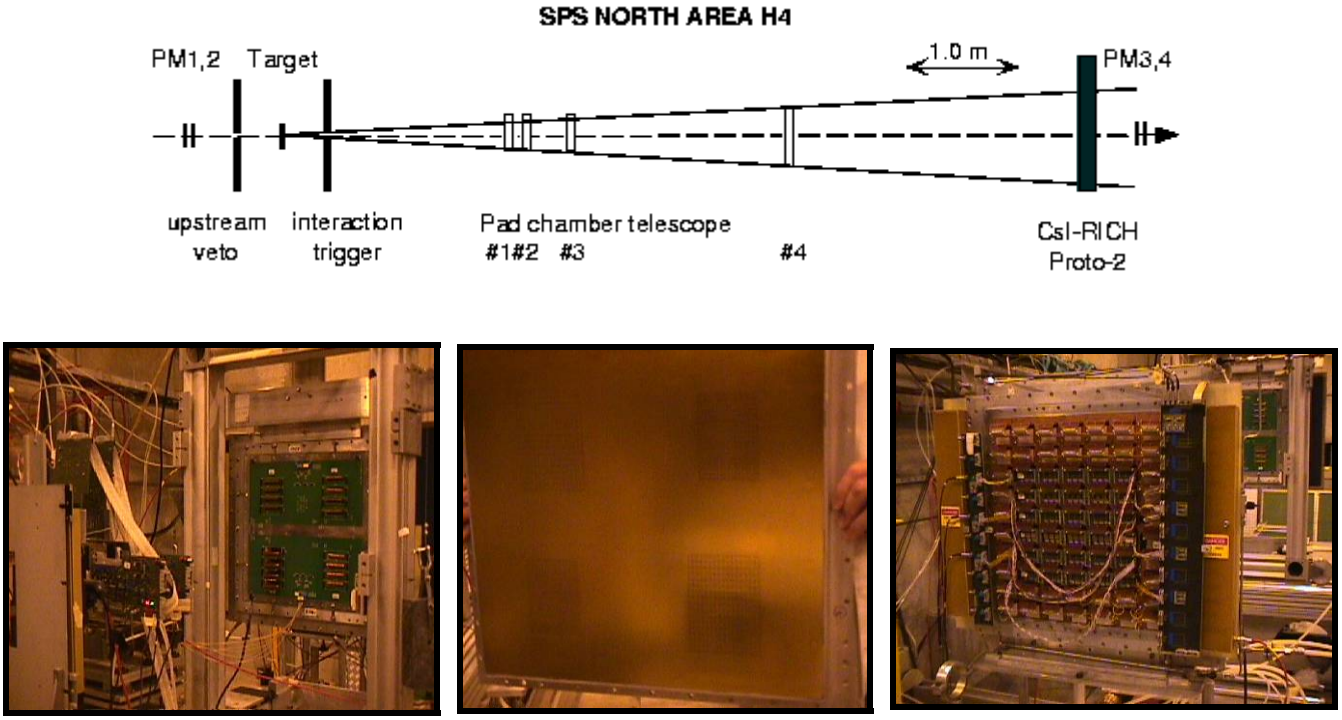

Figure 85 : (a) shows the ALICE3 prototype being tested, the four different pad areas are visible via the four output circuits (b) a view of the copper pad plane, and (c) the HMPID CPC used for multi-particle tracking.

Online monitoring

For the first time, the data stream was translated to an object oriented form. The objectification logic is shown in Figure 86 (see Appendix B for full details).

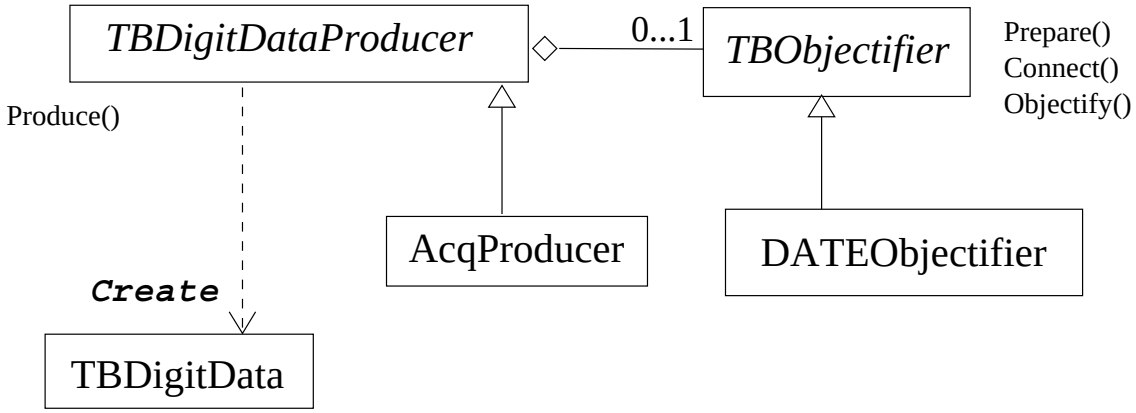

Figure 86 : UML diagram showing the general architecture of the data stream objectification.

The first Object Oriented online monitoring programme, written specifically for the test beams was also implemented in these tests. An online suite of monitoring programmes, named the TestBeam ToolBox, was developed using an architecture that provided more long-term flexibility, allowing modules to be added/taken-out/re-used between different test-beam periods. A general view of the TestBeam ToolBox screen is shown in Figure 87 with a sample of the active fields and buttons that provided easy-to-use access to the basic analysis parameters.

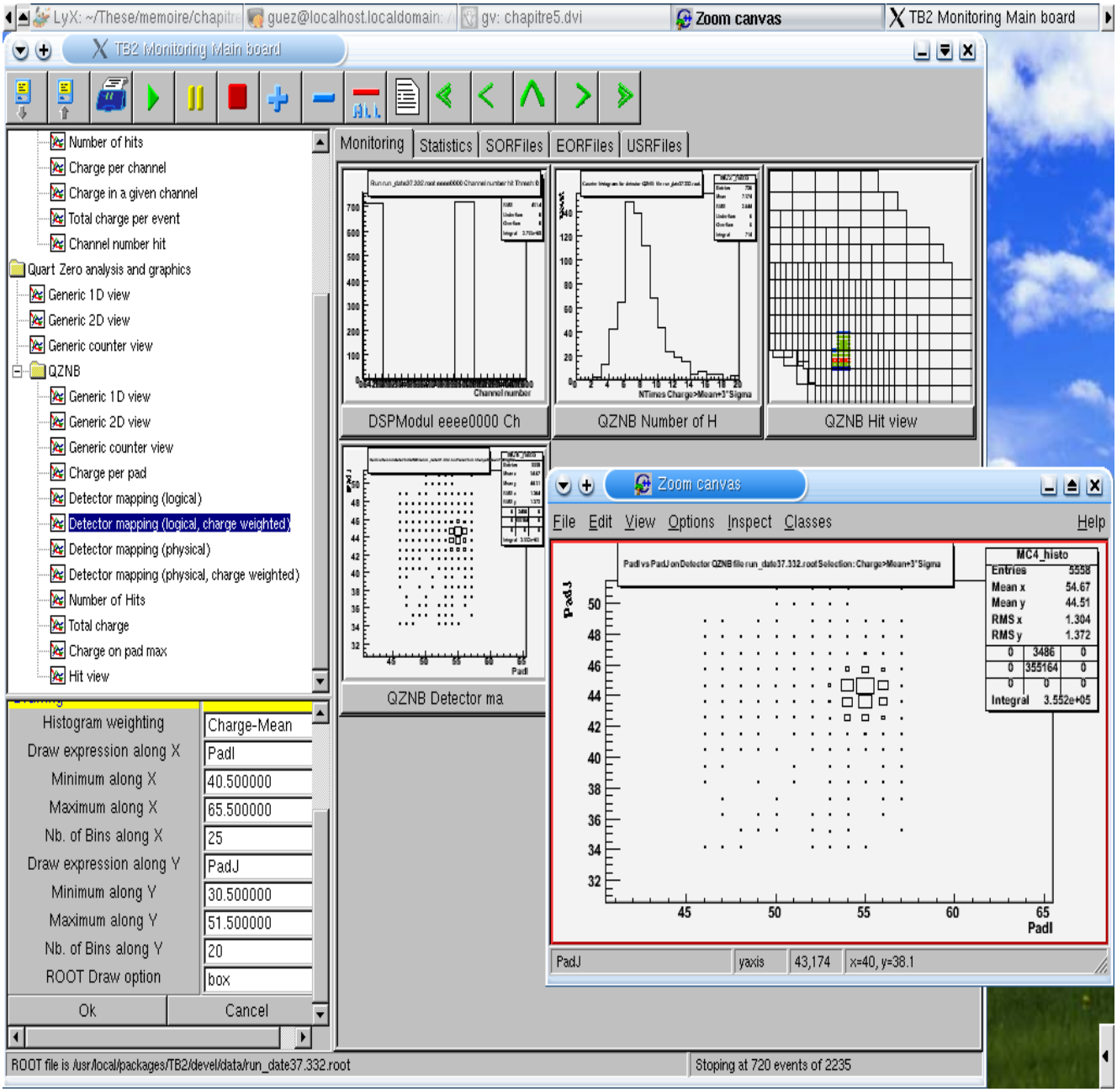

Figure 87 : Screen capture and active GUI of the TestBeam ToolBox. The LHS shows available graphics objects with active fields in the lower half, and the RHS shows an example of the online graphics results (the location of the detector pads hit, in this case) and the associated region on the detector. The first object oriented mapping algorithm was implemented here. The tabs at the top of the graphics panel, named Monitoring, Statistics, etc.... give details of the different support files request for the analysis. This was the very first general use OO program used in the test beams.

Offline reconstruction

A simple correlated plane reconstruction algorithm was written. Different criteria based on the number of pads hit and the number of pads used to reconstruct events were studied. Efficiencies and spatial resolutions were evaluated for different selection criteria.

The surprise in the data analysis of the correlated plane measurements is that the COG algorithm is sufficient to establish a high resolution impact point. The intrinsic default in the COG method for a single plane is automatically compensated for by the half-phase default on the opposing plane. This meant effective resolutions and efficiencies could be evaluated without an important contribution from the reconstruction algorithm itself.

Results were obtained by two MSc. students during the course of a 2-month project with the group. A formal presentation and a written report were given at the end of their project, and the results were published in the Addendum to TDR5 for the Muon Spectrometer and a separate study was also presented in document [**36**].

Results

Only the setup where the opposing cathode planes had a half-pad offset in both directions, was studied in detail. Having two active cathode planes has several beneficial effects on the reconstruction front. The far simpler centre-of-gravity algorithm could be implemented since the reconstructed impact points on opposing cathode planes have the natural position dependent default - but they have exactly one half-phase offset. So, in taking the average of the results, the two defaults annihilate. The idea is shown in Figure 88 with the final result given in Figure 89.

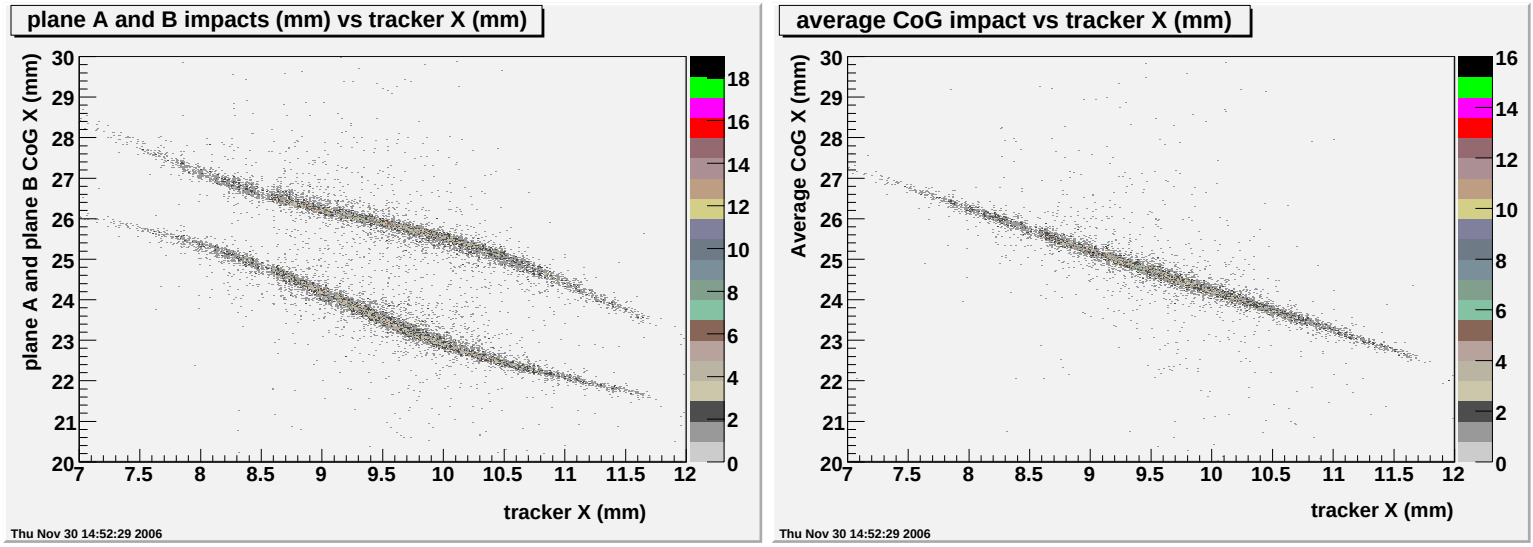

Figure 88 : On the LHS the response of the two cathode planes (A and B) as a function of the beam impact point is given. The correlation between the detector response and the beam impact point follows a 45˚ slope, but with a geometrical default that depends on the beam impact point relative to the pad center. This well understood topological default is naturally corrected by taking the average value of the two planes. The result is shown on the RHS.

These tests showed that the required specifications could be met. The reconstruction efficiency is acceptable, generally being above 95% at the time of the initial studies (and perhaps has been bettered since).

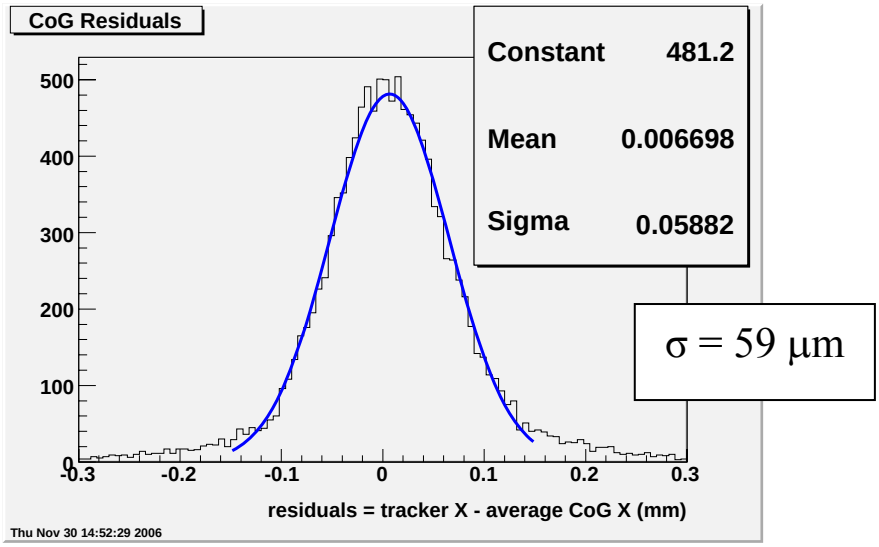

Figure 89 : Projected residuals for the impact points shown in Figure 88, the result is 59 μm. The anode wire HV was 1475 V, filling gas Ar/CO_2 at 80/20; the anode wire pitch was 2.5 mm, and the anode-cathode gap was 2 mm. The pad size was 4 mm in the high resolution direction and 6 mm in the other.


QUADRANT0

QUADRANT ZERO

Aims

Quadrant zero was originally to be the first fully functional quadrant and was to be the spare detector in the case of problems with the future system. It was the first detector designed to have two fully active cathode planes with an internal geometry corresponding to the best layout measured with the previous detector, ALICE3. However, since it turned out to be the detector that accumulated the greatest number of undesired mechanical characteristics, it was a very valuable test detector. Several issues may not have been noticed had it not been for the mixture of questions posed by the external referees, and the extra pressure put on the group as a whole to provide a true high performance detector, as opposed to a prototype.

Detector geometry

Several unresolved issues came to the forefront during the construction of this detector.

The aluminium detector frames, which took the load of the anode wire plane and provided external rigidity, proved to be an unacceptable source of multiple scattering. The shadow cast by the frames imposed an overall "nearly dead" zone. The beam pipe support mechanism was still being finalized during this period and it was noted that the detector frames and beam-pipe support wires would not overlap, thus creating a more complicated (and un-necessary) inefficient region. The result was the abandon of the aluminium frames, and the design of a new “frameless” detector, so QUADRANT 0 was still truly a prototype and not the final detector as hoped. Unfortunately, the first tests showed that the detector was not rigid enough, and that a central internal cathode-cathode spacer, which had already been designed, had to be implemented.

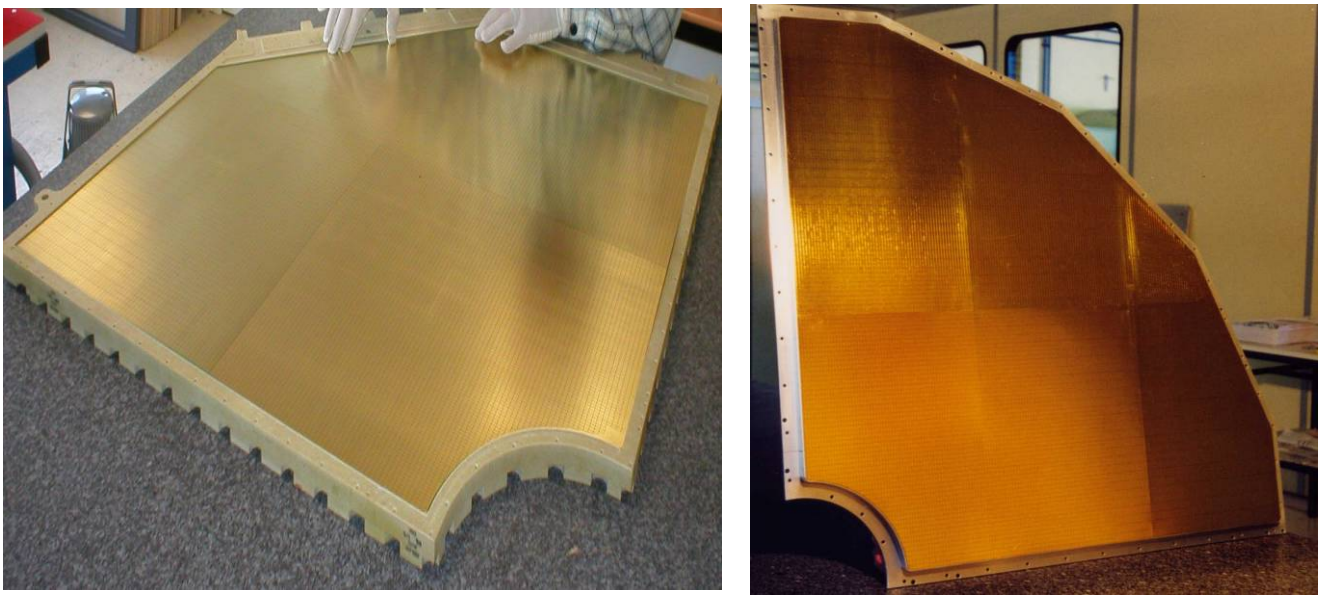

Figure 90 : On the LHS, the "frameless" QUADRANT0 and on the RHS the old Al framed detector.

It was known from the outset that stations 1 and 2 were to be enclosed in a front-end cone attached to the front absorber. The thermal constraint, applied to all detectors, is that the operational temperature stays below 40°C, no heat is to be evacuated to the ALICE cavern but to be extracted directly to the exterior. All exothermic heat sources were to be controlled in such a way that the detector performances, as measured in the more aerated test-beams, would be attainable in the final configuration. This had strong repercussions for the cooling of stations 1 and 2, where over 150,000 individual electronics channels would be running continuously, in a very enclosed space, over large surfaces and where a homogeneous detector is a pre-requisite for an accurate particle impact reconstruction. Thermal simulations were carried out, and a detailed report is given in reference [**37**].

Gas supply

The gas supply was not a source of worry in itself, the problem that appeared in the early stages of the detector manufacturing was that there was an important gas leak over the whole detector surface. This in turn was found to arise from the PCB construction where the connector vias, which had been pierced through the cathode plane boards, had not been filled with varnish to render them air-tight. This led to establishing more stringent quality controls.

Electronics

The electronics developments were slow to progress, the main characteristics were established on paper, but the manufacturing was not always such a straightforward process. The charge injection test circuitry was not implemented and the overall gain dispersion was a handicap to obtaining an optimal dynamic range.

A full range of tests on temperature control, detector gas-tightness, and electronics quality were carried out and the results were presented to the LHC Committee during 2003. Transparencies from these presentations can be consulted through the ALICE web pages [**38**], and a detailed report is found in reference [**39**]. Most issues were subsequently resolved, opening the way to the construction of the final detector.

A detailed report on the final electronics and acquisition strategy is presented in the Production Readiness Report (PRR) [**40**].

The end of the R&D tests - a personal note

Several series of prototype tests were carried out, both in-beam and in the laboratory. I analysed all sets of results, making the associated code evolve at the same time. I presented most of the prototype results in the various ALICE weeks and international meetings.

I co-ordinated the quadrant zero construction meetings where engineers, technicians, and physicists exchanged their news and concerns. The concrete design of the final detector being more-or-less established, the corresponding computing model had to be constructed, and so I turned my attention to the main software issues.

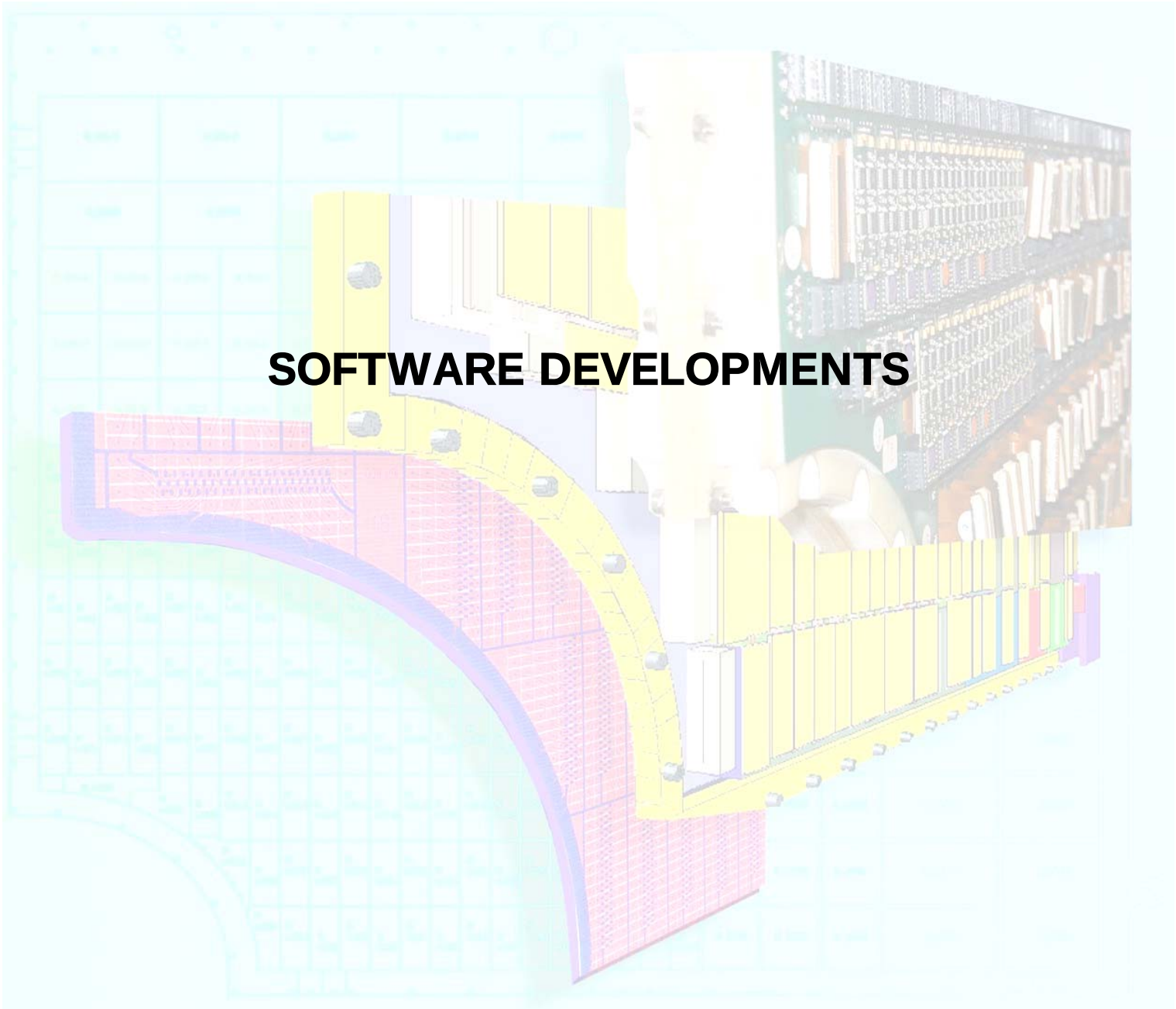

SOFTWARE DEVELOPMENTS

THE VIRTUAL DETECTOR IN AliROOT

The general framework for all the ALICE detector simulations had been an ongoing project over a number of years and the time was ripe to implement station 1 and 2 in the provided framework. The software equivalent of the mechanical, electronics and acquisition aspects had to be written for the Object Oriented AliROOT software.

The tasks were broken down into several modules, as follows:

- Phase 1
    - Compilation of the detector materials (Appendix C)
    - Detailed detector model in AliROOT (see Figure 91)
    - Evaluation of the radiation lengths over the detector surface
    - Development of a simplified model that reproduces all materials with equivalent thicknesses and surfaces (see Figure 92)
    - Implementation in AliROOT complete with all external support structures
- Phase 2
    - Creation of sensitive surfaces on both cathode planes with virtual electronics readout
    - Creation of the real detector number system for relating electronics channels ↔ Cartesian coordinates (mapping)
    - Implementation of the mapping in AliROOT
    - Use of the mapping to generate sensitive surfaces.
- Phase 3
    - Implementing the mapping in the reconstruction algorithm (Appendix D)

Three main documents covering this period were written and two of then are included as appendices at the end of this document. The third document is David Guez's thesis, presented at Paris XI in December 2003 [**41**].

A study of the impact of different types of electronics breakdowns on the overall particle reconstruction efficiency was carried out, and the most robust electronics cabling scenario was established.

Appendices C and D contain documents giving full details of the finished work.

The following images are included only to give an idea of the models developed and amount of detail included.

Berg connector Cu

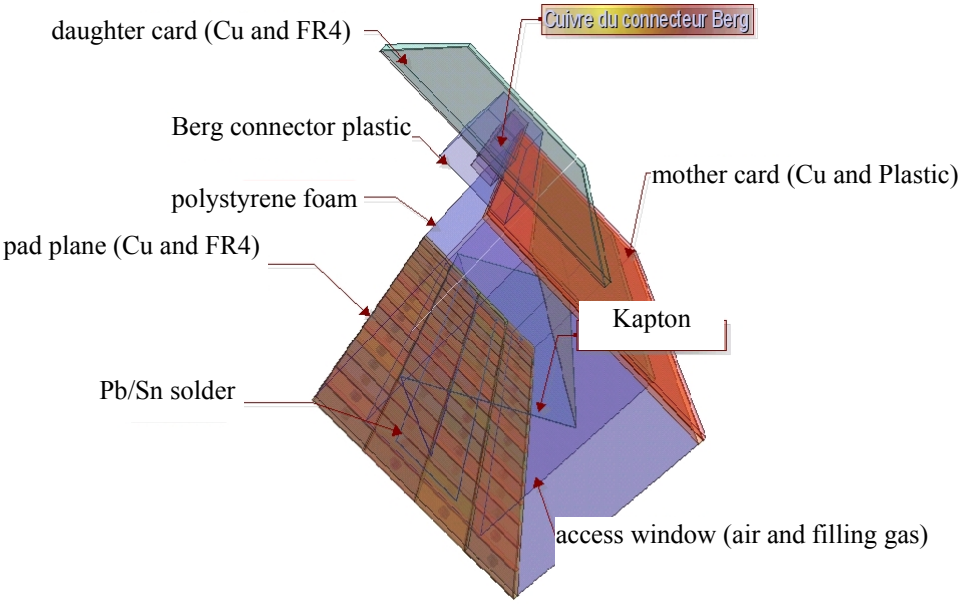

Figure 91 : Very detailed detector model using true materials, thicknesses and layout. The high level of detail allowed the essential physical characteristics to be established, the ultimate aim being to reproduce these characteristics with a simpler model.

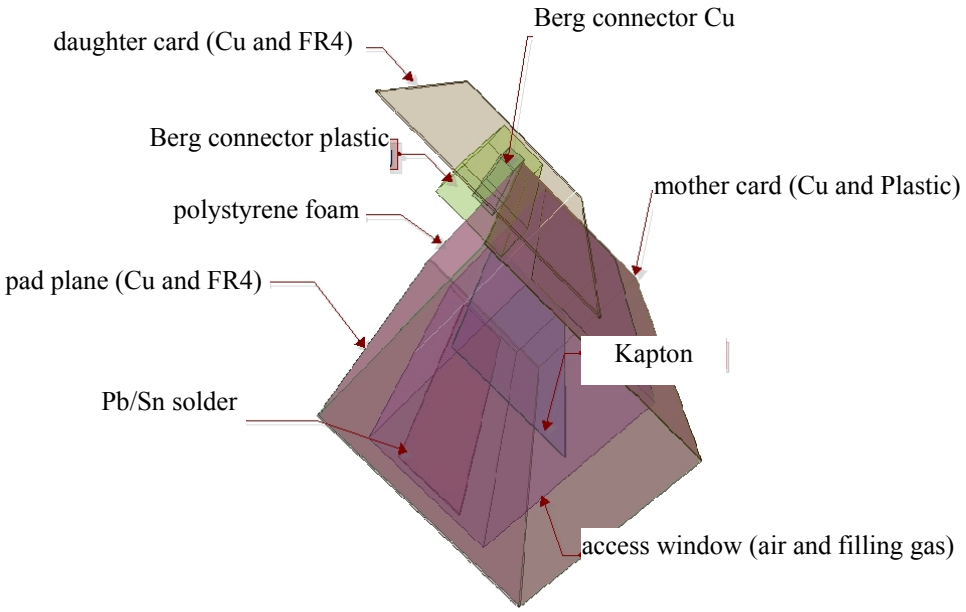

Figure 92 : Simplified detector model using equivalent materials, thicknesses and layout. This model reproduces the essential physical characteristics of the detailed model. Full details can be found in **[41]**.

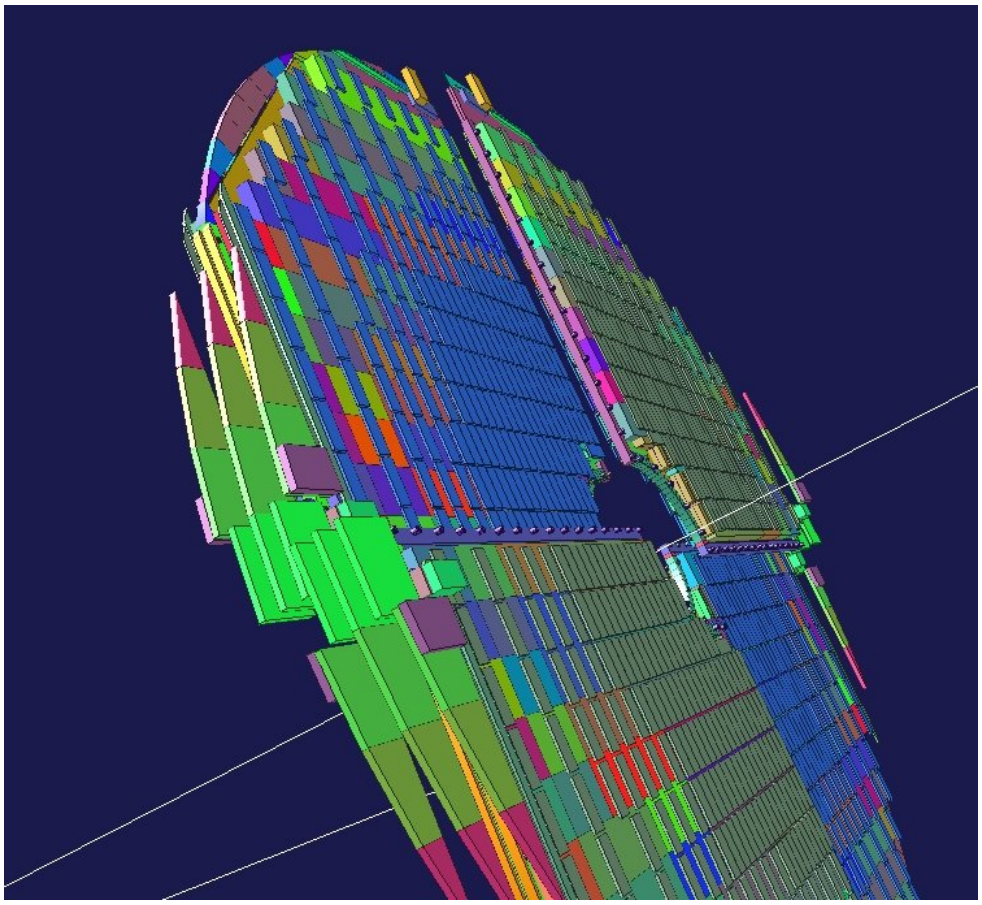

Figure 93 : General view of the station 1 detectors, complete with support frames, electronics cards and true layout.

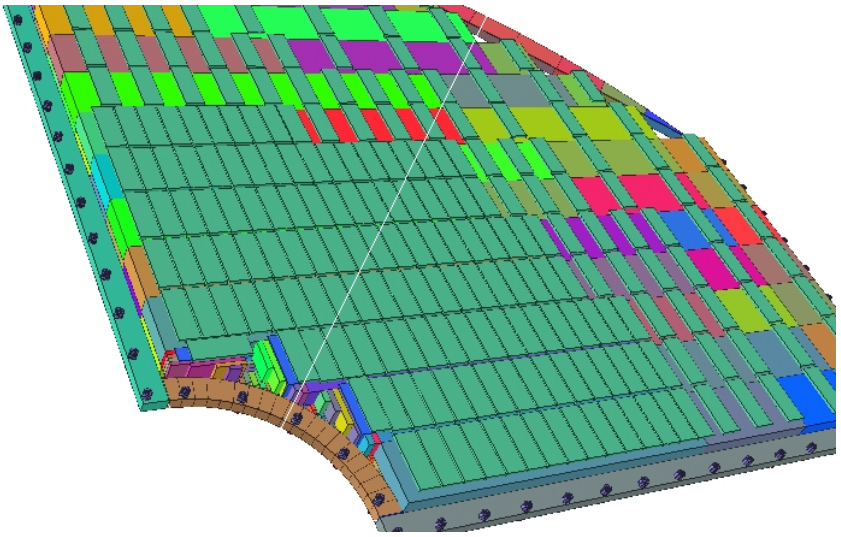

Figure 94 : View of one quadrant, from the simulation. The frame (nuts and bolts included!) are visible. The electronics cards are coloured in green, and the underlying layers are built up using the simplified geometry shown in Figure 92. The overall layout is established by placing a simple module at the positions defined in the mapping. The mapping algorithm is thus used to generate the simulated detector geometry.

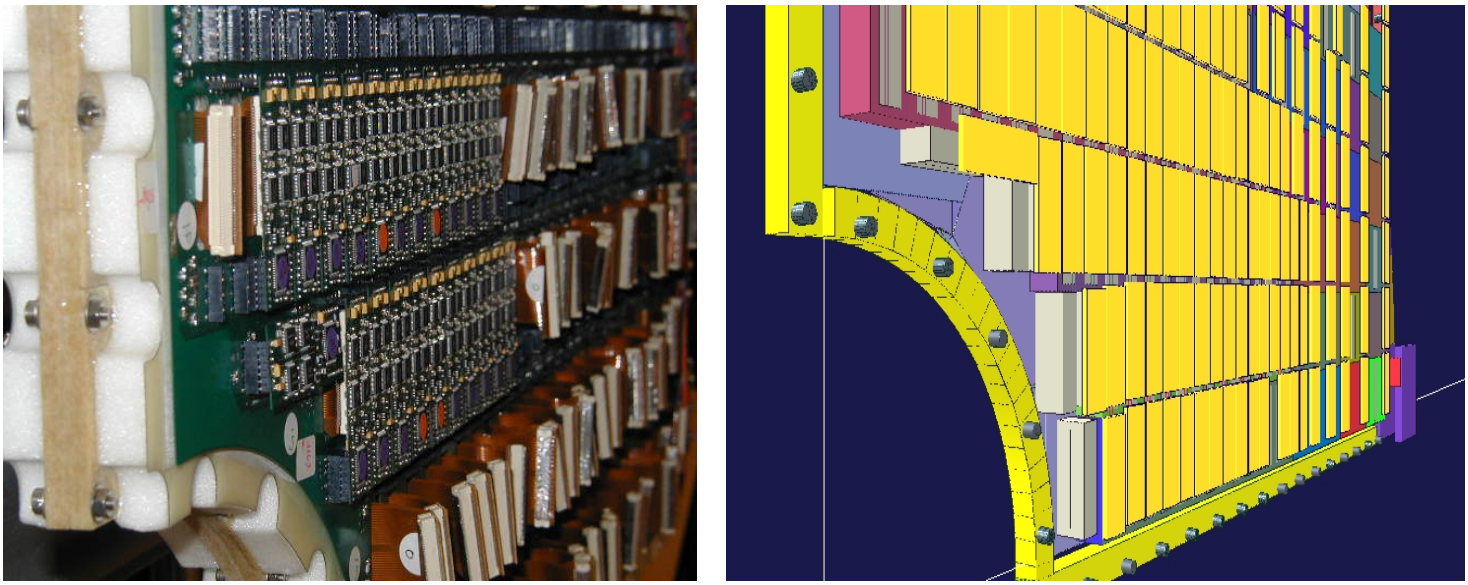

Figure 95 : On the LHS, photograph of the inner arch of QUADRANT0, and on the RHS the equivalent simulated object.

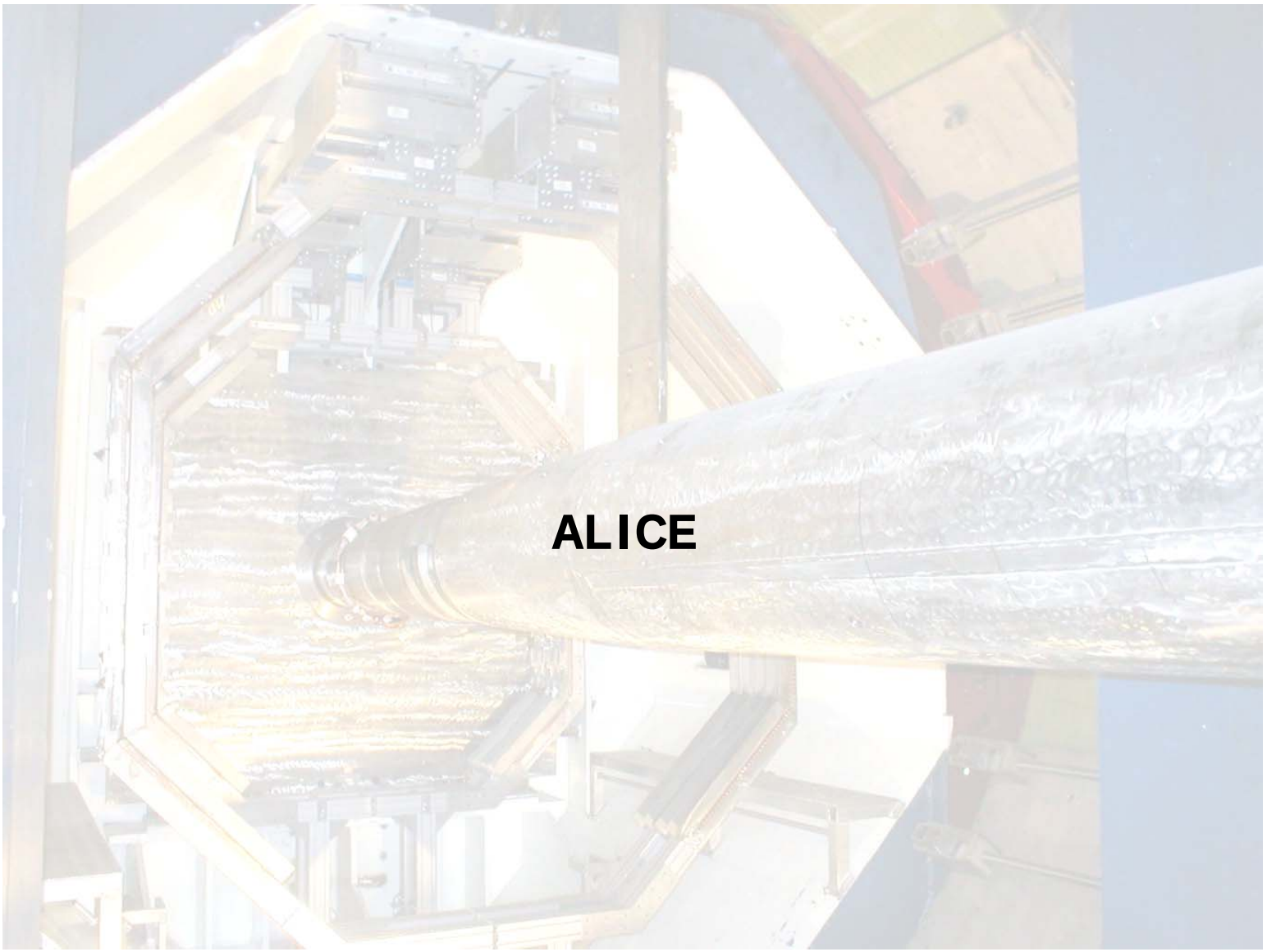
ALICE

ALICE

The construction of the final detector quadrants started in 2004 at the IPN in Orsay, following the basic design established through the years of R&D prototyping work. The quality control and testing takes place in the laboratory, and the full set of detectors, comprised of nine quadrants in all, is near completion (at the time of writing). A few photographs of the assembly and final product are shown in the following.

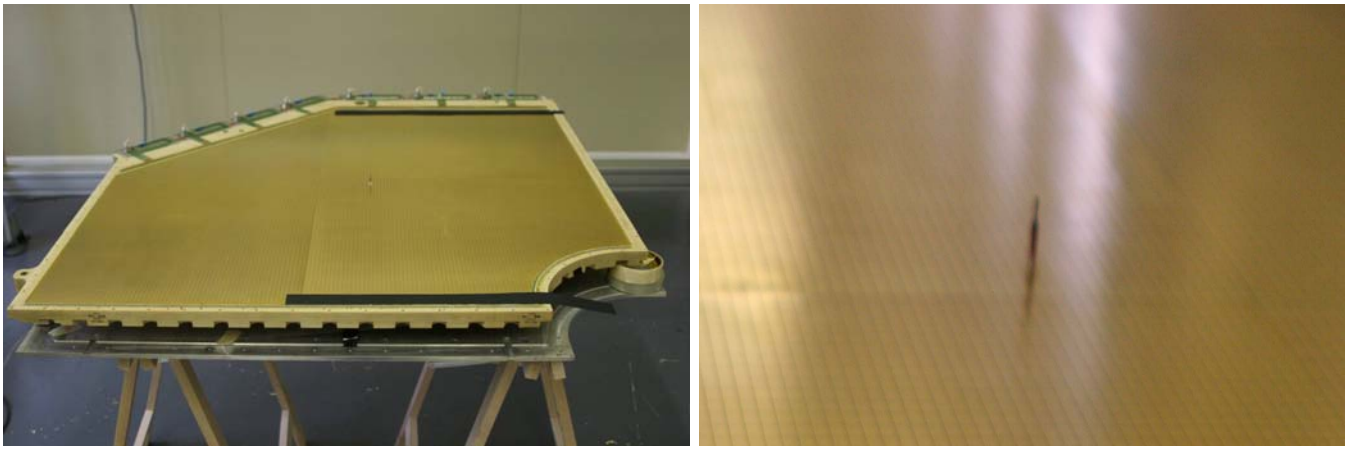

Figure 96 : The LHS shows a general view of the sensitive copper surface of one cathode plane. There is a central spacer which is used to ensure the cathode separation is as desired. A close up of this (difficult to see) spacer is shown on the RHS template.

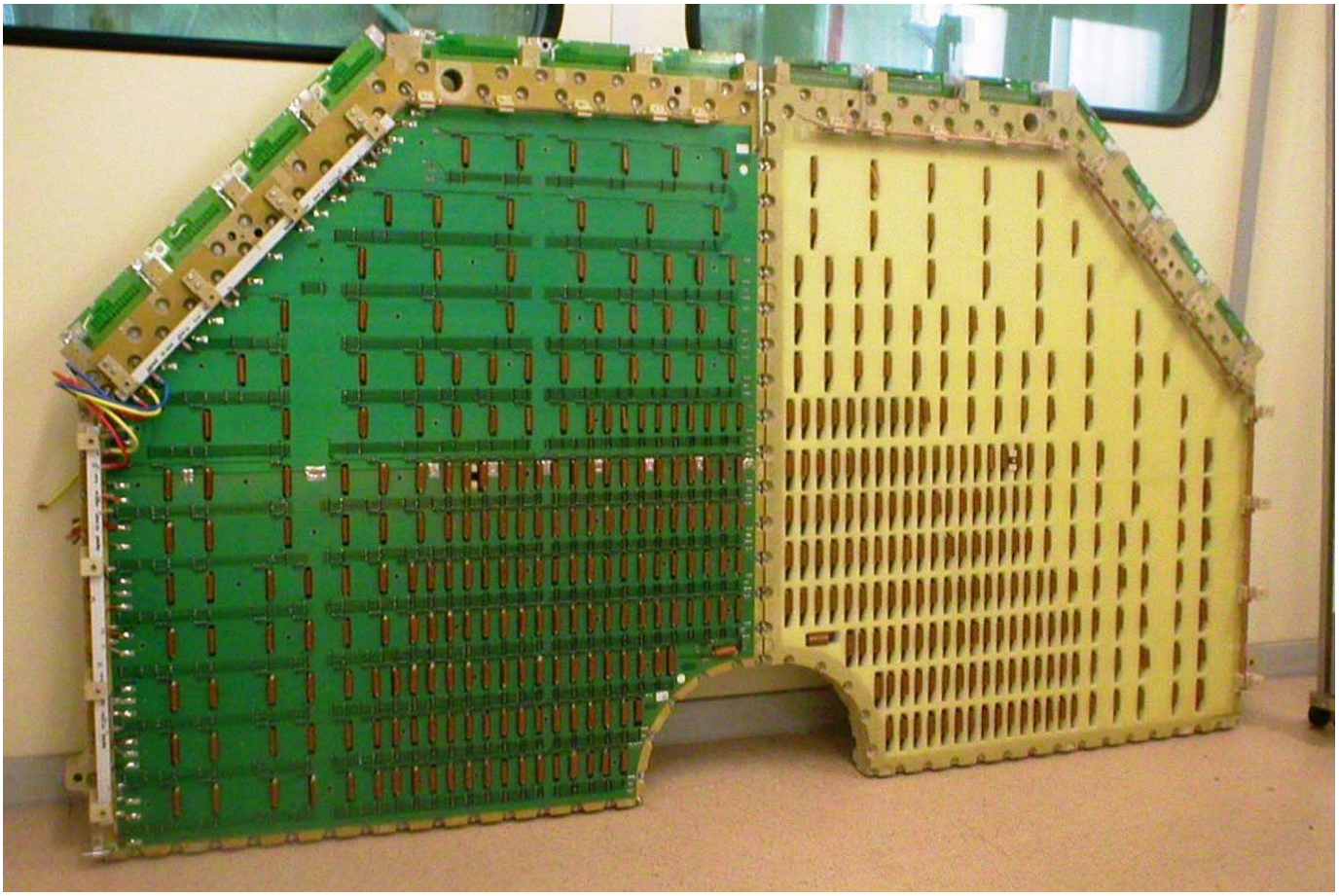

Figure 97 : Two quadrants, with (LHS) and without (RHS), the electronics motherboard.

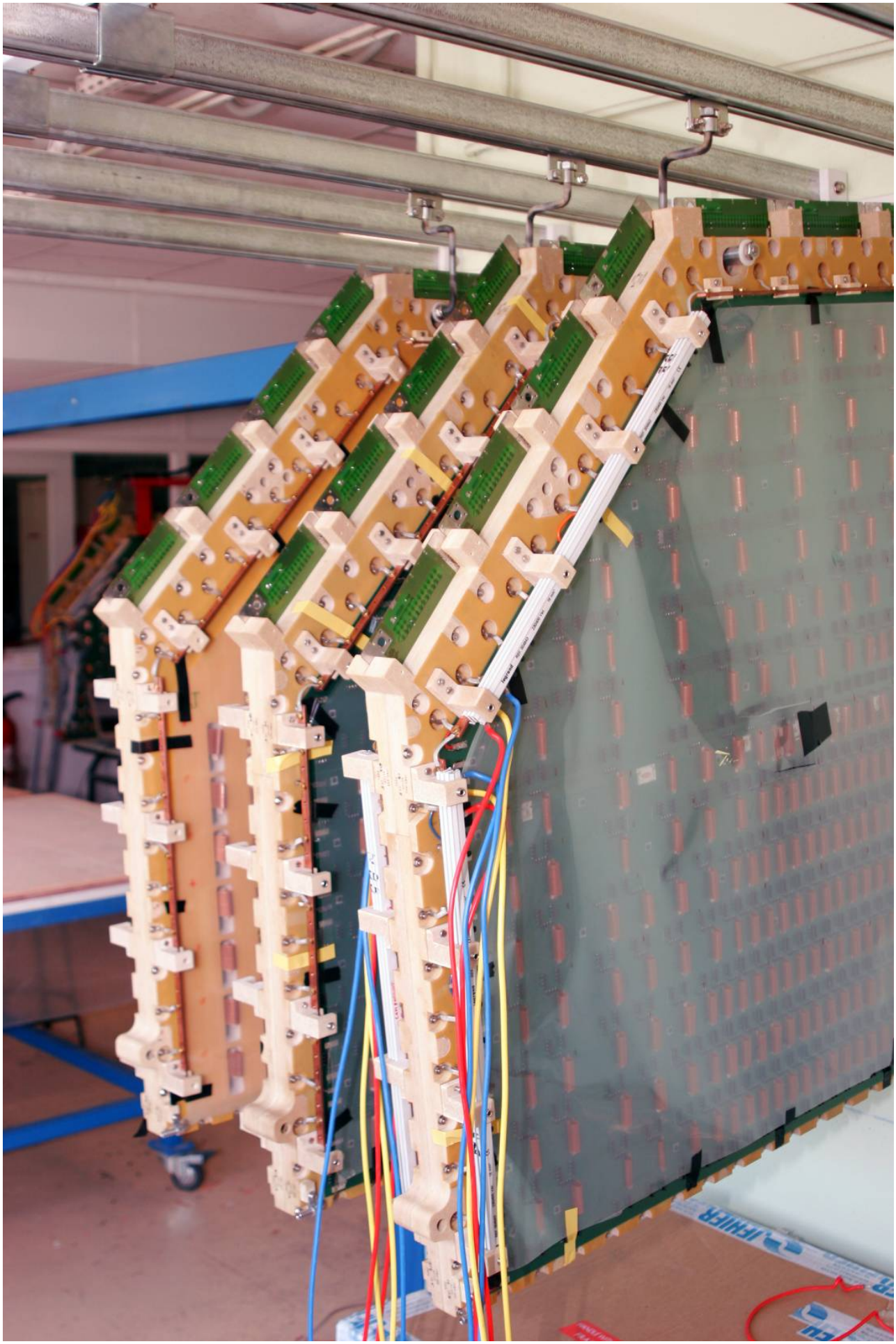

Figure 98 : Three quadrants, fresh off the press, patiently await quality control.

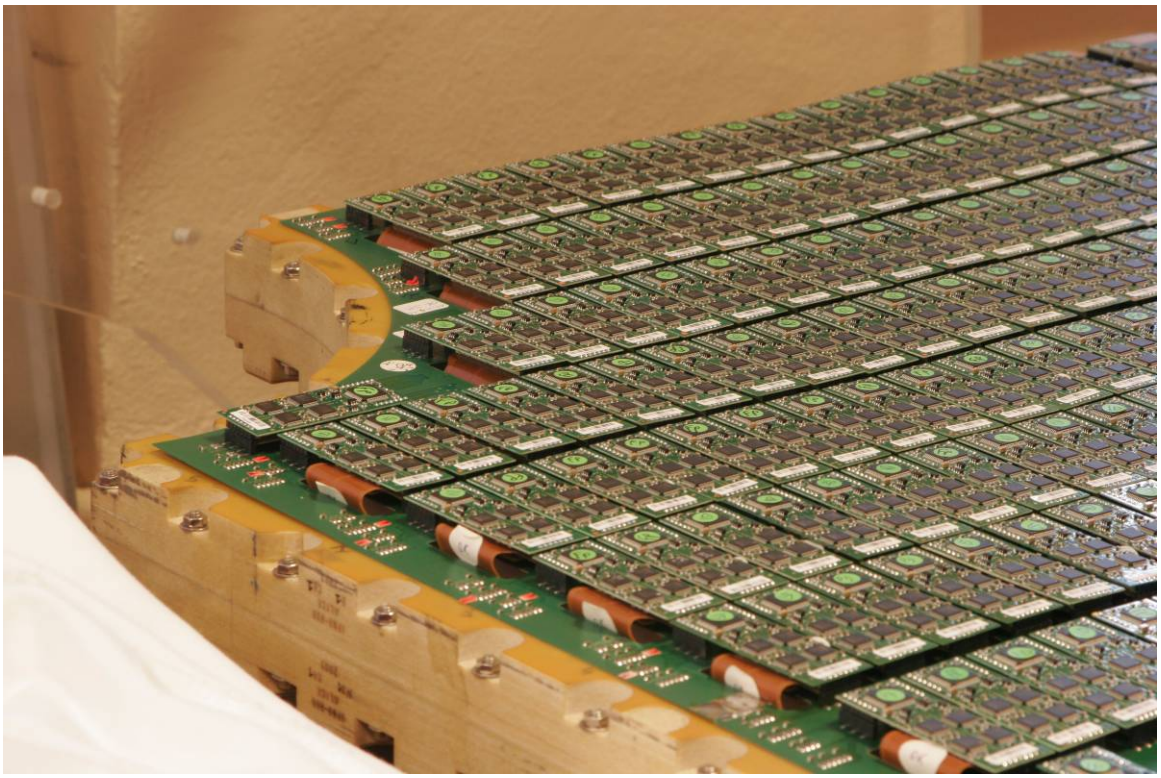

Figure 99 : A close up of the densely populated inner arc that will be next to the beam pipe. Around 80x64 readout channels are visible in this image.

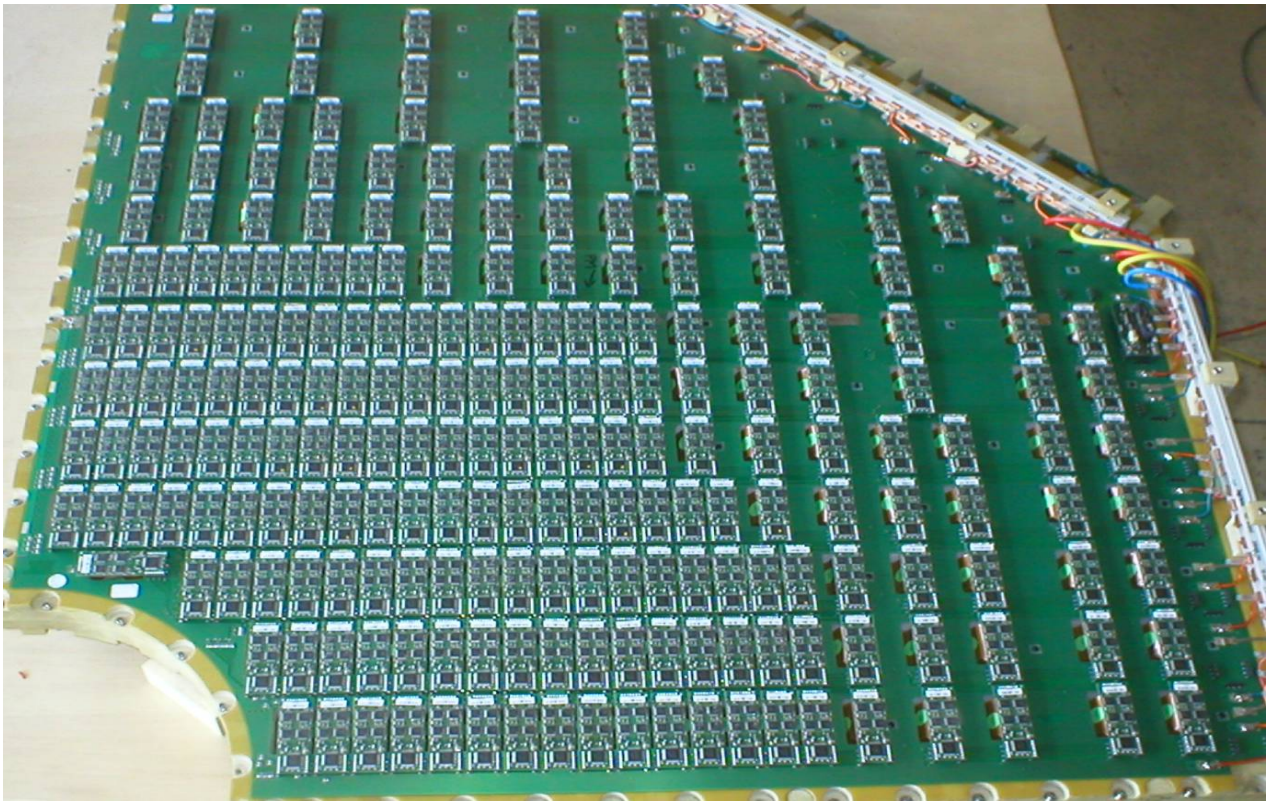

Figure 100 : General view of the final detector with the all electronics cards in place.

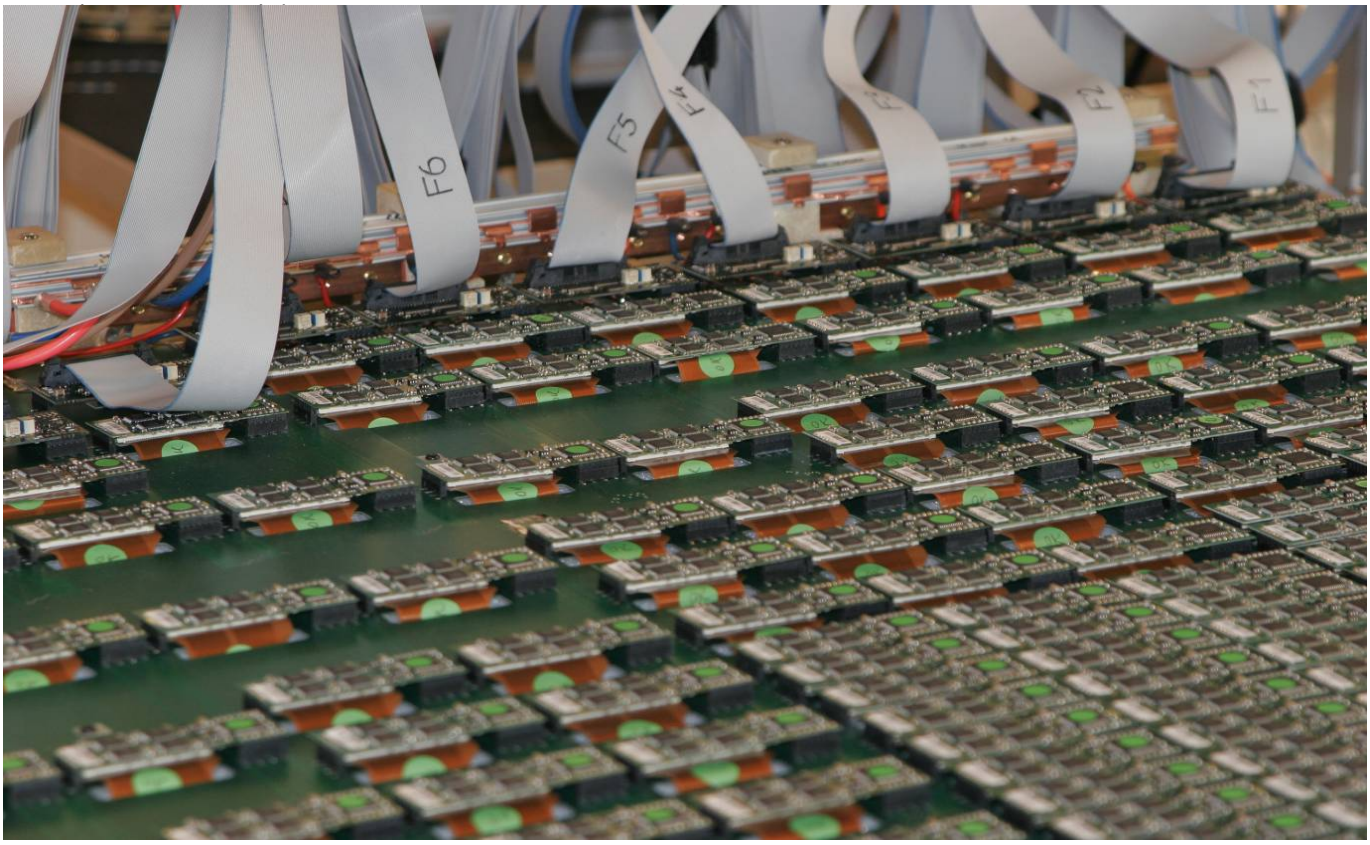

Figure 101 : The in/out control signals and data stream transit via flat cables.

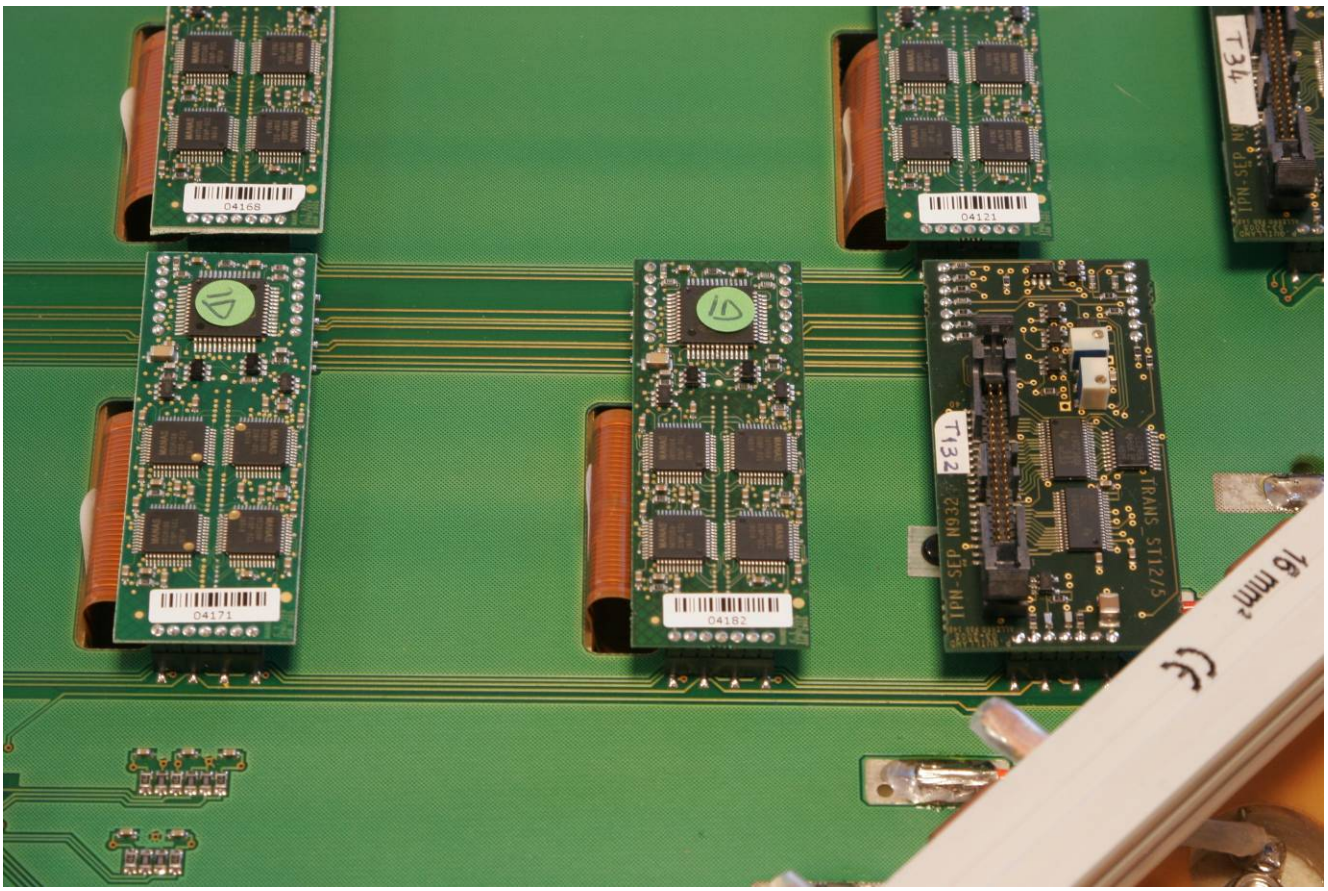

Figure 102 : Each row of electronics cards is connected to a local translator card (rightmost card on each row), that adapts the MANAS LVTTL signal levels to LVDS (Low Voltage differential Signals) suitable for the CROCUS board inputs.

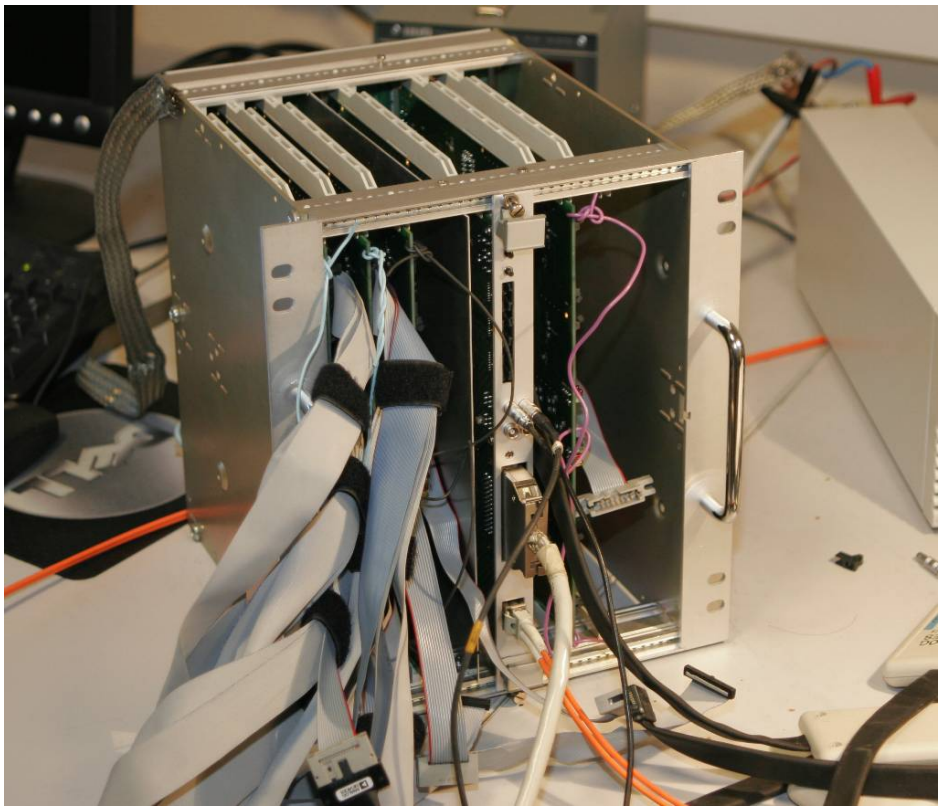

Figure 103 : A photograph of one of the 20 dimuon arm readout crates. This crate deals with the readout and transmission of one half chamber of station 1, totalling nearly 60,000 individual channels. The crate measures approximately 19 cm in width and 25 cm in height, and contains 5 CROCUS cards and 1 concentrator card.

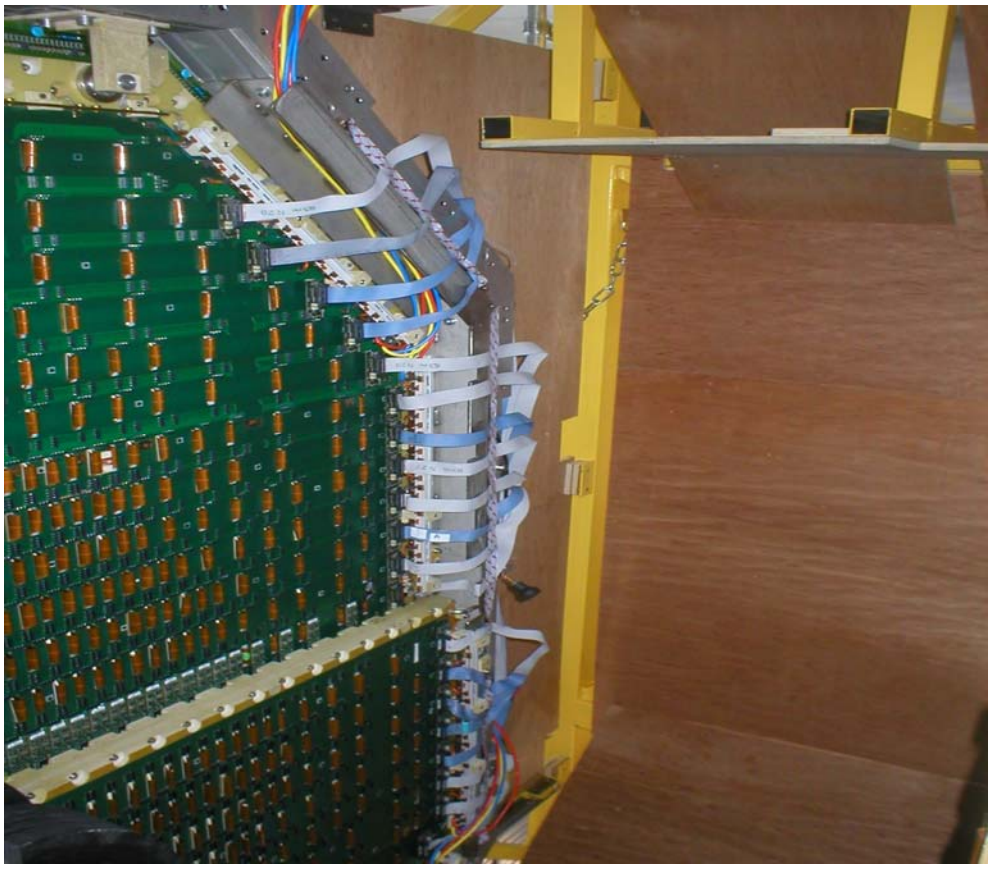

Figure 104 : A Test setup, with two quadrants, showing the strategy for positioning the readout cables (flat blue cables on the detectors' edge).

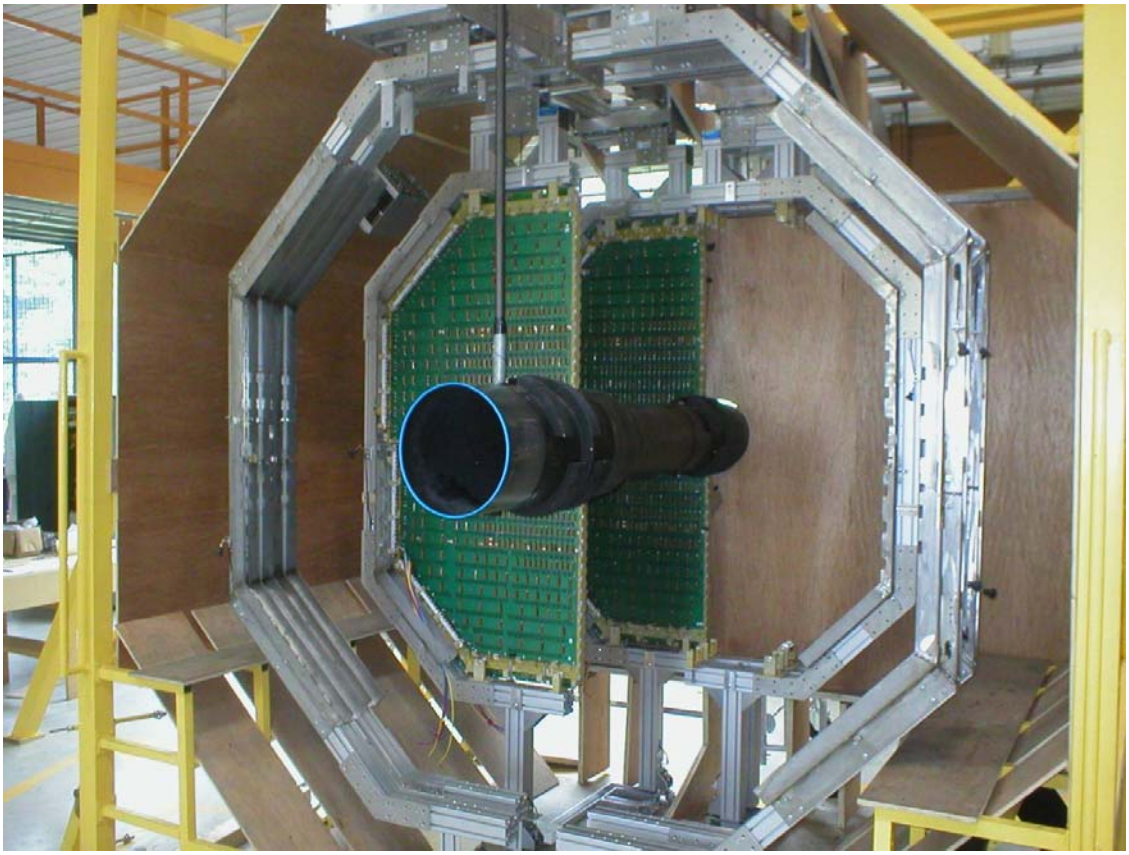

Figure 105 : A test setup, with the real detector quadrants and supports, a true to scale plastic beam-pipe and wooden front absorber support. One half of the two station 1 tracker chambers are in place.

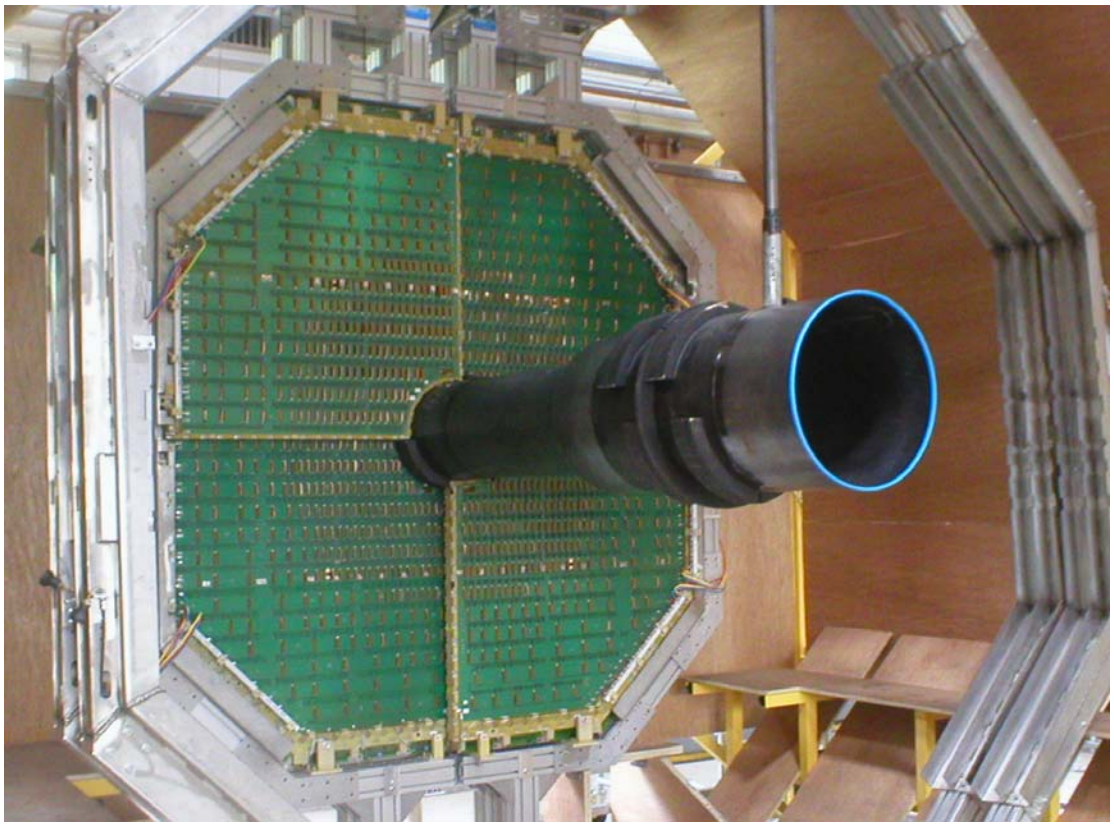

Figure 106 : The test setup showing the mechanical positioning for the whole of station 1.

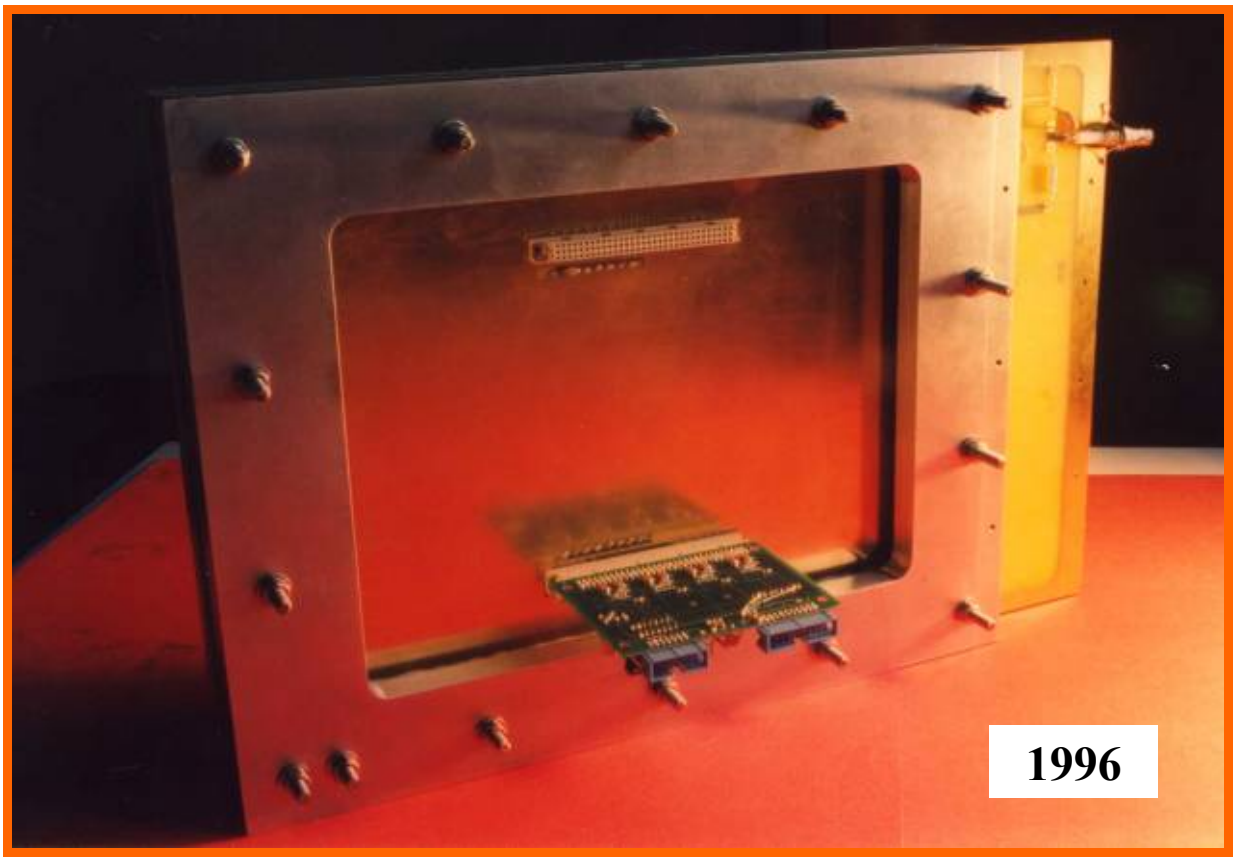
1996

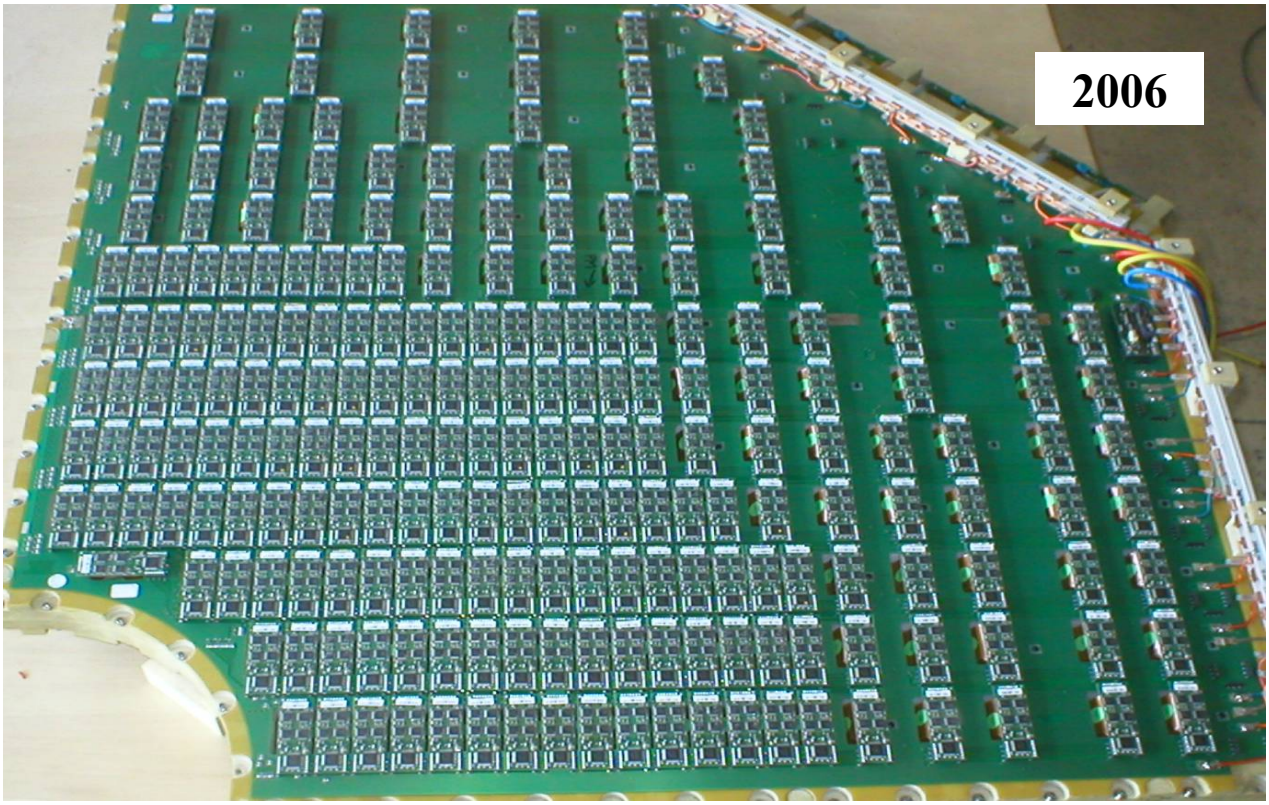
2006

Closing comments

The installation of station 1 in the ALICE cavern will start in 2007, as will the first LHC beams. All that will then remain is to get on with the physics.

I truly enjoyed putting this document together, and thank my colleagues in hadronic physics for their patience, since it has meant I have paid less attention to current projects whilst writing this manuscript.

I would like to thank the people who helped out in providing old and new images and information. There was a certain amount of detective work that had to be done and I appreciate the time accorded to me by my colleagues. In alphabetical order, particular thanks to Christine Le Galliard, Bernard Genolini, Yves Le Bornec, Jean-Pierre Le Normand, Jean Peyré, Luc Petizon, Emmanuel Rindel, Jean-Phillipe Rivenez, Sylvain Rousseau and, Nicole Willis.

Marion MacCormick

IPN, Orsay

10 January 2007

APPENDIX A

Ionization detectors – a brief history

The original widely used ionization detector dates back to the early 1900s. The ***cloud chamber*** was invented by CTR. Wilson in 1911 and earned him the Nobel Prize along with A.H. Compton, in 1927. It consisted of a closed container filled with a supersaturated vapour, for example, water in air. A traversing charged particle ionizes the gas, leaving a trail of ions that serve as condensation centers for the vapour. The path of the incident particle is thus indicated by the track of tiny droplets in the supersaturated vapour. The expansion cloud chamber and diffusion drift chamber were developed from this original idea. The major drawback of this technology is the relatively low density of the gas, which limits the number of primary ionizations, and is reflected by a low detector efficiency.

By 1952, D. Glaser had invented the ***bubble chamber***, which earned him the Nobel Prize in 1960. The large scale development of this technology, adapted to accelerator experiments by L. Alvarez, earned him the Nobel Prize in 1968. The detection efficiency problem was bettered by working with higher gas densities and pressures. The device consists of a sealed chamber filled with a liquefied gas and a fast pressure release valve. The filling liquid is originally at a temperature just below its boiling point. When the pressure inside the chamber is reduced, the boiling point is lowered to a value below that of the liquid temperature, leaving the liquid superheated. When a charged particle passes through this superheated liquid it leaves a trail of tiny gas bubbles that can be illuminated and photographed. This detector was highly successful and allowed the efficient, high precision localisation of multi-particle trajectories. Its main drawback is its fairly low repetition rate and the lack of a discriminator allowing triggering on selected events. Another development that matured in the same year as Alvarz's large scale bubble chamber was the ***spark chamber***. Sparks caused by intense ionization between parallel plates had already been observed in 1949 by Keuffel, and the technology was successfully mastered by 1959 by Drs. Fukui and Miyamoto, leading to a revolution in the accelerator experiments of the 1960s. These spark chambers, although having a lower spatial resolution, allowed selective triggering and operated with a superior repetition rate, thus allowing rare event experiments to be realized efficiently for the first time. The powerful combination of the bubble chamber, and its derivatives, with the spark chamber in experimental high energy physics opened new horizons in the study of event mechanisms and particle production. A whole series of derived detectors were conceived using spark technology, such as the series of gaseous chambers: ***parallel plate avalanche counter*** (PPAC), ***single wire detector*** (which uses large diameter wires), ***narrow-*** and ***wide-gap*** detectors, or ***projection chambers*** with wire or glass electrodes which allow optical readout in the direction perpendicular to the electrodes. The ***streamer chamber***, introduced by Dolgoshein in 1964, giving a superior angular definition of the ionizing trajectory was a refinement of the spark chamber which operated at lower high voltages. So successful were these detectors that the photographic development and analysis equipment was saturated by the mid-1960s. It was clear that a greater throughput for data recording and analysis was required, and this was becoming a reality through the expanding micro-electronics industry, and the development of computer technology in high energy physics. G. Charpak produced the first multi-wire proportional counter (MWPC) in 1968, earning him the Nobel Prize in 1992. This innovative detector was able to achieve the spatial resolutions and multi-particle capability previously reserved for bubble chambers; it also easily equalled the repetition rate of the spark chambers. Its readout system was via electrodes, thus providing the much desired interface to the rapidly evolving automated data acquisition systems. It effectively replaced the bubble-spark chamber combination in a very short space of time. The technology was very successful and different geometries were found to provide a wide range of timing and spatial resolution beyond that of all the previous detectors. Today, the wheels of invention continue to turn and the micro-dot/mesh/megas which provide much more lightweight and fast-reacting detectors, but still based on the ionization process, are part of the modern tools used in high energy physics.

Gas Gain

The whole series of gaseous detectors operate using the ionization process. This process can be broken down into several steps, and depending on the particular detector model, the ions and/or electrons will be displaced in a controlled manner (by the use of electric and/or magnetic fields). The cloud and bubble chambers exploit the primary ionization giving rise to the trail of ions in the detector; spark chambers multiply the primary ionization, to create intense localized secondary ionization signals that can be detected optically. In the MWPC series the secondary signal exploited is the less intense, and more controlled, avalanche signal. Today, the understanding and controlling of the different ionization processes in modern detectors is still a full time task for some experimental physicists and engineers. Understanding the gas gain is the key to building a successful detector. Describing the gas gain is not such a simple task, since primary and secondary ionization processes are environment dependent multi-step processes, making it a complex phenomenon difficult to model.

Describing gas gain through ionization – a potted history

The following paragraphs have been adapted from the original 1941 monograph [**42**], dedicated to Prof. J.J. Townsend.

The initial pioneering research that led to understanding the signal formation in proportional counters dates from a century ago, with Townsend's pioneering research into spark discharge theory [**43**]. Around the same time that Wilson developed the first cloud chamber, Townsend described the current density ***i*** in a gap ***x*** between electrodes in the direction of the electric field due to ionization by collisions, as being:

$$i(x) = \frac{i\mathrm{e}^{\alpha \mathrm{x}}}{1 - (\beta/\alpha)\left(\mathrm{e}^{\alpha \mathrm{d}} - 1\right)} \qquad [1]$$

where ***α*** is the first Townsend coefficient and represents the relative increase in current density per cm due to primary ionizations by collisions in the gap with an anode placed at position ***x=d*** from the cathode. The second Townsend coefficient ***β*** in the original theory denotes the efficiency of photo-electric production at the cathode due to positive ion impacts. The quantity ***α*** has been extensively studied and it varies with the ratio of field strength ***E*** to pressure ***P*** and its value depends on the nature of the gas. The reduced electric field, ***S***, is defined as being

$$S = \frac{E}{P} \qquad [2]$$

The quantity ***β*** had initially been evaluated as being a characteristic of the cathode material. However, it became clear that various mechanisms, other than positive ion impacts, give rise to secondary electrons in the avalanche process, thus leading to the demise of the second Townsend coefficient. In today's notation, the Townsend prescription for gas gain is:

$$\frac{\alpha}{P} = ae^{-b/S} \qquad [3]$$

where ***a***, ***b*** are constants.

The discovery of measurable photoelectric ionization the gas made it possible to explain the abundance of secondary electrons in the avalanche process. The exact way in which photoionization in the gas could operate to create a spark was not clear until Loeb&Meek [**44**, **45**, **46**] and Raether [**47**, **48**] independently presented their ***streamer theory*** in **1940/1941,** as applied to a parallel plate setup.

Loeb&Meek realized that accompanying the cumulative ionization produced by electrons there are ***four*** to ***ten times*** as many excited atoms and molecules. Some are excited to an energy exceeding the ionization potential of some of the atoms and molecules present, either by ionization and excitation, or in a gas mixture such as air, by the excitation of molecules of higher ionization potential, eg. N_2. These

excited atoms or molecules emit very short wavelength radiation in some 10^{-8} s. This *short UV radiation* is highly absorbed in the gas and *leads to ionization of the gas*. In fact the whole gas and the cathode as well, are subjected to a shower of photons of all energies travelling from the region of dense ionization with the velocity of light. Thus nearly instantaneously in the whole gap and from the cathode new photoelectrons are liberated which almost at once begin to ionize cumulatively.

Their formula for electron multiplication through the photoelectric effect at the cathode is given as:

$$i = io\frac{e^{ax}}{a - nQg[e^{(a-u)x} - 1]} \qquad [4]$$

where ***Q*** is the number of *photons* created per centimeter along the path of the initial electron from the cathode. ***G*** is a geometrical factor 0.5 which depends on the fraction of photons reaching the cathode. ***n*** is the fraction of photons reaching the cathode that actually succeed in liberating electrons from the cathode so they do not diffuse back. ***u*** is the absorption coefficient of the photons in the gas.

Comparing equations [1] and [4] the inspiration Loeb and Meek took from Townsend's formula is quite clear, as they acknowledged at the time in their monograph.

The limit for which the avalanche process transforms to the streamer process is gas dependent and is given by the Meek-Raether criterion as applied to a PPAC configuration:

$G = e^{\alpha d}$ where G is the gas gain and is generally attained for $\alpha d \approx$ 18-20.

The MWPC performs better than the PPAC since the charge development is limited by the anode wires, it therefore saturates first, before reaching the breakdown conditions. It's clear that the gas transparency to UV photons plays a fundamental role in the signal formation, as noted below in Rose&Korff's description of the gas gain [**49**].

Empirical Gas Gain Formulae

By 1956 several empirical description of the gas gain, dependant on the gas pressure and electric field, had been developed. The aim was to move from an abstract gas amplification theory - where it had become clear that the ionization processes were numerous and complex, rendering a full analytical description of ***α*** impossible - to a collective description based on the capacity for the detector's electric field to produce and store charge.

The average gas gain, supposing negligible recombination, negative ion formation, space charge and photo-electric effects, is written as **[23]**

$$\ln \overline{G} = \int_{r_c}^{a} \alpha \, \mathbf{d}r$$

where $\overline{\mathbf{G}}$ is the average gain between the critical radius r_c and the anode wire surface at ***a***. The average gain is therefore the exponential of the integrated value of the first Townsend coefficient. This formula, written so simply, has its roots in the physical properties of the ionization process. However, the first Townsend coefficient has to be measured for each gas medium, it also depends on two parameters ***a*** and ***b*** that also have to be established.

W. Diethorn presented his thesis in 1956 **[22]**, and proposed a "new" gas gain formula that was of a more empirical nature, but ultimately more practical to use. His work is particularly informative, as he describes the current theories of the time and puts them to test in the proportional single wire counter he developed for the measurement of ^{14}C radioactivity.

From Diethorn's perspective, the leading ideas of the time were those published by Rose&Korff in 1941 (the same year Loeb&Meek and Raether published their streamer theory).

Rose&Korff analysed the average number of ionizing collisions per unit distance as a function of the position in a proportional counter, and the spatial extent of the ionization region near the wire anode.

They proposed a formula is based on their observations of polyatomic Ar-ethane mixtures at different pressures. They suppose all secondaries are produced by electron impact, *with no photon emission in the counter gas and thus no photoelectric emission at the cathode*. This is substantiated by the idea that the energy loss of the shower electrons in a polyatomic (as opposed to monatomic) gas lose more energy to the molecules, but not enough to vibrationally or rotationally excite them, thus effectively quenching the UV photon emission seen in monoatomic gases. Their description is:

$$\ln A = 2\left[\frac{V\alpha a}{\ln(b/a)}\right]^{1/2}\left[\frac{V^{1/2}}{V_t^{1/2}} - 1\right] \qquad \text{[RK]}$$

where A is the amplification, V and V_t are applied and threshold voltages, and a and b are the anode wire radius and anode-cathode gap respectively. As Diethorn pointed out, they gave no indication as to how to establish the threshold voltage, and this was undertaken by Curran&Craggs in 1949 [**50**], and they re-wrote the formula as:

$$\ln A = 2\left[\frac{V\alpha a}{\ln(b/a)}\right]^{1/2}\left[\frac{(V\lambda_e)^{1/2}}{(V_i a \ln(b/a))^{1/2}} - 1\right] \qquad \text{[CC]}$$

where λ_e is the electron mean free path and V_i the gas ionization potential.

So we see the clear apparition of the detector's geometry, related to the gas gain. The ***ln(b/a)*** arises from the standard capacitance for a cylindrical detector geometry of gap b and wire radius a:

$$C = \frac{0.55}{\ln(b/a)}$$

The Rossi&Staub condition (1949) [**51**] states that the amplification factor must be a function of ***Pa*** where P is the gas pressure; and of ***V/ln(b/a)*** (Rossi specialized in low pressure chambers). These parameters can be directly introduced into equation [CC] by placing:

$$\lambda_e = \frac{k}{p} \text{ and } \beta = \frac{k}{V_i}, \text{ then}$$

$$\ln A = 2\left[\frac{V\alpha a}{\ln(b/a)}\right]^{1/2}\left[\left(\frac{\beta V}{Pa\ln(b/a)}\right)^{1/2} - 1\right] \qquad \text{[RK\&CC\&RS]}$$

Diethorn then rearranged the equation to introduce two constants, functions of α and β, with

$k_1 = \sqrt{\alpha}$ and $k_2 = \sqrt{\alpha\beta} = k_1\beta$, then,

$$\ln A \times \left[\frac{\ln(b/a)}{4aV}\right]^{1/2} = k_2\left[\frac{V}{Pa\ln(b/a)}\right]^{1/2} - k_1 \quad \text{[modified RK\&CC\&RS]}$$

If this equation holds for CH_4, then Diethorn expected his measurements, taken at different pressures and for two wire radii, to lie along a single straight line of gradient k_2 and offset k_1. The result, as displayed in Figure 107 show that k_1 and k_2 are not independent of P and a.

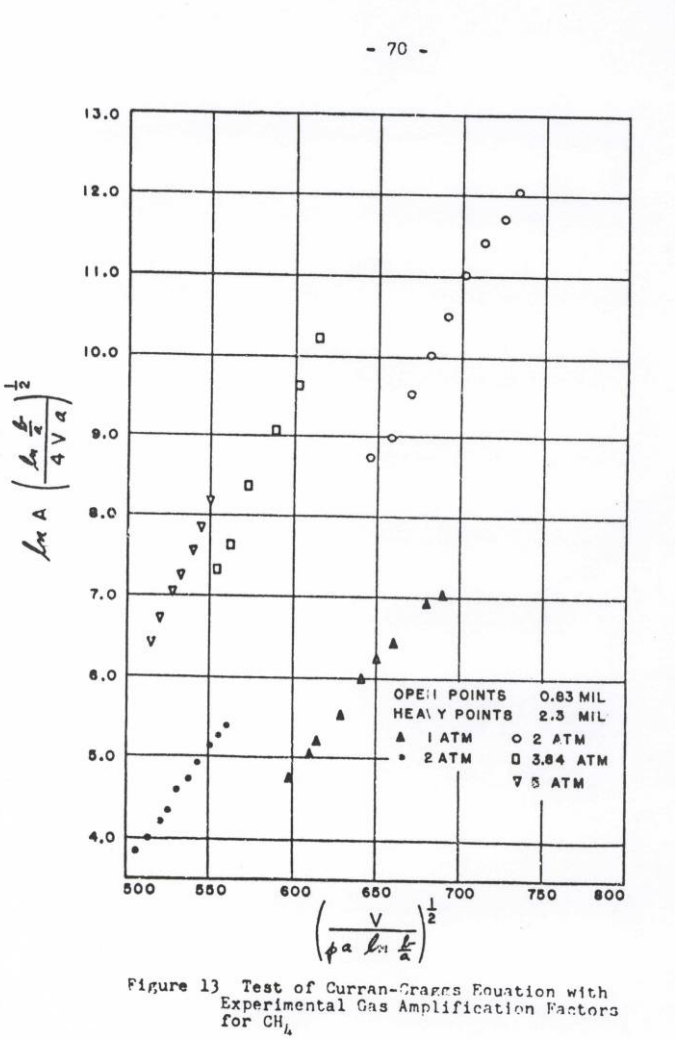

Figure 13 Test of Curran-Craggs Equation with Experimental Gas Amplification Factors for CH_4

Figure 107 : Diethorn's test of the modified Curran and Craggs equation on the CH_4 measurements.

He concluded that the modified Rose&Korff equation given by Curran&Craggs could not predict the amplification factors for CH_4.

The developed a new, simpler formula, based on two parameters. The first concerns the definition of a critical value of electric field at a certain distance from the proportional wire, at which the primary electron has gained enough energy to ionize the gas in its turn. He defines this through the critical electric field strength $\boldsymbol{E_0}$ and gas pressure $\boldsymbol{P}$ as being:

$$E_0 = \kappa P$$

where $\boldsymbol{\kappa}$ is in volts per cm per atm., and below which, no electron multiplication occurs. This in turn establishes the existence of a critical radius and critical volume around the anode wire.

He then defines, for constant pressure, the distance separating two successive ionizing events, as being dependent on the inverse of the electric field strength. This distance amounts to several times the electron mean free path and is associated with a potential drop of $\boldsymbol{\Delta V}$, constant for every successive ionizing event, and as such, is independent of $\boldsymbol{E}$ and $\boldsymbol{P}$ and is therefore a constant characteristic of the gas. an electron entering the critical ionizing volume directly produces

$$n = \frac{V_0}{\Delta V}$$

ionizing events.

His final equation is of the form:

$$\ln A = \frac{\ln 2}{\Delta V \ln(b/a)} V \ln\left[\frac{V}{\kappa P a \ln(b/a)}\right] \qquad \text{[WD]}$$

From this equation he deduced the values of the two constants ΔV and κ and used them to predict the gas amplification as a function of HV for different pressures, and also the HV required to obtain a given amplification factor at different gas pressures. His predictions were seen to be in good agreement with his measurements on CH_4 as shown in Figure 108.

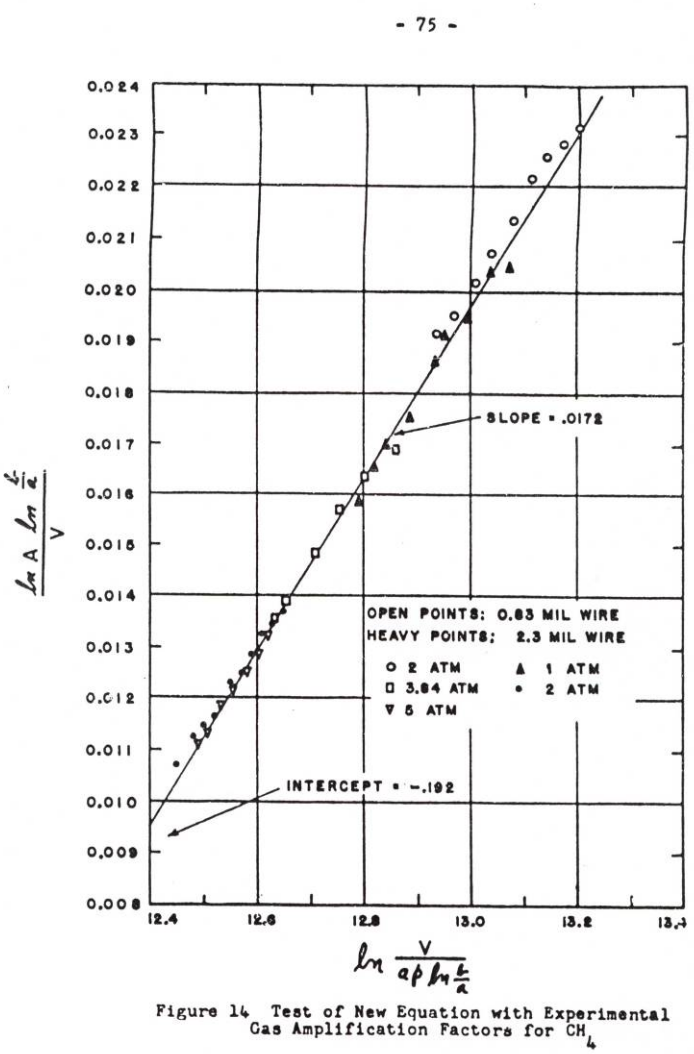

Figure 14 Test of New Equation with Experimental Gas Amplification Factors for CH_4

Figure 108 : Diethorn's "new" 2-parameter empirical gas gain formula for CH_4. The parameters depend on the nature of the gas, and are independent of the detector geometry and gas pressure.

So, moving through the century, the gas amplification factor varied form the original Townsend form where:

$\frac{\alpha}{p} = ae^{-b/S}$ where S is the reduced field strength in $Vcm^{-1}torr^{-1}$ [early 1900s]

to the Curran&Craggs modified Rose&Korff form where:

$\frac{\alpha}{p}$ is a function of $S^{1/2}$ [1949]

to the Diethorn form where:

$\frac{\alpha}{p}$ is a function of S [1956]

These forms were all evaluated with the SWPC but they hold true for the MWPC too.

By 1966, Zastawny [**24**] had proposed a new formula based on his CO_2 filled proportional counter measurements taken at different pressures. He added an extra term that described the non-linear behaviour of α/p as it tends to zero. In 1971, Charles wrote a very clear summary of, the then, five different gas gain formulae and proposed a sixth one. This situation has continued to evolve, the most recent refereed paper being from 1999 [**52**] where a tenth formula is proposed, and without going into any details, the proposed form is now:

$$A_{10} S \exp\left[-\left(\frac{S_0}{S} \right)^{1+m} \right]$$

where A_{10}, m, and S_0 are gas dependent constants. The authors give a review of the different approaches taken over the century and defend their approach as being a semi-microscopic derivation of gas gain formula. They point out - the well noticed fact - that the Townsend description only gives correct results if α/P are applied over a restricted E/P range - implying that α is not a "true" gas constant - and that further work is required to come to a better gas gain description.

Today (2006) there are still new publications that each claims the definitive, general overall formula for gas gain over the whole proportional plateau [**53**], and the attention has now turned to the saturated regime, where the more recent developments have been exploiting the new family of micro-gap detectors.

It's worth pointing out that the different empirical forms are generally accurate enough to allow the gas gain variations to be evaluated as a function of changing detector geometry, operating pressure or operating HV and the experimental trouble is more often related to polluants in the detector that can radically change the expected detector performance.

APPENDIX B - TestBeamToolBox.pdf

IPN Orsay
91406 ORSAY Cedex
France

ALICE Refrence Number
ALICE-INT-2001-45 version 1.0
Institute reference number
[-]
date of last change
20th December 2001

TestBeam ToolBox - TB2
A set of tools for online and offline analysis of test beam data

D. Guez and M. MacCormick,
M.P. Comets, B. Espagnon, Y. Le Bornec, T. Sinha, N. Willis
IPN Orsay, 91406 ORSAY, France

Abstract

A general use test beam monitoring program has been developed. It was successfully used at the CERN PS facility during recent in-beam detector prototype testing. This software is based on ROOT and consists of a user friendly graphical interface and a set of analysis libraries. The program architecture is described in this paper and is sufficiently generic and modular to allow multi-use developments. The analysis libraries can be extended to treat offline problems, and the graphical user interface (GUI) can also be applied to datasets other than test beam data.

(11th December 2001)

1 Introduction

During the course of the ALICE dimuon arm R&D project several detector prototypes have been constructed and tested in-beam. For each of these tests, specific software is required for the online and offline analysis and, until recently, this code has been written in FORTRAN with the user providing only their detector specific algorithms. However, the ALICE policy of C++/ROOT[1] programming has meant that the FORTRAN code developments, which are generally quicker for the average physicist to write, are difficult to integrate into the ALICE software environment, AliROOT (see http://alisoft.cern.ch/offline for more information). The TestBeam ToolBox was developed in order to provide a more efficient environment for developing code for the ongoing test beam activities. Particular attention was paid to the program structure so that algorithms developed for specific detectors can potentially be re-used within the AliROOT framework.

The most general description of the TB2 software is that it is a library of generic modules with pre-defined virtual interfaces. All actions to be done by the code (eg. read data, decode, analyse, view results, apply thresholds, etc.) are encapsulated within these modules. The libraries can be loaded either in an interactive ROOT session and/or through the graphical user interface (GUI). The GUI is built entirely from ROOT classes and is a by-product that can be applied independently to any dataset type other than DATE (the standard ALICE acquisition software)[2]. The code is highly modular and analyses can be constructed by simply invoking any chosen analysis block through the list available in the GUI.

The main novelty is that the online monitoring program for different test beam setups, using different detector types and electronics modules, can be built from the basic blocks provided with the TB2 software. It suffices to create the code that describes only the new experimental aspects and to add these new modules in the generic library of programs. The idea is not new, but the software is, and has been successfully used in conjunction with DATE in recent beam tests at the CERN PS facility.

In the following, after the user requirements a breakdown of the TB2 architecture is given and each of the independent modules will be described in detail. Further details, with a short example showing how to use the code for a particular test beam setup along with an outline of how to add a specific detector and/or analysis classes is given. Further information can be found in the README files that accompany the package distribution, available via the AliRoot CVS server, in the TestBeam directory. A copy can be obtained by typing the command "cvs -d :pserver:cvs@alisoft.cern.ch:/soft/cvsroot checkout TestBeam".

2 User requirements

The software was developed with the following configuration:

- ROOT v3.01/xx
- Linux OS RedHat 6.2
- gcc version egcs-2.91.66
- DATEv.3.7 if the user wants to translate DATE datasets

Other platforms where ROOT **and/or** DATEv.3.7 can be compiled should also work but have not been tested.

The TB2 code available via the AliROOT CVS server in the TestBeam directory is written for real datasets recorded with the ALICE data acquisition DATEv.3.7. Modules are provided describing two different experimental setups encountered during the development of TB2. A pre-built data file is also provided in the data subdirectory of the

distribution, and can be used to test the GUI analysis program. A generic program that allows to create objects from any data source is present and is called the "objectifier". This will be described in more detail in paragraph 3.1. If the standard DATE v3.7 is already installed on the system then the Date2Root program can be used to provide an "objectified" ROOT data file. This program is simply a small script which runs the objectifier program with modules specific to the DATE data source.

3 Architecture overview

In this particular context we consider that an "experiment" is composed of various shared libraries (electronics description, analysis algorithms, data access methods, etc.) split into independent modules that contain C++ class definitions. The main feature of the TB2 software is that generic, standard interfaces provide easy access methods to the specific classes. There are 4 main groups of classes and the communication between them is defined by purely virtual C++ object methods (functions). Writing a valid module then simply consists of writing a particular implementation of these functions (ie. writing a particular subclass of the predefined basic classes). The 4 groups of classes defined by TB2 are as follows:

1. **Objectification** - Classes that implement methods to create "objectified" data. This requires knowledge of the acquisition data structures on the input side and the TB2 tree structure on the output side.
2. **Electronics** - Classes describing the front-end electronics modules and how to decode them. The objectified raw data structure is principally made of a list of electronics modules which are filled event by event during the objectification procedure.
3. **Detectors** - Classes describing a detector. In this context a detector is described as an object that regroups specific electronics modules, mappings, threshold levels and auxilliary files such as calibration files, other special input files, etc..
4. **Analysis and graphical viewing** - Classes describing the analysis code and the way the results are presented (ie. graphical views and/or ASCII outputs).

The schema in figure 1 shows the flow of data throught these 4 groups of objects, going from the raw data stream to the analysis.

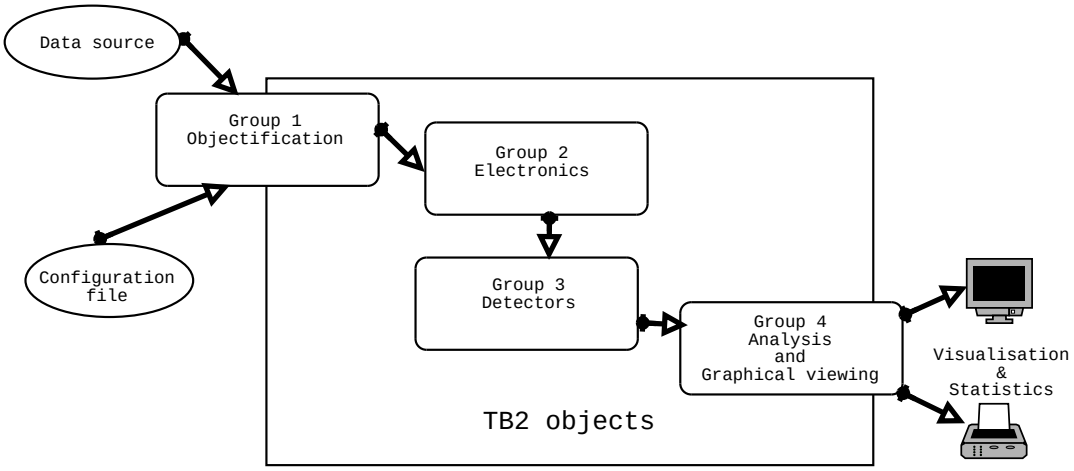

Figure 1: Data flow

Each of the major class groups will be looked at in more detail in the following. To highlight the different aspects, **bold face** characters are used for class names and associated methods or functions are written in THIS TYPEFACE. The overall class architecture is described in UML diagrams that can be found in appendix A.

3.1 Objectification

There are two main parts to the objectification procedure, namely:

1. Getting information about the experimental setup, in order to allocate the structures which will contain the data (eg. how to interpret the ASCII configuration files to learn how many electronics modules are present in a given experiment).
2. Accessing the external program which will be used to get the data themselves (eg. how to use DATE's event reader methods to interpret the data contents).

Creation of the objectified raw data object - TBDigitData

The objectified raw data object, named **TBDigitData**, is constructed from external information. In the specific case of DATE files, this corresponds to the information stored in the ASCII configuration file (usually found in SORfiles/config.dat) which contains the user defined description of the experiment.

The **TBDigitData** is instanciated by the **TBDigitDataProducer** base class, which defines the common behaviour of these objects via the purely virtual function PRODUCE(). This function must be implemented by any valid derived class. For example, the **AcqProducer** class is a particular derived class which implements this function for reading and decoding the configuration file defined for the test beam.

Connecting to the external data source

The classes used in this procedure define the method that establishes the link between TB2 and an external data source. For this purpose a generic **TBObjectifier** class is defined, which has two purely virtual functions named CONNECTTO() and OBJECTIFYNEXTEVENT().

For example, in order to retrieve DATE data a specific derived class must be provided that interfaces to the DATE external libraries. The four DATE specific routines used during objectification: monitorSetDataSource(); monitorGetEventDynamic(); monitorDecodeError() and monitorSetNowait() can then be run via this interface.

3.2 Electronics and ASCII file objects

The data are organised in a **TBDigitData** object, which is principally a standard ROOT **TTree** object. In addition to the **TTree** capabilities, it contains a set of electronic modules, each of them responsible for creating and filling a set of data branches. Each electronics module inherits from the **TBElecModule** class, which defines the purely virtual function ADDDATA() called at the objectification time, for filling the data tree with the value sent by the data source. For example, **TBCRAMSModule** is a particular **TBElecModule** derived class, which creates and fills the data tree with the branches necessary to describe a CRAMS module (the CRAMS is a multiplexed ADC, so these branches contain a list of digitized values for each of the clock pulses).

The **TBDigitData** also have a place reserved for the storage of all the ASCII files associated with the experiment, so that all the information about the data, and the associated files (DATE SORfiles for example) are accessible via the same object. This avoids the risk of inconsistancy which can easily arise if data from a given run are analysed

with the configuration files of another run (in particular it avoids possible confusion with the run dependent pedestal files).

3.3 Detector representation classes

The **TBDigitData** object contains the data and provides access to their content via a direct interface. For this reason, the "language" used by this interface is related to the frontend electronics elements. A higher level interface can be built on top of it, in order to give an access to the detector elements.

This kind of interface is provided by the **TBDetector** object, which takes a **TBDigitData** object as input, and gives access to the data contained within, but in a language centered on the detector elements.

With TB2, a detector consists of a set of general information (**TBInformation**) which is accessible by the GetInformation() method. An example of such a detector is given by the Cathode Pad Chamber detector. This detector is defined in TB2 by a particular subclass of **TBDetector,** named **CPCPlane**, which exports the generic information related to it. Parameters that are always associated with this type of detector are, for example, the charge measured or the pad coordinate system used, etc.. The mechanism for transmitting this general information is done through the **CPCPlane** class, namely, RawToCoord() and CoordToRaw(). These functions translate (in both directions) the "position" in terms of detector elements (pixels or pads) and the equivalent channel number on the electronics modules. This translation requires a pre-defined auxilliary "mapping file" which describes where each electronics module is plugged on the detector, and how the correspondance between each detector element and electronics channel is made. This conversion (or electronics mapping) can be different for each detector, so the information to export depends on the detector structure, it is the user who decides how the method should be implemented.

This approach means that all information available for electronic modules in the electronics classes, are also accessible from the detector classes. Classes for the description of other detectors can be built by following this model.

3.4 Analysis and graphical viewing classes

The last group of classes is related to the analysis algorithms and the graphical representation of their results. The analysis algorithms are grouped into objects that are subclasses of the **TBAnalysisBranch** base class, and which define the purely virtual function UseData(). This function is called for each event analysed, and updates the computed analysis value with the event data.

In the same way, the **TBVisuModule** class is the base class for all graphical representations, and also defines a UseData() function which must be overridden to update the graphical view (eg. a histogram) with the current event data.

Each of these objects can be associated with a list of **TBProperty**. A **TBProperty** is an object attached to a standard C++ variable, graphically editable by the user, via the **TBGPropertyEditor** graphical object (which is a subclass of the ROOT **TGWidget**). This facility allows the graphical views and analysis branches to be associated with parameters, such as selection criteria, that can be applied during the analysis. Since the code is encapsulated in classes, one can instantiate the same object many times, and apply different parameters (in the form of selection criteria) to each of these instances. As a result, the user will be able to obtain, in a single pass analysis, the effect of the modification of a given parameter on the analysis results. Figure 2 shows a sample image

where different selection criteria are simultaneously applied to separate instances of the same object.

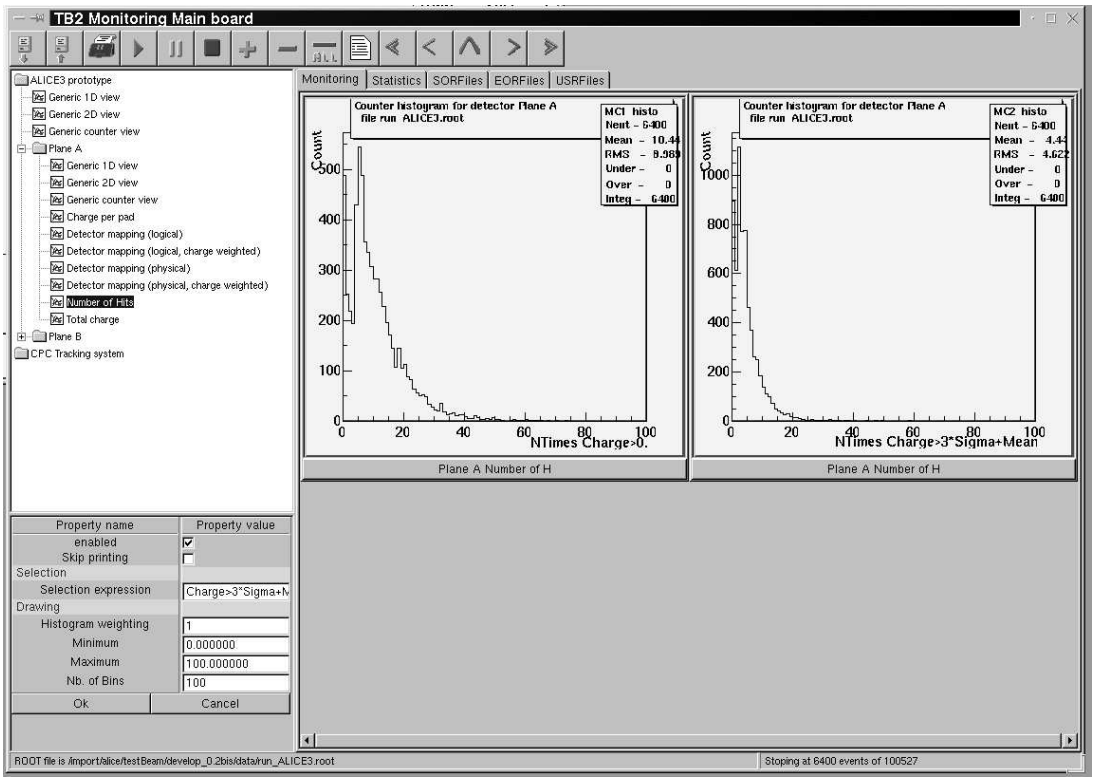

Figure 2: Effect of applying different selection parameters. The criteria applied to the right hand image can be read in the lower left hand property list. The selection criteria appear automatically on the x-axis of these 1D histograms.

Some graphical views are defined for the visualisation of histograms associated with the electronics and detectors. All these objects are related to real objects, so the access methods imitate the way we organise them in real life. This behaviour is simulated through a folder and sub-folder management system. The folder level consists of a valid class derived from the **TBVisuManager** base class, which defines only the pure virtual function MakeAnalyser(). This function must be overridden and return a **TBAnalyser,** which is a subclass of the standard ROOT **TFolder**, *plus* a list of properties. This folder can be filled with any number of sub-folders and **TBModuleProducer**. This last class is an object attached to a **TBVisuModule** class and will result in an icon that the user will select to instantiate the **TBVisuModule** attached to it.

A **TBAnalyser** also defines the UseData() function, which can be overridden to use event data for computing statistics about the entire run. Once the statistics are available, the MakeStats() function can be overridden to generate a string containing the result of any numerical calculations.

4 Programs that use TB2 classes

4.1 The "objectifier" program

This program searches for an available **TBDigitDataProducer** subclass for creating a new **TBDigitData** instance. In order to fill this instance with data, the program looks for a valid **TBObjectifier** subclass, and calls its ObjectifyNextEvent() method for all events in the run. The important point to note is that this program is unusable alone, since it does not provide any valid **TBDigitDataProducer** or **TBObjectifier** derived classes. For users working with data formats other than DATEv.3.7 the appropriate subclass would need to be written. The user can load their library modules with the "-l" option of the objectify program (more details are given by the online objectifier help by typing the command "objectifier -h"). This approach means that the same objectifer program can be used with *any* **TBDigitDataProducer** or **TBObjectifier** available now and in the future, without modification, provided the objects respect the interface defined by TB2.

For example, the Date2Root program is just an alias to "objectify", with the "-l PackAcqProducer.so, DATEInterface.so" options which automatically loads the **AcqProducer** and **DATEObjectifier** valid subclasses, **TBDigitDataProducer** and **TBObjectifier** respectively.

4.2 The monitoring program

This program is a Graphical User Interface (GUI), which allows the user to easily operate the objects described in paragraph 3.4. When an analysis package is loaded the program looks for all **TBVisuManager** derived classes, it instantiates them and calls their MakeAnalyser() methods. As a result, the program obtains a list of folders (and their subfolders containing the viewer modules). These are visible on the left hand panel of the Monitoring Main board shown in figure 3. It also loads the shutters of the SORFiles (Start Of Run Files), EORFiles (End Of Run Files) and USRFiles (USer Files) with the contents of the **TBDigitData** ASCII files (this is done via the GetxxxFiles() access methods).

Any folder or module producer icon can be selected and instantiated with a double-click of the mouse (or alternatively, using the "+" icon on the upper icon bar). This action results in a call to the Produce() method of the attached **TBModuleProducer** object, and a standard ROOT **TGEmbeddedCanvas** object is created, where the **TBVisuModule** object will be drawn.

The play button or the event-by-event navigator button can then be activated to start an analysis cycle. This in turn calls the GetEntry() method of the current **TBDigitData** for the given event number. Finally, all instantiated **TBVisuModule** UseData() methods are called along with all valid **TBAnalyser** UseData() methods.

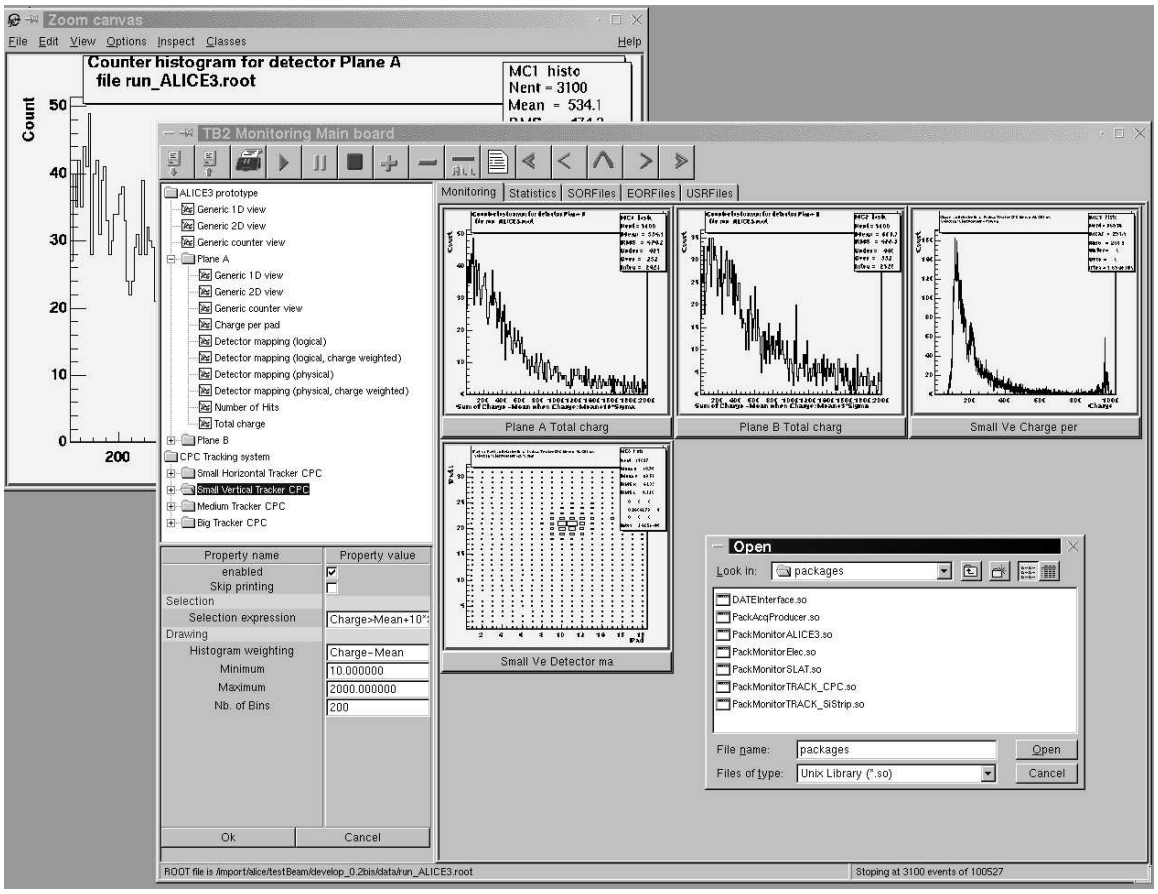

Figure 3: Screenshot of the monitoring program. The icon bar runs along the top of the Main board and loaded packages can be seen in the upper part of the left-hand panel. The dialog box for loading packages can be seen in the lower central part of the screen and was activated by double-clicking on the first icon box on the upper panel. The property list can be seen in the lower left-hand side of the Main board. Finally, the different pages (graphical monitoring, statistics, etc..) can be seen on the upper tabs in the right-hand side of the screenshot.

5 Development and testing

This program was first tested with data taken during beam tests at the CERN SPS facility in May 2000. The prototype and experiment were named "ALICE3" and the essential building blocks can be found in the two files "ALICE3CPC.cxx" and "ALICE3DetMapFile.cxx" in the source directory.

The program was subsequently tested online, at the PS in October 2001, with the new DSP (Digital Signal Processor) controlled electronics and the latest slat CSC prototype. The slat detector is a basic element of the large surface tracking stations in the dimuon arm.

There are two main differences between the May 2000 ALICE3 and October 2001 SLAT experiments. First, a new electronics module, the **TBDSPModule**, had to be added to the list of **TBElecModule** derived classes, and it naturally describes the particular DSP data structure. The second, and perhaps more interesting difference concerns the detectors in the basic experimental layout. In May 2000, large surface CPC's were used to provide a tracking telescope in a multi-particle environment, whereas in October 2001 small surface (2×2 cm^2) silicon strip detectors provided a high resolution ($\sim$13 μm) tracking system. Changing the tracking system allowed to test whether or not the TB2 code was genuinely generic. The trackers were described in the **SiStripDetector** class which is a **TBDetector** subclass, as is the **SLATDetector** class that gives the CPC slat prototype description. Once the new electronics module and the new detector classes were added, the monitoring program could easily cope with either an ALICE3 or a SLAT experiment.

The objectifier also had to be "updated" with the new DSP electronics module and a new field was added to the SORFiles/config.dat file to indicate how many of these modules were used in the experiment. The program was then able to generate the objectified data structure without any intervention in the generic part of the code.

Small libraries that regroup the different analysis packages can be created by modifying the GNUmakefile. The different packages follow the naming system PackMonitorxxx, where xxx is a self-explanatory name. This means that only the appropriate libraries need to be loaded for different experiments. (Normally, loading all the libraries will do no harm as unused parts will simply not be instantiated.) The objectified data must at least match the object descriptions, ie., if no CRAMS module is used in the experiment it would be illogical to expect an instance of the CRAMS analysis folder in the GUI left hand panel.

A more detailed account of the step by step procedure to follow for adding new classes is given in README_THIRD available with the CVS distribution. Feedback on the libraries and the help documents as well as new contributions are welcomed and can be sent to maccorm@ipno.in2p3.fr.

References

[1] F. Rademakers R. Brun,
ROOT - An Object Oriented Data Analysis Tool,
http://www.cern.ch/root.

[2] CERN ALICE DAQ Group,
ALICE DATE v.3 User's Guide,
ALICE Internal Report, 31-v2 (2000).

Appendix A

The relationships between all the TB2 classes are represented by UML diagrams in figures 5 to 8. A brief summary of the UML standard notation is given in figure 4. Class names written in *italics* are purely virtual.

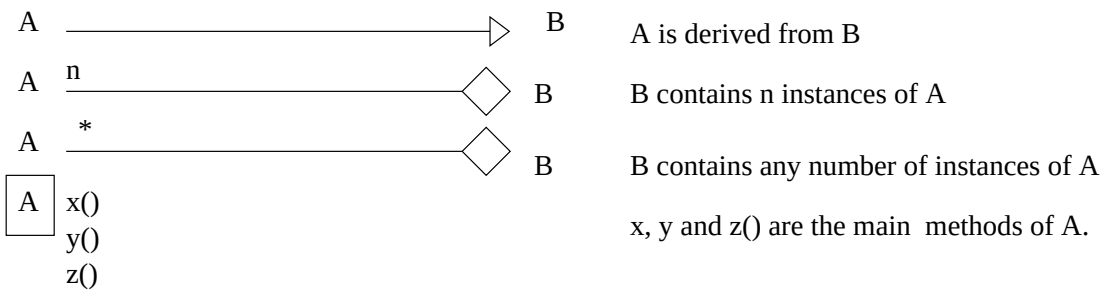

Figure 4: UML notation used to describe the class relationships.

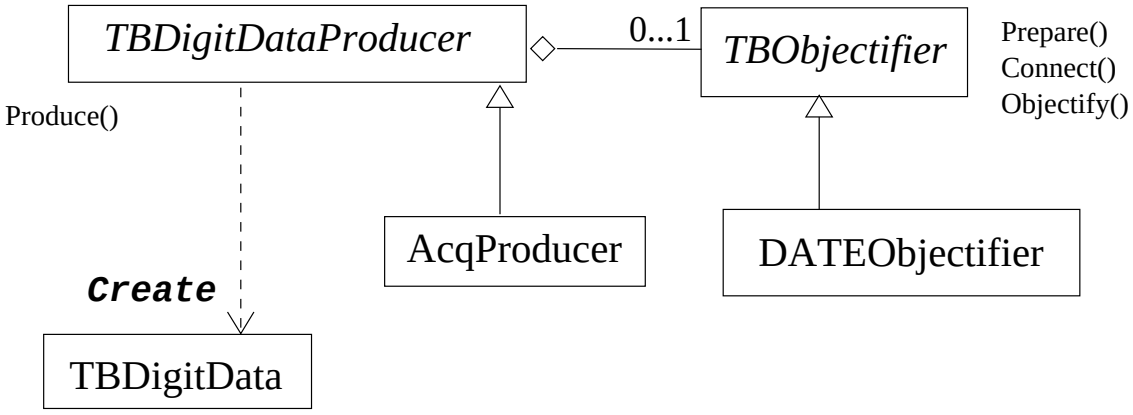

Figure 5: Objectification classes. See section 3.1 for more details.

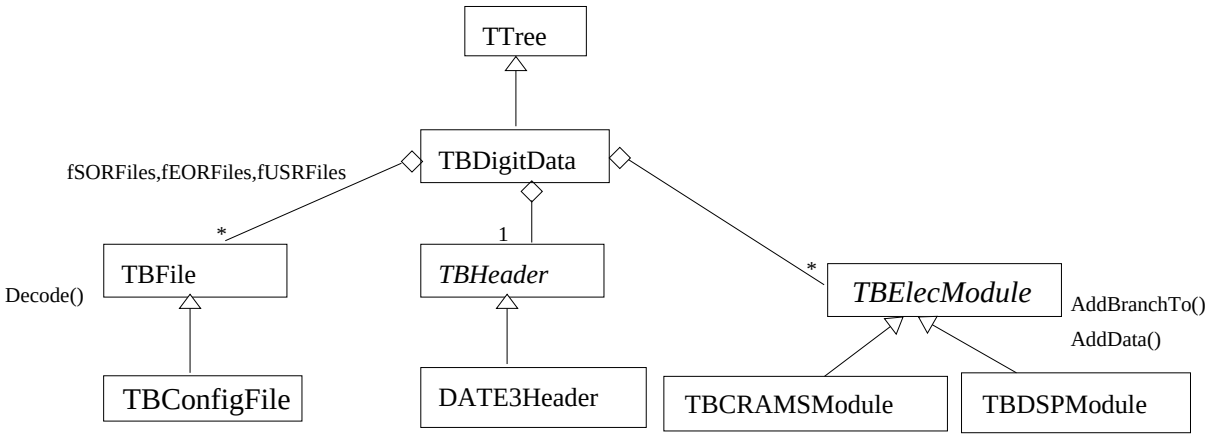

Figure 6: Electronics classes. See section 3.2 for more details.

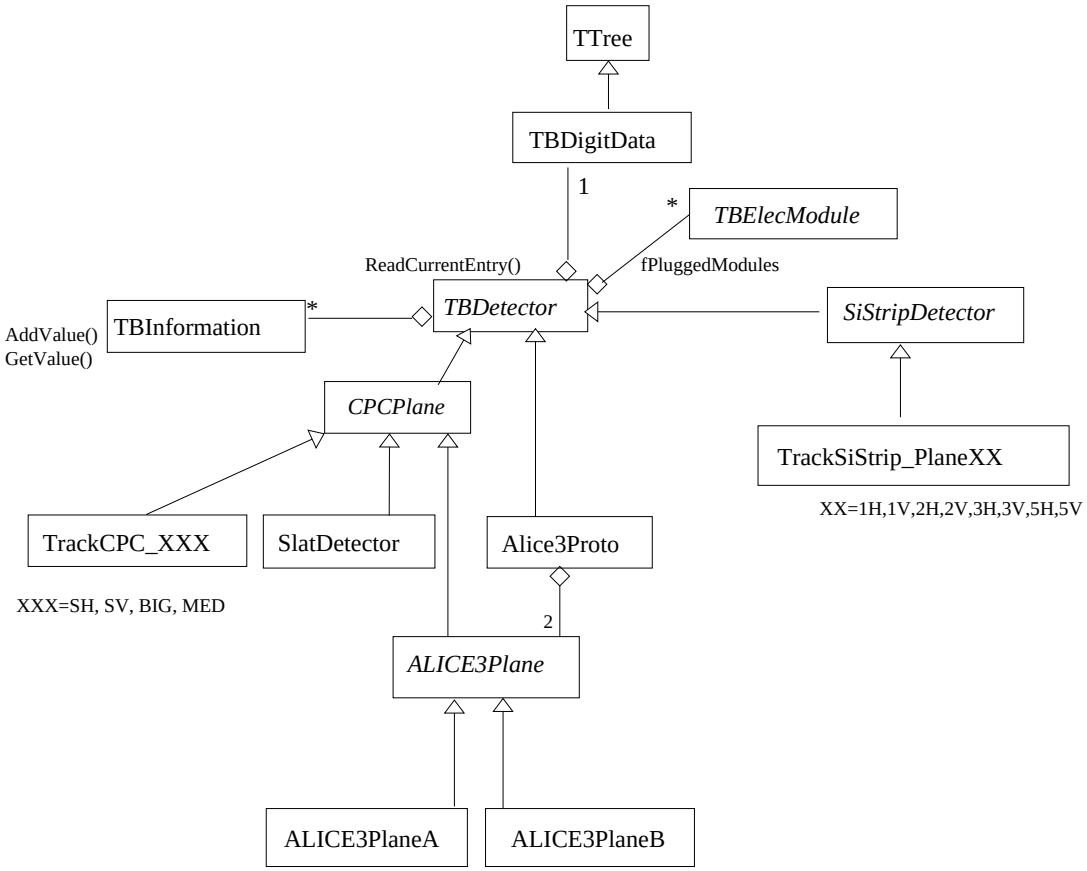

Figure 7: Detector classes. See section 3.3 for more details.

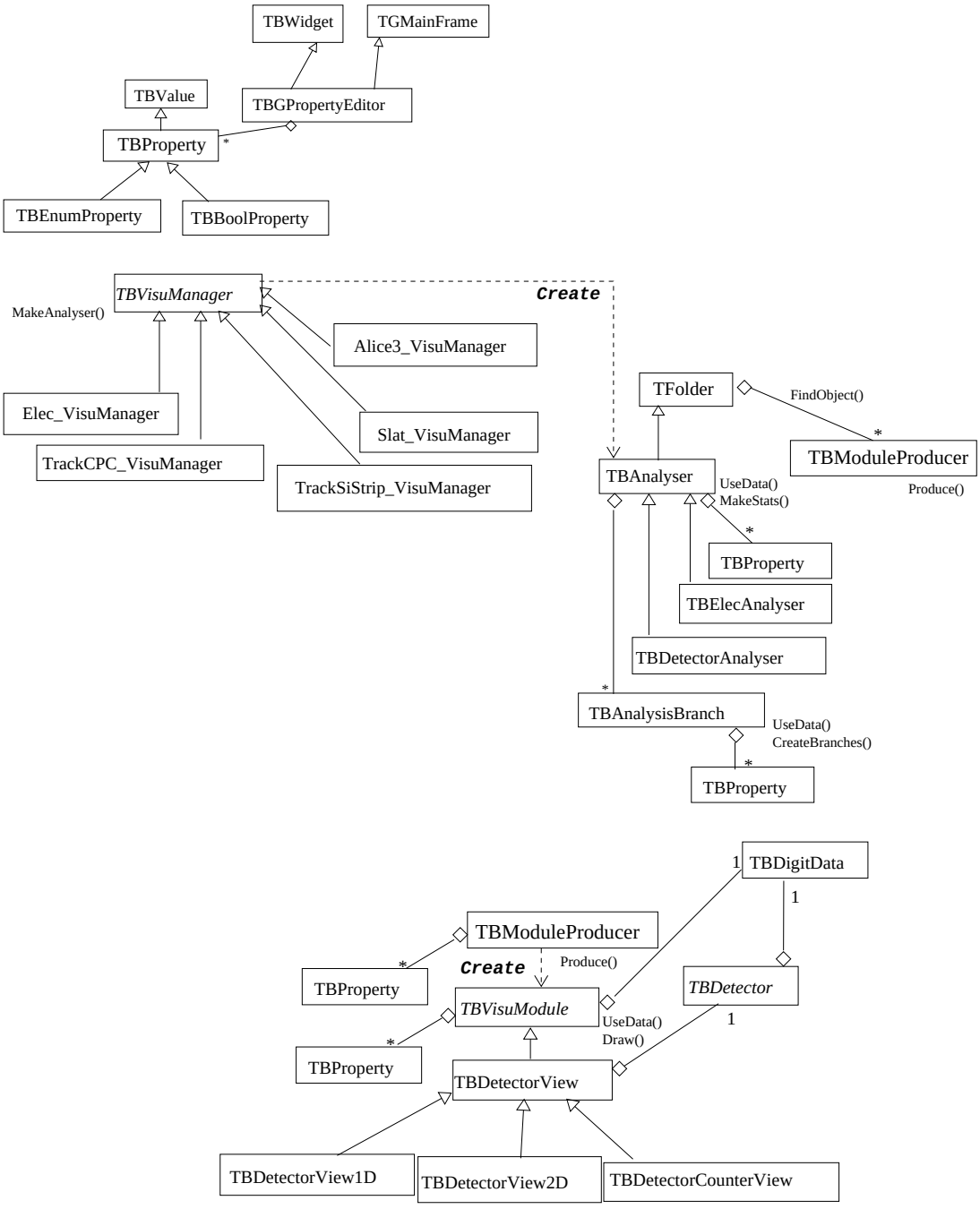

Figure 8: Analysis and graphical viewing classes. See section 3.4 for more details.

APPENDIX C - quadrant0.pdf

Matériaux, X_0 et sections géométriques du quadrant zéro du spectromètre dimuon d'ALICE

B. Espagnon, M. Mac Cormick,
M.P. Comets, D. Guez,
Y. Le Bornec, N. Willis
Groupe ALICE

24 avril 2002

IPNO DR-02-010

Ce dossier contient le détail des matériaux utilisés dans la construction du quadrant zéro. Les modèles permettant la description du quart de chambre en terme de longueur de radiation et de sections efficaces géométriques sont développés et accompagnés par les tableaux donnant les résultats numériques. Ces informations sont réunies ici pour constituer un dossier commun de consultation qui est destiné à servir de référence pour les paramètres des modèles programmés dans AliROOT.

Tous nos remerciements vont à nos collègues de RDD et SEP et plus particulièrement à D. Rougier, P. Courtat, J.M. Martin, C. Le Galliard, E. Rindel et J. Peyré, pour le temps qu'ils nous ont consacré et les secrets de fabrications qu'ils nous ont révélés ...

Table des matières

0.1 Introduction. 7
0.2 Définition des surfaces actives. 8
0.3 Structures du quart de chambre. 9
0.3.1 Le PCB des plans cathodiques. 9
0.3.1.1 *Côté pads* 10
0.3.1.2 *Côté circuit* 10
0.3.2 Le plan mécanique rigidificateur 10
0.3.3 Les connecteurs Kaptons 12
0.3.4 La carte mère 13
0.3.5 Les cartes filles - MANU12 14
0.3.6 Utilisation des tableaux 16
0.3.7 Simulations 16

Liste des tableaux

0.1 Surfaces actives des trois zones de chaque plan cathodique. 8
0.2 Surfaces des motifs "standards" de référence. 9
0.3 Nombre de lumières/Kaptons par zone et totaux. 11
0.4 Longueurs de radiation et surfaces utilisées dans les calculs. 19
0.5 Evaluation de la matière présentée par les plans cathodiques. 20
0.6 Evaluation de la matière présentée par les plans mécaniques. 21
0.7 Evaluation de la matière présentée par les Kaptons. Les trois sections, *couche 1*, *couche 2*, et *couche 3,* correspondent aux sections du modèle décrit sur la page 13. Les valeurs sont normalisées ici à la surface d'une lumière (qui vaut 849,73 mm^2). Pour pouvoir additionner ces valeurs avec celles normalisées par zone, il faut multiplier les valeurs (des trois dernières colonnes seulement) par un facteur 0,5, 0,25, et 0,125 pour les zones 1, 2, et 3 respectivement. 22
0.8 Evaluation des épaisseurs de matière dans les cartes mères. Les couches 1 et 2 sont expliquées dans la figure 0.10 sur la page 14. 23
0.9 Evaluation de la matière des principaux composants de la carte fille (MANU12). Notez que la surface de normalisation est celle d'un MANU12 ($surface_{MANU} = 63{\times}23$ mm^2). Pour pouvoir comparer ou additionner ces valeurs avec celles des autres tableaux où la normalisation est faite par zone (à l'exception des Kaptons), il faut appliquer un facteur multiplicatif de normalisation de 0,856, 0,428, et 0,214 pour les zones 1, 2, et 3 respectivement. 24
0.10 Resumé des longueurs de radiation du plan Bending (en haut) et Non Bending (en bas). Différents matériaux sont regroupés sous un même titre indicatif correspondant à la matière prépondérante. 33

Table des figures

0.1 (a) Vue schématique de l'assemblage des quarts de chambres des stations 1 et 2. Les lettres B et NB situées sur les faces indiquent respectivement les plans bending et non-bending. Le sens (X,Y,Z) des coordonnées est également indiqué. (b) Vue artistique d'un quart de chambre. 7
0.2 Plans cathodiques avec bending à gauche et non-bending à droite. On voit les trois zones distinctes de segmentation. 8
0.3 Dimensions d'un pad. On notera que la surface cuivrée est inférieure à la surface totale d'un pad. 9
0.4 Sur la gauche, vue de dessus d'une tranche d'un pad découpé au niveau du trait de l'image de droite (vue de profil), qui révèle la structure en couches du pad. Les matériaux de la surface, d'un via et de la partie interne d'un pad sont montrés. On voit dans ce modèle qu'un via traversant est constitué de deux bagues concentriques, dont la première est en Ni et la deuxième en cuivre. 10
0.5 Tous les détails (tels que l'emplacement des mires d'alignement et des masses) ne sont pas montrés sur l'image de gauche (a). On notera, sur l'image de droite (b), les circuits de masse autour de chaque motif et en bordure de PCB. 11
0.6 Vue schématique d'une coupe montrant les couches successives de matière qui constituent les plans cathodiques. Notez bien que l'étanchéité provient de la couche finale de vernis. 11
0.7 Détails du plan rigidificateur avec une vue de face et une vue de profil. 12
0.8 Dessin de base pour le Kapton gauche. Le Kapton droit est son symétrique par rapport à la verticale. 12
0.9 Modèle des Kaptons adopté dans l'évaluation de la matière et des sections qu'ils présentent pour les particules incidentes. 13
0.10 Une partie des couches cuivrées de la carte mère. Le dessin de gauche correspond à la couche de masse et aux pistes de transmission des signaux, tandis que celui de droit réprésente le plan des alimentations. 14
0.11 Vue schématique des couches successives de la carte mère. 14
0.12 Vue schématique de l'empilement des couches de la carte fille. 14
0.13 Couches de cuivre, vue de face, de la carte fille MANU12. 15
0.14 Vue schématique de l'emplacement des puces et des connecteurs SAMTEC sur les cartes filles (a). Les dimensions sont portées sur la figure (b) et l'emplacement du connecteur Berg, posé sur le dessous des cartes, est visible dans la partie (c). 15
0.15 Représentation synthétique du trajet d'une particule à traver un quart de chambre. Se référer aux autres organigrammes pour plus de détails. 25
0.16 Carte Manu12 zone A (connecteurs 7 points). Les valeurs sont normalisées à la surface de la carte. Voir text et table 0.9 pour le détail des calculs. 26
0.17 Carte Manu12 zone B (composants actifs). Les valeurs sont normalisées à la surface de la carte. Voir text et table 0.9 pour le détail des calculs. 27

0.18 Carte Manu12 zoneC (composants passifs). Les valeurs sont normalisées à la surface de la carte. Voir text et table 0.9 pour le détail des calculs. 28
0.19 Carte mère, support des cartes Manu12. Voir text et table 0.8(b) pour le détail des calculs. 29
0.20 Plan rigidificateur. Voir text et table 0.6(b) pour le détail des calculs. 30
0.21 Nappe Kapton. Les valeurs sont normalisées à la surface d'une lumière du plan rigidificateur. Voir text et table 0.7 pour le détail des calculs. 31
0.22 Plan de cathode. Voir text et table 0.5(b) pour le détail des calculs. 32

0.1 Introduction.

Le quadrant zéro est le premier quart de chambre construit pour la station 1 du spectromètre à dimuons. Il servira de quadrant de secours. Il est composé de deux plans cathodiques segmentés, nommés plans "bending" et "non-bending". Les points d'impacts mesurés avec une haute résolution sont fournis principalement par le bending, et ceux à basse résolution par le non-bending.

L'assemblage des quarts de chambres (figure 0.1(a)), permet de couvrir un cône géométrique d'acceptance de 2 à 9°, comme requis dans le cahier des charges (réf. *The Forward Muon Spectrometer*, CERN/LHCC 96-32, LHCC/P3-Addendum 1, 15 October 1996).

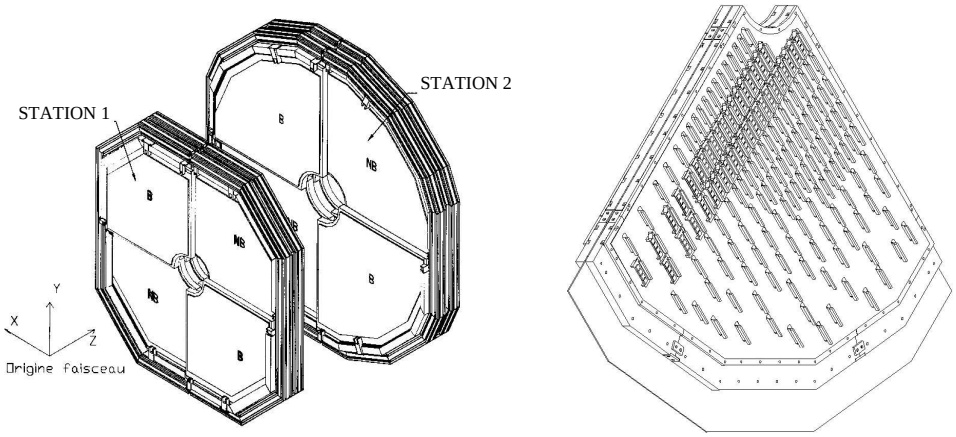

(a) (b)

FIG. 0.1 –: *(a) Vue schématique de l'assemblage des quarts de chambres des stations 1 et 2. Les lettres B et NB situées sur les faces indiquent respectivement les plans bending et non-bending. Le sens (X,Y,Z) des coordonnées est également indiqué. (b) Vue artistique d'un quart de chambre.*

Dans la figure 0.1(b), une vue artistique du quart est présentée et les principaux composants sont identifiés. Un quart est composé :

1. du PCB des plans cathodiques
2. du plan mécanique rigidificateur
3. des connecteurs flexs (Kaptons™)
4. de la carte mère
5. des MANU12
6. du plan des fils anodiques, cartes de lecture CROCUS, les berceaux

Dans la suite, les matériaux utilisés seront décrits en détail. Un modèle divisant le quart de chambre en 3 zones actives, reprenant les points 1 à 5 sera utilisé. Le sixième point, qui concerne des éléments encore non figés dans leur dessin et emplacement (telles que les cartes d'acquisition, CROCUS), ou qui sont en dehors de la surface active (tels que les berceaux), sera évalué dans un deuxième dossier.

Après la présentation des modèles, les tableaux détaillés des valeurs de références utilisées dans les calculs (page 19) et les résultats obtenus par composant et par zone sont présentés en annexe (pages 20 à 24). Les parcours possibles d'une particule incidente qui traverse à 90° tout le détecteur sont détaillés (pages 25 à 32). Enfin, une synthèse des longueurs de radiation termine le document (page 33).

Précisons que certaines valeurs sont basées sur des estimations fournies par les industriels et d'autres sont le résultat de mesures précises.

Dans le texte qui suit, par usage, nous utiliserons le terme Kaptons™, pour décrire les connecteurs flexs.

0.2 Définition des surfaces actives.

La surface active de chaque cathode est segmentée en 3 zones distinctes. Ces zones sont indiquées dans la figure 0.2 pour le bending (vue de gauche) et le non-bending (vue de droite). Une partie de la surface est appelée "active" (ou sensible) si elle est reliée à une voie d'électronique. A l'intérieur de

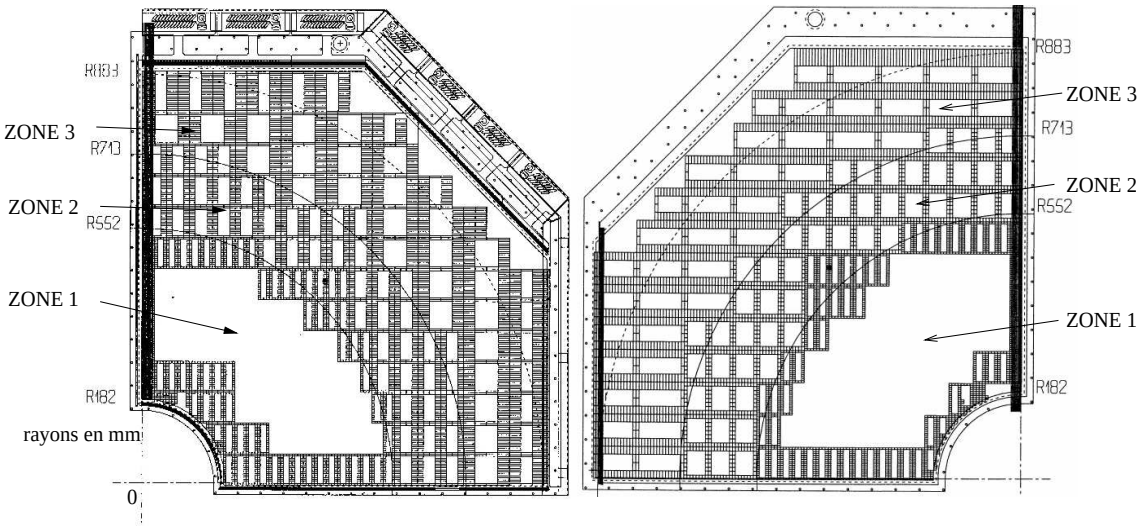

FIG. 0.2 –: *Plans cathodiques avec bending à gauche et non-bending à droite. On voit les trois zones distinctes de segmentation.*

chaque zone, la segmentation élémentaire est constante et, dans la mesure du possible, les segments individuels (appelés "pads") sont regroupés en "motifs" rectangulaires composés de 64 pads. Pour le bending, les 64 voies sont réparties en motifs de 16×4 pads. Ce regroupement reflète la modularité des connecteurs de lecture des pads, les Kaptons, qui eux transfèrent des signaux des pads par groupes de 64 voies. Pour la zone 3, due à des contraintes mécaniques, cette modularité n'est pas tout à fait respectée.

Les surfaces actives de chaque zone sont présentées dans la table 0.1. Ces surfaces servent dans

	Bending (mm^2)	Non-Bending (mm^2)
Zone 1	230307,8	226788,7
Zone 2	162570,2	172730,9
Zone 3	264917,5	267562,3

TAB. 0.1 –: *Surfaces actives des trois zones de chaque plan cathodique.*

la normalisation des quantités de matière pour l'évaluation des longueurs de radiation et des sections efficaces géométriques.

D'autres paramètres importants utilisés partout dans les évaluations concernent la dimension d'un motif "standard" de chaque zone. Les motifs "standards" de référence sont numérotés 4, 5, et 6 pour le

bending et 4, 12, et 13 pour le non-bending, respectivement pour zones 1 à 3. Les dimensions des pads élémentaires sont données dans le tableau 0.2.

	Bending			Non-Bending		
	Zone 1	Zone 2	Zone 3	Zone 1	Zone 2	Zone 3
numéro du motif standard	4	5	6	4	12	13
surface du motif standard (mm^2)	1693,44	3386,88	6773,76	1693,44	3386,88	6773,76
dimension d'un pad (mm^2)	6,3×4,2	12,6×4,2	25,2×4,2	4,2×6,3	8,4×6,3	16,8×6,3
dimension d'un motif régulier (pads)	4×16	4×16	4×16	4×16	8×8	16×4

TAB. 0.2 –: *Surfaces des motifs "standards" de référence.*

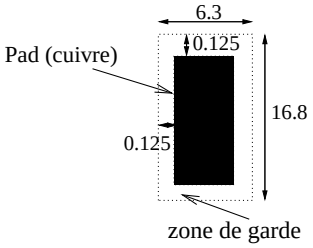

FIG. 0.3 –: *Dimensions d'un pad. On notera que la surface cuivrée est inférieure à la surface totale d'un pad.*

Précisons que la surface d'un pad est prise comme étant la surface réelle du pad plus la moitié de la surface inter-pad (la distance entre 2 pads étant de 0,25 mm). La figure 0.3 illustre ceci pour les pads du motif 4.

Les valeurs de référence des surfaces et longueurs de radiation des matériaux sont regroupées dans les tableaux 0.4(a) et (b) sur la page 19.

0.3 Structures du quart de chambre.

0.3.1 Le PCB des plans cathodiques.

Les plans cathodiques sont fabriqués à partir de PCB double face (0,4 mm d'épaisseur) comportant du cuivre de 17,5 μm d'épaisseur. Le plan se compose de plusieurs éléments:

1. les pads
2. le support FR4
3. le circuit imprimé

Pour mieux apprécier les épaisseurs et le poids à accorder aux mesures, il faut d'abord comprendre le processus de fabrication.

Une plaque de PCB double face, c'est à dire du FR4 (un type de fibre de verre), est recouverte d'une fine couche de Cu sur chaque face. Les dessins des circuits sont gravés chimiquement sur chaque côté et les vias, qui permettent de passer un signal d'une face vers l'autre, sont percés. La norme de fabrication est classe 4, ce qui implique des pistes et inter-pistes d'au moins 0,210 mm. Ensuite, d'autres couches métalliques sont posées pour compléter le circuit. Un traitement est nécessaire pour "coller" les différentes couches entre elles. Plusieurs techniques sont possibles, mais notre fabriquant pose une couche fine d'environ 3 à 5 μm de Ni sur toute la surface cuivrée et dans les vias. Le PCB est mis dans un bain galvanique de cuivre et une recharge d'environ 15 à 25 μm se pose sur la surface. On a donc une épaisseur de 37,5 μm de cuivre en moyenne. Les dernières étapes de fabrication côté pads sont différentes de celles pour la fabrication du circuit de lecture sur l'autre face du PCB.

0.3.1.1 *Côté pads*

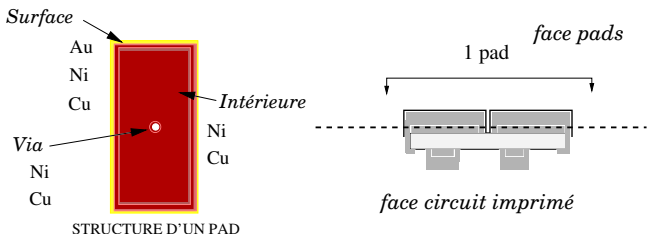

FIG. 0.4 –: *Sur la gauche, vue de dessus d'une tranche d'un pad découpé au niveau du trait de l'image de droite (vue de profil), qui révèle la structure en couches du pad. Les matériaux de la surface, d'un via et de la partie interne d'un pad sont montrés. On voit dans ce modèle qu'un via traversant est constitué de deux bagues concentriques, dont la première est en Ni et la deuxième en cuivre.*

La surface des pads doit être protégée de l'atmosphère. Pour cela, on pose une couche de préparation d'environ 4 μm de Ni suivie d'un "flash" d'Au de 0,1 μm. Ces métaux se trouvent sur la face externe et dans les vias. La figure 0.4 montre schématiquent les différentes couches successives.

0.3.1.2 *Côté circuit*

Cette surface est recouverte des pistes reliant les pads aux points de soudure des connecteurs "Kaptons". Une couche de 9 μm d'un mélange d'étain/plomb (supposé être 60 % Sn et 40 % Pb) est déposée sur les points de soudure.

La partie métallique d'un pad de la zone 1 est montrée dans la figure 0.5(a). Dans les évaluations de la matière qu'elle représente, la longueur de chaque piste a été mesurée, et sachant l'épaisseur et la profondeur de chacune, le volume total de métal a été calculé. La connaissance de la densité et de la masse déposée de cuivre permet d'en déduire le nombre de longueurs de radiation.

En plus de ces motifs répétitifs, les plans sont découpés en plusieurs circuits de base. Les sections sont entourées d'un trait plus large de cuivre pour permettre éventuellement de souder les circuits ensemble. En plus de cela, chaque motif est entouré d'une piste de masse qui représente localement une quantité de métal non négligeable. Un circuit témoin, du plan bending, est montré dans la figure 0.5(b).

Toute la surface passe sous un rideau de vernis qui, d'une part isole les pistes cuivrées de l'atmosphère, mais en plus assure l'étanchéité vis-à-vis du gaz au niveau des vias. Cette géométrie est montrée dans le schéma de la figure 0.6.

La table 0.5 résume les caractéristiques détaillées des plans cathodiques.

0.3.2 Le plan mécanique rigidificateur

La rigidité mécanique est assurée par deux couches de 20 mm de foam (mousse) et de 0,4 mm de PCB. La surface est percée de lumières pour laisser passer les nappes Kaptons. La figure 0.7(b) montre une vue en coupe à travers les couches. La table 0.3 résume le nombre de lumières par surface et la figure 0.7(a) montre le dessin de principe.

La table 0.6 (page 21) résume les caractéristiques détaillées des plans rigidificateurs, bending et non-bending.

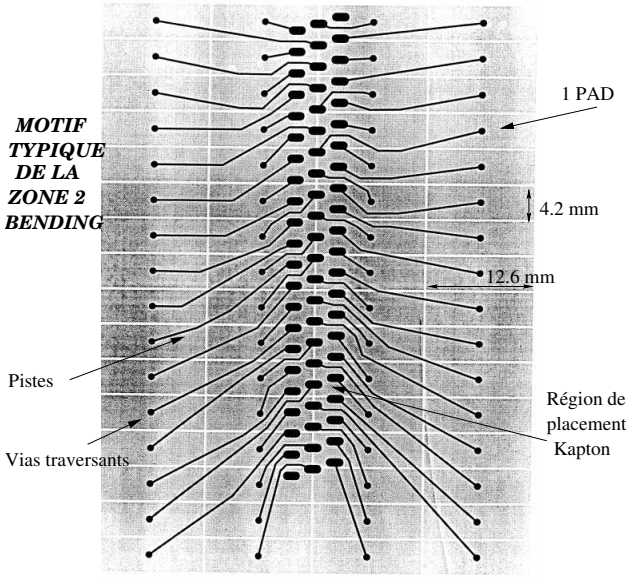

(a) Dessin d'un circuit (d'un seul motif) qui relie les pads au circuit électronique.

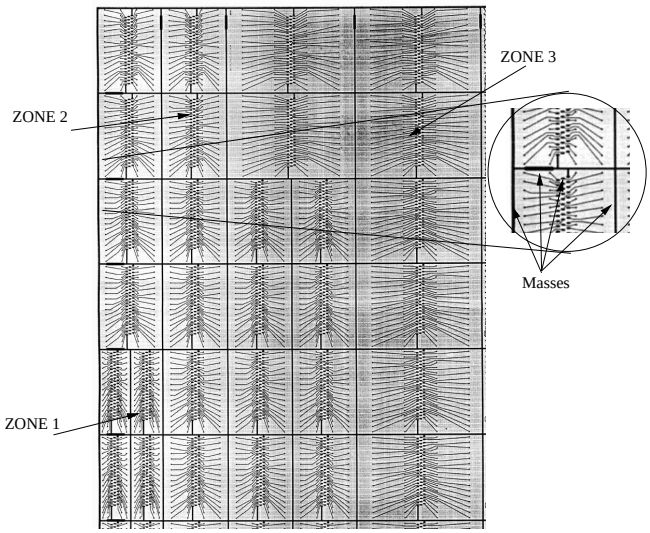

(b) Vue d'un morceau de circuit imprimé du plan bending.

FIG. 0.5 –: *Tous les détails (tels que l'emplacement des mires d'alignement et des masses) ne sont pas montrés sur l'image de gauche (a). On notera, sur l'image de droite (b), les circuits de masse autour de chaque motif et en bordure de PCB.*

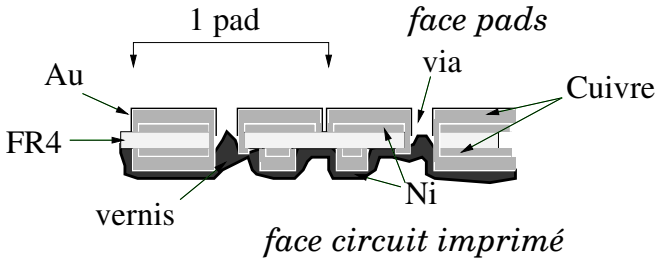

FIG. 0.6 –: *Vue schématique d'une coupe montrant les couches successives de matière qui constituent les plans cathodiques. Notez bien que l'étanchéité provient de la couche finale de vernis.*

	Bending	Non-bending
Zone 1	136	134
Zone 2	48	46
Zone 3	42	45
totaux	226	225

TAB. 0.3 –: *Nombre de lumières/Kaptons par zone et totaux.*

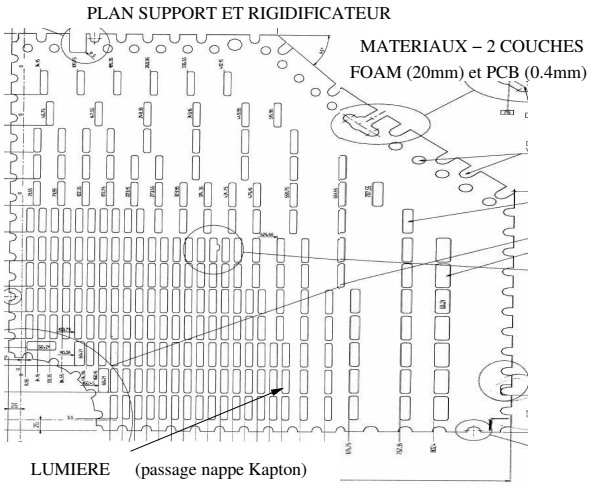

(a) Plan de principe qui montre la configuration géométrique de lumières.

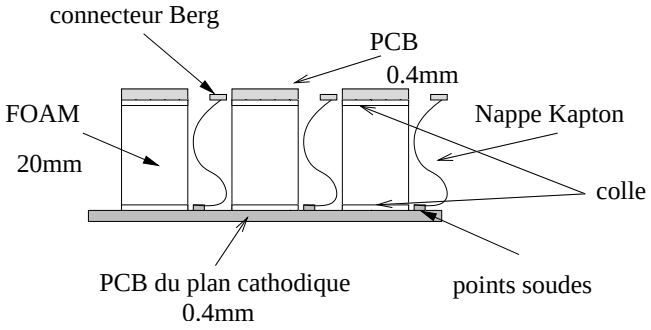

(b) Coupe à travers les couches du plan rigidificateur.

FIG. 0.7 –: *Détails du plan rigidificateur avec une vue de face et une vue de profil.*

0.3.3 Les connecteurs Kaptons

Ces connecteurs (figure 0.7(b)), passent les signaux des pads à l'électronique analogique située sur les faces externes du détecteur. Il y a autant de Kaptons que de lumières découpées dans le plan

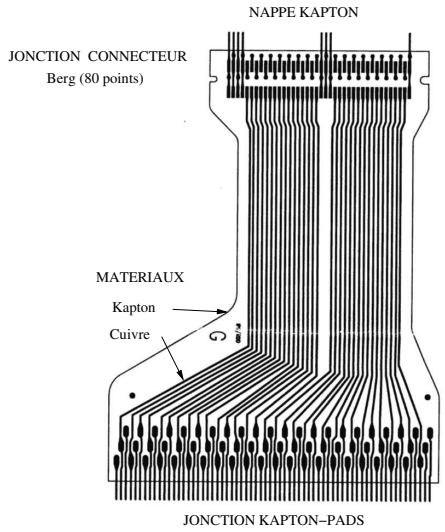

FIG. 0.8 –: *Dessin de base pour le Kapton gauche. Le Kapton droit est son symétrique par rapport à la verticale.*

rigidificateur. Il y a deux dessins de base: le Kapton gauche et le Kapton droit. Le premier sert à la lecture du plan bending et le second à la lecture du plan non-bending. Le dessin de principe du Kapton gauche est montré dans la figure 0.8.

La matière de base est le Kapton, un polyimide léger et flexible. Les lignes verticales dans la figure 0.8 représentent les pistes cuivrées. Celles-ci sont présentés sur les 2 faces du Kapton. Sur la figure 0.9, à droite, on peut voir la partie soudée manuellement sur le PCB des plans cathodiques. Pour

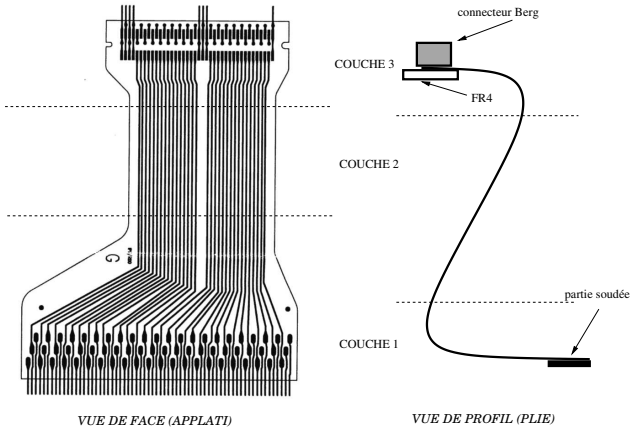

FIG. 0.9 –: *Modèle des Kaptons adopté dans l'évaluation de la matière et des sections qu'ils présentent pour les particules incidentes.*

l'autre extrémité, un connecteur (Berg, 80 points) mâle assure la liaison avec les cartes électroniques (les MANU12).

Dans l'évaluation de la quantité de matière que représentent ces nappes, des précautions particulières ont été prises pour améliorer la précision des calculs. Le poids de quelques connecteurs a été mesuré sur une balance de haute précision ($\pm$0,1 mg). Les teneurs en plastique et en métal (cuivre) ont été mesurées séparément. Couplée avec la connaissance du volume occupé par ces connecteurs, une meilleure évaluation de la densité de la composante plastique (et en conséquence des longueurs de radiation) qu'il représente a été possible. En plus, une fois les Kaptons en place, la section efficace géométrique vue par une particule traversant le détecteur le long de l'axe Z (voir la figure 0.1 sur la page 7 pour la convention des coordonnées) est dépendante de la manière dont les Kaptons sont pliés et de l'endroit de passage qui peut être plus ou moins dense suivant la combinaison de métal et plastique traversée. Pour essayer de prendre ceci en compte, un modèle où les Kaptons sont divisés en trois sections séparées, comme le montre la figure 0.9, a été adopté.

Les résultats des évaluations sont rapportés dans la table 0.7.

0.3.4 La carte mère

Cette couche est de nature purement électronique et n'est pas nécessaire pour la stabilité ou rigidité mécanique. Ses couches à double faces permettent principalement de distribuer les basses tensions de l'électronique d'analyse et de transmettre les signaux de contôle numérique. Afin d'assurer un courant convenable pour ces transmissions, une quantité importante de cuivre est requise dans la structure des plans. La carte mère est composée d'un PCB double face avec 12 μm de cuivre rechargé à 25 μm. Les 2 faces de la carte mère sont représentées sur la figure 0.10. Sur la gauche on peut voir la couche 1 comportant les pistes de transmission des signaux. La surface restante (en noire sur la figure) sert de plan de masse. Sur la droite est représentée la couche 2 correspondant au plan d'alimentation. Hormis des bandes horizontales, ce dernier est recouvert de cuivre à 100 %, tandis que le cuivre du plan de masse sur la face 1 est déposé sous forme d'une grille à 50 %. Un dernier point, où la quantité de matière est non négligeable, concerne les connecteurs femelles (SAMTEC, 7 points) implantés dans ce circuit. Les cartes filles (les MANU12) viennent se brancher sur ces emplacements.

La pose des couches successives est montrée sur la figure 0.11. Sur ce schéma, les différentes matières sont annotées et les épaisseurs évaluées sont rapportées dans la table 0.8.

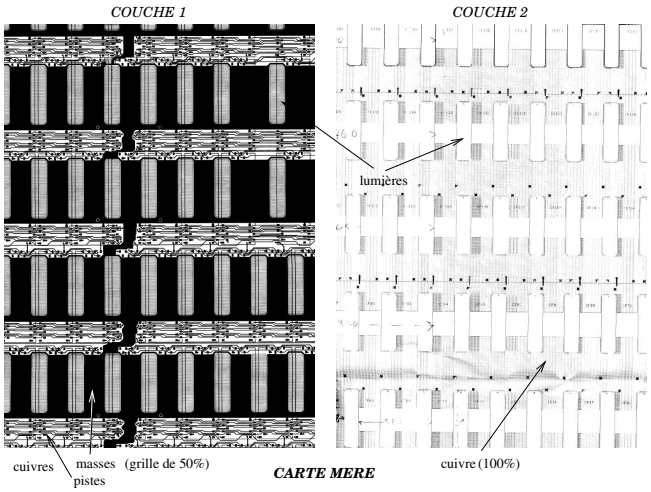

FIG. 0.10 –: *Une partie des couches cuivrées de la carte mère. Le dessin de gauche correspond à la couche de masse et aux pistes de transmission des signaux, tandis que celui de droit réprésente le plan des alimentations.*

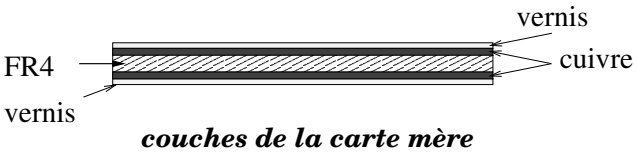

FIG. 0.11 –: *Vue schématique des couches successives de la carte mère.*

0.3.5 Les cartes filles - MANU12

Ces cartes constituent l'électronique embarquée de la chambre. En plus des composants actifs (puces électroniques) et passifs (capacités, résistances, etc.), elles sont composées d'un PCB de 6 couches de cuivre intercalées avec 5 couches de FR4. La technologie des cartes réalisées est de 12 μm de cuivre (rechargé à 25 μm pour les faces externes). Les vias sont percés à travers les 6 couches complètes. Les couches successives sont schématisées sur la figure 0.12 . La figure 0.13 montre les détails des 6 couches cuivrées.

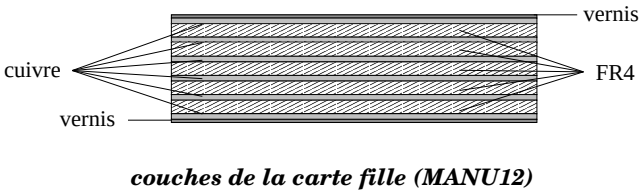

FIG. 0.12 –: *Vue schématique de l'empilement des couches de la carte fille.*

Les couches de masse et de pistes constituent un réseau en dentelle. Dans l'évaluation de l'épaisseur effective et du nombre de longueurs de radiation on a utilisé la connaissance de la quantité de cuivre par couche, fournie par le fabricant (et déterminée à l'origine pendant le processus de fabrication).

En plus des aspects multicouche des cartes MANU12, il y a aussi les connecteurs et les puces électroniques à comptabiliser.

Il y a deux types de connecteurs montés :

- le connecteur femelle (Berg, 80 points) qui réceptionne les données par l'intermédiaire des Kaptons
- les connecteurs SAMTEC (mâles, 7 points) à raison de trois par carte. Ces derniers permettent la connection de la carte fille sur la carte mère ainsi que la transmission des basses tensions et des signaux de contrôle. Il y a 4 puces qui assurent le traitement analogique. Elles sont principalement composées de Si et encapsulées dans du plastique. La puce MARC s'occupe du traitement numérique des données. Le résultat remonte vers les cartes CROCUS par les pistes implantées dans la carte mère

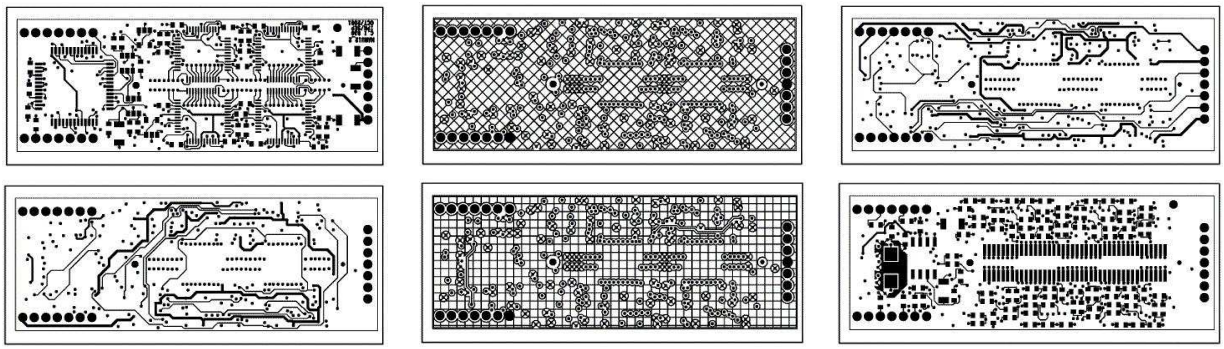

FIG. 0.13 –: *Couches de cuivre, vue de face, de la carte fille MANU12.*

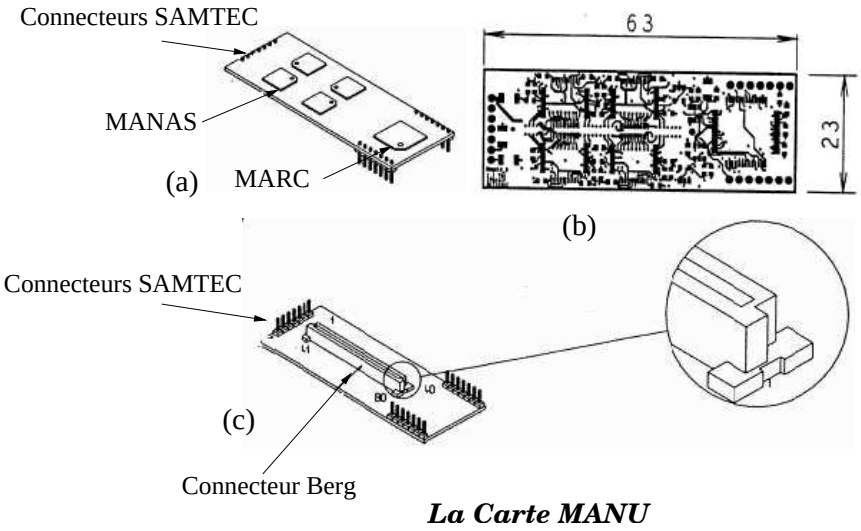

FIG. 0.14 –: *Vue schématique de l'emplacement des puces et des connecteurs SAMTEC sur les cartes filles (a). Les dimensions sont portées sur la figure (b) et l'emplacement du connecteur Berg, posé sur le dessous des cartes, est visible dans la partie (c).*

(dont la connexion se fait par des connecteurs SAMTEC). Une vue schématique de l'emplacement des puces et des connecteurs SAMTEC est représentée sur la figure 0.14(a). Les détails du connecteur Berg, posé sur le dessous des cartes est montré dans la partie (c), et les dimensions externes d'une carte sont décrits dans la partie (b) de la même figure. La quantité de matière représentée par une carte est rapportée dans la table 0.9.

0.3.6 Utilisation des tableaux

Les tableaux et organigrammes des parcours des particules donnés dans l'annexe peuvent servir comme base de données dans la construction des modèles de simulation. Il s'avère toutefois que l'interprétation des tableaux n'est pas toujours chose facile. Typiquement, chacun décrit l'épaisseur *maximale* et *moyenne* de chaque matière trouvée dans la construction de la chambre, accompagnée des longueurs de radiation X_0.

Les épaisseurs *maximales* donnent l'endroit où la couche de matière est la plus épaisse, et les $X_0 max$ sont les conversions direct de ces valeurs prenant en compte la nature précise de la matière.

Les épaisseurs équivalentes et les X_0 sont évalués à partir du *volume* de matière réparti sur une surface de référence. En géneral la surface de référence correspond à la surface d'un motif (par zone). Par exemple, dans le cas des pistes du plan cathodique, il est naturel de prendre le volume de celles-ci divisé par la surface d'un motif. Pour la carte fille, c'est la surface de celle-ci qui constitue la référence naturelle. Les épaisseurs *moyennes* couvrent 100% de la surface de référence. Elles peuvent servir dans la modélisation du détecteur où on cherche à reproduire les matériaux vus par une particule sans s'occuper des détails fins de la construction.

La dernière colonne décrit la section efficace géométrique couverte par la matière en question. Ces dernières valeurs doivent être utilisées avec précaution. Elles peuvent être également interpretées comme la probabilité de rencontrer une matière donnée pour une particule qui arrive à 90° sur une surface donnée. Pour faire ce calcul on prend un volume de matière et on projette ses composantes sur une surface de référence. C'est la section ainsi obtenue qui est décrite dans les dernières colonnes. Ces valeurs ne peuvent pas être mélangées avec celles des autres colonnes pour remonter à des volumes.

Pour illustrer comment lire une table, prenons la table 0.5 page 20. Intéressons nous à la ligne qui décrit le cuivre de recharge de la zone 1 du plan de cathode bending (table de gauche). Le fabricant nous a indiqué une recharge à environ 20 μm, ce qui est cité dans le descriptif de fabrication. Lisant les colonnes, on peut dire que cette matière représente une épaisseur moyenne de 18,2 μm sur toute la surface d'un motif de la zone 1 (qui représente 64 pads de 4,2×6,3 mm^2 en surface de référence), et qu'une particule qui arrive orthogonalement au plan a une probabilité de 89% de rencontrer ce cuivre. Dans le cas le plus extrême, une particule pourrait traverser une épaisseur de 41,5 μm. La probabilité de cet événement ne peut pas être déduit à partir des tableaux. Il faut consulter le déscriptif détaillé pour faire une telle évaluation.

En complément des tableaux est décrite, dans des organigrammes, la matière vue par une particule incidente à 90°, prenant en compte les géométries exclusives. Par exemple, une particule qui passe par une nappe Kapton ne pourrait pas, par la même occasion, passer par les couches de la carte mère car ce sont des surfaces complémentaires.

0.3.7 Simulations

La façon de construire un modèle de simulation dépend des questions auxquelles on souhaite répondre. Comme le détecteur est un objet complexe, il est commode de le convertir en une épaisseur équivalente d'une matière homogène, qui, dans le cas des chambres de notre spectromètre, est habituellement de l'aluminium. Une telle approximation est valable quand on souhaite estimer la contribution

de la diffusion multiple, c'est à dire, la contribution des collisions électromagnétiques élastiques où le processus dominant est le bremsstrahlung. Dans ce cas, l'approximation de la diffusion angulaire est faite à partir d'une formulation qui décrit le résultat attendu pour une épaisseur *totale* donnée. Or, si on se sert d'un modèle réaliste où chaque lamelle fine de matière est fidèlement décrite, on obtient un résultat erroné. Ceci souligne l'importance de bien saisir les détails (apparemment évident) des simulations. Cette situation provient du fait que l'approximation de Molière, qui décrit l'ouverture d'angle provenant des diffusions coulombiennes multiples, n'a pas le même comportement pour des lamelles fines que pour une seule tranche plus épaisse. Les petites diffusions ne peuvent pas être sommées quadratiquement, car cet effet cumulatif dépend de l'épaisseur *totale* de matière traversée. L'approximation de Molière permet de résumer l'étalement angulaire, pour tous Z, par un seule équation à condition que l'épaisseur soit adaptée.

En revanche, l'évaluation de la perte d'énergie, qui est principalement due à l'absorption/ionisation en ce qui nous concerne, dépend largement d'une bonne description du milieu en termes de A ***et*** Z. La réponse de Bethe et Bloch, pour une matière donnée, sera unique et ne pourra être évaluée avec une épaisseur équivalente de matériaux. En effet, on ne peut pas reproduire des rapports A/Z différents par un simple changement d'épaisseur (comme dans le cas précédent). La modélisation de la perte d'énergie des particules et l'étude des processus secondaires seront donc d'autant plus fiables que la nature des matériaux sera respectée.

En conclusion, pour pouvoir simuler la réponse du détecteur de la manière la plus fidèle qu'il soit, il faut trouver un compromis entre un modèle très détaillé constitué de différentes couches de matières et un modèle très simple constitué d'une seule couche de matière.

Annexe

(a) Surfaces de références

	Bending			Non-Bending		
	Zone 1	Zone 2	Zone 3	Zone 1	Zone 2	Zone 3
numéro du motif standard	4	5	6	4	12	13
surface du motif standard (mm^2)	1693,44	3386,88	6773,76	1693,44	3386,88	6773,76
dimension d'un pad (mm^2)	6,3×4,2	12,6×4,2	25,2×4,2	4,2×6,3	8,4×6,3	16,8×6,3
dimension d'un motif régulier (pads)	4×16	4×16	4×16	4×16	8×8	16×4
surfaces actives (mm^2)	230307,8	162570,2	264917,5	226788,7	172730,9	267562,3

(b) Longueurs de radiations.

matière	X_0 (mm)	densité (g/cm^3)	Référence
or	3,34	19,32	Yung-Su Tsai, Rev. of Mod. Phy., Vol. 46, N° 4, octobre 1974
nickel	14,25	8,902	Yung-Su Tsai
cuivre	14,35	8,96	Yung-Su Tsai
étain	12,06	7,31	Yung-Su Tsai
plomb	5,61	11,35	Yung-Su Tsai
étain/plomb (60%/40%)	8,56	8,926	voir Yung-Su Tsai pour le calcul d'un mélange
tungsten	3,5	19,3	Yung-Su Tsai
carbone	188,93	2,26	Yung-Su Tsai
kapton	286	1,42	Atomique and nuclear properties of materials (Particle Data Group)
foam (Rohacell 51 IG)	7807,7	0,052	$X_0 = 40{,}6\ g/cm^2$ dans chap 3 du TDR TRD d'ALICE
FR4 (NEMA G10 plate)	194	1,7	Atomique and nuclear properties of materials (Particle Data Group)
air (20°C, 76 mm Hg)	304200	0,001205	Atomique and nuclear properties of materials (Particle Data Group)
époxy	443,7		ATLAS (40 g/cm^2 dans une note interne de CDF)
vernis (traité comme époxy)	443,7		estimation
plastique (connecteur SAMTEC)	380	1,107	X_0 estimé à partir de A/Z = 0,55
plastique (plexiglas)	349	1,16	Atomique and nuclear properties of materials (Particle Data Group)
silicium	93,7	2,329	Yung-Su Tsai

TAB. 0.4 –: *Longueurs de radiation et surfaces utilisées dans les calculs.*

	ϵ_{max} (mm)	$\%X_0 max$	ϵ_{moy} (mm)			$\%X_0 moy$			%probabilité ($\sigma_{geom.}$)		
			Zone 1	Zone 2	Zone 3	Zone 1	Zone 2	Zone 3	Zone 1	Zone 2	Zone 3
Trous + interpistes (gaz = air)	0,0456	$\searrow 0$	0,0044	0,0036	0,0031	$\searrow 0$	$\searrow 0$	$\searrow 0$	9,68	7,84	6,88
Au (0,1μm)	0,0456	1,365	$\searrow 0$	$\searrow 0$	$\searrow 0$	$\searrow 0$	$\searrow 0$	$\searrow 0$	90,32	92,18	93,11
Ni (4μm)	0,0455	0,319	0,0037	0,0038	0,0038	0,026	0,027	0,027	90,31	92,18	93,07
Cu de recharge (20μm)	0,0425	0,296	0,0182	0,0186	0,0188	0,127	0,130	0,131	89,82	91,83	92,84
Ni (4μm)	0,0215	0,151	0,0035	0,0036	0,0037	0,024	0,025	0,026	88,25	90,57	91,73
Cu de base (17,5μm)	0,0175	0,122	0,0153	0,0158	0,0160	0,107	0,110	0,111	87,94	90,32	91,52
FR4 (0,4mm)	0,4	0,206	0,3989	0,3995	0,397	0,206	0,206	0,205	99,73	99,87	99,93
Bagues de Cu (20μm)	0,4	2,787	0,0003	0,0001	0,0001	0,002	0,001	0,001	0,07	0,03	0,02
Pistes du motif (Cu)	0,0375	0,261	0,0024	0,0018	0,0017	0,017	0,013	0,012	6,43	4,95	4,75
Masses au bord (Cu)	0,0375	0,261	0,0020	0,0013	0,0009	0,014	0,009	0,006	5,34	3,42	2,45
64 trous cuivrés	0,0375	0,261	$\searrow 0$	$\searrow 0$	$\searrow 0$	$\searrow 0$	$\searrow 0$	$\searrow 0$	0,07	0,03	0,02
Emplacements Kaptons	0,0375	0,261	0,0030	0,0015	0,0007	0,021	0,010	0,005	7,93	3,97	1,98
2 mires d'alignement (Cu)	0,0375	0,261	$\searrow 0$	$\searrow 0$	$\searrow 0$	$\searrow 0$	$\searrow 0$	$\searrow 0$	0,06	0,03	0,02
Etamage emplacement Kapton	0,009	0,105	0,0023	0,0012	0,0006	0,027	0,014	0,007	7,93	3,97	1,98
Vernis	0,0575	0,013	0,0481	0,0543	0,0531	0,011	0,012	0,011	100	100	100

côté circuit ***support*** ***côté pads***

(a) Plan bending

	ϵ_{max} (mm)	$\%X_0 max$	ϵ_{moy} (mm)			$\%X_0 moy$			%probabilité ($\sigma_{geom.}$)		
			Zone 1	Zone 2	Zone 3	Zone 1	Zone 2	Zone 3	Zone 1	Zone 2	Zone 3
Interpistes (gaz = air)	0,0456	$\searrow 0$	0,0044	0,0031	0,0023	$\searrow 0$	$\searrow 0$	$\searrow 0$	9,58	6,83	5,05
Au (0,1μm)	0,0456	1,365	0,0001	0,0001	0,0001	0,003	0,003	0,003	90,32	93,17	94,65
Ni (4μm)	0,0455	0,319	0,0037	0,0038	0,0039	0,026	0,027	0,027	90,31	93,17	94,65
Cu de recharge (20μm)	0,0425	0,296	0,0183	0,0188	0,0191	0,128	0,131	0,133	90,01	92,95	94,48
Ni (4μm)	0,0215	0,151	0,0036	0,0037	0,0038	0,025	0,026	0,026	88,50	91,88	93,63
Cu de base (17,5μm)	0,0175	0,122	0,0154	0,0160	0,0164	0,108	0,112	0,114	88,20	91,67	93,47
FR4 (0,4mm)	0,4	0,206	0,3989	0,3995	0,3998	0,206	0,206	0,206	99,73	99,87	99,94
Bagues de Cu (20μm)	0,4	2,787	0,0003	0,0001	0,0001	0,002	0,001	0,001	0,07	0,03	0,02
Pistes du motif (Cu)	0,0375	0,261	0,0022	0,0012	0,0013	0,015	0,009	0,009	5,81	3,29	3,49
Masses au bord (Cu)	0,0375	0,261	0,0020	0,0013	0,0009	0,014	0,009	0,006	5,40	3,44	2,46
64 trous cuivrés	0,0375	0,261	$\searrow 0$	$\searrow 0$	$\searrow 0$	0,002	0,001	0,001	0,07	0,03	0,02
Emplacements Kaptons (Cu)	0,0375	0,261	0,0026	0,0013	0,0007	0,018	0,009	0,005	6,96	3,48	1,76
2 mires d'alignement	0,0375	0,261	$\searrow 0$	$\searrow 0$	$\searrow 0$	$\searrow 0$	$\searrow 0$	$\searrow 0$	0,06	0,03	0,02
Etamage emplacement Kapton	0,009	0,105	0,0006	0,0003	0,0002	0,007	0,004	0,002	6,96	3,48	1,76
Vernis	0,0575	0,013	0,0575	0,0575	0,0575	0,013	0,013	0,013	100	100	100

côté circuit ***support*** ***côté pads***

(b) Plan non-bending

TAB. 0.5 –: *Evaluation de la matière présentée par les plans cathodiques.*

PLANS MECANIQUES

	ϵ_{max} (mm)	%X$_0 max$	ϵ_{moy} (mm)			%X$_0 moy$			%probabilité ($\sigma_{geom.}$)		
			Zone 1	Zone 2	Zone 3	Zone 1	Zone 2	Zone 3	Zone 1	Zone 2	Zone 3
Foam	20	0,256	9,964	14,98	17,49	0,128	0,192	0,224	49,82	74,91	87,46
FR4	0,4	0,206	0,199	0,300	0,350	0,103	0,155	0,180	49,82	74,91	87,46
Colle	0,2	0,045	0,100	0,150	0,175	0,022	0,034	0,039	49,82	74,91	87,46

(a) Plan bending

	ϵ_{max} (mm)	%X$_0 max$	ϵ_{moy} (mm)			%X$_0 moy$			%probabilité ($\sigma_{geom.}$)		
			Zone 1	Zone 2	Zone 3	Zone 1	Zone 2	Zone 3	Zone 1	Zone 2	Zone 3
Foam	20	0,256	9,46	14,766	17,146	0,121	0,189	0,219	47,3	73,83	85,73
FR4	0,4	0,206	0,189	0,295	0,343	0,098	0,152	0,177	47,3	73,83	85,73
Colle	0,2	0,045	0,095	0,148	0,172	0,021	0,033	0,039	47,3	73,83	85,73

(b) Plan non-bending

TAB. 0.6 –: *Evaluation de la matière présentée par les plans mécaniques.*

NAPPE KAPTON

		ϵ_{max} (mm)	%X$_0 max$	ϵ_{moy} (mm)	%X$_0 moy$	%probabilité ($\sigma_{geom.}$)
				(valeurs normalisés à la surface d'une lumière)		
couche 1	Etamage	0,070	0,818	0,0101	0,118	14,44
	Pistes (Cu)	0,035	0,244	0,0215	0,150	47,14
	Kapton	0,025	0,008	0,0381	0,013	152,60
	Vernis	0,010	0,004	0,0305	0,007	152,60
	Soudure (Sn/Pb)	0,100	1,168	0,0149	0,174	14,43
couche 2	Pistes (Cu)	0,035	0,244	0,0153	0,107	43,61
	Kapton	0,025	0,008	0,0213	0,007	85,30
	Vernis	0,020	0,004	0,0171	0,004	85,30
couche 3	Etamage	0,035	0,409	0,0012	0,014	3,46
	Pistes (Cu)	0,035	0,244	0,0155	0,108	44,25
	Kapton	0,025	0,008	0,0241	0,008	96,48
	FR4	0,800	0,412	0,0320	0,165	39,96
	Soudure (Sn/Pb)	0,100	1,168	0,0042	0,049	4,20
	Connecteurs plastique	4,000	1,146	0,1346	0,039	11,40
	Connecteurs cuivre	4,000	27,875	0,0603	0,420	0,020
	Vernis	0,020	0,004	0,0193	0,004	96,48

TAB. 0.7 –: *Evaluation de la matière présentée par les Kaptons. Les trois sections,* couche 1, couche 2, *et* couche 3, *correspondent aux sections du modèle décrit sur la page 13. Les valeurs sont normalisées ici à la surface d'une lumière (qui vaut 849,73 mm^2). Pour pouvoir additionner ces valeurs avec celles normalisées par zone, il faut multiplier les valeurs (des trois dernières colonnes seulement) par un facteur 0,5, 0,25, et 0,125 pour les zones 1, 2, et 3 respectivement.*

	ϵ_{max} (mm)	%$X_0 max$	ϵ_{moy} (mm)			%$X_0 moy$			%probabilité ($\sigma_{geom.}$)		
			Zone 1	Zone 2	Zone 3	Zone 1	Zone 2	Zone 3	Zone 1	Zone 2	Zone 3
FR4	0,4	0,206	0,286	0,348	0,375	0,147	0,179	0,193	71,54	86,95	93,78
Couche 1 (Cu et recharge)	0,037	0,258	0,009	0,011	0,012	0,060	0,074	0,087	23,24	30,44	33,59
Couche 2 (Cu et recharge)	0,037	0,258	0,024	0,026	0,027	0,169	0,181	0,188	65,51	70,47	73,83
C	0,006	0,0032	0,002	0,002	0,002	0,001	0,001	0,001	71,54	86,95	93,78
Sn/Pb (60/40)	0,024	0,280	0,009	0,010	0,011	0,104	0,117	0,128	71,54	86,95	93,78
Vernis	0,135	0,031	0,094	0,092	0,089	0,021	0,021	0,020	71,54	86,95	93,78
Connecteurs - plastique	4,47	1,176	0,185	0,092	0,051	0,049	0,024	0,013	5,31	2,66	1,46
Connecteurs - cuivre	3,87	26,97	0,0217	0,011	0,006	0,151	0,077	0,042	1,92	0,96	0,48

(a) Plan bending

	ϵ_{max} (mm)	%$X_0 max$	ϵ_{moy} (mm)			%$X_0 moy$			%probabilité ($\sigma_{geom.}$)		
			Zone 1	Zone 2	Zone 3	Zone 1	Zone 2	Zone 3	Zone 1	Zone 2	Zone 3
FR4	0,4	0,206	0,294	0,347	0,373	0,151	0,178	0,192	73,4	86,79	93,31
Couche 1 (Cu et recharge)	0,037	0,258	0,008	0,010	0,012	0,054	0,066	0,083	26,0	31,45	35,16
Couche 2 (Cu et recharge)	0,037	0,258	0,023	0,028	0,029	0,159	0,193	0,201	61,6	75,04	78,1
C	0,006	0,003	0,003	0,003	0,003	0,001	0,002	0,002	73,4	86,79	93,31
Sn/Pb	0,024	0,280	0,011	0,013	0,014	0,123	0,149	0,159	73,4	86,79	93,31
Vernis	0,135	0,031	0,099	0,117	0,126	0,026	0,031	0,034	73,4	86,79	93,31
Connecteurs - plastique	4,47	1,176	0,185	0,092	0,047	0,049	0,024	0,012	4,14	2,07	1,05
Connecteurs - cuivre	3,87	26,97	0,022	0,011	0,006	0,152	0,076	0,038	1,68	0,84	0,42

(b) Plan non-bending

TAB. 0.8 –: *Evaluation des épaisseurs de matière dans les cartes mères. Les couches 1 et 2 sont expliquées dans la figure 0.10 sur la page 14.*

	ϵ_{max} (mm)	%X$_0$*max*	ϵ_{moy} (mm) (valeurs normalisés à la surface d'un MANU)	%X$_0$*moy*	%probabilité ($\sigma_{geom.}$)
Cu - 6 couches	0,072	0,502	0,016	0,111	96,4
FR4 - 5 couches	0,50	0,258	0,500	0,258	98
Recharge - 2 couches	0,05	0,348	0,022	0,153	22
Vernis - 2 couches	0,02	0,004	0,020	0,004	100
Composants passifs (Si)	0,80	0,854	0,032	0,034	4
Composants actifs (Cu)	0,1	0,697	0,017	0,118	17
Composants actifs (Si)	0,40	0,427	0,040	0,043	10
Composants actifs (Encaps.)	1,4	0,722	0,238	0,123	17
Connecteur Berg plastique	0,91	0,261	0,079	0,023	8,70
Connecteur Berg Cu	0,40	2,787	0,035	0,244	0,88
Connecteurs SAMTEC Cu	8,5	59,233	0,030	0,209	0,33
Connecteurs SAMTEC plas.	4,0	1,333	0,105	0,035	2,58

TAB. 0.9 –: *Evaluation de la matière des principaux composants de la carte fille (MANU12). Notez que la surface de normalisation est celle d'un MANU12 (surface$_{MANU}$ = 63×23 mm^2). Pour pouvoir comparer ou additionner ces valeurs avec celles des autres tableaux où la normalisation est faite par zone (à l'exception des Kaptons), il faut appliquer un facteur multiplicatif de normalisation de 0,856, 0,428, et 0,214 pour les zones 1, 2, et 3 respectivement.*

Parcours d'une particule traversant le quadrant

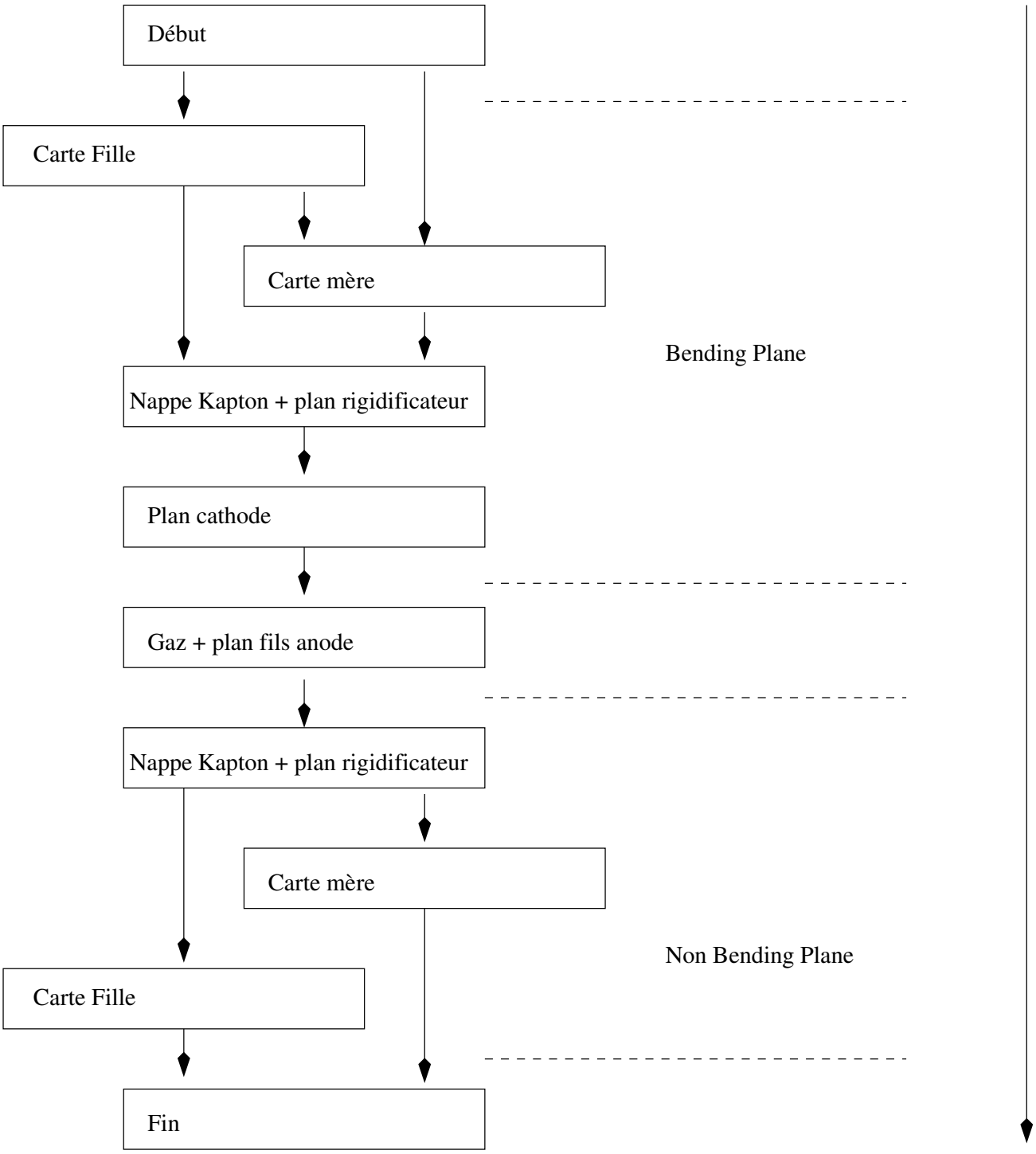

FIG. 0.15 –: *Représentation synthétique du trajet d'une particule à traver un quart de chambre. Se référer aux autres organigrammes pour plus de détails.*

MANU12 - parcours typique A - les connecteurs

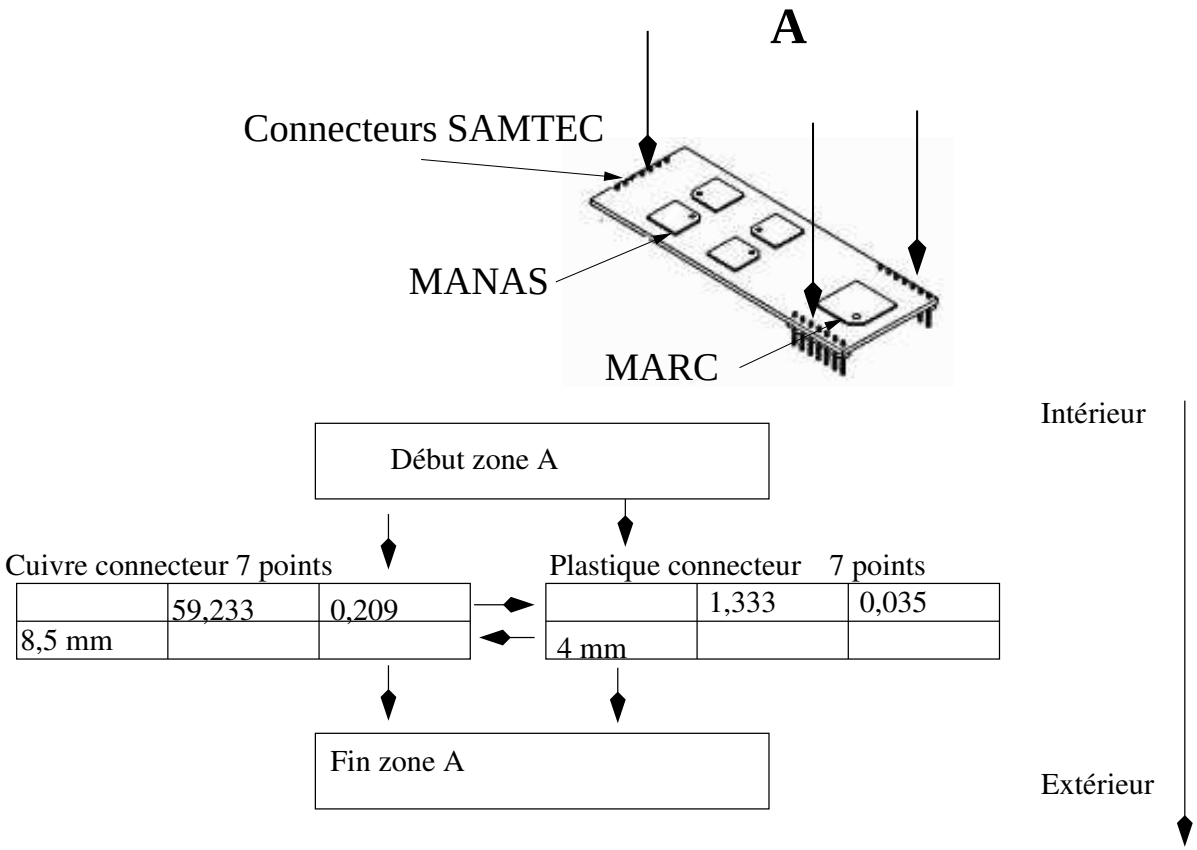

matière	X/X_0 Max	X/X_0
épaisseur		

X/X_0 en %

FIG. 0.16 –: *Carte Manu12 zone A (connecteurs 7 points). Les valeurs sont normalisées à la surface de la carte. Voir text et table 0.9 pour le détail des calculs.*

MANU12 - parcours typique B - les composants actifs

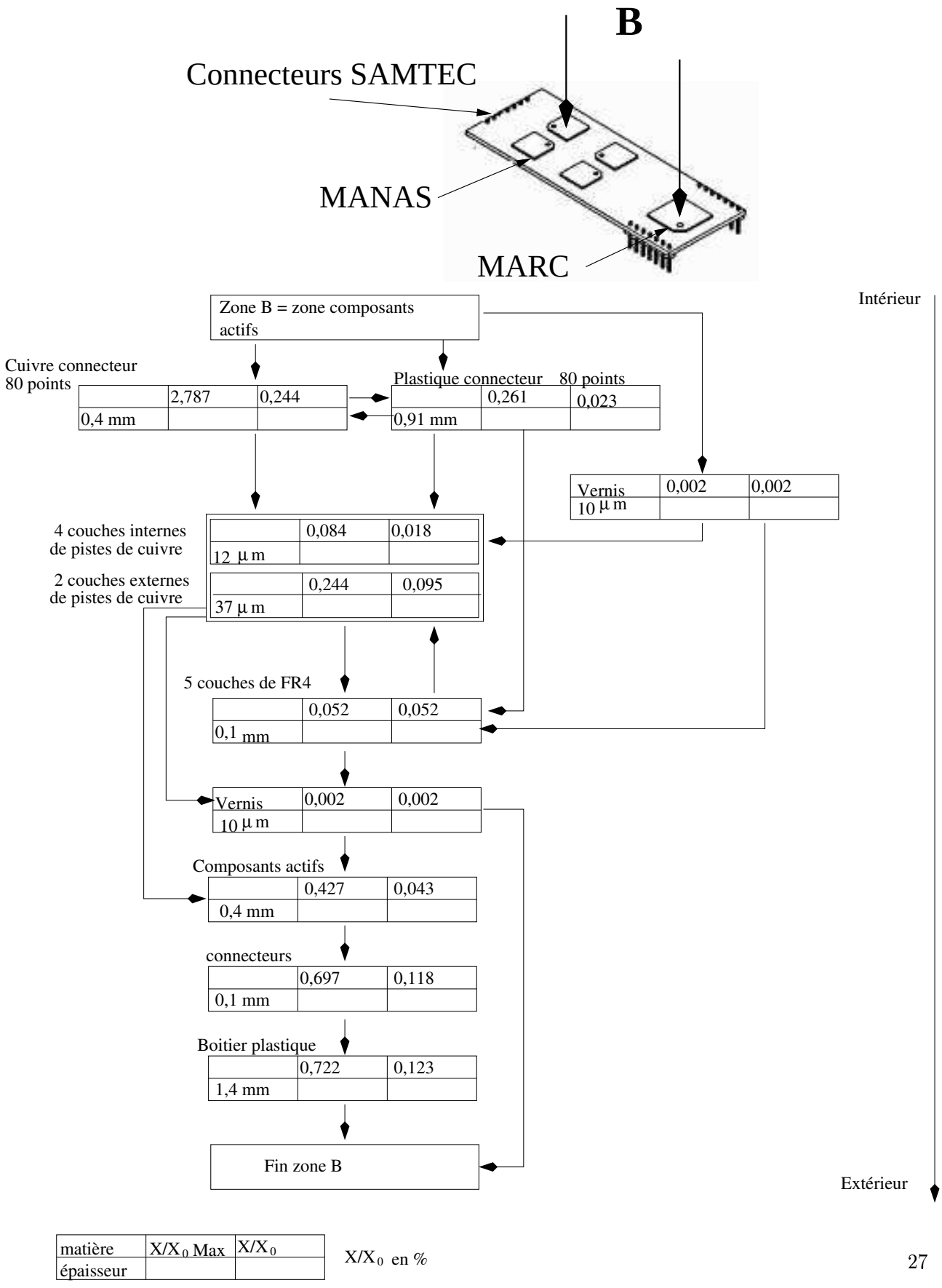

FIG. 0.17 –: *Carte Manu12 zone B (composants actifs). Les valeurs sont normalisées à la surface de la carte. Voir text et table 0.9 pour le détail des calculs.*

MANU12 - parcours typique C- les composants passifs

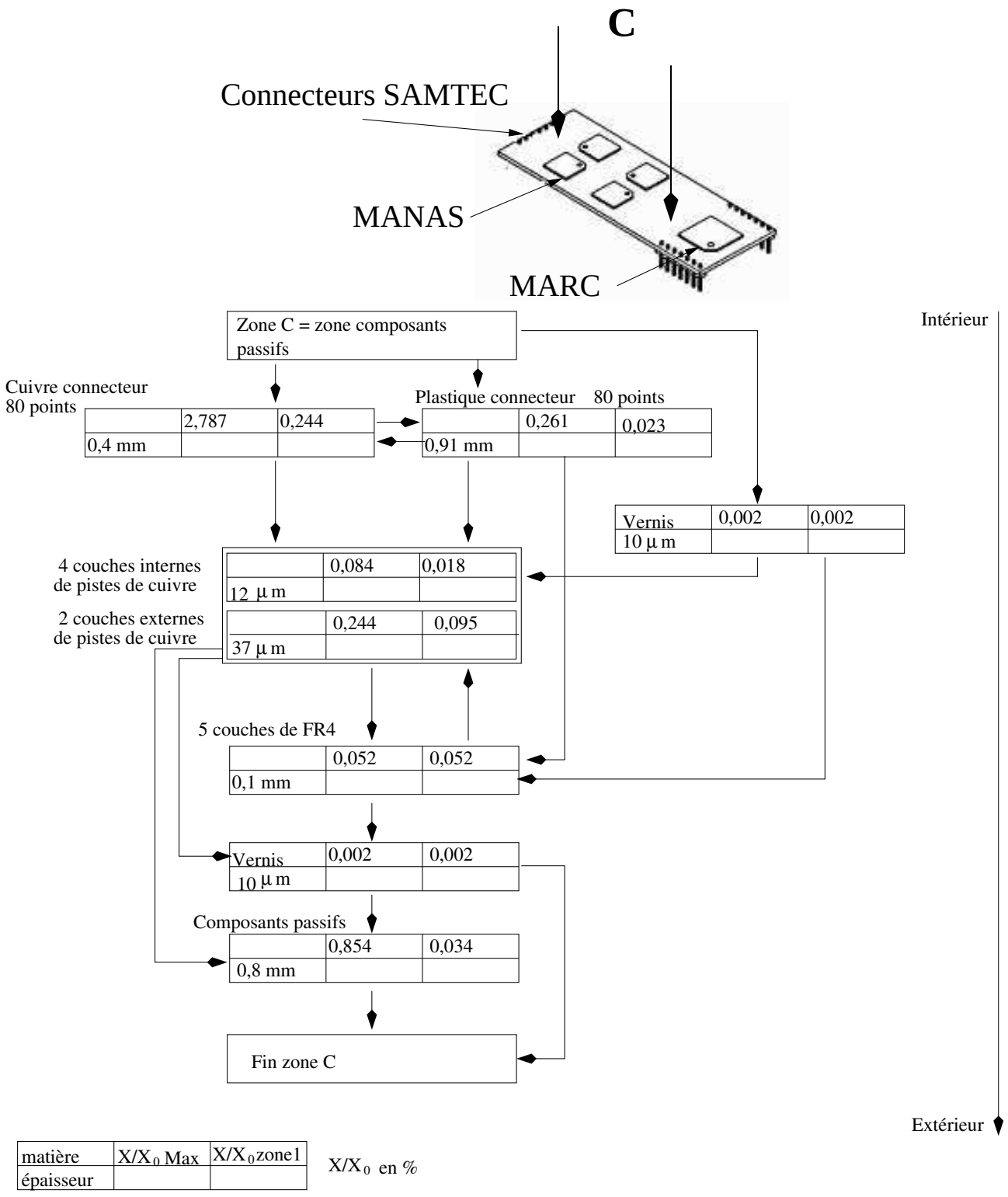

FIG. 0.18 –: *Carte Manu12 zoneC (composants passifs). Les valeurs sont normalisées à la surface de la carte. Voir text et table 0.9 pour le détail des calculs.*

Carte Mère - parcours possibles

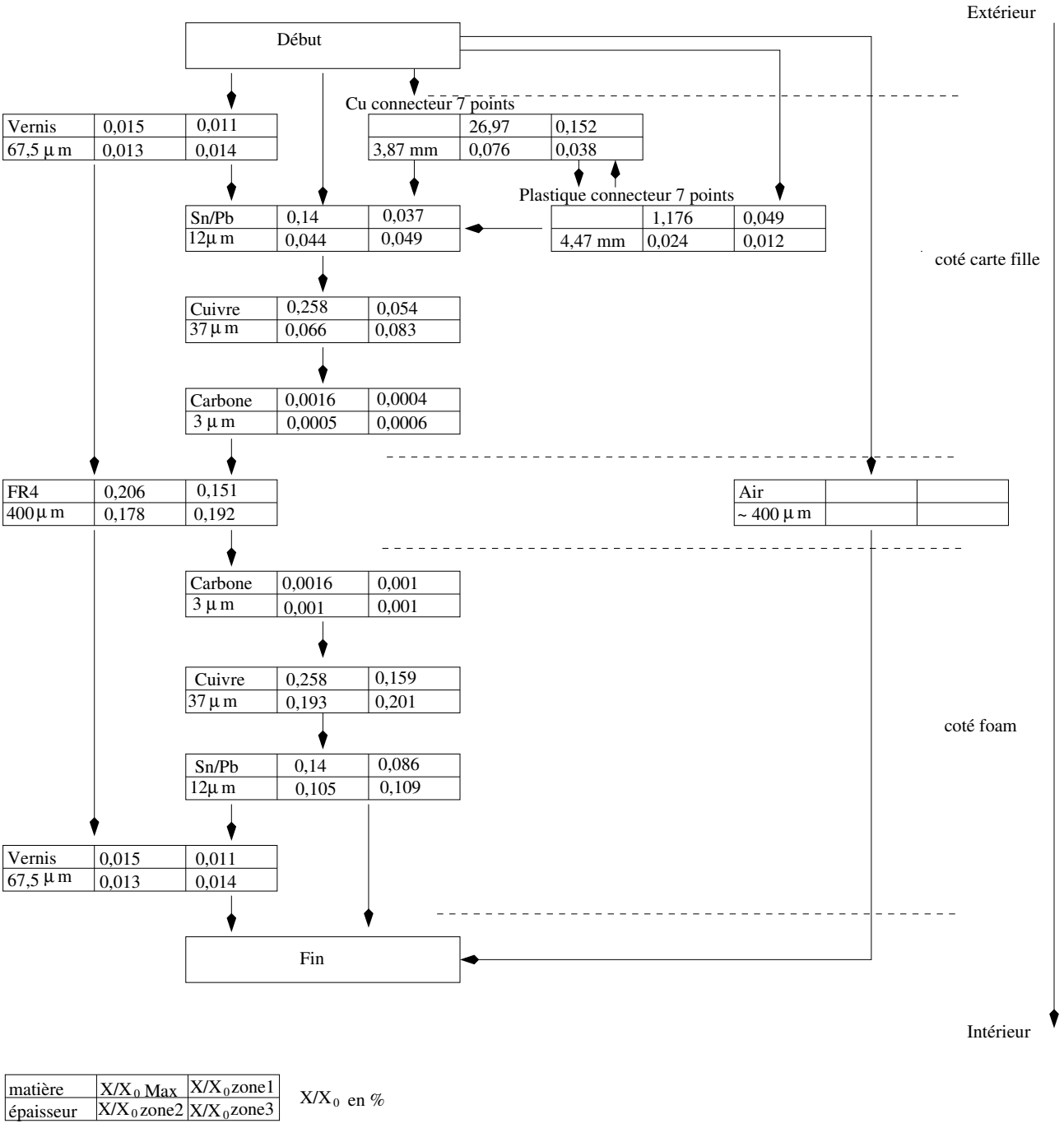

FIG. 0.19 –: *Carte mère, support des cartes Manu12. Voir text et table 0.8(b) pour le détail des calculs.*

Plan rigidificateur - parcours possibles

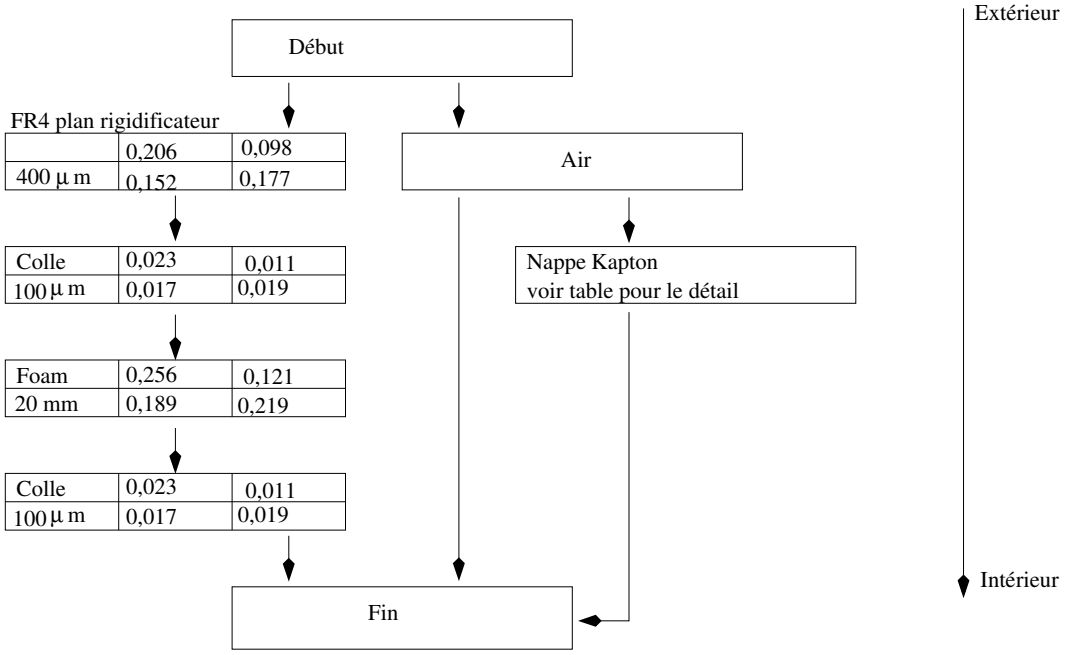

matière	X/X_0 Max	X/X_0 zone1
épaisseur	X/X_0 zone2	X/X_0 zone3

X/X_0 en %

FIG. 0.20 –: *Plan rigidificateur. Voir text et table 0.6(b) pour le détail des calculs.*

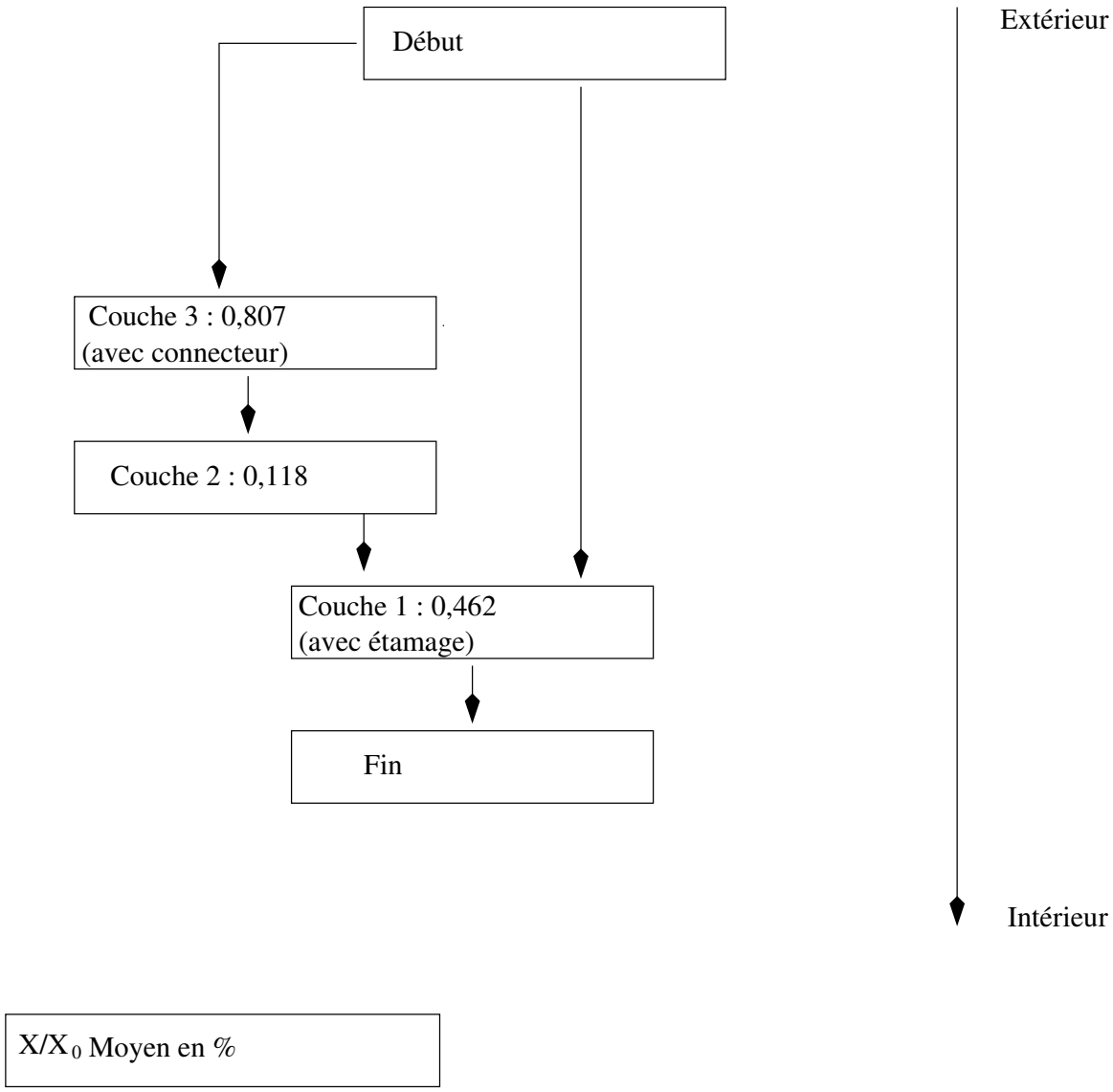

FIG. 0.21 –: *Nappe Kapton. Les valeurs sont normalisées à la surface d'une lumière du plan rigidificateur. Voir text et table 0.7 pour le détail des calculs.*

Plan cathodique - parcours possibles

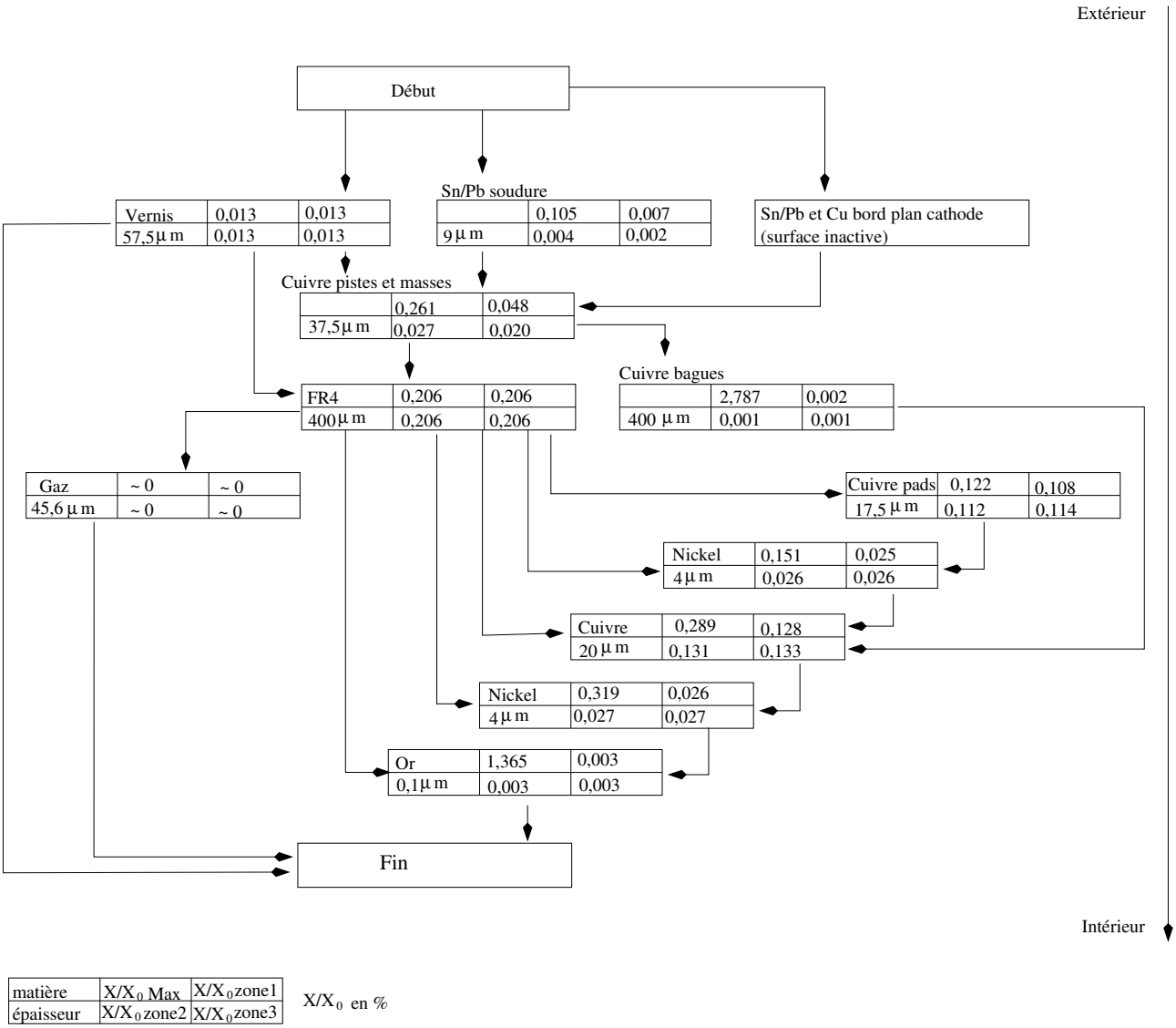

FIG. 0.22 –: *Plan de cathode. Voir text et table 0.5(b) pour le détail des calculs.*

% X_0 cumulé BENDING				
		ZONE 1	ZONE 2	ZONE 3
Plan Cathodique	Face Pads	0,284	0,292	0,295
	FR4	0,208	0,207	0,206
	Face Circuit	0,090	0,058	0,041
	total	0,582	0,557	0,542
Plan Mécanique	total	0,253	0,381	0,443
Kapton	total	0,694	0,347	0,173
Carte Mère	FR4	0,147	0,179	0,193
	Couches de Cu	0,355	0,394	0,424
	Connecteurs	0,200	0,101	0,055
	total	0,702	0,674	0,672
Carte Fille (MANU)	FR4 et Cu	0,480	0,240	0,120
	Composantes Actives	0,243	0,122	0,061
	Connecteurs	0,437	0,219	0,109
	total	1,160	0,581	0,290
X_0 total		3,391	2,540	2,120

% X_0 cumulé NON BENDING				
		ZONE 1	ZONE 2	ZONE 3
Plan Cathodique	Face Pads	0,290	0,299	0,303
	FR4	0,206	0,206	0,206
	Face Circuit	0,069	0,045	0,036
	total	0,565	0,550	0,545
Plan Mécanique	total	0,240	0,374	0,435
Kapton	total	0,696	0,348	0,176
Carte Mère	FR4	0,151	0,178	0,192
	Couches de Cu	0,408	0,497	0,530
	Connecteurs	0,201	0,100	0,050
	total	0,760	0,775	0,772
Carte Fille (MANU)	FR4 et Cu	0,479	0,240	0,121
	Composantes Actives	0,243	0,121	0,062
	Connecteurs	0,437	0,219	0,111
	total	1,160	0,580	0,294
X_0 total		3,421	2,627	2,222

TAB. 0.10 –: *Resumé des longueurs de radiation du plan Bending (en haut) et Non Bending (en bas). Différents matériaux sont regroupés sous un même titre indicatif correspondant à la matière prépondérante.*

APPENDIX D - mappingPackage.pdf

IPN Orsay
91406 ORSAY Cedex
France

ALICE Refrence Number
ALICE-INT-2003-025 version 1.0
Institute reference number
[-]
date of last change
24th September 2003

The mapping package for the ALICE Dimuon Arm Spectrometer

D. Guez, I. Hřivnáčová, M. MacCormick
IPN Orsay, 91406 ORSAY, France

Abstract

The ALICE Dimuon Arm Spectrometer mapping package is described in this report. It is a program that facilitates the definition of the detectors' geometrical and electronics parameters. A two-way mapping, giving access to electronics addresses through the geometrical location and vice-versa, lies at the heart of the program. After an introduction describing the relevant detector and electronics objects, the contents of the software package will be described. It is currently implemented for station 1, has been used successfully in test-beam prototype experiments and also in the general ALICE simulation program AliRoot. A guide to the program architecture, showing how to run and test the code is given.

(2nd July 2003)

1 Introduction

In the dimuon arm spectrometer [1], over the 10 tracking multi-wire proportional chambers, there are approximately 1.2 million individual charge coding channels. These channels are implemented in the form of pads which are etched onto the surfaces of the two cathode planes of each detector. The way in which they are distributed over station 1 (which regroups the first two tracking chambers) will be looked at in detail in the following paragraphs.

Each channel is connected to one unique pad segment of a cathode pad plane, each pad having a unique spatial location. All channels are read out individually via parallel, multiplexed lines and are stored event-by-event in 32 bit words containing the charge measured and its local electronics ID tag number. The output lines are funnelled into two successive levels of so-called "concentrator" boards, where they are concactenated and attributed a second ID tag. Consequently, a charge measured on a pad at position (x,y,z) is coded under two unique ID numbers, specified by the system designers. In the following, it is the first electronics ID tag that is of interest. The second one is treated by a separate acquisition code.

The overall mapping consists of :

- finding the electronics ID tag for a pad when given its spatial coordinates;
- determining spatial coordinates from an electronics ID tag;
- locating the nearest pad neighbours indifferently, starting from the electronics ID or pad position;
- providing the means to correlate the charge measurements on opposing cathode planes, and
- doing all of this in an efficient, user friendly way.

The elementary problem description is quite straightforward, and constitutes a standard experimental situation. As long as the key to decoding the electronics information is given, and the experimental layout is known, then there is no particular problem. In the dimuon spectrometer it is the volume of data, and its organisation into manageable entities which is of interest.

In order to explain this in greater detail, the overall layout of the different electronics entities will be presented along with their relationship to the geometrical pad layout scheme. The different kinds of mapping that are used in current detector work are given, and clearly define the different levels of interest of different working groups. Finally, the architecture of the program itself is described along with a description of how to run and test it.

Geometry, electronics, symmetries and terminology

The general layout of the 4 quadrants of the segmented cathode MWPC's that make up the two tracking chambers of station 1 is shown in figure 1 [1]. Station 2 is also shown, it has a different internal geometry, but is built on the same model as station 1. Each quadrant has two active planes, that measure the spatial coordinates $(x,y)_{mm}$ of incident particles. The spectrometer's dipole magnetic field curves trajectories in the "y" direction and is commonly called the "bending" coordinate. The "non-bending" coordinate therefore corresponds to the "x" direction. The bending cathode plane has a segmented pad geometry that gives a high resolution y-coordinate measurement, and its layout is different from that of the the non-bending plane which provides the lower resolution x-coordinate

There are three different zones defined on each cathode plane, going from smaller segments in the inner radii that will allow to resolve the higher density of impact points

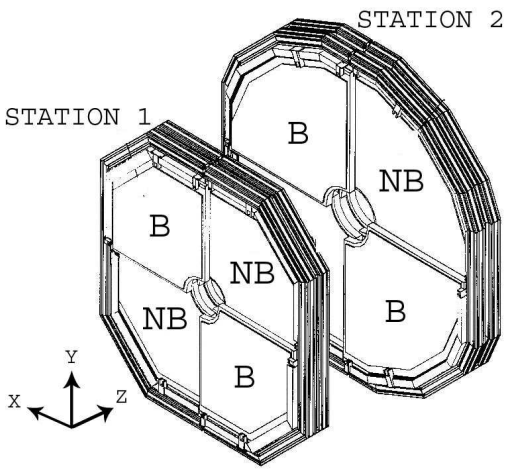

Figure 1: A view of the layout of the chambers of stations 1 and 2. Each station is composed of two independent chambers, and each chamber is composed of four quadrants.

in this region, to the larger segments in the outer zones. An example of the overall layout for a non-bending plane is shown in figure 2(a). The bending and non-bending template is repeated for each of the quadrants, and the final chamber layout is composed of 4 identical quarter chambers that are mounted together with a simple reflection symmetry. The coordinate system of each quadrant is a reflection in the common axis of adjacent elements.

The layout of the cathode surface is organized into groups of 64 elementary pad blocks called “motifs". The motifs' wiring schemes, are based on repetitive designs, the aim being to simplify the overall detector design and usage by having as much symmetry as possible. An example of a typical motif layout is shown in figure 2(b). The 8x8 rectangular grid represents the pad surfaces that measure the charge signal, and the lines are the feed-through copper rails that transmit the signal to the 66 point flexible Kapton^{TM} connector that would be soldered on to the 3 rows of points visible in the design. Located at the other end of the Kapton connector is an 80 point connector that allows to plug the flexible Kapton into the 64-channel front-end data analysis card. This connector is the so-called "Berg" connector referred to in the mapping package. A close-up of the two sides of a front-end data analysis card, with the major components highlighted, can be seen in figure 3(a).

A photograph of a quadrant is shown in figure 3(b) and the regular layout of the readout electronics can be seen. The system, similar in appearence for both cathode planes, is composed of lines of electronics cards, plugged into a common bus, that regroups up to a maximum of 26 front-end cards. Each front-end card allows to measure and code 64 individual pads (ie., one motif). It is the digital output from these cards that transit in the buses lines that run from left to right in the photograph 3(b).

These outputs are then input, in sets of 5, to a sequence of DSP's implanted on front-end and concentrator electronics boards. These boards regroup the data from the different detector buses (there are a total of 13 buses per quarter chamber regrouping the 30,000 elementary channels), concactenate them and, eventually communicate them through the ALICE DDL (Detector Data Link) and on to the common part of the ALICE acquisition system [2].

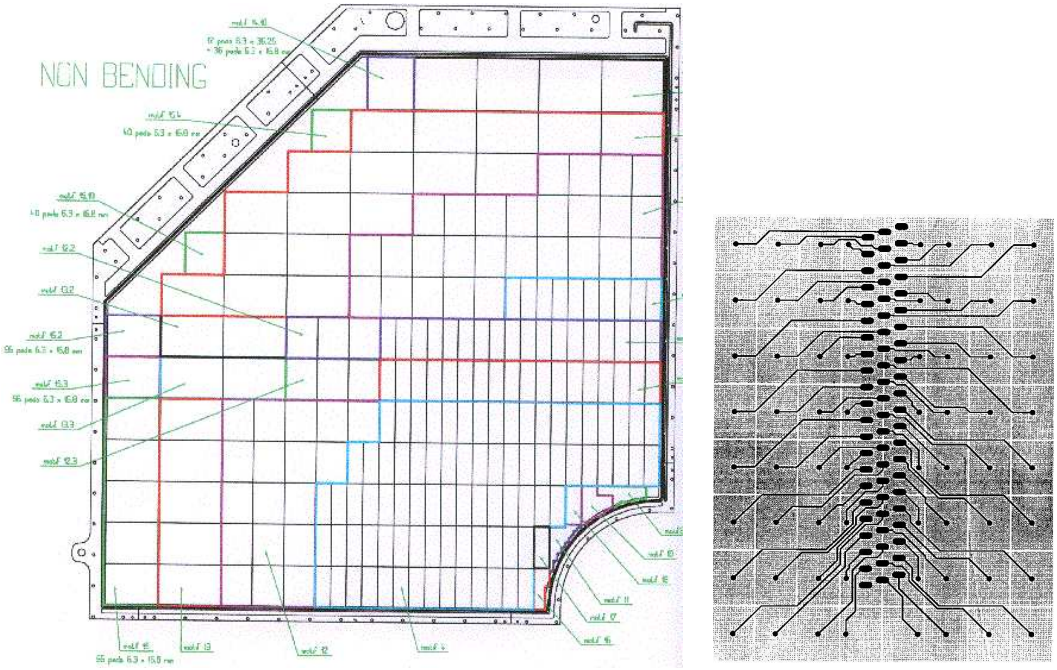

(a) (b)

Figure 2: (a) Layout of the major elements on the non-bending plane. Three distinct zones, corresponding to three different elementary pad sizes can be seen. Each rectangle symbolises the outline of the individuals motifs. (b) An example of a typical motif showing a set of 64 pads and the wiring scheme to the central connector is visible.

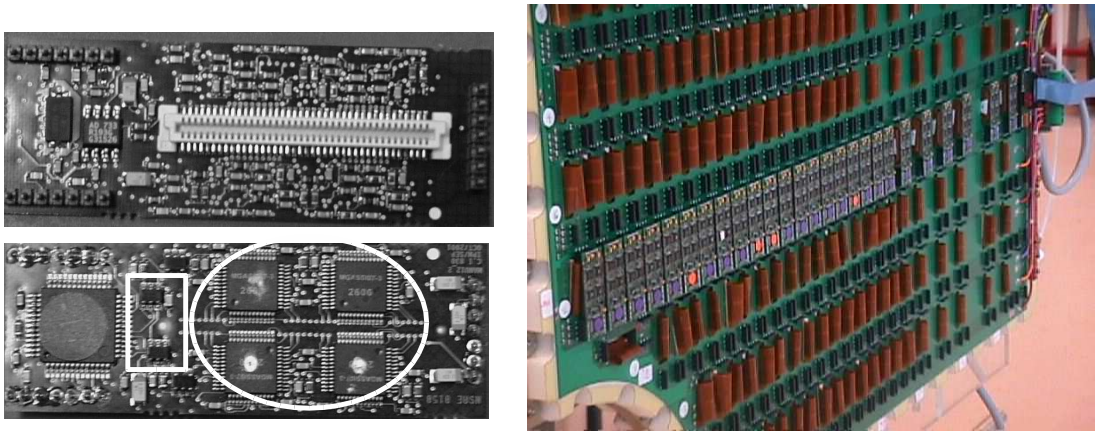

(a) (b)

Figure 3: (a) A close-up of a 64 channel data analysis card. The upper image show the back-side of the card. The 80 point “Berg" connector that links up with the pads via the flexible Kapton connector can be seen. This is therefore the entry point for the charge signals. The lower image shows the front view, and the main charge analysis components are identified. The 4 GASSIPLEX/Manas chips are highlighted by the oval shape, and the white rectangle shows the position of the two ADC chips. The card deals with a total of 64 channels, corresponding to one whole motif. (b) A photograph of a quarter chamber. The regular electronics readout scheme can be seen on the outside of the detector. One readout bus is implemented with its front-end cards, each card has a multiplexed 64 channel digital output that contain the coded charge measurement from 64 individual pads. The bus is read from left to right in the photograph.

The different tasks

Different kinds of mapping are required, depending on the task in hand. In the mapping software, this has been taken into account. The path followed by a single charge measurement, in going from a unique pad at position (x,y) (in mm) on a cathode plane to its final storage position the general ALICE event architecture, is shown symbolically in table 1. In this simplified view, there are different interfaces with each unique pad signal being attributed a fixed transit channel at each level. In order to retain the memory of this trip, and to provide a unique address, the datum picks up two ID tags along the way. The first ID tag, attributed at the output of the 64 channel analysis card, identifies the channels used for each pad signal on the analysis card. This ID is held in a 17-bit word that allows to identify the GASSIPLEX/Manas and ADC channels as well as the card ID itself. The second tag is attributed during the data concatenation on the "CROCUS" data concentrator boards. Its coding and decoding is treated by a separate code. It is only through decoding both ID tags that the original pad position of a measurement can be determined in the full spectrometer layout. However, for an isolated quadrant, the first level ID contains enough information for identifying a unique pad location, and it is this ID that is of interest here.

Charge measurement	$\longrightarrow (x,y)_{mm/pad\ units}$		Data Taking	
HARDWIRED	IN : 66 PT CONNECTOR OUT : 80 PT CONNECTOR	flexible Kapton^{TM} connector	⇓ ⇓ ⇓ ⇓	
ELECTRONICS ID TAG #1	16 CHANNEL GASSIPLEX/MANAS ANALYSIS CHIP 32 CHANNEL 12 BIT ADC	64 channel analysis card		⇑
ELECTRONICS ID TAG #2	SUCCESSIVE DATA CONCENTRATOR CARDS	"CROCUS" system		⇑ ⇑ ⇑ ⇑
Charge storage	→ ALICE DDL			Data Analysis

Table 1: Summary of the different elements through which a single charge measurement transits. Only the main electronics functions are highlighted. The mapping at each interface must be accessible for debugging and monitoring. The initial and final points are used for the event reconstruction in the online, offline and simulation work.

The arrows in the end columns of table 1 show the usual direction of interest, depending on whether data is being taken or analysed. However, the end point is not the same for all users.

In table 2 the minimum requirements for different types of work are given. For the sake of simplicity, the most common tasks are listed. The cross marks the type of mapping level that is usually required in each of these situations. In the physics simulation world, one does not care too much about the order in which the electronics cards are plugged in, since the main aim is to simulate and manipulate the information on the detectors' cathode planes. The important point here, is that functions, such as determining the nearest neighbour, use the same interface as in the offline data analysis. In this way the same analysis code can be used in both cases, hence rendering the overall effort more efficient.

On the other hand, the detailed detector simulation, which uses real experimental data as an input, requires a different level of mapping. Each individual channel is associated with its full set of experimental characteristics, ie. pedestal, noise and threshold levels, calibration factor and status flag. The mapping of the electronics numbering system

is essential in coordinating and associating this information in the correct way. Every effort has been made to ensure that the detailed detector simulation code truly corresponds to the experimental, data taking environment.

	pad $(x,y)_{mm}$	Elecronics coding filters	Final electronics ID
physics simulation	X		
detector simulation	X	X	
offline analysis	X	X	X
online monitoring		X	X
laboratory tests		X	

Table 2: The most frequent tasks that use the same mapping are listed in the left-hand column. The column headings are the major mapping levels, as annotated in table 1, while the cross marks the minimum need for each task. All tasks can use all the mapping levels if so desired.

In test-beam activities, where online monitoring is used, the first questions asked are generally to do with the state of the electronics readout and detector tuning. It's therefore more appropriate to be able to efficiently view the response from individual electronics modules. The intermediate electronics mapping levels are more important in this case.

Although all tasks can use all the mapping levels if so desired, it is in the offline analysis, where the full mapping is used. In this case, data are delivered with their full electronics ID, the associated charge may be submitted to various cuts and calibrations before being united with its unique physical pad location. Event reconstruction is built up from different sources of information for example, mapping information, calibration data, and dead channel masks.

The mapping package was developed in order to have a generic mapping code that could be used indifferently in full scale simulation, test-beam data taking or offline data analysis. It can also be used in laboratory electronics testing, in situations where only the electronics chain, minus the detector is generally used. As will be shown in the following, all of this can be done for partially or fully implemented detectors, using exactly the same code, the user only needs to provide some data files.

2 Program architecture

The mapping package exploits object-oriented technology and is written in C++. It is based on the ROOT framework [3] and has been developed for the ALICE experiment [4], it consequently follows the ALICE C++ Coding Conventions [6].

The various classes have been structured into categories that reflect the physical design of stations 1 and 2 (as previously shown in figures 1 and 2). These categories are as follows :

basic - common elementary classes, interfaces;
motif - classes related to the motif;
sector - classes related to the composition of sector;
plane - classes related to the plane, and
graphics - classes for visualization.

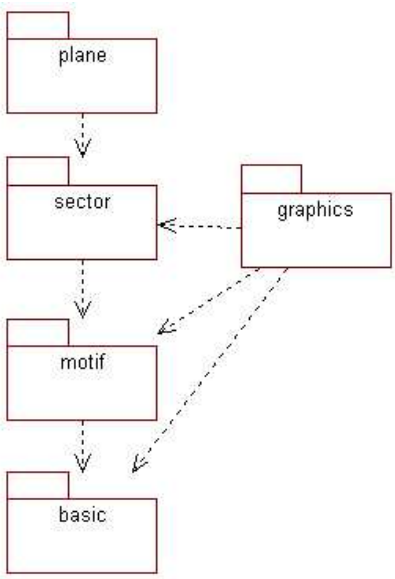

Figure 4: Class categories

As can be seen from the class diagram structure in figure 4, the category dependencies are unidirectional.

The detector description uses the following entity definitions :

pad - smallest element;
motif - repeatedly placed ensemble of pads (in most cases rectangular) with given characteristics;
row segment - a segment of a row of motifs containing motifs of the same type;
row- row of motifs composed of row segments;
subzone - region of the plane with the same motifs;
zone - region of the plane with pads of the same dimension;
sector - plane quadrant;
there is a requirement for a constant pad size in one direction, and
plane - whole plane, composed of four sector positions.

The relationship between these entities and the physical components of the detector can be deduced from figures 1 and 2.

For some areas of the detector description, there are special cases that need to be taken into account. This is done through the definition of abstract base classes, the derived

classes are then implemented in both standard and specific cases. In the case of motif, the standard motif is composed of pads of the same dimensions while a special motif can be composed of pads with varying dimensions. In the case of row segment, the standard row segment is composed of the same, rectangular motifs, while the special row segment is composed of unique, not rectangular motifs that can go beyond the standard row area.

Besides the entities that make up the plane composition, there are also logical entities that allow to navigate between the pads :

segmentation - provides functions for retrieving pads, starting from given characteristics (ie., position, location, and indices) and for finding pad neighbours (ie., up, down, right, and left), and

pad iterator - which provides the means to iterate over the pads.

In the folowing paragraphs the key classes for each category will be described.

2.1 Basic classes

The category overview is presented in the class diagram of figure 5. This category includes all the common elementary classes, the interfaces and utility classes.

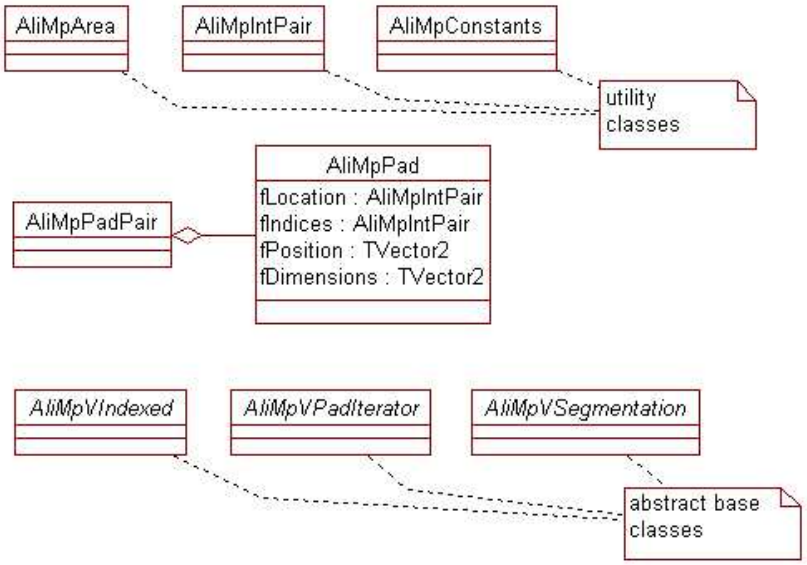

Figure 5: Basic class diagram.

AliMpPad is the most frequently used elementary class, it defines the pad object with the following characteristics :

position - position of the pad (x,y) in the global coordinate system;

dimensions - half length of the pad size in x and y;

indices - the number of the pad in the row, and the column in the plane (ix,iy);

location - motif position identifier plus the "Berg" connector number of the pad

The interfaces *AliMpVSegmentation* and *AliMpVPadIterator* are introduced for the logical entities segmentation and pad iterator, they will be discussed further in section 2.5. The *AliMpVIndexed* interface defines the common properties for all structural elements with indices.

2.2 Motif classes

The category overview is presented in the class diagrams of figures 6 and 7.

The motif in the cathode plane is represented by the motif object which is defined as being a composition of the information concerning the pad size (or pad sizes in the special motif case) and the motif type. The motif type contains, among other characteristics,

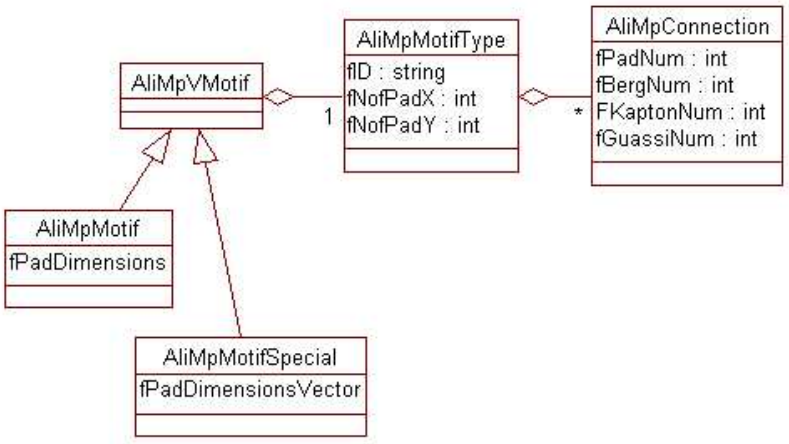

Figure 6: Motif class diagram.

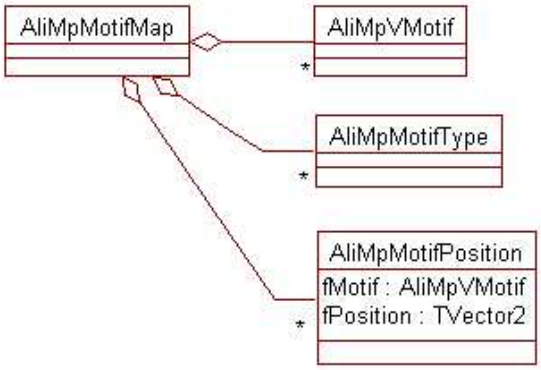

Figure 7: Motif map class diagram.

a map of all its connections. The connection describes the local electronics channel/pad characteristics :

Berg connector number;

Kapton connector number, and

GASSIPLEX/Manas channel number.

The relationships between the key classes *AliMpVMotif*, *AliMpMotifType*, and *AliMpConnection* are shown in the class diagram of figure 6. The physical objects are shown in figure 2(b) and the photographs of figure 3.

The placing of the motif on the cathode plane is represented by the motif position object. Each motif position has a unique integer identifier, which is specified in the input data and is identical to the one used during data acquisition.

In order to provide a fast access to the motif, motif types and, motif position objects, the maps between the object identifiers (string or integer) and the pointers to these object are built. These maps are contained in the motif map object defined by the *AliMpMotifMap* class (shown in figure 7).

2.3 Sector classes

The category overview is presented in the class diagrams of figures 8 and 9. To

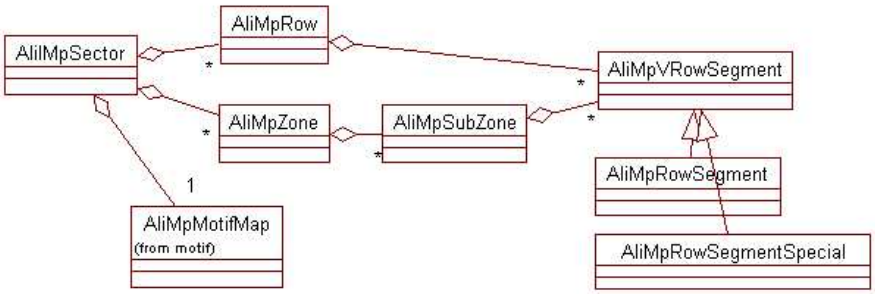

Figure 8: Sector class diagram

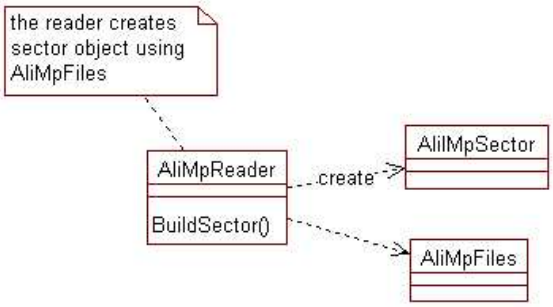

Figure 9: Sector reader class diagram.

facilitate the definition of the sector layout, the row segment entity was introduced. The standard row segment is defined as being a row of motifs of the same type; the mapping package requires that the motif position identifiers that belonging to the same row segment are sequentially increasing or decreasing. The special row segment case will be described later in this section.

The key class of this category is the sector class, named *AliMpSector*, that represents a physical quadrant of the plane, and can be compared to figure 2(a). The sector is composed of row segments which are organised into two complementary logical structures, namely:

- in rows - this logical structure follows the physical design of the plane; the row is composed of row segments having the same y coordinate value.
- in zones and subzones - subzones are composed of the row segments which have motifs of the same type and pad dimensions; zone is a set of subzones which all have the same pad dimensions.

The relevant classes, and their relationships, are shown in the class diagram of figure 8.

The sector is built up from the ASCII data files provided by a user and read by the sector reader object, defined by the *AliMpReader* class. More will be said about data files in section 3.1. All file names and paths are defined in the *AliMpFiles* class. The sector reader classes are shown in figure 9.

Special zones

In the inner part of the non-bending quadrant of station 1 the motifs have a unique and irregular pad layout (see figure 2(a)). As well as this, the y-coordinate can go beyond the standard row size (the standard layout is 8 pads high). This area, which has been called a special zone in the mapping, is then decomposed into special row segment objects, defined in the *AliMpRowSegmentSpecial* class. This class follows the row segment interface *AliMpVRowSegment*, as shown in figure 8. A special row segment is defined via pad rows, defined in the *AliMpPadRow* class which are composed of pad row segments, defined in the *AliMpPadRowSegment* class. The pad row segments then define which pads belong to the same motif.

The current implementation supports the inner special zones and is now being extended to include the special zones that exist in the outer edges of station 2.

2.4 Plane classes

The category overview is presented in the class diagram of figure 10. The plane class

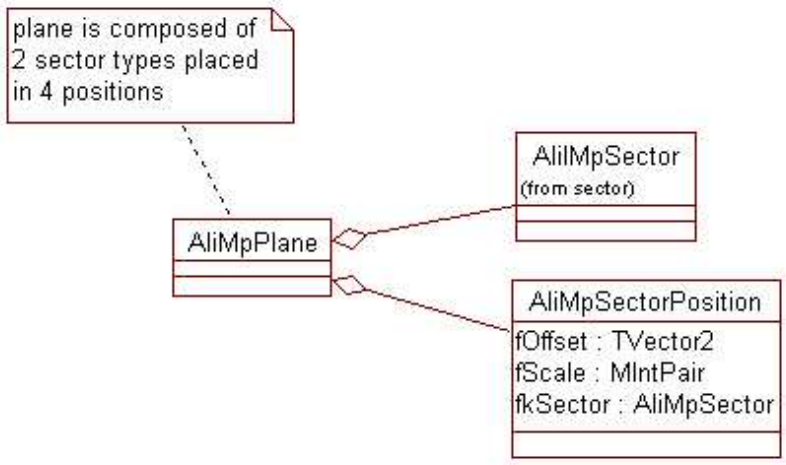

Figure 10: Plane class diagram.

AliMpPlane, defines a plane as being a composition of four sector positions, as defined by the *AliMpSectorPosition* class. The position of each sector is specified through 2D translations and reflections.

The current plane definition is defined in only 2-dimensions, the 3D transformation is not yet available. This functionality will be provided in future in order to accomodate the information provided by the external geometrical alignment procedure [7]. The plane class can also be easily generalized so that any number of sector positions can be instantiated. This is a requirement for stations 3, 4 and 5 where ladders of slats (as opposed to quadrants) are used to build these larger detectors.

2.5 Segmentation and Pad Iterator classes

The segmentation and pad iterator are logical entities that allow to navigate through the pads. As both these entities can be applied at different levels (ie., motif, sector and plane), the segmentation and pad iterator classes are present in almost all categories.

For both the segmentation and pad iterator instances, the abstract base classes are first defined. The segmentation concrete classes are then implemented for sector and plane

elements. The iterator concrete classes are implemented to iterate over various structural elements (such as motif, row segment, sector, etc...) as well as over a rectangular area in the plane, or in the sector.

The abstract factory pattern [8] is applied to the segmentation and pad iterator classes. The segmentation concrete classes implement the function for creating the iterator. The iterator is made in such a way that is the appropriate one for the associated component (ie., motif, row segment, sector, etc...). The efficient searching algorithms in the implementation of the segmentation and pad iterator classes were developed using the standard C++ library.

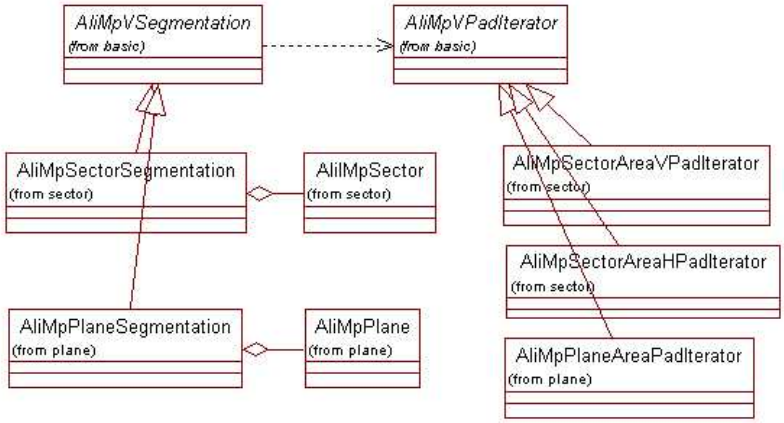

Figure 11: Segmentation and pad iterator (class diagram).

The category overview is presented in the class diagram of figure 11.

2.6 Graphics classes

The category overview is presented in the class diagram of figure 12.

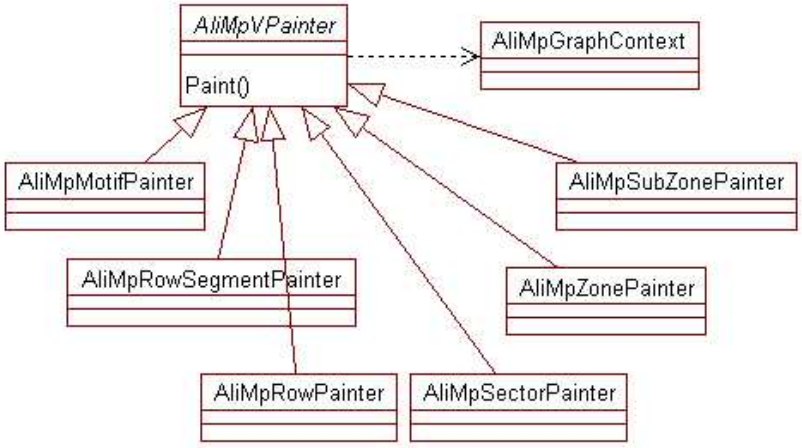

Figure 12: Graphics class diagram.

For most entities in the mapping package that represent real life objects, there is an associated graphics class that allows it to be drawn on the screen. *AliMpVPainter* is the base class for all such classes. These concrete “painter" classes essentially overload the

standard ROOT Paint() method with the appropriate code. In all, there are six classes that derive from *AliMpVPainter* that allow to draw the motif, row segment, row, subzone, zone and sector objects.

As well as the Paint() method, each concrete class also has a Draw() function, as required by ROOT, which can take an input argument. If no argument is provided, the object will draw itself on the screen. However, if an argument is supplied the object can be drawn, not only by the painter itself, but also by instanciating a painter for each component of the object. A full detailed example is provided in the mapping package documentation.

3 How to use and test

In order to use the mapping package the user needs to provide the data files describing the detector. The front-end mapping classes (segmentation and pad iterator) can then be used directly from a ROOT UI (terminal or macro), or from the user client code. The description of the mapping data files and an example of how to use the mapping in a client code will be given in the following sections.

3.1 Data files

All input parameters that define the plane topology, as well as the electronics properties, have to be specified in the set of ASCI data files :

zones.dat - definition of the sector layout;

zones_special.dat - special zones definitions;

motifX.dat - motif type characteristics and electronics wiring;
(X represents a motif type identifier), and

motifPosX.dat - mapping between indices in the motifX.dat file and local (i,j) on the motif.

The detailed desription of the files' format is provided in the mapping package documentation.

3.2 Use of mapping in client code

The mapping package is currently used in the TestBeam ToolBox [9] online monitoring program, in the test-beam data analysis and in the AliRoot simulation program [5]. The front-end classes for the client code are the segmentation and pad iterator classes. In example 3, we show how the user can instantiate the plane object, create its segmentation and use the iterator to print the properties of all pads in a specified rectangle of the plane.

3.3 Using the graphics classes

The graphics classes are used at different stages of the project. When verifying the mapping code itself, errors can be easily pinpointed by viewing the positions of the individual elements. In the client code used in prototype test experiments, being able to easily superimpose the beam impact points on the mapped elements has greatly speeded up the setting up process. As well as this, should any error occur during data taking, the exact location of the problem can be quickly identified visually via its electronics ID, hence making the monitoring process more efficient. A typical monitor image is shown in figure 13. Finally, in the latest developments in the data analysis code, the graphics classes have been implemented so as to have a visual comparison of the zone where data was measured and the reconstructed impact point. Once again, this facilitates the event by event debugging process.

3.4 Test suite

When developing the code, a test ROOT macro was written for each new part and as a result there are around 15 test macros. The testing procedure has been simplified by writing a Perl script which executes all the macros automatically, and compares the output with the reference output.

Graphics output from the test macros is demonstrated in figures 14 and 15. The first figure, figure 14, shows the sector elements, namely the zones, subzones, row segments, and motifs. The layout of each element is drawn in the canvases. In figure 15 the motifs, with their motif position identifiers, are shown.

```
AliMpPlane* plane
   = AliMpPlane::Create(kBendingPlane);
                    // The plane object is created in this function;
                    // the AliMpReader class is used to read the
                    // input data files and build the sectors with
                    // all their structural elements

AliMpVSegmentation* segmentation
   = new AliMpPlaneSegmentation(plane);
                    // Create the segmentation associated with the plane

AliMpArea area(TVector2(10., 20.), TVector2(20., 20.));
                    // Define the area over which to iterate;
                    // the first argument is the position of the center,
                    // the second argument are the half-lengths

AliMpVPadIterator* it = segmentation -> CreateIterator(area);
                    // Creates the iterator over the area

for (it -> First(); ! it -> IsDone(); it -> Next()) {
                    // Loop over the pads

      cout << iterator << CurrentItem() << endl;
                    // Print the properties of the current pad
}
```

Table 3: An example of a user code

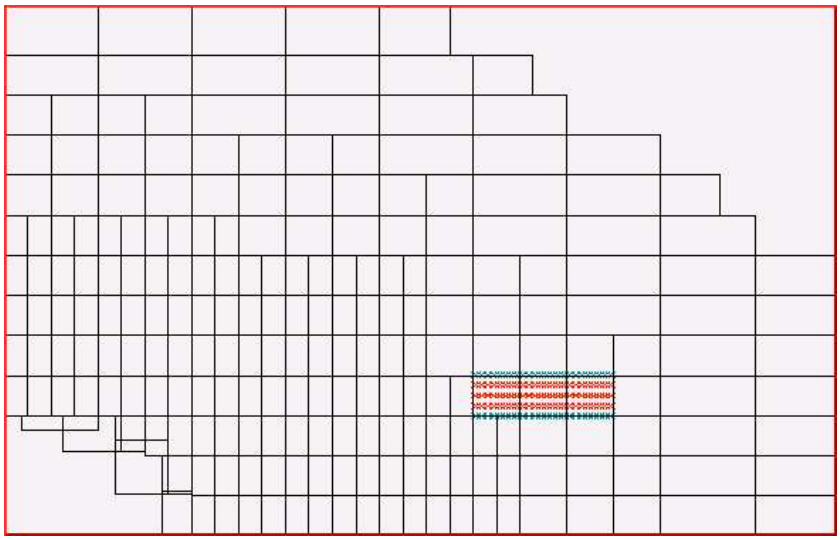

Figure 13: An example of an online monitoring image. The overall detector mapping can be seen with the zone of accumulated beam impact points marked by the small crosses.

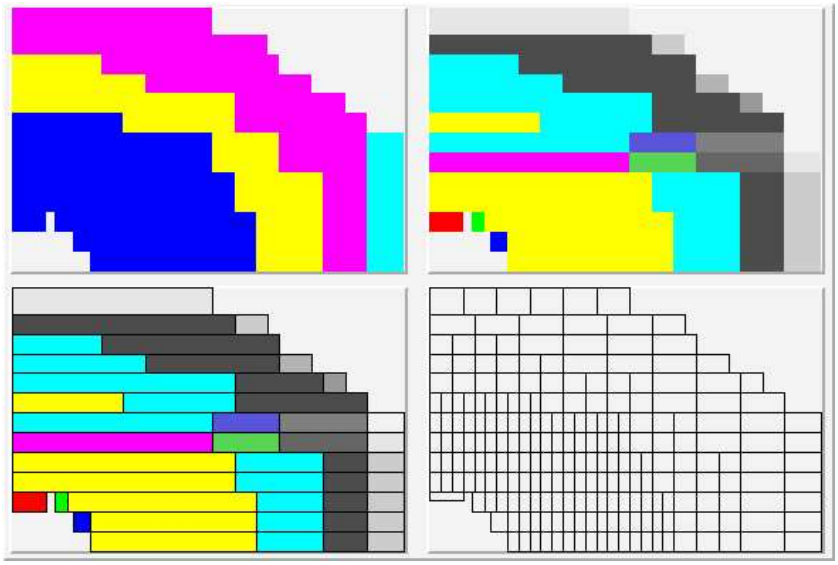

Figure 14: The sector elements: zones, subzones, row segments and motifs as drawn from a test ROOT macro.

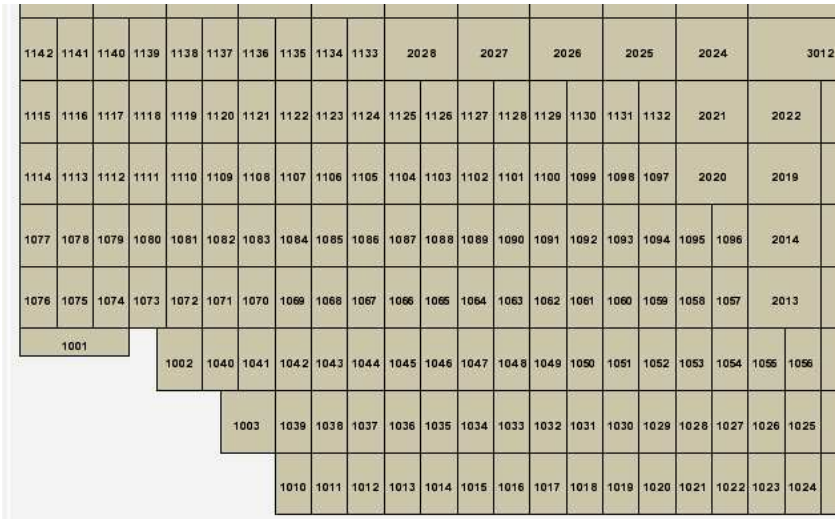

Figure 15: Motifs with motif position identifiers as drawn from a test ROOT macro.

4 Distribution

The mapping package has been included in AliRoot version 3.09, in the MUON library. In order to obtain a copy, and to install AliRoot, the procedure described at [5] should be followed.

Locally, a stand-alone version is used by physicists and engeneers for the purposes of testing electronics and test-beam data analysis. The installation procedure is described in the mapping package documentation.

5 Conclusions

The mapping package has been successfully implemented on station 1 of the ALICE Dimuon Arm Spectrometer for test-beam online monitoring and data analysis, and also in the detailed AliRoot detector simulation program.

Applying the object-oriented methodology allowed to define the technical parameters in a manageable, user-friendly way and will facilitate any future data file modifications. The graphics functions, based on the ROOT system, makes the mapping package interesting for a bench test user.

References

[1] "ALICE Dimuon Forward Spectrometer TDR", CERN/LHCC 99-22, 13 August 1999.
[2] ALICE DATE, CERN ALICE Data Acquisition Group.
[3] http://root.cern.ch
[4] "ALICE - Technical Proposal for A Large Ion Collider Experiment at the CERN LHC", CERN/LHC/95-71, December 1995.
[5] http://AliSoft.cern.ch/offline
[6] http://AliSoft.cern.ch/offline/codingconv.html
[7] "Addendum 1 to ALICE TDR 5", Chapter 4 and references therein, CERN/LHCC 2000-046, December 2000.
[8] E. Gamma, R. Helm, R. Johnson, J. Vlissides: Design Patterns, Elements of Reusable Object-Oriented Software. Addison Wesley, 1995.
[9] D. Guez and M. MacCormick, et al.: TestBeam ToolBox Reference Guide; ALICE-INT-2001-45, IPNO DR-02-001.

REFERENCES

1 Ralph Würzinger, *et al.*,
"Monte Carlo on cathode strip/pad chambers for the ALICE dimuon arm",
IPNO-96-08, Internal Note/DIM ALICE/ 97-10.

2 Attila Rimai, *et al.,*
"Spatial resolution studies in cathode pad and in cathode strip chambers",
IPNO-DRE-97-17; ALICE 97-23.

3 T. Matsui and H. Satz, Nucl. Phys. A 418 (1984) 447c.

4 H. Satz,
"Colour deconfinement and quarkonium binding",
J. Phys.G, 32 (2006) R25.

5 E772 Collaboration; D.M. Alde *et al.*, Phys. Rev. Lett. 66 (1991) 13.3

6 E772 Collaboration; D.M. Alde *et al.,* Phys. Rev. Lett. 64 (1990) 2479.

7 NA50 Collaboration; B. Alessandro *et al.,* Phys. Lett. B553 (2003) 167.

8 NA50 Collaboration; M.C. Abreu *et al.*, Phys. Lett. B410, (1997) 327.

9 NA50 Collaboration; B. Alessandro *et al*.,
Accepted for publication in European Physics Journal C,
CERN-PH-EP/2006-019

10 C. Lurenço, PhD Thesis, Universidade Técnica de Lisboa, IST, January 1995.
Available at http://www.cern.ch/NA38/theses/carlosl.ps.gz;
H. Santos, PhD Thesis, Universidade Técnica de Lisboa, IST, April 2001.
L. Capeli, PhD Thesis, Université Claude Bernard, Lyon, 2001.
R. Shahoian, PhD Thesis, Instituto Superior Técnico, Lisbon, 2001.
G. Borges, PhD Thesis, Instituto Superior Técnico, Lisbon, 2005.
Available at *http://www.cern.ch/NA50/theses.html*

11 NA50 Collaboration; B. Alessandro *et al.*,
Eur. Phys. J. C, 48 (2006) 329-341,
CERN-PH-EP/2006-018

12 NA50 Collaboration; B. Alessandro *et al.*, Eur. Phys. J. C., 39 (2005) 335-345.

13 ALICE Technical Proposal, CERN/LHCC 95-71

14 ALICE Technical Proposal Addendum 1, CERN/LHCC 96-32

15 ALICE PRR, Vol 1, J. Phys. G : Nucl. Part. Phys. 30 (2004) 1517-1763

16 ALICE Technical Design Report 5, Dimuon Forward Spectrometer, CERN/LHCC 99-22

17 ALICE Technical Design Report 5 Addendum 1, CERN/LHCC 2000-046

18 G. Charpak's illustrated Nobel Prize speech;
see *http://nobelprize.org/nobel_prizes/physics/laureates/1992/illpres*

19 GARFIELD by Rob Veenhof, Nucl**.** Instr. and Meth. A 419
see *http://garfield.web.cern.ch/garfield* (CERN W5050)

20 E. Mathieson, NIM in Phys. Res., A270 (1988) 602.

21 W.W.M. Allison and J.H. Cobb, Ann. Rev. Nucl. Part. Sci., 30 (1980) 253-298.

22 Ward Diethorn,
"A methane proportional counter system for natural radiocarbon measurements",
Carnegie Institute of Technology, Pennsylvania, Thesis report NYO-6628.

23 M.W. Charles ,
"Gas gain measurements in proportional counters",
Journal of Physics E: Scientific Instruments 1972 Volume 5, pp.95-100.

24 A. Zastawny,
"Gas amplification in a proportioanl counter with carbon dioxide",
Journ. Sci. Instrum. 43 (1966) pp. 179-181.

25 A. Zastawny,
"On a new formula for the gas amplification in a proportional counter",
J. Sci. instrum. 44 (1967) pp. 395-395.

26 A. Zastawny,
"Standardization of gas amplification description in proportional counters",
NIM A 385 (1997) 239-242.

27 J. C. Santiard *et al*., DIGIPLEX Chip Development, CERN-EPC/94-17.

28 J.C. Santiard and K. Marent, ALICE-PUB-2001-49.

29 M. Brooks, V. Cherniatin and A. Chikanian, BNL computer simulation CSCSIM,
private communication (1996, updated 1997).

30 MAGBOLTZ by Steve F. Biagi, Nucl. Instr. and Meth. A 421 (1999) 234;
see *http://consult.cern.ch/writeup/magboltz*

31 HEED by Igor B. Smirnov, Nucl. Instr. and Meth. A 554 (2005) 474;
see *http://consult.cern.ch/writeup/heed*

32 Original authors A. Willis (matrix inversion routine) and N. Willis (Mathieson charge distribution and signal integration)

33 Domenico Di Bari, INFN University Of Bari: Display program for the ALICE-RICH test beam (1997). Private communication.

34 OASIS acquisition system - Open Acquisition Systen IPN-Saturne.

35 Liliane Kharmandarian, PhD Thesis, Universite de Paris XI, IPNO-T-00-02 (1999)

36 IPN ALICE group; Nicole Willis *et al*.,
"Summary of the R&D performed at IPN Orsay for the Alice dimuon tracking chambers",
IPNO DR 02-024

37 F. Launay, Internal Note IPNO-03-0 (2003).

38 Y. Le Bornec, LHCC Report March 2004, see hypertext
//pcaliceweb02.cern.ch/static/Documents/LHCC/CR4/PSV_dimuon/dimuon_tracking.ppt

39 IPN ALICE group; M.P. Comets *et al*.,
"Results of the in-beam tests performed with Quadrant 0 of station 1 For the ALICE dimuon arm",
IPNO-DR 03-07.

40 Production Readiness Report, "Electronics of the ALICE dimuon tracking chambers ",
PRR_v09, ALICE-INT-2004-026.

41 David Guez, PhD Thesis No.7329, Universite de Paris XI , IPNO-T-03-05 (2003).

42 Loeb and Meek, "The mechanism of the electric spark", Stanford University Press, 1941.

43 J.S. Townsend,
"Ionization by collision",
Philisophical Magazine (1898-1977): 45 (1923) 444-456. ISSN: 0031-8086.

44 L.B. Loeb,
"Fundamental processes of electrical discharge in gases",
John Wiley and Sons, Inc., New York 1939.

45 J.M. Meek, Phys. Rev. 57 722 (1940).

46 Loeb and Meek, J. App. Phys. II (1940) 438-459

47 H. Raether, Zeits. f. Physik 110 (1938) 611.

48 H. Raether, Zeits. f. Physik 117 (1940) 386, 524.

49 M.E. Rose and S.A. Korff, Phys. Rev. 59 (1941) 850.

50 J.C. Curran and J.D. Craggs,
"Counting Tubes",
Butterworth, London, 1949

51 B. Rossi and H.H. Staub,
"Ionization chambers and counters",
McGraw-Hill, Inc., New York, First Edition, 1949.

52 D. Mazed, M. Baaliouamer,
"A semi-microscopic derivation of gas gain formula for proportional counters",
Nucl. Instr. and Meth. A 437 (1999) 381-392.

53 J.E. Bateman,

"A general model for the gain of gas avalanche counters",
RAL-TR-2002-007.